

# Advancing Empirical Models for the Hydrothermal Liquefaction of Microalgae

by

David C. Hietala

A dissertation submitted in partial fulfillment  
of the requirements for the degree of  
Doctor of Philosophy  
(Chemical Engineering)  
in The University of Michigan  
2018

Doctoral Committee:

Emeritus Professor Phillip E. Savage, Co-Chair  
Associate Professor Xiaoxia (Nina) Lin, Co-Chair  
Professor Bradley J. Cardinale  
Assistant Professor Heather B. Mayes

David C. Hietala

[hietala@umich.edu](mailto:hietala@umich.edu)

ORCID iD: [0000-0001-9469-6093](https://orcid.org/0000-0001-9469-6093)

© David C. Hietala 2018

For all of those who imbued my life with boundless inspiration.  
To my family, friends, and colleagues who made this dissertation possible.

## ACKNOWLEDGEMENTS

I would like to thank Phil Savage for his wisdom and guidance as my research advisor. I credit a lot of my growth as a critical thinker and a problem solver to our long-distance advising arrangement. Although Phil has been at Penn State throughout most of my time as a graduate student, he has always been committed to making himself available whenever I sought his advice. This setup of physical distance with virtual availability encouraged me to learn how to seek out the knowledge for problem solving on a routine basis, while limiting our interactions to only higher-level discussion. As a result, I became a very independent and confident researcher, and for that I thank Phil for being so accommodating throughout my time in graduate school.

I am grateful to my committee members, Brad Cardinale, Nina Lin, and Heather Mayes, who have provided excellent critical feedback over time as I have designed, conducted, and analyzed the experimental and computational results for this dissertation. I also had the pleasure of working with Brad, Nina, and Phil as well as Casey Godwin, Anita Narwani, and Aubrey Lashaway on an interdisciplinary collaboration between different teams of ecologists, engineers, and geneticists. That collaboration provided me with boundless new insights and information, including new ways to think about experimental design, how to analyze data with statistical rigor, and ways that researchers from different fields approach problem solving. The level of my research quality improved dramatically through these interactions, and for that I am thankful to everyone I worked with through the collaboration.

Casey Godwin, in particular, is an incredible colleague who has been a pleasure to work with over the last few years. Casey and I worked together on several projects, and he was

instrumental in the success of my final experimental project by agreeing to grow different batches of *Chlorella sorokiniana* for hydrothermal liquefaction experiments. He also helped with ammonium, phosphate, and total phosphorus measurements from many, many samples from that project. Through all of the troubleshooting and redo measurements, he was always there to help, and I truly cannot thank him enough for his efforts. Beyond the experimental assistance, he has always provided meticulous, thoughtful, and extensive feedback on my manuscript drafts. My technical writing and critical thinking abilities strengthened considerably as a result of his efforts. It has been a privilege to work with Casey, and I thank him again for everything.

Special thanks to Catherine Griffith, who provided HTL and FAMEs experimental assistance on many of my projects. She was often my go-to undergraduate research assistant whenever I needed help in the laboratory, and it was a pleasure working with her. I also thank Cristina Koss for all of her work with measuring FAMEs for the collaboration. Additionally, I gratefully acknowledge the following research assistants for their contributions to the collaboration: Angela Hoang, Kathryn Lindstrom, Matthew Craig Meader, David Mees, Hao Chen, Ching Shen Chan, Wincent Tandar, Lindsay Miller, and Matthew Irish.

I would like to thank all of the past and present members of the Savage group at Michigan and Penn State for their contributions, including Peter Valdez, Jacob Dickinson, Chad Huelsman, Thomas Yeh, Yingda Lu, Julia Faeth, Allison Franck, Na (Tiffany) Mo, Jennifer Jocz, Le (Claire) Yang, Donghai Xu, Ligang Luo, Nattapol (Mink) Arunattanamook, Teri Gule, Sha (Lisa) Li, James Sheehan, Jimeng Jiang, Yang Guo, Lili Qian, and Akhila Gollakota. I have learned a great deal from all of them, and I hope they have learned a few things from me along the way too. I especially thank Thomas and Jake for teaching me everything I know about gas chromatography and best practices for experimentalists in reaction engineering. Yingda was instrumental in teaching me and my undergraduate assistants about fatty acid transesterification methods and analyses, many of which were pioneered by another Savage group alumnus, Bobby Levine. I overlapped with Peter Valdez briefly, however he pioneered

kinetic analyses for microalgal HTL, and his approach laid much of the foundational work for me to build upon in my dissertation. The final kinetic model I developed is in many ways an homage to his original work while also a bold step forward for modeling within the field. I also thank James and Lili for their feedback and comments during group meetings and on my approaches for kinetic modeling. James's expertise in hydrothermal reactions of proteins in particular has been very helpful, and several reaction pathways in my model are based on his experimental observations.

I especially thank Julia for imparting all of her knowledge of HTL to me, both through experimental techniques and her knowledge of the state of the field. She was a great mentor to me during the first few years of graduate school, and I learned a lot about presentation design and problem solving from her, in particular.

I extend a very special thanks to Jenn, who has been with me as a Savage group colleague through nearly my entire journey as a graduate student. She has been an invaluable source of critical feedback, experimental expertise, and office comradery. Looking back at our various projects, it is clear that her experimental intuitions and my computational skills have permeated into each other's work, and we have both become better researchers as a result.

Mary Wakumoto, T. Michael Duncan, and Charles Monroe were easily the most influential teachers and professors I had in high school, college, and graduate school, respectively. They each contributed toward developing my passion for science, technology, engineering and mathematics, and I am grateful for the impact they had on my education. I thank Paulette Clancy and Brian Koo for working with me while I was an undergraduate research assistant at Cornell. That experience was also influential in my decision to start a Ph.D. program. Luke Griffith and Saeed Rahimian from the Monroe group were both very helpful with troubleshooting for projects involving my experimental and computational work, respectively.

Thanks to my parents, Jim and Johnna, my sister, Kristen, and my grandparents, Gerry

and Barb, for being so supportive, loving, and encouraging during my time in graduate school, and all the years leading up to it. They have been my foundation during each and every stage of my life, and I would not have gotten to this point without them. I am thankful for all of the time and energy they each have invested in me, and I will be forever grateful for their support.

I thank my girlfriend, Andrea Roberts, and my friends, Nishanth (Bob) Bhardwaj, Sumit Bhatnagar, Sarah Carl, Vikesh Chandrashekar, Cornelius Cilliers, Nora Evans, Nina Gasbarro, Savannah Hatt, Brett Hill, Rohil Pathak, Mason Smith, and Trenton Wilke for giving me endless activities to look forward to over these five years. I know without a doubt that I will look back on my time in graduate school fondly because of the memories we all made together. Thanks for making the experience so special, and I am excited to see what the future holds for all of us.

Thanks to the incredible Department of Chemical Engineering, including Kelly Raickovich, Susan Hamlin, Shelley Fellers, Pam Bogdanski, Jennifer Downey, and Sandy Swisher for their administrative support and assistance. Special thanks to Jennifer, Shelley, and Kelly for assisting with my numerous orders and Concur reports. Thanks to Michael Africa for providing technical support and helping set up our VLAN network and various computers for the laboratory and office. The modeling work in this dissertation would not have been possible without his support.

The University of Michigan College of Engineering, the U.S. National Science Foundation (Emerging Frontiers in Research Innovation grant award no. 1332342), and the Rackham Predoctoral Fellowship from the University of Michigan provided financial support. This research was supported in part through computational resources and services provided by Advanced Research Computing at the University of Michigan, Ann Arbor.

# TABLE OF CONTENTS

DEDICATION . . . . .	ii
ACKNOWLEDGEMENTS . . . . .	iii
LIST OF FIGURES . . . . .	xi
LIST OF TABLES . . . . .	xv
LIST OF APPENDICES . . . . .	xvii
LIST OF ABBREVIATIONS . . . . .	xviii
ABSTRACT . . . . .	xx
<b>CHAPTER</b>	
<b>I. Introduction . . . . .</b>	<b>1</b>
1.1 Motivation . . . . .	1
1.2 Hydrothermal liquefaction . . . . .	2
1.3 Factors affecting hydrothermal liquefaction . . . . .	3
1.4 Quantitative models for hydrothermal liquefaction . . . . .	5
1.5 Summary of research motivation . . . . .	6
<b>II. A quantitative kinetic model for the fast and isothermal hydrother-</b>	
<b>    mal liquefaction of <i>Nannochloropsis oculata</i> . . . . .</b>	<b>8</b>
2.1 Introduction . . . . .	9
2.2 Materials and Methods . . . . .	10
2.2.1 Experimental . . . . .	10
2.3 Results and Discussion . . . . .	13
2.3.1 Product fraction yields . . . . .	13
2.3.2 Kinetic model development . . . . .	18
2.3.3 Kinetic model results . . . . .	21
2.3.4 Calculated yields . . . . .	25

2.4	Conclusion . . . . .	30
<b>III. Influence of biodiversity, biochemical composition, and species identity on the quality of biomass and biocrude oil produced via hydrothermal liquefaction . . . . .</b>		
3.1	Introduction . . . . .	32
3.2	Materials and methods . . . . .	35
3.2.1	Microalgae cultivation . . . . .	35
3.2.2	Fatty acid esterification . . . . .	36
3.2.3	Ash content . . . . .	37
3.2.4	Protein and carbohydrate estimation . . . . .	38
3.2.5	Hydrothermal liquefaction . . . . .	38
3.3	Results and Discussion . . . . .	40
3.3.1	Species distribution . . . . .	40
3.3.2	Biomass properties . . . . .	40
3.3.3	Biocrude properties . . . . .	43
3.3.4	Polyculture performance relative to monocultures . . . . .	45
3.3.5	Extent of overyielding and underyielding by species in bi-cultures . . . . .	49
3.3.6	Effect of species identity and biochemical composition . . . . .	51
3.3.7	Trade-offs between product quality and quantity . . . . .	56
3.4	Conclusion . . . . .	58
<b>IV. The effects of biochemical composition, microalgal species, concentration, temperature, and time on biocrude production by hydrothermal liquefaction . . . . .</b>		
4.1	Introduction . . . . .	60
4.2	Materials and methods . . . . .	61
4.2.1	Microalgae feedstocks . . . . .	61
4.2.2	Slurry preparation . . . . .	62
4.2.3	Hydrothermal liquefaction . . . . .	63
4.2.4	Fatty-acid esterification . . . . .	67
4.2.5	Elemental content . . . . .	69
4.2.6	Biomass biochemical content . . . . .	69
4.2.7	Statistical analysis . . . . .	70
4.3	Results and discussion . . . . .	70
4.3.1	Biocrude yield . . . . .	70
4.3.2	Carbon content and recovery . . . . .	75
4.3.3	Hydrogen content and recovery . . . . .	77
4.3.4	Nitrogen content . . . . .	78
4.3.5	Nitrogen recovery . . . . .	81
4.3.6	Sulfur content . . . . .	82
4.3.7	Sulfur recovery . . . . .	84

4.3.8	Oxygen content and recovery . . . . .	85
4.3.9	Phosphorus content and recovery . . . . .	87
4.3.10	Higher-heating value . . . . .	88
4.3.11	Energy recovery . . . . .	89
4.3.12	Mass balances, solid characteristics, and gas yield . . . . .	90
4.3.13	Fatty-acid recovery . . . . .	90
4.4	Further discussion and conclusion . . . . .	95
4.4.1	Mild-reaction-severity reference point . . . . .	95
4.4.2	High-reaction-severity reference point . . . . .	96
4.4.3	Additional conclusions . . . . .	97
<b>V.</b>	<b>The impacts of temperature, time, concentration, biochemical composition, and microalgal species on the aqueous co-product from hydrothermal liquefaction . . . . .</b>	<b>98</b>
5.1	Introduction . . . . .	99
5.2	Materials and methods . . . . .	101
5.2.1	Microalgae feedstocks and slurry preparation . . . . .	101
5.2.2	Hydrothermal liquefaction . . . . .	101
5.2.3	Elemental content, ammonium, and phosphate . . . . .	102
5.2.4	Biomass biochemical content . . . . .	103
5.2.5	Statistical analysis . . . . .	103
5.3	Results and discussion . . . . .	103
5.3.1	Aqueous-phase-product yield . . . . .	104
5.3.2	Nitrogen recovery . . . . .	107
5.3.3	Phosphorus recovery . . . . .	112
5.3.4	Sulfur recovery . . . . .	115
5.3.5	Carbon recovery . . . . .	117
5.3.6	pH . . . . .	120
5.3.7	Engineering nutrient recovery and recycling . . . . .	122
5.4	Further discussion and conclusion . . . . .	125
5.4.1	Mild-reaction-severity reference point . . . . .	126
5.4.2	High-reaction-severity reference point . . . . .	128
5.4.3	Additional conclusions . . . . .	129
<b>VI.</b>	<b>A gravimetric, elemental, and multiphase kinetic model for the hydrothermal liquefaction of microalgae . . . . .</b>	<b>130</b>
6.1	Introduction . . . . .	131
6.2	Methods and model development . . . . .	131
6.2.1	Reaction network development . . . . .	131
6.2.2	Summary of governing equations and system components . . . . .	144
6.2.3	Model development in MATLAB . . . . .	147
6.3	Results and discussion . . . . .	148
6.3.1	Parity plots . . . . .	150

6.3.2	Product yields . . . . .	152
6.3.3	Carbon distribution . . . . .	155
6.3.4	Nitrogen distribution . . . . .	156
6.4	Conclusion . . . . .	159
<b>VII. Conclusion and recommendations . . . . .</b>		<b>160</b>
7.1	Significance of results in algal biofuel production . . . . .	160
7.2	Conclusion . . . . .	163
7.3	Recommendations for future research . . . . .	165
<b>APPENDICES . . . . .</b>		<b>168</b>
A.1	Representative 1.67-mL reactor heat-up temperature profiles . . . . .	170
A.2	Applying the Valdez and Savage (2013) model . . . . .	171
A.3	Product fraction yield adjustments . . . . .	171
A.4	Product fraction residuals . . . . .	174
A.5	Model validation . . . . .	175
A.6	Modeling carbon dioxide dissolution into the aqueous phase . . . . .	176
A.6.1	Kinetic limitations . . . . .	176
A.6.2	Thermodynamic limitations . . . . .	176
A.6.3	Mass transfer limitations . . . . .	177
B.1	Figures with constant-growth-temperature data . . . . .	183
B.2	Properties of biomass and biocrude for constant- and variable-growth-temperature cultures . . . . .	186
B.3	Additional quality vs. quantity sector charts . . . . .	190
C.1	Coefficients for Set 10 and 11 models . . . . .	192
D.1	Materials and methods . . . . .	194
D.2	Mass balance . . . . .	198
E.1	Biocrude elemental properties . . . . .	199
E.2	Biocrude fatty acid data . . . . .	204
F.1	Solid yield and elemental properties . . . . .	206
F.2	Solid fatty acid data . . . . .	210
G.1	Gas yield . . . . .	211
H.1	Aqueous yield . . . . .	212
H.2	Aqueous elemental properties . . . . .	214
I.1	Kinetic model constants and designations . . . . .	217
I.2	Carbon distribution solutions . . . . .	219
<b>BIBLIOGRAPHY . . . . .</b>		<b>220</b>

## LIST OF FIGURES

### Figure

2.1	Product fraction yields from the hydrothermal liquefaction of <i>Nannochloropsis oculata</i> as functions of final reactor temperature and holding time. . . .	14
2.2	Reaction network for the fast and isothermal hydrothermal liquefaction of <i>Nannochloropsis oculata</i> . . . . .	19
2.3	Instantaneous solids and aqueous-phase product conversion selectivities with respect to temperature. . . . .	22
2.4	Model solutions and experimentally observed yields over time at different set-point temperatures for solids, aqueous-phase products, biocrude, gas, and volatiles. . . . .	23
2.5	Parity plot of observed vs. calculated biocrude yields for literature data. . .	25
2.6	Solid, biocrude, gas, aqueous-phase, volatile, and aqueous-phase and volatile product yields calculated as functions of time, $t$ , and isothermal temperature, $T$ . . . . .	27
3.1	Species distribution within each species combination. . . . .	40
3.2	SAFA, MUFA, and PUFA yields and lipid, protein, and carbohydrate content for 1-, 2-, 4-, and 6-species combinations of <i>Ankistrodesmus falcatus</i> (A), <i>Chlorella sorokiniana</i> (B), <i>Pediastrum duplex</i> (C), <i>Scenedesmus acuminatus</i> (D), <i>Scenedesmus ecornis</i> (E), and <i>Selenastrum capricornutum</i> (F). . . . .	42
3.3	Biocrude yield, H/C, N content, O content, and HHV of 1-, 2-, 4-, and 6-species combinations of <i>Ankistrodesmus falcatus</i> (A), <i>Chlorella sorokiniana</i> (B), <i>Pediastrum duplex</i> (C), <i>Scenedesmus acuminatus</i> (D), <i>Scenedesmus ecornis</i> (E), and <i>Selenastrum capricornutum</i> (F). . . . .	44
3.4	Polyculture performance relative to thresholds for TO, AWA, and TU for SAFA, MUFA, and PUFA yields, lipid, protein, and carbohydrate contents, and biocrude yield, H/C, N content, O content, and HHV. . . . .	47
3.5	Relative extent ( $\xi^{\text{TO}}$ ) of net TO and TU in bicultures as a function of species inclusion of <i>Ankistrodesmus falcatus</i> (A), <i>Chlorella sorokiniana</i> (B), <i>Pediastrum duplex</i> (C), <i>Scenedesmus acuminatus</i> (D), <i>Scenedesmus ecornis</i> (E), and <i>Selenastrum capricornutum</i> (F) for SAFA, MUFA, and PUFA yields, lipid, protein, and carbohydrate contents, and biocrude yield, H/C, N content, O content, and HHV. . . . .	50

3.6	Quality vs. quantity sector charts for selected species combinations of <i>Ankistrodesmus falcatus</i> (A), <i>Chlorella sorokiniana</i> (B), <i>Pediastrum duplex</i> (C), <i>Scenedesmus acuminatus</i> (D), <i>Scenedesmus ecornis</i> (E), and <i>Selenastrum capricornutum</i> (F). . . . .	56
4.1	Biochemical profile ternary diagrams of six different microalgal feedstocks.	71
4.2	Biocrude yield versus reaction time grouped by temperature and initial concentration. . . . .	72
4.3	Biocrude carbon content and H/C ratio versus reaction time grouped by temperature and initial concentration. . . . .	76
4.4	Biocrude nitrogen content and recovery versus reaction time grouped by temperature and initial concentration. . . . .	79
4.5	Biocrude sulfur content and recovery versus reaction time grouped by temperature and initial concentration. . . . .	83
4.6	Biocrude oxygen content and recovery versus reaction time grouped by temperature and initial concentration. . . . .	86
4.7	Biocrude HHV and ER versus reaction time grouped by temperature and initial concentration. . . . .	89
4.8	SAFA, MUFA, and PUFA recoveries in the biocrude and solids as functions of temperature and time for low-lipid <i>Nannochloropsis</i> and high-lipid <i>Chlorella</i> .	91
5.1	Non-volatile aqueous-phase-product yield versus reaction time grouped by temperature and initial concentration. . . . .	105
5.2	Aqueous-phase-product nitrogen recovery as ammonium, as organic nitrogen, in total, and as ammonium relative to total aqueous nitrogen versus reaction time grouped by temperature and initial concentration. . . . .	109
5.3	Aqueous-phase-product phosphorus recovery as phosphate, as non-phosphate, in total, and phosphate relative to total aqueous phosphorus versus reaction time grouped by temperature and initial concentration. . . . .	114
5.4	Aqueous-phase-product sulfur recovery versus reaction time grouped by temperature and initial concentration. . . . .	116
5.5	Aqueous-phase-product carbon recovery versus reaction time and versus protein content grouped by temperature and initial concentration. . . . .	118
5.6	Aqueous phase pH versus reaction time and versus protein content grouped by temperature and initial concentration. . . . .	120
5.7	Nitrogen, phosphorus, sulfur, and carbon recoveries in the aqueous, biocrude, and solid phases versus reaction severities. . . . .	124
6.1	Parity plots of observed vs. calculated total, carbon, and nitrogen yields for solid, biocrude, and the collective aqueous, volatile, and gas products. . . . .	151
6.2	Model solutions for HTL product total yields versus reaction time grouped by temperature and initial concentration . . . . .	153
6.3	Carbon recovery residual versus total yield residual for solid, biocrude, and the collective aqueous, volatile, and gas products. . . . .	155
6.4	Model solutions for HTL product nitrogen recoveries and biocrude nitrogen content versus reaction time grouped by temperature and initial concentration.	157
A.1	Parity plots of observed vs. Valdez and Savage (2013) model-calculated yields for solids, aqueous-phase and volatile products, biocrude, and gas. . . . .	171

A.2	Product fraction residuals ( $x_i^{obs} - x_i^{calc}$ ) from the HTL of <i>Nannochloropsis oculata</i> plotted as functions of final reactor temperature and holding time. . . . .	174
A.3	Relative concentration profiles, $c(t, z)/c_H$ , of dissolved $\text{CO}_{2(aq)}$ with respect to depth of aqueous phase at different times. . . . .	182
B.1	Species abundance for constant-growth-temperature species combinations. . . . .	183
B.2	Polyculture performance relative to thresholds for TO, AWA, and TU for SAFA, MUFA, and PUFA yields, lipid, protein, and carbohydrate contents, and biocrude yield, H/C, N content, O content, and higher heating value under constant growth temperature. . . . .	184
B.3	Relative extent ( $\xi^{TO}$ ) of net TO and TU in bicultures as a function of species inclusion of <i>Ankistrodesmus falcatus</i> (A), <i>Chlorella sorokiniana</i> (B), <i>Pediastrum duplex</i> (C), <i>Scenedesmus acuminatus</i> (D), <i>Scenedesmus ecornis</i> (E), and <i>Selenastrum capricornutum</i> (F) for SAFA, MUFA, and PUFA yields, lipid, protein, and carbohydrate contents, and biocrude yield, H/C, N content, O content, and HHV for constant growth temperature. . . . .	185
B.4	Quality vs. quantity sector charts for constant-growth-temperature species combinations of <i>Ankistrodesmus falcatus</i> (A), <i>Chlorella sorokiniana</i> (B), <i>Pediastrum duplex</i> (C), <i>Scenedesmus acuminatus</i> (D), <i>Scenedesmus ecornis</i> (E), and <i>Selenastrum capricornutum</i> (F). . . . .	190
B.5	Quality vs. quantity sector charts for variable-growth-temperature species combinations of <i>Ankistrodesmus falcatus</i> (A), <i>Chlorella sorokiniana</i> (B), <i>Pediastrum duplex</i> (C), <i>Scenedesmus acuminatus</i> (D), <i>Scenedesmus ecornis</i> (E), and <i>Selenastrum capricornutum</i> (F). . . . .	191
D.1	Maximum growth rate and biomass productivity for nitrogen-replete and limited cultures of <i>Chlorella sorokiniana</i> . . . . .	195
D.2	Mass balances from direct measurements, including solid, biocrude, aqueous, and ammonia yields, and total mass balance, including gas yields, versus reaction time grouped by temperature and initial concentration. . . . .	198
E.1	Biocrude yield versus lipid content grouped by temperature and initial concentration. . . . .	199
E.2	Biocrude carbon recovery versus reaction time grouped by temperature and initial concentration. . . . .	200
E.3	Biocrude hydrogen content and recovery versus reaction time grouped by temperature and initial concentration. . . . .	200
E.4	Biocrude nitrogen content and recovery versus protein content grouped by temperature and initial concentration. . . . .	201
E.5	Biocrude sulfur content and recovery versus protein content grouped by temperature and initial concentration. . . . .	201
E.6	Biocrude oxygen content and recovery versus carbohydrate content grouped by temperature and initial concentration. . . . .	202
E.7	Biocrude phosphorus content and recovery versus reaction time grouped by temperature and initial concentration. . . . .	202
E.8	Biocrude HHV and ER versus lipid content grouped by temperature and initial concentration. . . . .	203

E.9	Biocrude SAFA, MUFA, PUFA, and total FA recovery versus reaction time grouped by temperature and initial concentration. . . . .	204
E.10	Biocrude C18:0 recovery relative to biomass C18:0 and total biomass C18 FAs versus reaction time grouped by temperature and initial concentration. . . . .	205
F.1	Solid yields versus reaction time grouped by temperature and initial concentration. . . . .	206
F.2	Solid carbon content and recovery versus reaction time grouped by temperature and initial concentration. . . . .	207
F.3	Solid hydrogen content and recovery versus reaction time grouped by temperature and initial concentration. . . . .	207
F.4	Solid nitrogen content and recovery versus reaction time grouped by temperature and initial concentration. . . . .	208
F.5	Solid sulfur content and recovery versus reaction time grouped by temperature and initial concentration. . . . .	208
F.6	Solid oxygen content and recovery versus reaction time grouped by temperature and initial concentration. . . . .	209
F.7	Solid phosphorus content and recovery versus reaction time grouped by temperature and initial concentration. . . . .	209
F.8	Solid SAFA, MUFA, PUFA, and total FA recovery versus reaction time grouped by temperature and initial concentration. . . . .	210
G.1	Gas yields versus reaction time grouped by temperature and initial concentration. . . . .	211
H.1	Non-volatile aqueous-phase-product yield versus protein content grouped by temperature and initial concentration. . . . .	212
H.2	Ammonia yield versus reaction time and protein content grouped by temperature and initial concentration. . . . .	213
H.3	Aqueous nitrogen recovery as ammonium, as organic nitrogen, in total, and as ammonium relative to total aqueous nitrogen versus protein content grouped by temperature and initial concentration. . . . .	214
H.4	Aqueous phosphorus recovery as phosphate and in total versus lipid content and ash content grouped by temperature and initial concentration. . . . .	215
H.5	Aqueous sulfur recovery versus biomass sulfur content grouped by temperature and initial concentration. . . . .	216
I.1	Model solutions for HTL product carbon recoveries versus reaction time grouped by temperature and initial concentration. . . . .	219

## LIST OF TABLES

### Table

2.1	Arrhenius parameters for reaction pathways in Figure 2.2. . . . .	21
3.1	Scientific names and identifiers of species employed. . . . .	36
3.2	Model types considered for correlating biocrude property $Y$ . . . . .	53
3.3	Summary of the best models for correlating biocrude properties based on only biochemical composition (Set 10) and based on biochemical composition and species identity (Set 11). . . . .	54
4.1	Biomass type legend. . . . .	71
4.2	Summary of differences in biocrude properties as a result of changing six different independent variables from two different reference points. . . . .	96
5.1	Summary of differences in ACP properties as a result of changing six different independent variables from two different reference points. . . . .	126
6.1	Reaction pathways incorporated in the kinetic model. . . . .	145
6.2	Component names, product fractions, and participating pathways in the kinetic model. . . . .	146
6.3	Types of residuals between observed ( $Y$ ) and calculated ( $\Gamma$ ) yields used in calculation of model objective function. . . . .	148
6.4	Arrhenius parameters for each pathway in the kinetic model. . . . .	149
7.1	Examples for strategies to either minimize process unit inputs locally or employ relatively more inputs locally to reduce inputs of other process units. . . . .	160
A.1	Representative heat-up temperature profiles for 1.67 mL stainless-steel batch reactors filled with deionized water at different set-point temperatures. . . . .	170
A.2	Original and adjusted product yields obtained after hydrothermal liquefaction of <i>Nannochloropsis oculata</i> . . . . .	173
A.3	Product fraction yields used for model validation. . . . .	175
B.1	Biochemical composition of constant-growth-temperature species combinations. . . . .	186
B.2	Biocrude properties of constant-growth-temperature species combinations. . . . .	187
B.3	Biochemical composition of variable-growth-temperature species combinations. . . . .	188
B.4	Biocrude properties of variable-growth-temperature species combinations. . . . .	189
C.1	Coefficients for Set 10 and 11 models in Table 3.2 (part 1). . . . .	192
C.2	Coefficients for Set 10 and 11 models in Table 3.2 (part 2). . . . .	192
C.3	Coefficients for Set 10 and 11 models in Table 3.2 (part 3). . . . .	193

C.4	Coefficients for Set 10 and 11 models in Table 3.2 (part 4). . . . .	193
C.5	Coefficients for Set 11 models in Table 3.2 (part 5). . . . .	193
D.1	Target solids content for different initial slurry concentrations as functions of reaction temperature. . . . .	194
D.2	Average heat-up temperature profiles for stainless-steel batch reactors filled with deionized water at different set-point temperatures. . . . .	196
D.3	Biomass elemental contents. . . . .	196
D.4	Biomass fatty acid contents and class distributions. . . . .	197
I.1	Molar mass, carbon content, and nitrogen content constants employed in the kinetic model. . . . .	217
I.2	Abundances of amino acids and dipeptides employed in the kinetic model. .	218
I.3	Group designations for different amino acids present in microalgae. . . . .	218

## LIST OF APPENDICES

### Appendix

A. Additional figures and calculations for Chapter II . . . . .	169
B. Constant-growth-temperature figures and tabular data for Chapter III . . . .	183
C. Parameters for multiple linear regression models in Chapter III . . . . .	192
D. Additional biomass data and figures, calculations, temperature profiles, and mass balances for Chapter IV . . . . .	194
E. Additional biocrude property figures for Chapter IV . . . . .	199
F. Additional solid property data and figures for Chapter IV . . . . .	206
G. Additional gas data and figure for Chapter IV . . . . .	211
H. Additional aqueous property figures for Chapter V . . . . .	212
I. Constants and additional figures for Chapter VI . . . . .	217

## LIST OF ABBREVIATIONS

<b>AA</b>	amino acid
<b>ACP</b>	aqueous co-product
<b>AICc</b>	Akaike Information Criterion with correction for finite sample size
<b>AWA</b>	abundance-weighted average
<b>AQ</b>	aqueous-phase product
<b>BC</b>	biocrude
<b>BCH</b>	biochar
<b>CAR</b>	carbohydrate
<b>DAS</b>	dissolved ash
<b>DCM</b>	dichloromethane
<b>ER</b>	energy recovery
<b>EROI</b>	energy return on investment
<b>ESS</b>	explained sum of squares
<b>FA</b>	fatty acid
<b>FAME</b>	fatty acid methyl ester
<b>FT-ICR MS</b>	Fourier-transform ion cyclotron resonance mass spectrometry
<b>GC</b>	gas chromatography
<b>GC-MS</b>	gas chromatograph with mass spectrophotometer
<b>GC-FID</b>	gas chromatograph with flame ionization detector
<b>HHV</b>	higher-heating value

**ICP-OES** inductively coupled plasma optical emission spectrometry

**HTL** hydrothermal liquefaction

**HPLC** high-performance liquid chromatography

**LIP** lipid

**MUFA** monounsaturated fatty acid

**ODE** ordinary differential equation

**PEP** peptide

**PPE** polypeptide

**PSA** polysaccharide

**PSS** partial sum of squares

**PRO** protein

**PUFA** polyunsaturated fatty acid

**rcf** relative centrifugal force

**RMSD** root-mean-square deviation

**rpm** revolutions per minute

**SAFA** saturated fatty acid

**SAC** saccharide

**SD** standard deviation

**SE** standard error

**SSE** sum of squared errors

**TO** transgressive overyielding

**TU** transgressive underyielding

## ABSTRACT

Hydrothermal liquefaction (HTL) is a sustainable-energy technology used to convert microalgae into an energy-dense biofuel precursor known as biocrude oil. This dissertation illuminates myriad effects of HTL process inputs on product distribution and composition that provide the foundation for advancing new quantitative models of HTL. Employing fast-heating reactors with measured temperature profiles for the HTL of *Nannochloropsis oculata* enabled kinetic modeling over significantly shorter timescales (10 s – 10 min) than previously established. This improved model demonstrated that the kinetics of biocrude and aqueous co-product (ACP) formation at 300 °C occur on the timescale of just seconds, significantly shorter than previously thought. Regression models of biocrude properties as functions of feedstock characteristics enabled quantification of species-identity effects for the first time, which ranged from 11 to 40 % of those of biochemical composition.

The aforementioned insights, along with identified gaps in the literature, informed a more comprehensive and rigorous design of experiments probing the effects of temperature, reaction time, slurry concentration, biochemical composition, and species identity on HTL product yields and elemental compositions. All examined factors affected the yield and makeup of the biocrude, aqueous, solid, and gas products, especially temperature and biochemical composition. The data suggested that increased slurry concentration promotes Maillard reactions between amino acids and saccharides that result in increased biocrude yield, C content, and N content and the inhibition of aqueous ammonium recovery (a nutrient for recycling). Fast HTL (300 °C, 3.2 min) of high-lipid, low-concentration slurries

provided recoveries of high-value saturated, monounsaturated, and polyunsaturated fatty acids in the biocrude of up to 89, 80, and 65 wt%, respectively. The same slurries reacted at 200 °C for 31.6 min maximized ACP recyclability while limiting N and S recovery in the biocrude to less than 5 and 8 %, respectively.

These empirical results enabled the development of a novel gravimetric, elemental, and multiphase kinetic model for microalgal HTL. This model leverages known classes of reactions that occur during HTL, such as hydrolysis, Maillard reactions, and deamination, to construct a reaction network with 16 unique pathways. These pathways established a system of coupled rate equations governing the temporal evolution of total, carbon, and nitrogen yields for 22 unique lumped-product fractions. The model captures many empirical trends over a broad range of reaction conditions and feedstock biochemical profiles. In particular, slurry concentration and Maillard-reaction effects are quantified for the first time. Agreement between calculated and observed quantities was particularly high for the biocrude and ammonia fractions, substantiating the utility of the model for optimizing important HTL process metrics that will ultimately enhance overall process sustainability and energy return on investment.

# CHAPTER I

## Introduction

### 1.1 Motivation

In 2016, the transportation sector produced 1.86 billion metric tons of CO<sub>2</sub>-equivalent emissions, or about 28.5 % of total United States greenhouse gas emissions [1]. 90 % of those emissions originated from petroleum-based sources, contributing toward the rise of atmospheric carbon dioxide concentrations and associated effects of climate change. Thus, the engineering of viable sustainable energy technologies to curtail these anthropogenic emissions is one of the greatest global challenges of the 21<sup>st</sup> century.

Algal biomass has emerged as a compelling feedstock for renewable fuel production due to its high photosynthetic efficiency, ability to grow on non-arable land, and comparatively high energy density [2, 3]. Algae can also provide supplementary environmental benefits via wastewater treatment and nutrient recovery from agricultural systems [4, 5]. Different species of microalgae can also be grown together as polycultures to achieve enhanced process sustainability, for example through more stable biomass production over time [6], improved resource use efficiency [7], and improved multifunctionality [8]. Given that algae grow in aqueous media to concentrations of 0.01 to 0.04 wt % [6], processing technologies that avoid drying the biomass have the potential for higher overall energy return on investment (EROI).

## 1.2 Hydrothermal liquefaction

One such technology is hydrothermal liquefaction (HTL), which employs hot ( $150 < T < 400$  °C), compressed ( $5 < P < 250$  bar) water as the reaction medium to convert whole algal biomass into an energy-dense biocrude oil, a nutrient-rich aqueous co-product (ACP), a solid by-product, and gases [9, 10]. HTL exploits the properties of subcritical, high-temperature water, including an increased ion product to facilitate acid- and base-catalyzed reactions and decreased dielectric constant to solvate significantly less polar compounds than possible at ambient conditions [11]. These properties enable water to degrade the lipid, protein, and carbohydrate biomolecules in microalgae into smaller compounds that further react with water or each other to form the biocrude, aqueous, solid, and gas products [12].

The lumped HTL product fractions can contain tens of thousands of compounds spanning a variety of chemical classes that impact their quality. For example, the biocrude fraction contains fatty acids derived from the biomass lipid fraction that represent some of the highest-quality fuel components in microalgae due to their long-methylene-chain structure. The biomass protein fraction hydrolyzes into peptides and amino acids that further react into secondary products that significantly contribute to the quantity of biocrude and ACP yielded [13]; however, the nitrogen content introduced by those compounds is detrimental to biocrude quality but desired in the ACP for subsequent nutrient recycling. Finally, biomass carbohydrates contribute the least to biocrude formation [13] and largely degrade into aqueous-phase soluble sugars, aldehydes, ketones, and organic acids that eventually gasify, or convert to biochar in the solid fraction [14, 15].

Due to the variability in the composition of the compounds in biocrude oil and the prevalence of undesired heteroatoms such as nitrogen, oxygen, and sulfur, catalytic upgrading is required to improve biocrude quality before it can be processed in existing refineries [16, 17]. This catalytic upgrading step is also energy intensive, potentially costly, and imposes its own environmental impacts. Furthermore, the nutrient-rich ACP can be recycled whole for algal cultivation [18, 19] or gasified to obtain fuel gases [20], both of which are crucial

for overall process sustainability. It is therefore desirable to engineer HTL in a way that maximizes carbon and hydrogen recovery in the biocrude to increase energy density and recovery (instead of in the ACP, where it would need to be hydrothermally gasified), while also maximizing nitrogen, phosphorus, and sulfur recoveries in the ACP for recycling (instead of in the biocrude, which requires catalytic removal).

### 1.3 Factors affecting hydrothermal liquefaction

The reactivity of the algal biomass during HTL and the yield and properties of the different reaction products are affected by a host of factors. The most prominent input variables include temperature and time [21–37], slurry concentration [21, 23, 24, 32, 37, 38], biochemical composition (e.g., lipids, proteins, and carbohydrates) [13, 15, 28, 29, 36, 39–44], and the identity of the species employed (e.g., via differing cellular morphology) [28, 39, 42]. Many previous studies of these factors have various limitations, however. Long heat-up times ( $> 3$  min) frequently observed in previous studies [21–23, 27, 28, 31, 32] obfuscated the independent effects of temperature and time. Concentration is typically viewed as a less significant factor than temperature and time, despite being examined generally only at one or two reaction conditions [21, 23, 24, 37, 38]; without a holistic exploration of concentration effects over a wide range of reaction conditions, any deductions about its impacts are tentative. Biochemical composition has been a subject of scrutiny at high reaction severity (i.e., temperature and time), but often only for one or two reaction conditions [13, 15, 39–45]. This factor remains relatively unexplored at low and mild reaction severities, which are regions of interest for kinetic analysis. A more complete examination of the effects of slurry concentration and biochemical composition over a broad range of temperatures and times using fast-heating reactors could illuminate previously unobserved effects on product yield and distribution that may have been missed by previous studies.

Prior efforts showed that any differences in product distribution between different species of microalgae at high reaction severity can be largely explained by proximate biochemical

composition (lipids, proteins, carbohydrates) [13, 15, 41]. Variability in biocrude and ACP properties between different species after controlling for proximate biochemical composition has received little attention to date [28, 39]. In the hydrothermal environment, especially at low to moderate reaction severities conducive to hydrolysis, differences in cell morphology (e.g., cell wall strength and surface-area-to-volume ratio) may affect microalgal reactivity, independent of proximate biochemical composition. Even at high reaction severity, proximate biochemical composition may be insufficient for adequately correlating product characteristics, and more detailed information about biochemical composition (e.g., DNA, RNA, and unsaponifiable lipid contents) may be important for explaining product yield and property variation.

Although the aforementioned variables are typically only examined individually, they can be coupled during HTL. As an example, different types of biomolecules exhibit different rates of hydrolysis as a function of reaction severity, yielding myriad degradation products [12]. Increased slurry concentration can promote interactions between these degradation products through reaction pathways such as the Maillard reaction between reducing sugars and amino acids [46, 47]. Furthermore, even with the same biochemical composition, differences in cell wall resiliency to hydrothermal degradation [39] and possibly cell morphology between different microalgal species may affect their reactivity during HTL, depending on slurry concentration (decreased concentration increases exposure to high-temperature water) and reaction severity (increased severity increases rate of degradation). No previous study has probed all of these factors together when examining HTL product yield and properties. There could, therefore, be previously unexamined synergistic or antagonistic effects between different feedstock characteristics and reaction conditions. Generally only a few of these variables are considered over relatively narrow ranges, which limits the ability of the field to holistically understand and ultimately model HTL kinetics and may miss sets of HTL parameters that offer improved biocrude yield and quality and/or improved nutrient recovery in the ACP. This dissertation aims to address many of these shortcomings exhibited by

prior studies in the literature to provide an empirical basis for developing new mathematical models for microalgal HTL.

## 1.4 Quantitative models for hydrothermal liquefaction

There have been several previous attempts to model microalgal HTL product yields and properties via multiple linear regression of biochemical composition at fixed HTL reaction conditions [13, 15, 40, 41, 48, 49] or multiple linear regression of reaction conditions for a fixed microalgal species and biochemical profile [32, 50]. These models are useful for understanding the effects of continuously varying specific HTL inputs; however, they are limited to certain regions of the reaction domain, often  $\geq 300$  °C and  $\geq 30$  min, or a specific type of microalgae. A mathematical model of HTL product composition and yield that allows for both reaction conditions and feedstock conditions to be varied has yet to be developed, but would significantly increase the capacity for HTL process optimization of biocrude production and ACP nutrient recycling. A chemical-kinetics approach is well suited for the development of such a model because it enables tracking of the components of the system governed by a reaction network and associated rates of reaction. Such components, including their yield and elemental properties, could be tracked as functions of temperature, time, concentration, and biochemical composition.

One “bottom-up” method for this approach is to assemble the behavior of microalgae during HTL through the amalgamation of microkinetic models describing the behavior of individual components or classes of biomolecules in the microalgae. For example, such models could describe the individual hydrothermal reaction pathways for specific amino acids, such as alanine, glycine, phenylalanine, and cysteine, or the broader behavior of amino acids in general. Indeed, there have been myriad examinations of hydrothermal reactions for various biochemical components of microalgae, including lipids, proteins, carbohydrates, and their associated degradation products [12], including one such study of cholesterol by the author of this dissertation [51]. One issue with such an approach is that reactions between

biomolecule degradation products, such as the Maillard reaction between sugars and amino acids [46, 47, 52], are difficult to account for in their entirety without testing all possible binary interactions. Another issue is that such models, which could contain hundreds or thousands of rate equations, may be inaccessible without sufficient computing power and time.

Conversely, a “top-down” approach instead attempts to quantitatively describe product yield and composition evolution through experimental data of microalgae themselves [53]. As an example, one such model describes the time-dependent evolution of the HTL product fractions as functions of the biochemical profile of the microalgae and temperature [54]. These models have several clear advantages over the bottom-up approach. Critically, top-down models are constructed using real microalgal experimental data, and thus are more likely to predict HTL product distribution with higher fidelity. Additionally, they may be more tractable than otherwise unwieldy bottom-up models comprising a collection of microkinetic models. To date, there have been relatively few attempts to model microalgal HTL using this approach, and none have considered slurry concentration or attempted to correlate the elemental content of the product fractions. A more comprehensive kinetic model that fills gaps in our understanding of how the HTL product distribution responds to different inputs would have tremendous value for optimization of biocrude production and ACP recycling.

## 1.5 Summary of research motivation

The objective of this dissertation is to illuminate many of the areas that were previously unexplored in the literature through comprehensive experiments that provide the basis for developing more advanced mathematical models for HTL. In Chapter II, we explore HTL for the microalga *Nannochloropsis oculata* over a broader range of temperatures and times to establish a kinetic model valid over shorter timescales than previous models. We consider the effects of using algal polycultures on the quality of biocrude oil produced by HTL in Chapter III, and, for the first time, quantitatively decouple the effects of biochemical com-

position and species identity on biocrude properties. These two studies, along with insights from the literature, inform a comprehensive examination of the effects of temperature, time, slurry concentration, biochemical composition, and species identity on the biocrude and aqueous product fractions in Chapter IV and Chapter V, respectively. Finally, we use these data and documented reaction pathways from the literature to create the most advanced kinetic model of microalgal HTL to date in Chapter VI. For the first time, we employ known, molecular-scale reaction pathways to establish a reaction network and governing system of rate equations to predict the total mass, carbon, and nitrogen yields for the solid, biocrude, aqueous, and gas products. This model pioneers a new approach for HTL reaction engineering that allows for much more holistic optimization than previously possible, ultimately enabling improved process sustainability and EROI.

## CHAPTER II

# A quantitative kinetic model for the fast and isothermal hydrothermal liquefaction of *Nannochloropsis oculata*

This chapter contains results that were originally published in *Bioresource Technology* written along with co-authors Julia L. Faeth and Phillip E. Savage [34]. To elucidate the underlying kinetics for this process, we conducted isothermal and non-isothermal reactions over a broad range of holding times (10 s – 60 min), temperatures (100 – 400 °C), and average heating rates (110 – 350 °C min<sup>-1</sup>). Biocrude reached high yields ( $\geq 37$  wt %) within 2 min for set-point temperatures of 350 °C or higher. We developed a microalgal HTL kinetic model valid from 10 s – 60 min, including significantly shorter timescales (10 s – 10 min) than any previous model. The model predicts that up to 46 wt % biocrude yields are achievable at 400 °C and 1 min, reaffirming the utility of short holding times and “fast” HTL. We highlight potential trade-offs between maximizing biocrude quantity and facilitating aqueous phase recovery, which may improve biocrude quality. The illumination of the relevant timescales for HTL kinetics at different temperatures via the quantitative model presented herein informed the expanded design of HTL experiments described in Chapters IV and V.

## 2.1 Introduction

Numerous studies have examined the effects of temperature and holding time on the product distribution created by isothermal HTL of microalgae [21, 22, 24, 27]. These studies all concluded that temperature has a much greater effect on product distribution than holding time; however the holding times employed were long (10 – 120 min) and reactions were generally quenched well after most algal solids had reacted to form products at temperatures relevant to HTL ( $T \geq 250$  °C).

Compared to prior work on isothermal HTL, far fewer studies have examined non-isothermal HTL with rapid heating (fast HTL). Faeth et al. [25] used average heating rates of 170 – 350 °C min<sup>-1</sup> and obtained comparable or higher biocrude yields than from isothermal conditions but over much shorter timescales (1 – 5 min). The results suggest that microalgal HTL occurs on timescales much shorter than previously thought. Others have demonstrated similar results for fast HTL in batch reactors of corn stover [55], bacteria and yeast [56], and macroalgae [57], and for continuous HTL of microalgae (200 – 990 °C min<sup>-1</sup>) [38, 58]. Moreover, recently Cheng et al. [59] developed a glass- and silicon-based chip to achieve even more rapid heating rates ( $\sim 900$  °C min<sup>-1</sup>). They observed appreciable biocrude formation (38 % of maximum fluorescence intensity) at 1 min for at set-point temperature of 300 °C, further demonstrating the short timescales of algal HTL kinetics.

Despite this recent shift toward shorter holding times (1 – 5 min) [25, 38, 58, 59], the field currently lacks a comprehensive examination of HTL product fraction evolution with respect to time, temperature, and heating rate over timescales short enough to elucidate reaction kinetics. This gap in the literature presents an opportunity to explore these process variables in a more systematic manner. Additionally, few attempts have been made to quantitatively model microalgal HTL kinetics. There have been several attempts to model HTL product distribution at specific isothermal HTL conditions based on the biochemical composition of the microalgae [13, 40, 48], but none of those models attempt to predict kinetic behavior. Valdez and Savage [53] developed a reaction network and posited the

first kinetic model for the (isothermal) HTL of *Nannochloropsis oculata*, a marine species of microalgae, encompassing a wide range of temperatures (250 – 400 °C) and holding times (10 – 90 min). This model successfully correlated the yields of solid, biocrude, aqueous-phase, and gas products for the reaction conditions within the scope of the study. However, the data used to develop the model only included experiments with holding times of 10 min or longer, with no data at low solids conversion and little variation in product distribution by 20 min. This restriction on reaction times was imposed such that all reactions operated under predominantly isothermal conditions (reactor heat-up contributed to  $\leq 50$  % of the holding time).

It is essential that a microalgal HTL kinetic model incorporates data collected on the same timescale over which reactions occur and that the actual temperature profile experienced inside the reactor is known if the heat-up time is comparable to the holding time. In this chapter, we sought to investigate and decouple the effects of time, temperature, and heating rate on HTL product yields. We then used this database to develop a modified reaction network and quantitative kinetic model to calculate HTL product yields over a broad range of temperatures (200 – 400 °C), holding times (10 s – 60 min), and average heating rates (110 – 350 °C min<sup>-1</sup>). This is the first kinetic model for fast HTL.

## 2.2 Materials and Methods

### 2.2.1 Experimental

A preservative-free slurry of  $31 \pm 1$  wt % (standard deviation, SD) *Nannochloropsis oculata* and water was purchased from Reed Mariculture, who reported its composition to be 59 wt % proteins, 14 wt % lipids, and 20 wt % carbohydrates. The ash content was previously reported to be 6 wt % [25]. We constructed 1.67 mL batch reactors from a  $\frac{3}{8}$  in. Swagelok<sup>®</sup> port connector and two caps, all of 316 stainless-steel construction. We loaded each reactor with enough algae slurry (0.309 – 0.589 g) and deionized water (0.353 – 0.673

g) to constitute a 15 wt % slurry of algae in water. We calculated reactor loadings such that reactor pressures would not exceed 400 bar at the final temperature. After loading, reactors were sealed to 45 ft-lbs. using a torque wrench.

Additional 1.50 mL proxy reactors for temperature measurements were constructed using a  $3/8$ -in. port connector, a cap, and a bored-through reducing union (reducing the internal diameter from  $3/8$  in. to  $1/8$  in.). An Omega Engineering, Inc.  $1/8$ -in.-diameter 18-in.-long stainless-steel-clad K-type thermocouple was inserted into the  $1/8$ -in. end of the reducing union such that the tip of the thermocouple resided in the middle of the reactor body when closed. We loaded each proxy reactor with enough deionized water to match approximately the total density in the HTL reactors. An Omega Engineering, Inc. UWBT-TC-UST-NA Datalogger recorded the temperature measured by the thermocouples in the proxy reactors every 0.1 s.

The loaded, sealed reactors were submerged in a Techne IFB-51 fluidized sand bath preheated to the specified set-point temperature. We define holding time as the time from the instant the reactor begins to heat up to the instant the reactor starts to cool down. At the end of the holding time, reactors were removed from the fluidized sand bath and quickly quenched in cold water. After about 3 min, the exterior of the reactors was dried with paper towels. For reactions with holding times less than 1 min, we placed proxy reactors in the sand bath simultaneously with the reaction vessels, and for all other reactions ( $t > 1$  min) we used temperature profiles previously recorded at the same set-point temperature, averaged over at least two independent trials. Typically, reactors immersed at set-point temperatures of 200, 300, 400, 500, and 600 °C exhibited average heating rates of 110, 170, 230, 290, and 350 °C min<sup>-1</sup>, respectively. These heating rates were calculated as linear averages over the time it took reactors to reach within 95 % of the maximum temperature change, typically about 95 s. For example, this threshold for a set-point temperature of 300 °C would occur when the temperature is about 286 °C ( $0.95 = (286 - 25)/(300 - 25)$ ). Representative temperature profiles are listed in Table A.1 in Appendix A.

Within 2 h after quenching and drying, reactors were weighed, tapped forcefully on the benchtop three times, opened to release gases, and weighed again. We calculated the mass of gas evolved as the difference between these two reactor masses. Biocrude, aqueous-phase, and solid products were recovered according to the procedure described previously [24]. This procedure involves pouring the reactor contents into a glass conical centrifuge tube, rinsing the reactor with 9 mL of dichloromethane (DCM) (> 95 % optima grade, Fisher Scientific) in small aliquots, and collecting these rinsings in the same glass tube. This tube was then mixed using a vortex mixer and centrifuged to facilitate phase separation.

Following centrifugation, the organic (DCM-soluble) phase was manually collected using a pipette and transferred to a pre-weighed glass tube. The remaining aqueous phase and solid products were again mixed using a vortex mixer and centrifuged. The aqueous phase was transferred to a pre-weighed vial via pipette and the residual solids were left in the original glass tube. Tubes containing the DCM-dissolved organics, remaining solids, and wet aqueous phase were each dried under nitrogen (99.998 %, Metro Welding Supply Corp.), using a Labconco<sup>®</sup> RapidVap<sup>®</sup> Vertex<sup>™</sup> Dry Evaporator with a solid aluminum heating block at 35, 35, and 70 °C, respectively, and weighed until two consecutive cycles of drying and weighing produced tube masses varying by < 2 mg. The dried organic, solid, and aqueous phases are what we term the biocrude, solid, and aqueous-phase products, respectively. Furthermore, we define the volatiles fraction to be the compounds primarily dissolved in the aqueous phase but lost due to evaporation upon drying at 70 °C [24]. We also report the sum of the aqueous-phase and volatile product fractions, which is an estimate of the total material in the aqueous phase immediately post HTL [21]. Product yields were calculated by dividing the mass of product collected by the initial mass of dry algae for a given reaction. The yield of volatiles was calculated by difference. In a few cases we observed gas yields that were higher than expected based on other data collected under similar reaction conditions. In these rare cases we used interpolation to estimate the gas yields. For some reactions conducted below 250 °C, the insolubility of unreacted algae in DCM made it difficult to

recover all of the material. In these cases we scaled the solid and aqueous-phase product yields to close the mass balance. Details about the procedure used for adjustment along with both the unadjusted and adjusted yields appear in Appendix A.

## 2.3 Results and Discussion

This section reports the product yields from HTL of *Nannochloropsis oculata* at temperatures of 100 – 400 °C, holding times of 10 s – 60 min, and average heating rates of 110 – 350 °C min<sup>-1</sup>. Following the experimental results, we propose a reaction network and kinetic model.

### 2.3.1 Product fraction yields

Figure 2.1 depicts the yields of product fraction  $i$  ( $x_i$ ) from HTL of *Nannochloropsis oculata*. The black lines on the plots represent typical reactor temperature profiles resulting from set-point temperatures of 200, 300, 400, and 500 °C. Each individual point represents a single HTL reaction shaded to show the product fraction yield and plotted at the holding time and final reactor temperature reached. Table A.2 in Appendix A lists the exact product yields used in Figure 2.1.

Figure 2.1a depicts solid yields. To the best of our knowledge, this is the first study to capture the shift from low conversion (< 30 %) at short holding times ( $t < 1$  min) and low temperatures ( $T < 250$  °C) to high conversion ( $\sim 100$  %) at typical isothermal HTL conditions ( $t > 20$  min,  $T > 300$  °C). As expected, solid yields are highest at short holding times and low temperatures (bottom left) and lowest at long holding times and high temperatures (top right). Solid yields decrease monotonically with increasing reaction severity throughout the entire range of HTL reaction conditions examined until a lower bound (on the order of the ash content) is reached. At a set-point temperature of 300 °C, for example, this lower bound is observed for  $t > 3$  min, and this time decreases with increasing temperature. At  $t > 3$  min, and  $T = 200$  °C, solid product yields decrease with increasing holding times, though complete

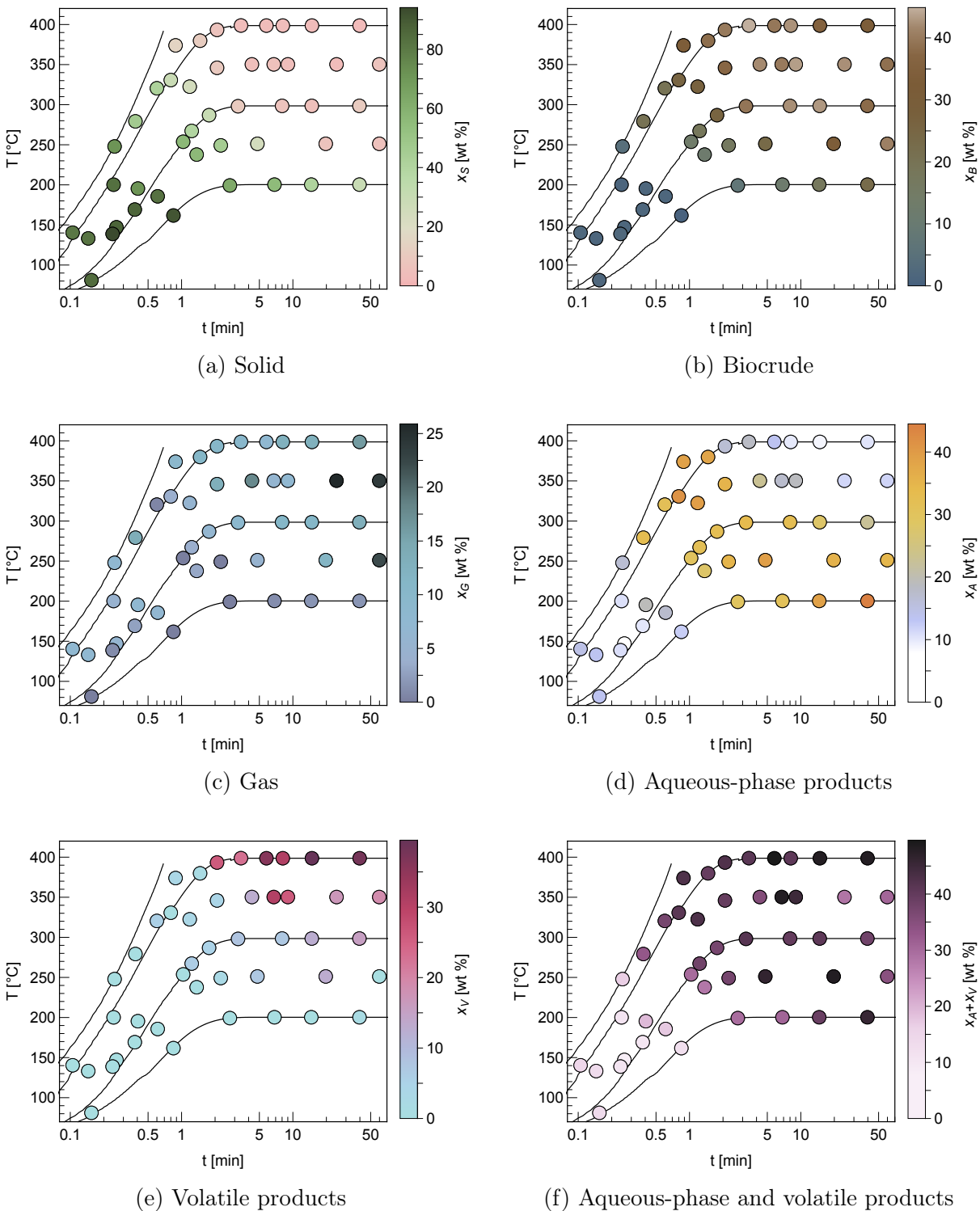


Figure 2.1: Product fraction yields from the hydrothermal liquefaction of *Nannochloropsis oculata* as functions of final reactor temperature and holding time. Solid lines represent typical temperature profiles based on sand-bath set-point temperatures of 200, 300, 400, and 500 °C.

conversion is not observed within the range of reaction times examined at this temperature. Above 200 °C, solids yields decrease dramatically with increasing temperature; moreover, solids conversion at 200 °C is remarkably slower than at 250 °C, compared to other 50 °C increments (e.g., 250 °C compared to 300 °C). This may indicate that hydrolysis of algal biomolecules becomes much more kinetically favorable in the range of 200 – 250 °C, which is consistent with temperatures reported in the literature [22, 60, 61].

Figure 2.1b displays biocrude yields. The trends in biocrude yield were of comparable magnitude and opposite to those of solid yields, with yields generally increasing as a function of temperature and time. At short holding times, a maximum yield was reached at around 300 – 400 °C and 3 – 7 min. At longer times characteristic of isothermal HTL, this maximum yield shifts to a lower range of 250 – 350 °C, with little variation in yields after 5 min. This temperature range for maximizing biocrude yield and these trends are in agreement with myriad studies for isothermal HTL [24, 27, 62–64]. At 400 °C, biocrude yields show a slight, yet non-negligible decrease with increasing reaction time. Decreasing biocrude yields with increasing time at temperatures above 350 °C has also been observed previously [21, 24].

Figure 2.1c shows that gas yields generally increase with increasing temperature and time. Although the trend at long reaction times is consistent with previous studies [21, 22, 24, 27], the gas yields in the present work are higher than those reported previously for *Nannochloropsis oculata* [24] but on the same magnitude as those for other microalgae [21, 22]. This difference in observed gas product yields may be a consequence of measurement technique. In this study, we measured the mass of gas evolved shortly after the reaction by the difference in mass of vented and unvented reactors, however Valdez et al. [24] employed reactors equipped with gas valves to measure gas by gas chromatography (GC) analysis. We took care to ensure that the mass of gas evolved was measured within 2 h after reactions were quenched to limit the extent that carbon dioxide, the principal component of the gas phase [10, 21, 22], dissolves in the aqueous phase. The dissolution kinetics of carbon dioxide from the gas phase into the aqueous phase are fast, with a forward rate constant of  $1 \times 10^{10}$

$\text{s}^{-1}$  [65]. However, diffusion of dissolved carbon dioxide in water is slow, with a diffusion coefficient of  $\mathcal{D} = 2.233 \times 10^{-9} \text{ m}^2/\text{s}$  [66]. Our analysis shows that  $< 25 \%$  of the carbon dioxide would have dissolved in the aqueous phase within 2 h of time between quenching a reaction and gas measurement. Moreover, we agitated the reactors by forcefully tapping them on the benchtop three times before opening to further liberate carbon dioxide back into the gas phase. See Section A.6 in Appendix A for an extensive analysis of this phenomenon.

Figure 2.1d depicts aqueous-phase product yields. At every set-point temperature except 200 °C, aqueous-phase product yields increase initially to a maximum value at moderate reaction severity, then decrease at high reaction severity. At short times, they reach a maximum at about 320 – 380 °C and 45 s – 2 min. We postulate that rapid heating (175 – 375 °C  $\text{min}^{-1}$ ) could be facilitating protein and amino acid recovery in the aqueous phase. Garcia-Moscoso et al. [67] developed a similar, yet more rapid process they refer to as flash hydrolysis (240 – 320 °C, 6 – 12 s) with essentially instantaneous heating achieved by mixing pre-heated, pressurized water with algal slurry in a continuous reaction system. These conditions allowed peptides and arginine, among other protein-derived co-products, to be readily recovered while simultaneously preserving the lipid content of the algal solids. Rapidly heating reaction mixtures to elevated temperatures seems to favor protein-derived product recovery in the aqueous-phase while also apparently minimizing cross-reactions between lipids and protein [67].

At longer times and isothermal conditions, aqueous-phase product yields monotonically decrease with increasing temperature and reaction time (for set-point temperatures above 200 °C only), reaching a minimum at 400 °C and 40 min and a maximum at 200 °C and 40 min. These trends are consistent with those reported previously for yields of aqueous-phase products [21, 22, 24, 27]. Moreover, a number of recent studies have explored low-temperature (125 – 225 °C) pre-treatment steps, usually as a means of reducing the nitrogen content of the algal solids thereby improving the quality of the resulting biocrude oil produced from a subsequent HTL reaction [23, 30, 31] or transesterification reaction [68, 69]

while simultaneously producing a nutrient-enriched aqueous phase. In terms of the solid and aqueous-phase product yields, our results at 200 °C are consistent with the findings of those studies. Moreover, Costanzo et al. [31] and Jazrawi et al. [30] showed that reactions responsible for nitrogen recovery in the aqueous phase are acid catalyzed with rates that increase with reaction severity.

Figure 2.1e illustrates the volatile product yields. Volatile yields are essentially zero for  $T < 250$  °C, and very low at short holding times ( $t < 2$  min). At high reaction severity, volatile yields increase substantially, especially at  $T \geq 350$  °C and  $t \geq 2$  min. These values for volatile yields and the aforementioned trends are consistent with those reported by Valdez et al. [24] and Christensen et al. [27] (through the difference between their mass recovery and unity in the latter case). Moreover, these trends are nearly equal and opposite of those for aqueous-phase products, suggesting that aqueous-phase components are degrading to form smaller, more volatile compounds in this region. The aqueous phase was dried at 70 °C, and it is likely that some of these compounds become volatile in the range of  $25 < T < 70$  °C. Increases in volatile yields also occur simultaneously with small decreases in biocrude at high reaction temperature ( $T \geq 300$  °C) and long reaction times ( $t \geq 40$  min). These concurrent phenomena suggest that aqueous-phase product degradation is the primary reaction pathway to produce volatiles, but that some degradation of biocrude at elevated temperatures and long reaction times cannot be ruled out.

Given the results in Figures 2.1d and 2.1e, along with previous studies indicating that volatile products are produced primarily from aqueous-phase products [24], we also plot aqueous-phase product and volatile yields combined in Figure 2.1f. The trends for the combined volatile and aqueous-phase products match those of just the aqueous-phase products in Figure 2.1d at low reaction severity and those of the volatiles in Figure 2.1e at high reaction severity. Some experiments at extended holding time ( $t \geq 20$  min) show decreased volatile and aqueous-phase product yields and increased gas yields, suggesting that gasification of aqueous-phase products occurs at those conditions. We expect these values to show more

variability than the other products because, like volatile yields, these values were calculated by difference rather than by direct measurement.

### 2.3.2 Kinetic model development

We sought to derive a reaction network and develop a corresponding kinetic model that accurately describes the behavior of microalgal HTL over the entire range of reaction conditions employed. We began with the kinetic model and associated reaction network developed by Valdez and Savage [53], which was corroborated both by isothermal algal HTL reactions [24] and additional isothermal reactions of the individual product fractions (solid, biocrude, and aqueous-phase products) [53]. Using their model to predict the results discussed in Section 2.3.1 resulted in the parity plots shown in Figure A.1. This model reasonably calculates biocrude yields from HTL at the conditions employed in that study (Figure A.1b), although the aqueous-phase and volatile product yields were over-calculated and gas yields were under-calculated, likely due to the differences in gas quantification discussed in Section 2.3.1. However, the model breaks down ( $\sigma = 17$  wt %) at holding times shorter than 10 min (Figure A.1a), clearly demonstrating the need for a model that describes fast HTL.

In general, the results discussed in Section 2.3.1 support the reaction network developed by Valdez and Savage [53]. The exception is that our results do not immediately suggest that a biocrude to gas pathway exists. Given that small but appreciable gas formation occurs at low reaction severity conditions, where no biocrude is present, we instead employ a direct solids to gas pathway instead of biocrude to gas. Moreover we add an aqueous-product to volatile pathway to describe that transition shown in Figures 2.1d and 2.1e. Figure 2.2 presents this modified reaction network with pathways that lead to biocrude (B), aqueous-phase product (A), gas (G), and volatile (V) formation from algal solids (S).

We assume each reaction pathway in Figure 2.2 to be pseudo-first-order and follow Arrhenius kinetics:

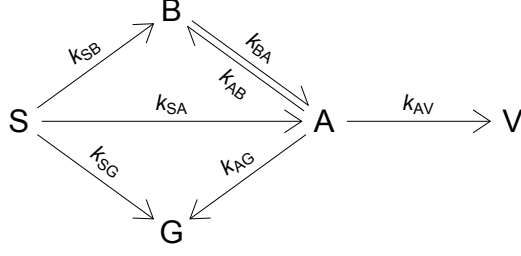


Figure 2.2: Reaction network for the fast and isothermal hydrothermal liquefaction of *Nannochloropsis oculata*. S, B, A, G, and V represent solids, biocrude, aqueous-phase products, gases, and volatiles, respectively.

$$k_{ij}(t) = A_{ij} \exp\left(\frac{-E_{ij}}{RT(t)}\right) \quad (2.1)$$

Here,  $k_{ij}(t)$  is the rate constant for the reaction pathway from reactant  $i$  to product fraction  $j$ ,  $A_{ij}$  is the pre-exponential factor,  $E_{ij}$  is the activation energy,  $R$  is the gas constant, and  $T(t)$  is the temperature, which is time-dependent during the non-isothermal part of each experiment. Applying Equation (2.1) and the batch reactor design equation to the reaction network in Figure 2.2 yields the following system of first-order ordinary differential equations (ODEs) for the temporal evolution of the product fraction yields,  $x_i$ :

$$\frac{dx_S^*}{dt} = -(k_{SB} + k_{SA} + k_{SG})x_S^* \quad (2.2)$$

$$\frac{dx_B}{dt} = k_{SB}x_S^* + k_{AB}x_A^* - k_{BA}x_B \quad (2.3)$$

$$\frac{dx_G}{dt} = k_{SG}x_S^* + k_{AG}x_A^* \quad (2.4)$$

$$\frac{dx_A^*}{dt} = k_{SA}x_S^* + k_{BA}x_B - (k_{AB} + k_{AG} + k_{AV})x_A^* \quad (2.5)$$

$$\frac{dx_V}{dt} = k_{AV}x_A^* \quad (2.6)$$

Given that solids and aqueous-phase product yields approach steady nonzero values at the highest reaction severities explored herein, we also employed the following change of variables:

$$x_S = x_S^\infty + x_S^* \quad (2.7)$$

$$x_A = x_A^\infty + x_A^* \quad (2.8)$$

$x_S$  and  $x_A$  are measured directly (Figures 2.1a and 2.1d, respectively) and we calculated  $x_S^\infty = 4 \pm 1$  wt % and  $x_A^\infty = 12 \pm 4$  wt % based on the average values of  $x_S$  and  $x_A$  for all experiments above 300 °C with holding times longer than 8 min.  $x_S^\infty$  represents the average amount of unreacted (primarily ash) and repolymerized solids remaining at high reaction severity, and our reported value is consistent with reported solid yields in the literature for HTL of *Desmodesmus* sp. [22], *Nannochloropsis oculata* [24], *Phaeodactylum tricornutum* [27], and *Spirulina platensis* [21] at these conditions.  $x_A^\infty$  represents the average amount of aqueous-phase compounds remaining at high reaction severity, and our reported value is consistent with reported aqueous-phase product yields for *Desmodesmus* sp. [22] at these conditions (also dried at 70 °C). Incorporating  $x_S^\infty$  and  $x_A^\infty$  in the model ensured that it would always calculate reasonable yields for those product fractions.

We performed three control experiments, following the same procedure outlined in Section 2.2 at room temperature (25 °C) and a holding time of 60 min, to determine the initial condition for the model to be  $x_{S,0} = 84 \pm 2$  wt % ( $x_{S,0}^* = 80 \pm 3$  wt %),  $x_{A,0} = 15 \pm 2$  wt % ( $x_{A,0}^* = 3 \pm 4$  wt %),  $x_{B,0} = 1 \pm 0$  wt %,  $x_{G,0} = 0$  wt %, and  $x_{V,0} = 0$  wt %. Using the temperature profiles and product yield data from each experiment, we calculated values for all kinetic parameters by simultaneously solving the system of first-order, ODEs in MATLAB® with the function `ode23s`. We then used `lsqnonlin` to minimize the objective function, which consisted of a 45 (experiment) by 5 (product) matrix of differences between the observed and calculated weight fractions. Confidence intervals for parameters were calculated using the function `nlparci`.

### 2.3.3 Kinetic model results

Table 2.1 displays the Arrhenius parameters for the chemical reaction pathways, with confidence intervals representing the SD. These parameters are valid on the temperature, holding-time, and average-heating-rate ranges of 100 – 400 °C, 10 s – 60 min, and 110 – 350 °C min<sup>-1</sup>, respectively.

Pathway	log(A) [log(s <sup>-1</sup> )]	$E_a$ [kJ mol <sup>-1</sup> ]
S → B	5.0 ± 0.6	74 ± 6
S → A	4.0 ± 0.5	65 ± 6
S → G	3.9 ± 0.7	68 ± 8
B → A	3.8 ± 1.0	99 ± 19
A → B	1.7 ± 0.5	59 ± 8
A → G	2.3 ± 0.5	64 ± 7
A → V	7.6 ± 1.5	119 ± 17

Table 2.1: Arrhenius parameters for reaction pathways in Figure 2.2.

The activation energies for the solids conversion pathways ( $S \rightarrow B$ ,  $S \rightarrow A$ , and  $S \rightarrow G$ ) are comparable to those reported for the hydrolysis of various compounds in high-temperature water, including proteins to amino acids (46 – 191 kJ mol<sup>-1</sup>) and acylglycerides to free fatty acids (50 – 105 kJ mol<sup>-1</sup>) [12]. The values are lower than those reported for carbohydrate conversion, including cellulose, starch, and mono- and disaccharides (92 – 164 kJ mol<sup>-1</sup>) [12], perhaps because carbohydrates constituted just 20 wt % of the initial biomass. Moreover, carbohydrate conversion has been demonstrated to be slower than the conversion of proteins and lipids [13, 48]. The activation energies in Table 2.1 for gas formation pathways ( $S \rightarrow G$  and  $A \rightarrow G$ ) are comparable to those reported by Guan et al. [70] for hydrothermal gasification of algae, when the reported rate constants for individual gaseous species are lumped together [53]. In general, our model features pre-exponential factors and activation energies higher than those reported by Valdez and Savage [53]. This translates to calculated values for  $k_{SB}$  and  $k_{SA}$  that are about an order of magnitude higher than those calculated using the Valdez and Savage [53] model.

Figure 2.3a shows the instantaneous selectivity,  $S_{Sj} = k_{Sj}/k_{S,T}$ , of solids conversion

reactions  $S \rightarrow j$ , where  $j = A, B, G$ , with respect to temperature. Here  $k_{S,T} = k_{SA} + k_{SB} + k_{SG}$  is the total rate constant for disappearance of solids. The selectivities of solids to aqueous-phase products and biocrude decrease and increase monotonically, respectively, with increasing reaction temperature, with the rate of biocrude formation from solids exceeding that of aqueous-phase product formation at around 275 °C. This trend suggests that rapidly heating the reaction mixture to 275 °C or higher would maximize biocrude production from algal solids.

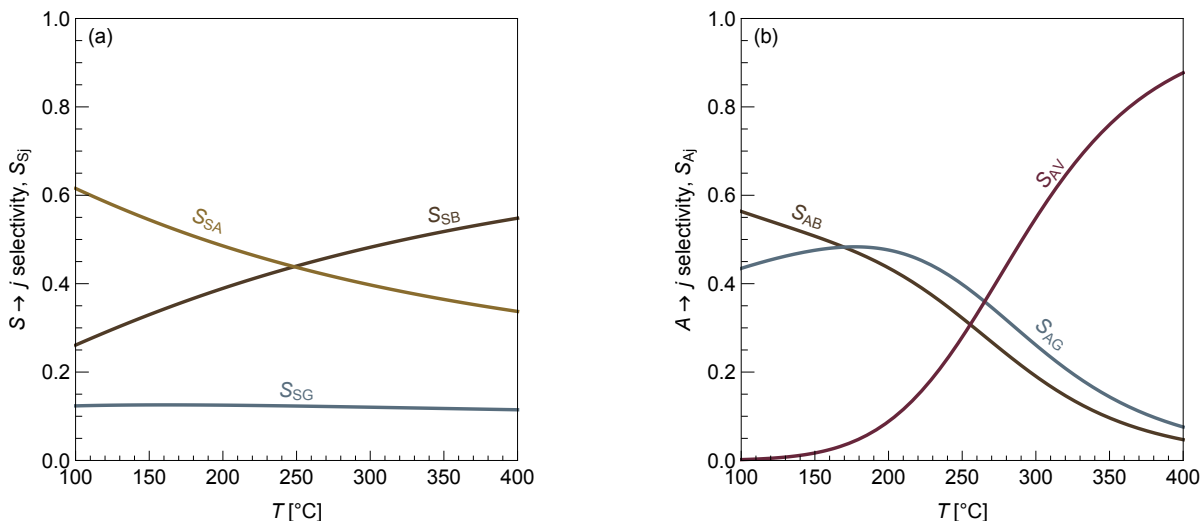


Figure 2.3: Instantaneous (a) solids and (b) aqueous-phase product conversion selectivities with respect to temperature.  $S_{Sj} = k_{Sj}/k_{S,T}$  and  $S_{Aj} = k_{Aj}/k_{A,T}$ , where  $k_{S,T} = k_{SB} + k_{SA} + k_{SG}$  and  $k_{A,T} = k_{AB} + k_{AG} + k_{AV}$ , respectively. Dark gold, brown, gray-blue, and dark magenta lines correspond to aqueous-phase products (A), biocrude (B), gas (G), and volatiles (V), respectively.

Figure 2.3b depicts the instantaneous selectivity,  $S_{Aj} = k_{Aj}/k_{A,T}$ , of aqueous-phase product conversion reactions  $A \rightarrow j$ , where  $j = B, G, V$ , with respect to temperature. Here  $k_{A,T} = k_{AB} + k_{AG} + k_{AV}$  is the total rate constant of disappearance of aqueous-phase products. The selectivity of aqueous-phase products to biocrude follows that of aqueous-phase products to gas closely throughout the entire range of temperatures plotted, although biocrude is slightly favored below 170 °C, and gas is slightly favored for 170 – 270 °C. The selectivity of volatile product formation,  $S_{AV}$ , increases substantially with reaction temperature, rendering volatiles the favored product fraction above 270 °C.

Figure 2.4 depicts observed product fraction yields and model solutions calculated us-

ing representative temperature profiles for each set-point temperature. Several data also show dashed-line error bars (SD) obtained from replicate reactions (dotted lines); these experimental uncertainties are comparable to those reported by Valdez and Savage [53] and Faeth et al. [25]. Figures 2.4d and e show that the model correlates the data very well at set-point temperatures of 350 and 400 °C, respectively. The model solutions at 250 and 300 °C (Fig. 2.4b and 2.4c, respectively) are generally good, with the exception of an over-prediction of aqueous-phase product yields at intermediate holding times. Model calculations for solid, biocrude, and gas yields remain well correlated in this region, however. The model exhibits the lowest accuracy in Figure 2.4a for a set-point temperature of 200 °C. Here, the model under-predicts solid yields (over-predicts conversion) and correspondingly over-predicts aqueous-phase product, biocrude, and gas yields.

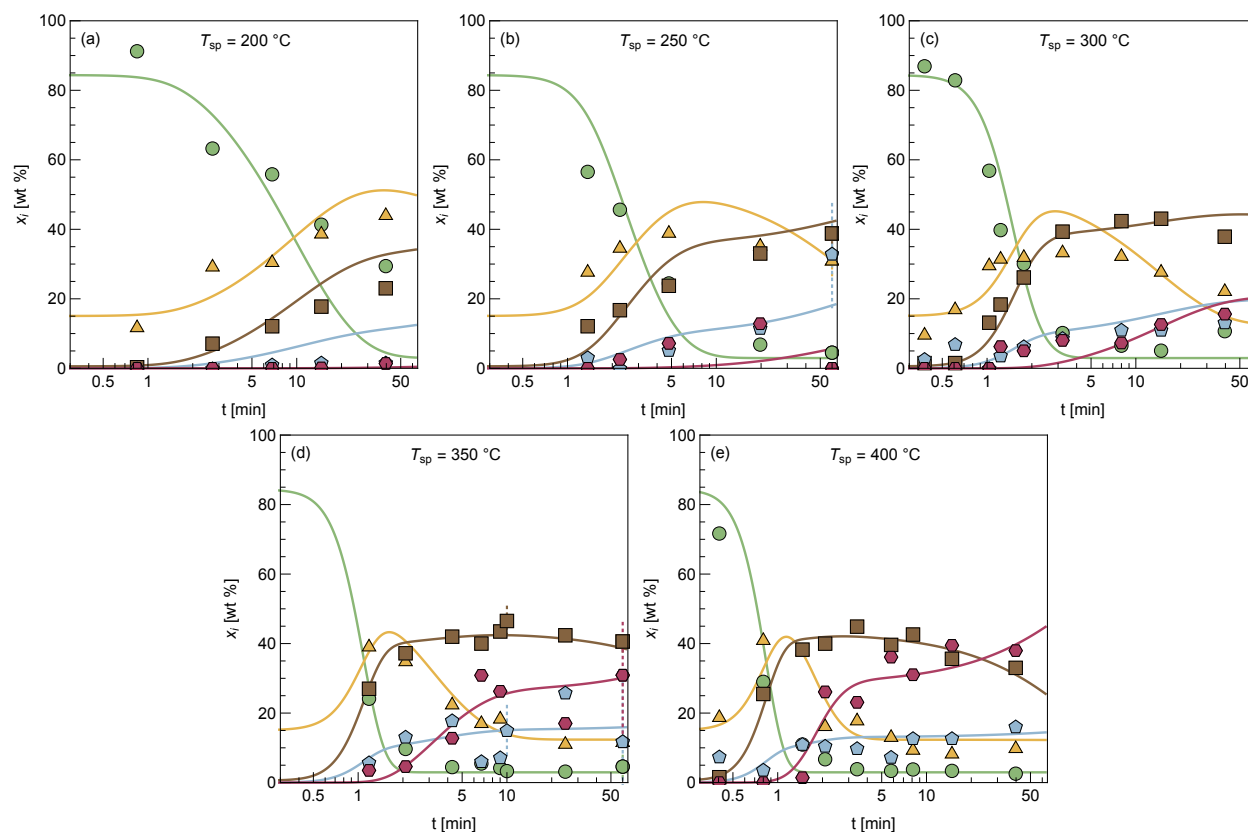


Figure 2.4: Model solutions (solid lines) and experimentally observed yields ( $x_i$ ) over time at different set-point temperatures ( $T_{sp}$ ) for solids (green circles), aqueous-phase products (gold triangles), biocrude (brown squares), gas (pale blue pentagons), and volatiles (purple hexagons). Dotted lines show SD for selected experiments.

One possible explanation for the reduced accuracy in Fig. 2.4a and 2.4b is that the non-homogeneity of the algal slurry causes the reaction mixture to deviate from pseudo-first-order and/or Arrhenius kinetics behavior, with the cell walls potentially imposing an energy threshold for liberating the intracellular components of the algae. Garcia Alba et al. [22] examined scanning-electron-microscope images of the solids product fraction before and after conducting hydrothermal liquefaction of *Desmodesmus* sp. at temperatures in the range of 200 – 275 °C. They found that there were significant morphological differences in the solids fraction in this region, with major degradation observed between 225 and 250 °C [22]. The reduced model accuracy at  $T_{sp} \leq 250$  °C and the results presented by Garcia Alba et al. [22] demonstrate that further studies of hydrothermal conversion at low temperatures of microalgae with different types of cell walls may be required to improve model accuracy in that region. In general, however, the quality of the agreement between observed and calculated product yields at  $T_{sp} \geq 300$  °C demonstrates the utility of the present kinetic parameters and reaction network at calculating yields for both non-isothermal and isothermal HTL conditions.

Figure A.2 shows residual plots for each product fraction. The model over-calculates solid yields (Figure A.2a) at moderate reaction severity; above 280 °C the residuals are significantly smaller. The residual plots highlight that, at low to moderate reaction severity ( $T < 280$  °C,  $20 \text{ s} < t < 3 \text{ min}$ ), the model tends to deviate from observed product fraction yields by a larger magnitude than at moderate to high reaction severity, with the exception of volatile yields. This observation reaffirms a need to further elucidate reaction kinetics in this low-to-moderate severity region, which we address in Chapters IV and V.

Figure 2.5 depicts parity plots of the observed and calculated biocrude yields, for several previous studies [13, 24, 25, 39, 40]. The specific data points that were selected appear in Table A.3 in Appendix A. We chose data within the scope of our model limits, including experiments conducted at 400 °C or lower for microalgae of the genus *Nannochloropsis*. Moreover, due to limited availability of temperature profile information, we assumed an

isothermal temperature for data from the López Barreiro et al. [39], Biller and Ross [13], and [40] studies and assumed temperature profiles typical for this study for data from the [25] and [24] studies. The SD was 5 wt %, which is comparable to the experimental uncertainties shown in Figure 2.4 and demonstrated in studies with a similar experimental procedure [25, 53]. Figure 2.5 demonstrates that the model can be successfully applied for biocrude prediction to microalgae within the *Nannochloropsis* genus and of a similar biochemical composition over a broad range of reaction conditions. Comparison of model-predicted yields to literature data for other products is much less meaningful, due to differences in experimental procedures. See Section A.5 in Appendix A for further explanation on model validation for other product fractions.

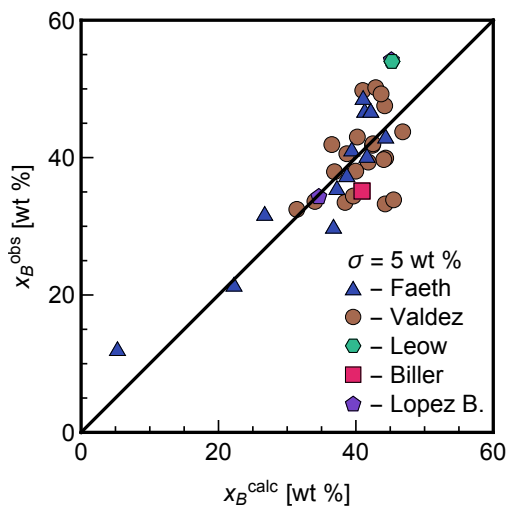


Figure 2.5: Parity plot of observed vs. calculated biocrude yields for literature data [13, 24, 25, 39, 40].

### 2.3.4 Calculated yields

With the establishment of a kinetic model that can describe algal HTL as a function of temperature and time, irrespective of heating rate, we now use it to improve our understanding of the kinetics that govern this process. Figure 2.6 depicts density plots of product fraction yields as functions of temperature and time for isothermal HTL. Dashed lines correspond to the maximum aqueous-phase product ( $x_A^{\text{max}}$ ) and biocrude ( $x_B^{\text{max}}$ ) yields achievable

as a function of isothermal HTL temperature.

Figure 2.6a illustrates the change in the calculated solids yields,  $x_S^{calc}$ , over time for different temperatures. At short times ( $t < 30$  s) and low temperature ( $T < 250$  °C), little solids conversion occurs. Beyond this region, solids react readily with increasing temperature and time, and complete solids conversion can be achieved for all temperatures examined. The curve for the maximum aqueous-phase product yield,  $x_A^{max}$ , coincides with the region where the solids completely disappear (i.e.,  $x_S^{calc} \approx x_S^\infty$ ), which seems reasonable if the algal solids are the main producers of aqueous-phase products. Moreover, the curve for the maximum biocrude yield,  $x_B^{max}$ , always occurs well beyond the point of solids depletion, indicating that secondary reactions contribute significantly to biocrude production.

Figure 2.6b shows the calculated biocrude yields. Biocrude formation increases substantially with reaction temperature at short times, coinciding with the corresponding decrease in solids (Figure 2.6a). Biocrude yields as high as 46 wt % are achievable after 1 min at 400 °C. Once solids completely disappear, the biocrude yield is much less sensitive to reaction severity. This trend of little variation also holds over a fairly wide region of temperature and times, but shifts downward with increasing reaction time, from a range of 325 – 400 °C at 1 min to a range of 225 – 350 °C at 60 min, for example. In general, the biocrude yield increases with reaction severity, but the existence of maxima indicates that it does decrease at elevated temperatures ( $T > 350$  °C) and long reaction times ( $t > 20$  min). At times of 10 – 60 min, these maximum yields occur between 300 – 350 °C. This range of temperatures is in excellent agreement with numerous previous studies conducted under isothermal conditions for various microalgae, including 375 °C for *Desmodesmus* sp. [22], 300 – 350 °C for *Nannochloropsis oculata* [10, 24], 350 °C for *Phaeodactylum tricornutum* [27], and 350 °C for *Spirulina platensis* [21]. The maximum biocrude yield ranged only from 45 – 46 wt % regardless of temperature ( $T \geq 300$  °C). This modest variation is within the uncertainty in the data, and it indicates that HTL is a very robust process in that it can achieve nearly the same maximum biocrude yields over a very wide range of temperatures and times. This

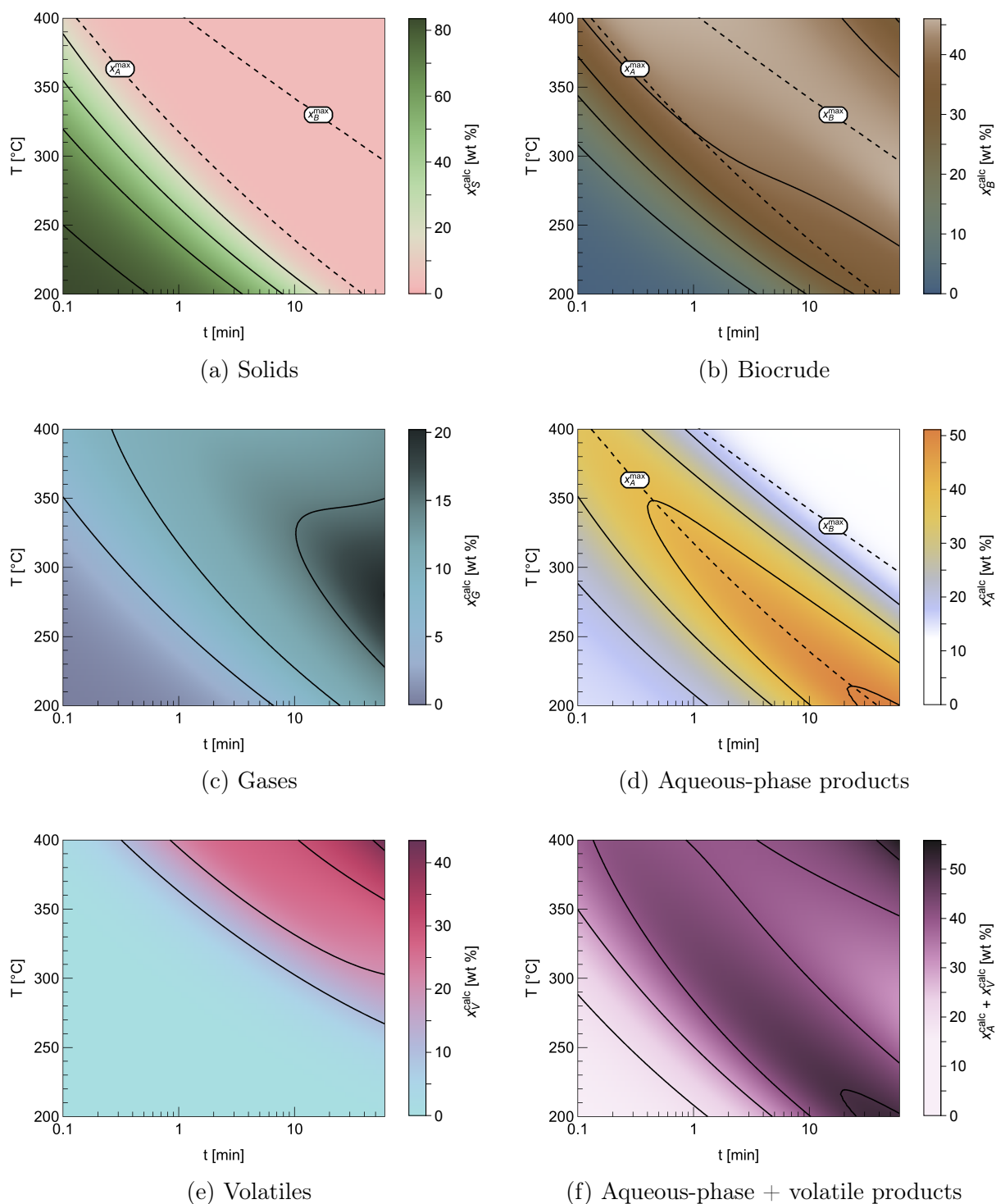


Figure 2.6: (a) Solid, (b) biocrude, (c) gas, (d) aqueous-phase, (e) volatile, and (f) aqueous-phase and volatile product yields calculated as functions of time,  $t$ , and isothermal temperature,  $T$ . Solid black lines correspond to the yield contours marked by numbered ticks on the bar legend. Dashed lines show the maximum aqueous-phase product ( $x_A^{max}$ ) and biocrude ( $x_B^{max}$ ) yields at each temperature.

robustness may provide opportunities to select HTL conditions that provide high biocrude yields and also optimize some other desired outcome (e.g., biocrude quality, nitrogen recovery in the aqueous phase, etc.).

Figure 2.6c displays gas yields,  $x_G^{calc}$ , calculated over time for several temperature profiles. Gas yields are fairly low at low reaction severity, but increase with increasing temperature and time beyond the point of solids depletion (Figure 2.6a). At longer reaction times ( $t > 30$  min), gas formation is favored at moderate temperatures (250 – 350 °C). The global maximum calculated gas yield of 20 wt % occurs at  $T = 280$  °C and  $t = 60$  min.

Figure 2.6d depicts the calculated yields of aqueous-phase products,  $x_A^{calc}$ . At low reaction severity, aqueous-phase product yields increase significantly with increasing temperature and time until solids are depleted and then decrease with further increases in reaction severity. Moreover, the maximum aqueous-phase product yield itself,  $x_A^{max}$ , decreases monotonically with increasing temperature, from a global maximum of 52 wt % at  $T = 200$  °C and  $t = 50$  min, to 35 wt % at  $T = 400$  °C and  $t = 10$  s. Notably, the temperature range that maximum aqueous-phase products are produced at long times is consistent with those reported in the literature, including 225 – 250 °C for *Desmodosmus* sp. [22], 250 °C for *Nannochloropsis oculata* [24], and 200 °C for *Spirulina platensis* [21]. Similar to  $x_A^{max}$  occurring at the point of solids depletion (Figure 2.6a), the maximum biocrude yield,  $x_B^{max}$ , always occurs when the yield of aqueous-phase products reaches approximately 20 wt % or less.

Figure 2.6e shows  $x_V^{calc}$ , the calculated volatile yields. At short times, volatile formation only occurs at  $T > 300$  °C, increasing rapidly in the range of 350 – 450 °C. At longer times, volatile yields become appreciable only at  $T > 275$  °C. Similarly to gas yields, the volatiles yield increases monotonically with increasing reaction time, due to the irreversibility imposed by the reaction network in Figure 2.2. The global maximum is 44 wt % at  $T = 400$  °C and  $t = 60$  min, the most severe reaction condition shown. Volatiles are also the most favored product at elevated temperatures ( $T > 350$  °C), given the high values of the Arrhenius parameters for the rate constant for the  $A \rightarrow V$  reaction pathway. For completeness, we also

show aqueous-phase and volatile product yields together in Figure 2.6f.

Examined together, the plots in Figure 2.6 illustrate that one can decouple effects of temperature and time on the HTL product distribution. Above 250 °C and 30 s, biocrude and aqueous-phase product yields increase dramatically with increasing reaction severity until solids are depleted. Aqueous-phase product yields reach a maximum at that region and decrease with increasing reaction severity while biocrude yields increase modestly and volatile yields become appreciable. At extreme reaction severities, biocrude yields begin to decrease modestly and volatile yields increase substantially. Examination of longer reaction times in Figure 2.6 shows that temperature plays a larger role than time in determining product distribution; aqueous-phase products, biocrude and gas (collectively), and volatiles are favored below 225 °C, between 225 – 350 °C, and above 350 °C, respectively.

Examining Figure 2.6 also demonstrates an interplay between aqueous-phase products and biocrude. For a given reaction time, the maximum biocrude yield generally occurs at temperatures about 100 °C higher than the maximum aqueous-phase product yield. As previously discussed, the increase in biocrude yield observed between  $x_A^{max}$  and  $x_B^{max}$  can be entirely attributed to aqueous-phase products reacting to form DCM-soluble products (biocrude) because solids are essentially depleted in that region ( $x_S^{calc}$  is of order  $x_S^\infty$ ). Aqueous-phase products are rich in nitrogen, and it has been demonstrated that nitrogen incorporation in the biocrude increases with reaction time and temperature in this range [21, 22, 24, 25, 38, 59]. Therefore, it seems plausible that this increase in biocrude yield with holding time is the result of nitrogen-containing aqueous-phase compounds reacting to become less polar or incorporating themselves with larger organic molecules through mechanisms like the Maillard reaction [12, 48, 71]. We speculate that maximizing aqueous-phase product formation either through short reaction times and rapid heating or longer reaction times at lower temperatures (200 – 225 °C) may be desirable from a biocrude quality and energy input standpoint. Doing so may lower nitrogen incorporation into the biocrude (and maximize nitrogen recovery into the aqueous phase for recycling), reducing the burden of

downstream catalytic hydrodenitrogenation reactions necessary for biocrude refinement [71].

## 2.4 Conclusion

We elucidated algal HTL kinetics through a comprehensive study of the coupled effects of temperature, reaction time, and heating rate on algal HTL product yields. We used these data to develop a reaction network and kinetic model valid over a broad range of holding times (10 s – 60 min), including much shorter timescales (10 s – 10 min) than previously established. Calculated yields correlate well with observed yields, and the model shows that biocrude yields as high as 46 wt % are achievable at 400 °C and 1 min. The model highlights potential trade-offs between biocrude quantity and quality.

## CHAPTER III

# Influence of biodiversity, biochemical composition, and species identity on the quality of biomass and biocrude oil produced via hydrothermal liquefaction

This chapter contains results that were originally published in *Algal Research* written along with co-authors Cristina K. Koss, Anita Narwani, Aubrey R. Lashaway, Casey M. Godwin, Bradley J. Cardinale, and Phillip E. Savage [42]. Herein, our objective was to characterize the extent that multi-species cultures of microalgae, or polycultures, could improve HTL process sustainability and illuminate differences in biocrude properties arising from feedstock characteristics (e.g., biochemical composition and species identity). More specifically, we compared several measures of quality for biomass and biocrude oil produced via HTL for monocultures and polycultures of the freshwater microalgae *Ankistrodesmus falcatus*, *Chlorella sorokiniana*, *Pediastrum duplex*, *Scenedesmus acuminatus*, *Scenedesmus ecornis*, and *Selenastrum capricornutum*. On average, the 2-species cultures provided product quality comparable to that of the monocultures, while that of the average 4- and 6-species polycultures was lower. No single monoculture or polyculture performed the best with respect to all quality metrics considered, including biomass fatty acid content and biocrude elemental content and higher heating value. However, for each measure of quality, some polycultures did outperform or match the performance of the best monoculture for each respective

metric. Numerous polycultures performed outside the range of product quality exhibited by their constituent species (transgressive overyielding), and polycultures with *Chlorella* did so to the greatest extent. We highlight several polycultures that offer potentially compelling trade-offs between product quantity and quality compared to the most productive monoculture; such trade-offs contribute to the portfolio of polyculture attributes that could be employed to improve overall sustainability of algal biofuel production. Microalgal biochemical composition was correlated with biocrude properties, however including species identity as an additional correlation variable further explained the observed variation. A regression model incorporating these variables helped inform the design of the more expansive set of HTL experiments presented in Chapters IV and V.

### 3.1 Introduction

The vast majority of current research on the production of renewable fuels from algal biomass focuses on the growth of monocultures of highly productive species. These species can either be highly productive in nature [3] or engineered to improve disease and invader resistance, lipid productivity, photosynthetic efficiency, or tolerance to abiotic environmental factors [72, 73]. These design goals have drawbacks from an ecological and sustainability perspective, however. The use of intensive farming practices to support engineered monocultures in agriculture, for example, has led to biodiversity losses that in some cases result in impacts to ecosystems that rival the effects of climate change and eutrophication [74, 75]. Moreover, such monocultures require more maintenance in terms of fertilizers and biocides and cannot be sustained in open ponds indefinitely due to continuous environmental perturbations (e.g., changes in weather), outbreak of disease, and invasion by undesirable species [76].

A more sustainable approach to algal biomass production may involve designing communities containing multiple species of microalgae, with each performing a separate set of functions that are complementary to one another [77, 78]. For example, resource-use effi-

ciency and disease resistance would mitigate the need for fertilizers and pesticides, thereby reducing their impact on the surrounding environment. Several studies have examined how algal biodiversity affects different metrics of interest for biofuel production, although the results to date have been highly variable. Some of these studies have shown that algal biodiversity may help stabilize biomass production over time [76, 79], increase lipid content in freshwater algae communities via competition-induced nutrient stress [80, 81], and increase the total biovolume of algal communities [78]. Meanwhile, other studies have shown that monocultures may be more stable and resistant to invaders when growing in wastewater [82] and that there is no stabilization effect achieved with polycultures [83].

Although several studies have examined how algal biodiversity can improve biomass yield, biomass stability, and lipid content, the recent work from our collaboration marked the beginning of efforts to directly examine how algal biodiversity affects the products from biomass conversion technologies, including HTL [6]. We probed the impact of biodiversity on the total biocrude production (mass biocrude produced per unit growth volume) and its temporal stability (biocrude production temporal mean divided by SD) as measured by HTL. On average, biodiversity did not lead to an increase in total biocrude production but did lead to more stable biocrude production over time. Only a small number of the species combinations could match the biocrude production and stability for the best monoculture, *Selenastrum capricornutum*. Moreover, some follow-up studies found that polycultures were able to grow in the presence of aqueous co-product from HTL to a much greater extent than monocultures [84], that polycultures exhibit more balanced nutrient resource use efficiency between nitrogen and phosphorus than do monocultures [7], and that when grown outdoors, polycultures demonstrate enhanced multifunctionality for long-term production compared to monocultures [8].

The impact of algal biodiversity on the quality of biocrude oil produced via HTL has yet to be explored; however inter-species interactions, including competition for nutrients for example, can induce changes in biochemical composition and cell morphology, both of which

have been shown to affect biomass reactivity in high-temperature water and by extension the properties of the resulting biocrude [22, 39, 40]. Phytoplankton species vary on average in their biochemical quality, for example in terms of their elemental stoichiometry, but they also vary in response to abiotic environmental variation [85, 86]. Many species increase their cellular carbon content (relative to nitrogen and phosphorus), and specifically their lipid content when stressed, including in response to nutrient limitation [87]. Some species also increase their cellular lipid content when mixotrophic growth is stimulated by the addition of organic carbon [88]. As a result, biodiversity may enhance biochemical quality of polycultures via a few mechanisms. First, it may increase the likelihood of the polyculture containing a species whose biochemical properties are desirable for HTL production on average (known as a “sampling effect” in the biodiversity literature [89]). Second, it may induce a shift in metabolism resulting in high cellular carbon or lipid content via stress response to nutrient limitation due to competition for resources. Last, excretion of organic waste or other exudates by interspecific neighbors may stimulate mixotrophic metabolism, enhancing lipid production.

In this chapter, we elucidate how algal biodiversity, and by extension biochemical composition and species identity, affects the quality of the biomass (i.e., fatty acid content) and resulting biocrude oil produced via HTL. To the authors’ knowledge, this is the first study to directly evaluate quality by measuring the elemental composition of the biocrude and by quantifying the fatty acid content of the algal biomass via acid-catalyzed *in situ* transesterification to fatty acid methyl esters (FAMES) in the context of microalgal polycultures. To determine whether or not polycultures simply act as additive mixtures of their component species, we compare the performance of specific species combinations to expected values based on the performance of the monocultures of the species constituting those combinations. We also contrast the performance of average polycultures at each level of species richness to that of the component monocultures. Moreover we elucidate the relative extent to which biochemical composition and species identity affect the properties of the resulting

biocrude oil. The relative influence of these feedstock characteristics on biocrude properties has not been previously quantified and may be important for understanding the underlying mechanisms governing product quality evolution during HTL.

## 3.2 Materials and methods

### 3.2.1 Microalgae cultivation

For a detailed description of cultivation procedures, see Narwani et al. [6]. To summarize briefly, we selected the freshwater microalgae *Ankistrodesmus falcatus* (A), *Chlorella sorokiniana* (B), *Pediastrum duplex* (C), *Scenedesmus acuminatus* (D), *Scenedesmus ecornis* (E), and *Selenastrum capricornutum* (F) and occasionally refer to them by a letter identifier, shown in Table 3.1. We chose these species for several reasons [6]; in short, they were part of the U.S. Department of Energy’s Aquatic species program, included in the Solar Energy Research Program’s collection, and/or highlighted as species of interest for biofuel production [90–92]. Moreover, they are all common in lakes across North America and as a result would not pose a risk of introducing non-native taxa into surrounding natural ecosystems if cultivated at scale. We grew these species in all possible 1-, 2-, 4-, and 6-species combinations in replication with the temperature set to vary from 17 to 27 °C from week to week once the cultures reached steady state. This temperature profile was intended to simulate real-world temperature fluctuations that might be caused by weather fronts in open environments. We note that additional replicates were grown under a constant temperature of 22 °C, but were not the focus of the present study; the constant-temperature analogues of the data and figures presented in the main text can be found in Appendix B. We sampled cultures weekly for seven weeks once they reached steady state. Cell counts (cell mL<sup>-1</sup>) were performed on all 1-, 2-, and 6-species cultures in addition to a single replicate of each 4-species combination. We removed a small number of aquaria from consideration that showed at least one time point in which a contaminant species (i.e., not part of the inoculated community) made up

5 % or more of the community biovolume. We calculated average cell volumes of 30.9, 39.0, 680.9, 122.0, 143.1, and 57.0  $\mu\text{m}^3 \text{ cell}^{-1}$  for *A. falcatus*, *C. sorokiniana*, *P. duplex*, *S. acuminatus*, *S. ecornis*, and *S. capricornutum*, respectively, according to the procedure outlined by Hillebrand et al. [93]. We then used a cell density equivalent to that of water, 1 g mL<sup>-1</sup>, to convert cell counts into species abundance weight percentages.

Identifier	Scientific name
A	<i>Ankistrodesmus falcatus</i>
B	<i>Chlorella sorokiniana</i>
C	<i>Pediastrum duplex</i>
D	<i>Scenedesmus acuminatus</i>
E	<i>Scenedesmus ecornis</i>
F	<i>Selenastrum capricornutum</i>

Table 3.1: Scientific names and identifiers of species employed.

### 3.2.2 Fatty acid esterification

The procedure used to extract, esterify, and quantify the microalgal fatty acids was adapted from the method used by Levine et al. [94]. We typically prepared an acidified methanol stock solution for a set of ten esterification reactions by adding 1.5 mL of acetyl chloride (ACROS Organics, ACS reagent grade) to 30 mL of methanol (Fisher Scientific, HPLC grade). We then combined 50 mg of algal biomass, a Teflon coated stir bar, and 2 mL of the acidified methanol solution in each round-bottom vial and securely tightened them with Teflon-lined caps to prevent evaporation.

All vials were placed on a preheated Fisher Scientific Isotemp Dynabloc<sup>®</sup> stirring hotplate maintained at 100 °C and 800 revolutions per minute (rpm) for 90 min. Every 30 min, the vials were agitated to ensure that all solids remained in contact with the solution. After 90 min, the vials were removed from the hot plate and allowed to cool to room temperature. An internal standard stock solution of tricosanoic methyl ester (C23:0) in n-heptane was prepared by combining 10 mg of tricosanoic methyl ester (Sigma-Aldrich,  $\geq 99.0\%$ ) with 40 mL of n-heptane (ACROS Organics,  $\geq 99.0\%$ ). Once the vials reached room temperature, 1

mL of deionized water and 3 mL of internal standard was added to each vial. The vials were then vortexed for 4 min and centrifuged at 2000 relative centrifugal force (rcf) for 10 min. 2 mL of each heptane layer were then transferred by pipette into GC vials and promptly sealed.

We used an Agilent 7890A gas chromatograph with flame ionization detector (GC-FID) and an Agilent Biodiesel GC column (1909BD-113) to quantify FAMES. Helium served as the carrier gas at a flow rate of 1 mL min<sup>-1</sup>. The oven temperature was initially held at 150 °C for 3 min, after which it ramped to the final temperature of 260 °C at a rate of 6 °C min<sup>-1</sup>. The final temperature was held for 9 min for a total run time of 30.3 min. The FID temperature was 300 °C and N<sub>2</sub> was the make-up gas. We identified compounds by comparing retention times to those of a Supelco 37 Component FAME mix. We quantified compound yields by relating each peak area to the known concentration and peak area of the internal standard, adjusting for carbon number and molar mass, and normalizing by the mass of dry biomass used for the analysis. We converted FAME yields into fatty acid (FA) yields (mass fatty acid / mass dry biomass) and report values grouped by saturation as SAFAs, MUFAs, and PUFAs. We report the total fatty acid content as lipid content with the understanding that minor components derived from the “backbone” of lipids, such as phosphate and glycerol, will be neglected.

We performed this analysis on all samples from the seventh week of steady-state sampling (see Section 3.2.1). In cases where there was not enough sample mass and we had fewer than two replicates of a given species combination and temperature treatment, we analyzed samples from earlier sampling weeks.

### **3.2.3 Ash content**

We ground each biomass sample into a fine powder and measured 25 mg into a small aluminum weigh boat. We then incinerated the samples in a Ney Vulcan 3-130 muffle furnace with an initial ramp of 10 °C min<sup>-1</sup> to 250 °C with a hold time of 30 min, followed by a ramp of

20 °C min<sup>-1</sup> to 550 °C with a hold time of 30 h. Upon cooling we transferred the weigh boats to a desiccator for 1 h before measuring the final weigh boat masses. We then calculated the ash content as the difference in weigh boat mass divided by the mass of dry biomass incinerated.

### 3.2.4 Protein and carbohydrate estimation

We measured biomass nitrogen content in all of the available samples from the sixth and seventh weeks of steady-state sampling. We used a wet persulfate oxidation step [95] to convert the biomass nitrogen to nitrate. We then measured the nitrate by neutralizing the digests with phosphate buffer (100 mM, pH 7.4), reducing the nitrate to nitrite using the enzyme nitrate reductase (Nitrate Elimination Company AtNAR-RPK), then measuring the nitrite using the sulfanilamide-naphthyl (ethylene) diamine method [96, 97]. In each set of persulfate digestions, we checked for complete recovery of organic nitrogen using cyanocobalamin as a recovery standard. We estimated protein content (mass protein / mass dry biomass) by multiplying the nitrogen content for each combination by 6.25, which assumes that the majority of the nitrogen in algal biomass is present as amino acids [98]. We estimated carbohydrate content as the difference between unity and the sum of protein, lipid, and ash content, with the understanding that this group will also contain other minor compounds (e.g., sterols and DNA).

### 3.2.5 Hydrothermal liquefaction

We describe the full procedure for HTL reactions in previous work [6]. In brief, all reactions occurred in 1.67 mL (internal volume) batch reactors built using <sup>3</sup>/<sub>8</sub>-in. 316-stainless-steel Swagelok tube fittings (one port connector and two caps). We loaded all reactors with 48 mg of dry algae and 910 mg of deionized water. These loadings correspond to a concentration of 5 wt % algae and enough liquid water to occupy 95 % of the reactor volume at 350 °C, based on the density of pure, saturated liquid water at that temperature.

We placed loaded reactors in a fluidized sand bath, preheated to 350 °C, for 20 min. The reactor heat-up time is about 2 min [34], which is short relative to the batch holding time employed in this study.

We opened the reactors and poured their contents into glass conical tubes. We used 9 mL DCM to further rinse the reactor walls and collect remaining products. We vortexed the conical tubes at 3000 rpm for 10 s and then centrifuged them at 500 rcf for 1 min. After transferring the organic phases to separate glass vials by pipette, we centrifuged the original glass conical tubes again at 1500 rcf for 3 min. We then transferred the aqueous phases from the conical tubes to small plastic vials, leaving only the solid phase behind in the conical tubes (albeit with small amounts of organic and aqueous phase). We dried the organic and solid phases using a Labconco<sup>®</sup> RapidVap<sup>®</sup> Vertex<sup>™</sup> evaporator set to a block temperature of 35 °C with a N<sub>2</sub> pressure of 25 psi for 65 and 30 min, respectively. We measured and recorded the mass of each phase, with the biocrude defined as the product remaining in the glass vial after solvent removal. We calculated biocrude yields as the mass of biocrude divided by the mass of initial dry algal biomass. Atlantic Microlabs, Inc. analyzed biocrude samples for C, H, and N content. We calculated O content by difference and estimated the higher-heating value (HHV) using the correlation developed by Channiwala and Parikh [99].

HTL reactions were performed on all aquaria and each sampling week outlined in our previous study [6]. CHN analyses were generally conducted in at least duplicate on samples from the seventh week of steady-state sampling. In rare cases where not enough sample was produced for a given combination in the seventh week, we instead used samples from other weeks with preference given to weeks closer to the seventh week.

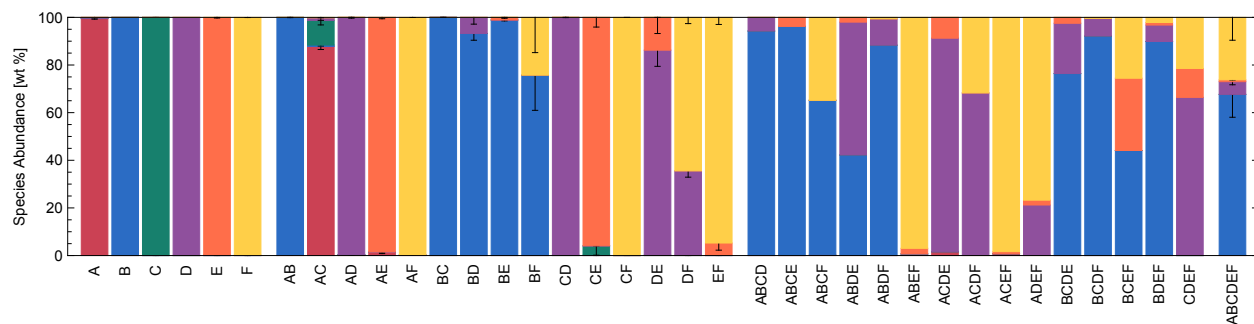


Figure 3.1: Species distribution (wt %) within each species combination. *Ankistrodesmus falcatus* (A), *Chlorella sorokiniana* (B), *Pediastrum duplex* (C), *Scenedesmus acuminatus* (D), *Scenedesmus ecornis* (E), and *Selenastrum capricornutum* (F) are indicated as red, blue, green, purple, orange, and yellow, respectively. Only single estimates for species distribution available for 4-species polycultures. Error bars represent SE.

### 3.3 Results and Discussion

#### 3.3.1 Species distribution

By week seven of steady-state sampling, each species follows a general trend of “dominance” when part of a polyculture in the order of *C. sorokiniana* (B) > *S. acuminatus* (D) > *S. capricornutum* (F) > *S. ecornis* (E) > *A. falcatus* (A) > *P. duplex* (C) (Figure 3.1). In other words, when present in a polyculture, *C. sorokiniana* generally constitutes the single largest share of the species distribution. *S. acuminatus* follows similarly and is the second largest in cases where *C. sorokiniana* is present. Moreover, *A. falcatus* and *P. duplex* are generally present in only trace amounts (excluding the AC biculture).

#### 3.3.2 Biomass properties

Figures Figure 3.2a–c summarize the fatty acid content data grouped by degree of saturation into SAFAs, MUFAs, and PUFAs, with each class possessing different attributes from a quality perspective (see Table B.3 in Appendix B for exact values). For example, fatty acids with higher degrees of unsaturation (more double bonds) possess less hydrothermal [100] and oxidative [101, 102] stability. However, they also enable cracking, oligomerization, isomerization, aromatization, and addition reactions during the refinement step [103], each of which could be individually and selectively targeted by different catalysts depending on

the desired product composition.

No one monoculture produced the highest yields for a given class of fatty acids, with *S. capricornutum* (F), *A. falcatus* (A), and *C. sorokiniana* (B) producing the highest saturated fatty acid (SAFA), monounsaturated fatty acid (MUFA), and polyunsaturated fatty acid (PUFA) yields, respectively. A few polycultures produced yields that were statistically equivalent to these monocultures, including CF and ACEF for SAFA content, AC for MUFA content, and BCDE, BC, ABCE, BD, and CE for PUFA content. Notably A and AC produced MUFA yields that were at least 35 % higher than all other cultures. On average across each level of species richness, SAFA and PUFA yields remained relatively constant (perhaps increasing slightly) up to four species present and then decreased thereafter, while MUFA yields decreased monotonically.

The biochemical composition of the different species combinations varied considerably, from 6.1 to 14.2 wt % for lipid, 22.9 to 48.6 wt % for protein, and from 34.6 to 59.3 wt% for carbohydrate content, respectively, shown in Figures 3.2d–f. The monocultures of *A. falcatus*, *C. sorokiniana*, and *S. capricornutum* contained the highest lipid, protein, and carbohydrate content, respectively, while *S. ecorinis*, *S. capricornutum*, and *C. sorokiniana* contained the lowest, respectively. Only one polyculture, BCDE, contained higher lipid content than the monoculture of *A. falcatus* (Fig. Figure 3.2d). A few polycultures contained lower protein content than the *S. capricornutum* monoculture, including CF and CE (Figure 3.2e), and several contained lower carbohydrate content than the *C. sorokiniana* monoculture, including ABCD, BC, and ABEF (Figure 3.2f). From one to four species present, on average, lipid content remained relatively constant, protein content increased significantly, and carbohydrate content decreased significantly.

Notably *C. sorokiniana* was present in four of the top-5 bicultures and nine of the top-10 4-species polycultures for PUFA and protein content (Figure 3.2c and e). Examining the species distribution data in Figure 3.1 highlights that when *C. sorokiniana* is present in a polyculture, it represents at least half of the total biomass, with the exception of ABDE

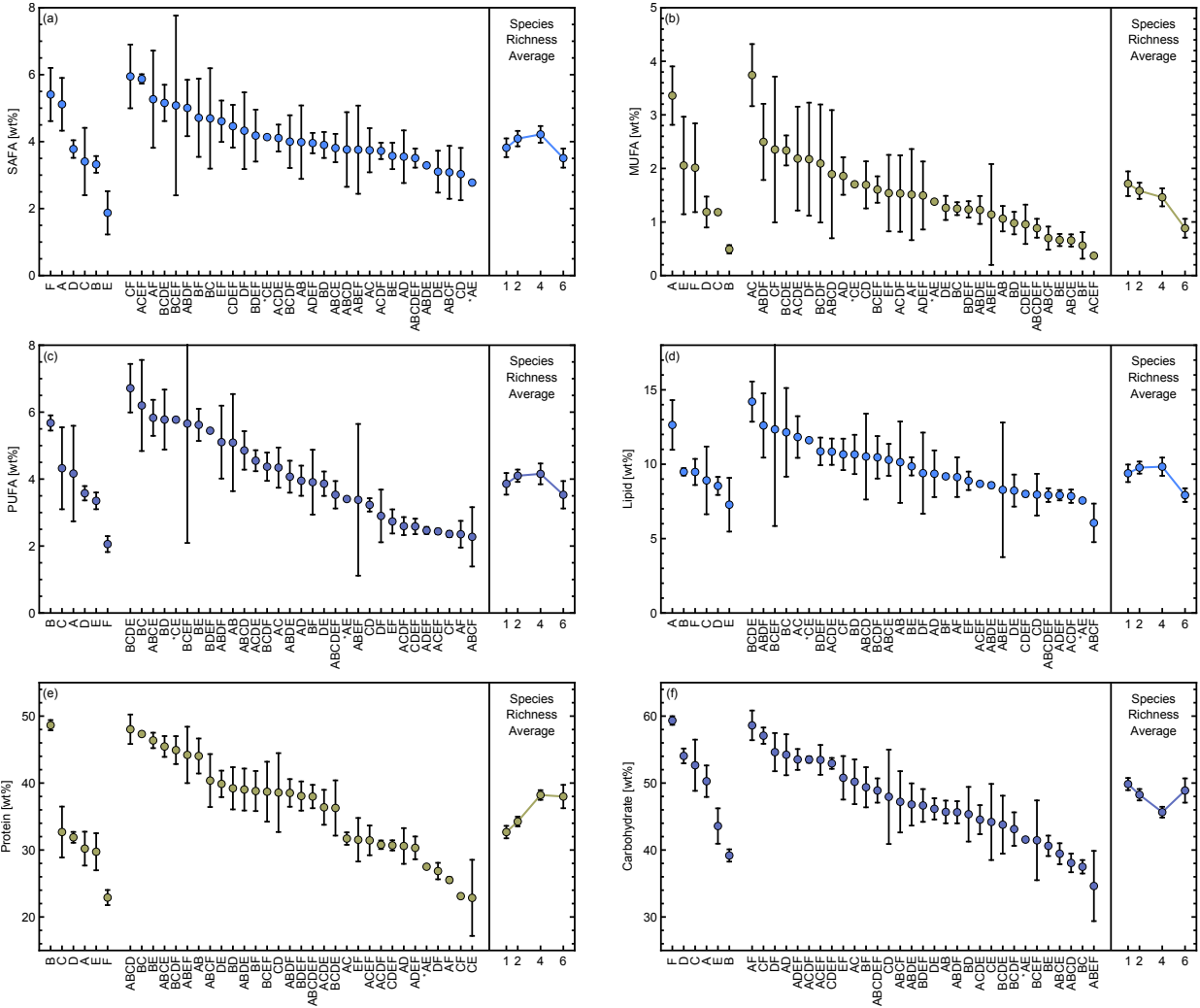


Figure 3.2: (a) SAFA, (b) MUFA, and (c) PUFA yields (wt %) and (d) lipid, (e) protein, and (f) carbohydrate content for 1-, 2-, 4-, and 6-species combinations of *Ankistrodesmus falcatus* (A), *Chlorella sorokiniana* (B), *Pediastrum duplex* (C), *Scenedesmus acuminatus* (D), *Scenedesmus ecornis* (E), and *Selenastrum capricornutum* (F). Values measured in at least duplicate, unless otherwise noted by \*. Error bars represent SE.

and BCEF. Given that *C. sorokiniana* produced the highest PUFA and protein content of the monocultures, we suspect that the presence and abundance of *C. sorokiniana* in the top polycultures is the reason for the higher PUFA and protein production. PUFA and protein content both increase with increasing species richness, with the exception of the 6-species polyculture, although this is likely due to the increased weighting of cultures with *C. sorokiniana* present (i.e.,  $1/6$ ,  $5/15$ , and  $10/15$  of the 1-, 2-, and 4-species cultures contain *C. sorokiniana*, respectively). There are alternative designs of experiment that target the decoupling of species-specific effects by probing only a subset of the complete array of species combinations, thus maintaining a constant weighting of each species with respect to varying species richness [104]. However, those approaches are more amenable to species pools wherein a full factorial design is tedious. In the present study and our previous study [6], we instead sought to examine the complete set of all possible 2-, 4-, and 6-species polycultures.

### 3.3.3 Biocrude properties

Figure 3.3 shows the yield (mass biocrude per unit dry mass algae), H/C ratio, N content, O content, and HHV of biocrude oils produced from HTL of each monoculture and polyculture (see Table B.4 in Appendix B for exact values). The ideal biocrude oil would exhibit low N and O content and high H/C; for comparison, typical petroleum crudes have N and O contents of 0.001 to 0.53 and 0.47 to 1.62 wt %, respectively, H/C ratios of 1.72 to 2.27 [105], and HHVs of 41.9 to 47.0 MJ kg<sup>-1</sup> (calculated using the correlation posed by Channiwala and Parikh [99]). The values for biocrude oil produced from microalgal HTL typically fall outside these ranges [13, 22, 24]. The present results fit this trend, with biocrude H/C, N content, O content, and HHV ranging from 1.41 to 1.54, 4.8 to 6.3 wt %, 11.4 to 13.4 wt %, and 34.1 to 35.7 MJ kg<sup>-1</sup>, respectively. Recall that catalytic upgrading will be required to improve the quality of the biocrude oil before traditional refining processes can be employed, however improvements in H/C and HHV and reductions in N and O content in the direct HTL product will lower the energy and catalyst requirements for the upgrading step.

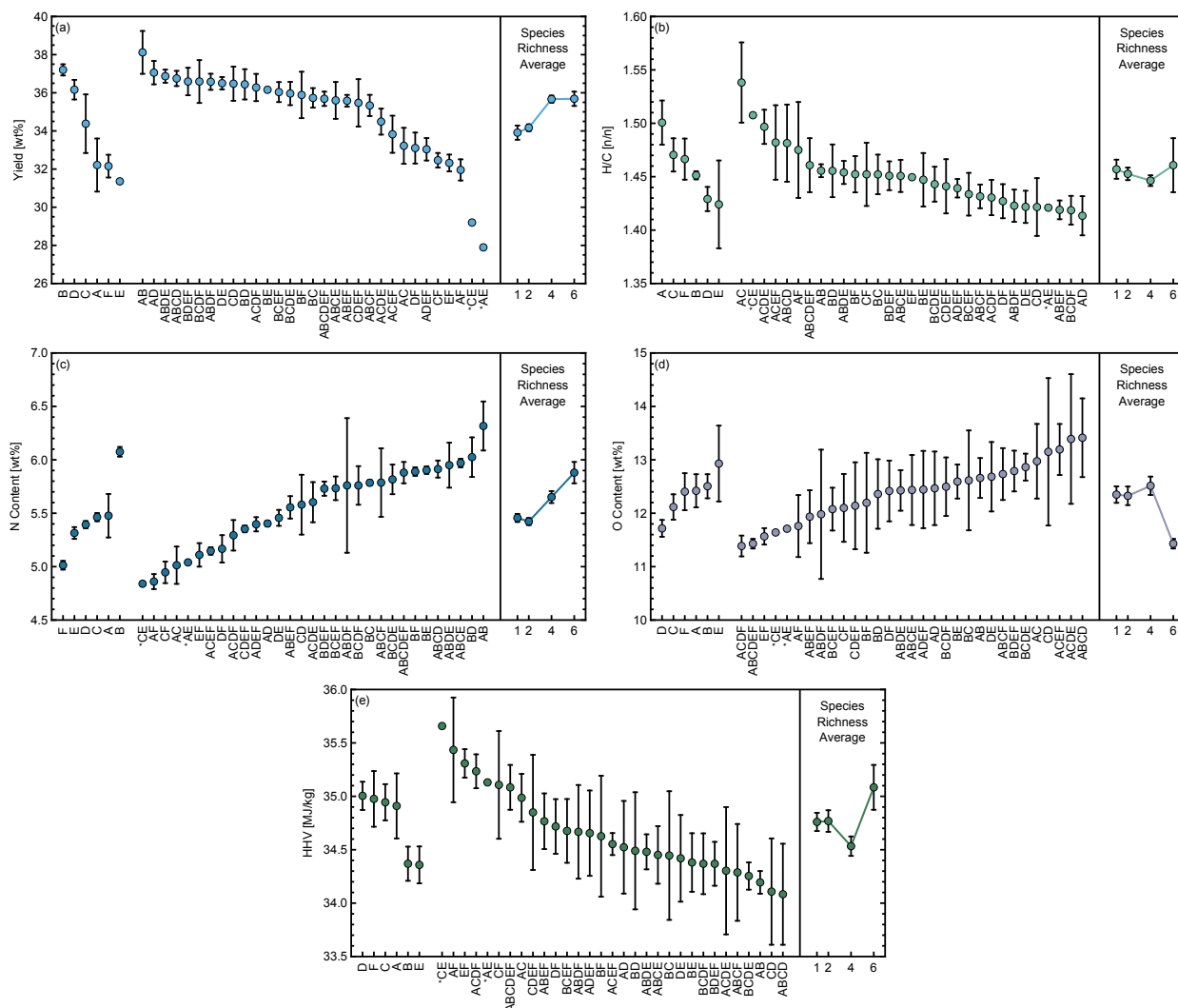


Figure 3.3: Biocrude (a) yield, (b) H/C, (c) N content, (d) O content, and (e) HHV of 1-, 2-, 4-, and 6-species combinations of *Ankistrodesmus falcatus* (A), *Chlorella sorokiniana* (B), *Pediastrum duplex* (C), *Scenedesmus acuminatus* (D), *Scenedesmus ecornis* (E), and *Selenastrum capricornutum* (F). N and O contents are sorted from low to high for readability (lower N and O content is more desirable). Values measured in at least duplicate, unless otherwise noted by \*. Error bars represent SE.

Similar to the results for biochemical composition, no single monoculture produced biocrude with the highest yield (mass biocrude per unit mass dry algae), and overall quality, by all measures considered. The monocultures of *C. sorokiniana* (B), *A. falcatus* (A), *S. capricornutum* (F), and *S. acuminatus* (D) produced biocrude with the highest yield, highest H/C ratio, lowest N content, and lowest O content (in addition to highest HHV), respectively. Only a few polycultures gave higher biocrude yields (AB) or biocrude with higher H/C (AC and CE), while several produced biocrude with lower N content (CE, AF, and

CF), lower O content (ACDF, ABCDEF, EF, and CE), and higher HHV (CE, EF, ACDF, AE, and CF). Although these differences were not statistically significant (calculated here and henceforth by comparing the difference in means using `LocationTest` in Mathematica 10.4), they show that some polycultures were at worst equivalent to the top monocultures for each respective property. Moreover, these data show that different monocultures and polycultures provide certain advantages from a product quality standpoint.

On average across each level of species richness, biocrude yield increased with species richness up to the 4-species cultures. Biocrude H/C and O content was insensitive to changes in species richness on average, with the exception of the 6-species culture for the latter. Biocrude N content remained constant between the 1- and 2-species cultures and then increased monotonically with increasing species richness. Biocrude HHV similarly did not change on average between the 1- and 2-species cultures; it did, however, decrease for the 4-species cultures and increase for the 6-species cultures.

Notably, the high biocrude H/C exhibited by the A and AC cultures is interesting because these were the same top cultures for MUFA content in Figure 3.2b, suggesting that higher biomass MUFA content may be translating directly into higher biocrude H/C. We further note that the fifteen cultures with the highest biocrude N content were all inoculated with *C. sorokiniana* (B). As discussed in Section 3.3.2, Figure 3.1 shows that when *C. sorokiniana* is present in a polyculture, it generally represents the majority of the biomass. Given that the *C. sorokiniana* monoculture produced biocrude with the highest N content of the monocultures by far, it follows reasonably that polycultures containing *C. sorokiniana* would also produce biocrude with higher N content.

### 3.3.4 Polyculture performance relative to monocultures

We use three statistics to evaluate the performance of polycultures relative to the monocultures of their constituent species. The first is the abundance-weighted average (AWA), which for a given quality metric is calculated as the average for the monocultures of the

species constituting a given polyculture, weighted by the mass percentage of each respective species in that polyculture (see Figure 3.1). transgressive overyielding (TO) is the threshold represented by the highest-yielding monoculture of the different species constituting a polyculture. transgressive underyielding (TU) follows similarly for the lowest-yielding monocultures. The concepts of TO and TU are conventionally applied to biomass productivity and lipid production [76], however this terminology is useful for comparing the additional metrics of interest presented in this study, such as biocrude H/C and N content. We can represent the three statistics (AWA, TO, and TU) by Equations (3.1) to (3.3), which can be applied to any metric of interest:

$$Y_i^{\text{AWA}} = \sum_{j \in i} w_{ij} Y_j \quad (3.1)$$

$$Y_i^{\text{TO}} = \max_{j \in i} Y_j \quad (3.2)$$

$$Y_i^{\text{TU}} = \min_{j \in i} Y_j \quad (3.3)$$

$$\Delta_{max} = \max \left\{ \max_i (Y_i - Y_i^{\text{TO}}), \max_i (Y_i^{\text{TU}} - Y_i) \right\} \quad (3.4)$$

Here  $Y_i^{\text{AWA}}$ ,  $Y_i^{\text{TO}}$ , and  $Y_i^{\text{TU}}$  are the AWA, TO, and TU thresholds, respectively, for the polyculture with species composition  $i$ ,  $w_{ij}$  is the weight fraction of species  $j$  in polyculture  $i$ ,  $Y_i$  and  $Y_j$  are the values for the culture with species composition  $i$  or species identity  $j$ , respectively, and  $\Delta_{max}$  is the maximum deviation above or below the TO or TU threshold, respectively, among all species combinations. The summation and max and min functions operate over all monoculture species  $j$  in a given polyculture species composition  $i$ . We note that generally TO is the desired outcome, although for some metrics we wish to minimize, like biocrude N content, TU is desired. Figure 3.4 summarizes the performance of each polyculture relative to AWA, TO, and TU thresholds for each biochemical class and biocrude property. Areas where overyielding or underyielding are desirable for improving quality and quantity are highlighted as goals at the bottom (gray cells indicate no clear preference).

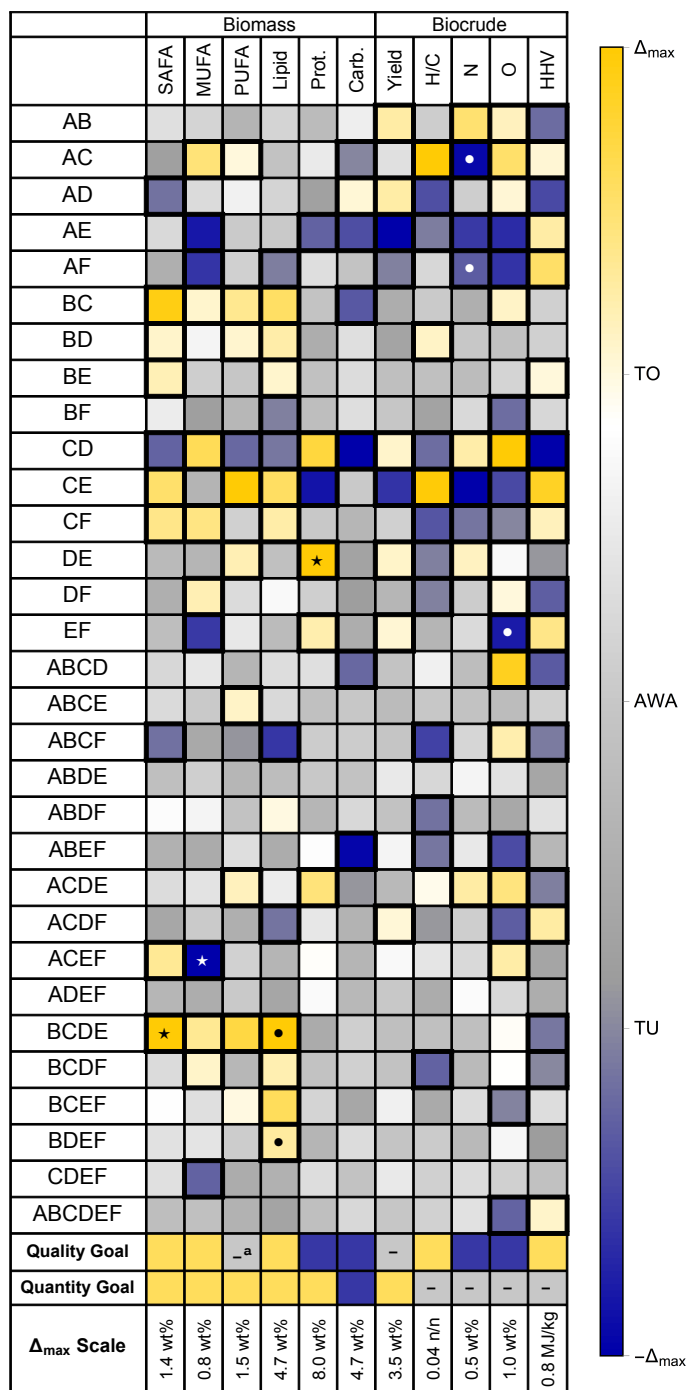


Figure 3.4: Polyculture performance relative to thresholds for TO (maize, bold-outline cells), AWA (gray), and TU (blue, bold-outline cells) for SAFAs, MUFA, PUFA yields, lipid, protein, and carbohydrate contents, and biocrude yield, H/C, N content, O content, and HHV. Polycultures comprised 2-, 4-, and 6-species combinations of *Ankistrodesmus falcatus* (A), *Chlorella sorokiniana* (B), *Pediastrum duplex* (C), *Scenedesmus acuminatus* (D), *Scenedesmus ecornis* (E), and *Selenastrum capricornutum* (F). \* and • indicate statistically significant differences with  $\alpha = 0.05$  and  $0.15$ , respectively.  $\Delta_{max}$  defined in Equation (3.4). <sup>a</sup>Denotes goal not applicable for this metric.

Examining biculture fatty acid production, one sees that each culture inoculated with *P. duplex* (C) demonstrated TO (maize shading) of at least one class of fatty acids, and in several cases, including BC, CE, and CF, this resulted in overyielding of the overall lipid content of the biomass. This outcome is especially interesting given that *Chlorella* was largely absent in cell counts after seven weeks of steady state (see Figure 3.1). Several of the bicultures with *C. sorokiniana* (B), including BC, BD, and BE, showed higher levels of fatty acids than expected by the AWA (lighter gray shading), especially with respect to SAFAs. These cultures largely consisted of *C. sorokiniana* (> 90 wt %) by week 7. Several bicultures showed overyielding of biocrude yield, including AB and AD, with DE and EF demonstrating marginal overyielding as well. Interestingly, the increase observed with AB and AD was not accompanied by increases in lipid or protein content and only by a slight increase in carbohydrate content (AB only). This observation suggests the biochemical content alone might not control biocrude yield for a given set of HTL conditions. The composition within the biochemical classes (e.g., neutral and polar lipids) and/or species identity, as examples, may be playing a role. We note, however, that the aforementioned increases were not statistically significant and all explanations should be viewed as tentative.

Numerous bicultures, including AC, AE, AF, CE, CF, and EF, produced biocrude oil with higher H/C, lower N content, and lower O content than expected based on the abundance-weighted averages. The biocrude N contents for AC (8 % less,  $p = 0.07$ ) and AF (3 % less,  $p = 0.13$ ) were both lower than the TU threshold, but just outside of statistical significance. Six bicultures met or exceeded the threshold for biocrude HHV overyielding, including AC, AE, CE, CF, and EF. Notably, none of the aforementioned bicultures included *C. sorokiniana* (B) or *S. acuminatus* (D). Moreover, the biculture EF uniquely demonstrated both slight overyielding of biocrude yield, a metric of quantity, in addition to biocrude O content underyielding ( $p = 0.09$ ) and HHV overyielding, both metrics of quality.

There were significantly fewer instances of overyielding and underyielding for the 4- and 6-species polycultures compared to the bicultures; however, it is important to recall that the

thresholds in these cases are inherently more stringent given that a polyculture would need to exceed the best monoculture of four or six constituent species, rather than just two, to surpass the overyielding threshold. BCDE ( $p = 0.07$ ), BCDF, BCEF, and BDEF ( $p = 0.11$ ) all demonstrated overyielding of lipid content. This set notably contains all polycultures without *A. falcatus* (A) but with *C. sorokiniana* (B). Note that ABDF essentially met but did not exceed the overyielding threshold for SAFA, MUFA, and lipid content as well. One 4-species polyculture, ACDF, also produced biocrude with higher HHV than the A, C, D, or F monocultures.

### 3.3.5 Extent of overyielding and underyielding by species in bicultures

Another aspect of polyculture performance to consider is the relative extent that each species is involved with community-wide overyielding or underyielding in bicultures. To examine this, we calculated the extent of TO ( $\xi_j^{\text{TO}}$ ) for each response variable and constituent species  $j$ :

$$\delta_i^{\text{TO}} = \begin{cases} Y_i - Y_i^{\text{TO}} & Y_i > Y_i^{\text{TO}} \\ 0 & Y_i^{\text{TU}} \leq Y_i \leq Y_i^{\text{TO}} \\ Y_i - Y_i^{\text{TU}} & Y_i < Y_i^{\text{TU}} \end{cases} \quad (3.5)$$

$$\eta_j^{\text{TO}} = \sum_{i \text{ with } j} \delta_i^{\text{TO}} \quad (3.6)$$

$$\xi_j^{\text{TO}} = \frac{\eta_j^{\text{TO}}}{\max_j^S |\eta_j^{\text{TO}}|} \quad (3.7)$$

Here,  $\delta_i^{\text{TO}}$  is the net TO for species combination  $i$  (which will be positive or negative for net overyielding or underyielding, respectively),  $\eta_j^{\text{TO}}$  is the sum of net TO of all species combinations  $i$  with species  $j$ , and  $\xi_j^{\text{TO}}$  is the extent of overyielding and underyielding, normalized to fall between 1 (maximum overyielding) and -1 (maximum underyielding). Figure 3.5 depicts  $\xi_j^{\text{TO}}$  for each species and quality metric.

Bicultures with *P. duplex* (C) demonstrated the greatest extent of deviations above overyielding and below underyielding thresholds in favorable directions with respect to prod-

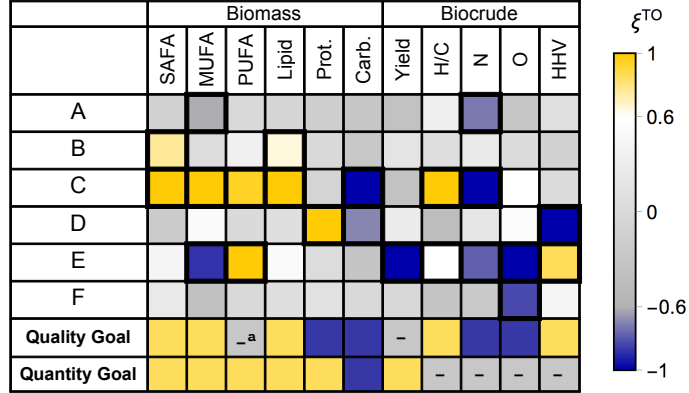


Figure 3.5: Relative extent ( $\xi^{\text{TO}}$ ) of net TO (maize) and TU (blue) in bicultures as a function of species inclusion of *Ankistrodesmus falcatus* (A), *Chlorella sorokiniana* (B), *Pediastrum duplex* (C), *Scenedesmus acuminatus* (D), *Scenedesmus ecornis* (E), and *Selenastrum capricornutum* (F) for SAFA, MUFA, and PUFA yields, lipid, protein, and carbohydrate contents, and biocrude yield, H/C, N content, O content, and HHV. <sup>a</sup>Denotes goal not applicable for this metric.

uct quality; these trends include net overyielding for all three groups of fatty acids, net overyielding of biocrude H/C, and net underyielding of biocrude N content. This is especially interesting considering that *Chlorella* represented only 0 to 10 wt % of the biomass in the AC, BC, CD, CE, and CF bicultures by week seven of steady-state sampling. This observation suggests that the aforementioned trends are unlikely to be explained by the *Chlorella* biomass itself. One potential explanation is that the inoculation of *Chlorella* induced shifts in the biochemical composition (particularly the lipid content) of many if not all of the other species. This could be due to the presence of the *Chlorella* microalgal biomass itself, the non-algal microbial communities that coexist with *Chlorella* in its inoculum, and/or changes in the medium induced by *Chlorella* (e.g., organic compounds used for mixotrophy). Future studies of the interactions between *Chlorella*, its associated microbes, and other species of microalgae are necessary to elucidate the underlying mechanism behind the observed overyielding and underyielding effects. Bicultures with *S. ecornis* (E) also consistently showed benefits from a quality perspective, including net overyielding of biocrude H/C and HHV and underyielding of biocrude N and O content. To a lesser extent, bicultures with *A. falcatus* (A) also underyielded biocrude N content and those with *S. capricornutum* (F) showed net underyielding of biocrude O content.

### 3.3.6 Effect of species identity and biochemical composition

The results presented in the previous sections show that some polycultures produce biomass and biocrude with properties comparable to those of the best monocultures for each metric and that some polycultures performed differently than expected based on AWA, TO, and TU thresholds. The goal of the following exercise is to determine whether or not the observed variation in biocrude H/C, N and O content, HHV, and yield can be explained solely by changes in biochemical composition induced by the presence of certain species, or whether these effects are due to specific species themselves after controlling for changes in biochemical composition. The latter could indicate that differences in cellular morphology between species (e.g., surface-area-to-volume ratio, geometry, and cell wall thickness) may affect reactivity during HTL and as a result the distribution and composition of the reaction products. Previous studies have employed biochemical composition as a means for predicting the properties of biocrude oil produced from HTL [13, 15, 40, 48]. Biller and Ross [13] were the first to model biocrude by a first order polynomial of biochemical composition (lipid, protein, carbohydrate):

$$Y^B = \sum_i \beta_i B_i \quad (3.8)$$

Here  $Y^B$  is biocrude yield (mass/mass) and  $B_i$  is the content (mass/mass) of biochemical component  $i$ . This model assumed that each biochemical class reacts differently, independently, and additively to form biocrude. As such, they approximated the model coefficients  $\beta_i$  by using the biocrude yields obtained from conducting HTL on pure model compounds for lipids, proteins, and carbohydrates. This approach predicted the biocrude yields for some algal species (*Chlorella vulgaris* and *Nannochloropsis oculata*), but not all (*Spirulina* sp. and *Porphyridium cruentum*). Teri et al. [48] expanded this concept to account for cross reactions between biochemical components:

$$Y^B = \sum_i \beta_i B_i + \sum_{ij} \epsilon_{ij} B_i B_j \quad (3.9)$$

They approximated the model coefficients  $\beta_i$  similar to Biller and Ross [13] and approximated the model coefficients  $\epsilon_{ij}$  by using the biocrude yields obtained from conducting HTL on binary mixtures of model compounds for lipids, protein, and carbohydrates. They found this model with cross terms accurately predicted the yield of some ternary mixtures of model compounds better than the simpler first order model, while for other mixtures it produced a poorer prediction. Leow et al. [40] and Li et al. [15] also adopted this approach used in Equation (3.8) but instead used multiple linear regression on HTL data generated from samples of microalgae with varying biochemical composition. Moreover, they used similar approaches to correlate biocrude elemental content based on lipid content, protein content, or the average oxidation state of feedstock carbon.

The present dataset of 37 species combinations featuring six different species of microalgae is well suited for this multiple linear regression approach (for these analyses we also include the constant-growth-temperature results reported in Appendix B for a total of 74 biomass types). Moreover, because the biomass samples comprise all 1-, 2-, 4-, and 6-species combinations, these data are ideal for elucidating species-specific effects that exist, if any, in addition to those related to biochemical composition. Species identity has been suggested as a parameter that affects the properties of biocrude produced from HTL, for example via differences in cellular morphology that affect reactivity [22, 31, 39, 56]; however, no previous study has attempted to decouple the effects of biochemical composition and species identity. To apply the multiple linear regression method to the data in the present study to account for both biochemical composition and species identity, we considered the twelve different model types listed in Table 3.2.

Each of these types comprises a set of five models, each correlating biocrude H/C, N content, O content, HHV, and yield, respectively. These models apply different polynomial orders, biochemical terms, and species terms, including:

- First order (similar to Biller and Ross [13]; Sets 1–6) and second order (similar to Teri et al. [48] but including squared terms; Sets 7–12). The former assumes each

Model Set	Model Form	Biochemical Terms ( $B$ )	Species Terms ( $S$ )
1			-
2		<i>Lip, Pro, Car</i>	$b_k$
3	$Y = \beta_0 + \sum_i \beta_i B_i$		$w_k$
4	$+ \sum_i \beta_i S_i$		-
5		<i>Sat, Mon, Pol,</i>	$b_k$
6		<i>Pro, Car</i>	$w_k$
7			-
8	$Y = \beta_0 + \sum_i \beta_i B_i$	<i>Lip, Pro, Car</i>	$b_k$
9	$+ \sum_i \beta_i S_i$		$w_k$
10	$+ \sum_i \gamma_i B_i^2$		-
11	$+ \sum_{ij} \epsilon_{ij} B_i B_j$	<i>Sat, Mon, Pol,</i>	$b_k$
12		<i>Pro, Car</i>	$w_k$

Table 3.2: Model types considered for correlating biocrude property  $Y$ .  $\beta$ ,  $\gamma$ , and  $\epsilon$  denote model coefficients. *Lip, Pro*, and *Car* represent biomass lipid, protein, and carbohydrate content, respectively. *Sat, Mon*, and *Pol* represent biomass SAFA, MUFA, and PUFA content, respectively.  $b_k$  and  $w_k$  denote binary presence (true or false) and weight percentage of species  $k$ , respectively ( $k \in A, B, C, D, E, F$ ).

biochemical class contributes independently, while the latter allows for second order interactions between the classes.

- Biochemical composition based on proximate analysis (i.e., lipid, protein, carbohydrate; Sets 1–3, 7–9) and proximate analysis with fatty acid classes (i.e., SAFA, MUFA, PUFA, protein, carbohydrate; Sets 4–6, 10–12).
- No species identity (Sets 1, 4, 7, 10), species identity as nominal variables (i.e., species are either present or absent; Sets 2, 5, 8, 11), and weight percentages of each species (see Figures B.1 and 3.1; sets 3, 6, 9, 12).

We used `LinearModelFit` in Mathematica 10.4 to obtain the parameters in the 60 different models (5 properties x 12 types). Note that we included the intercept ( $\beta_0$ ) rather than forcing the models to intersect with the origin because a value of zero for any biocrude property would be aphysical for microalgae. The intention for these models was to provide a statistical basis for quantifying how much of the variation in biocrude properties could be explained by only biochemical composition and by the inclusion of species identity. As such, we do not necessarily expect the correlations to be predictive outside of the range of

lipid (6.1 to 14.2 wt %), protein (22.9 to 48.6 wt %), and carbohydrate (34.6 to 59.3 wt %) contents in this study. For each model describing each biocrude property, we calculated the Akaike Information Criterion with correction for finite sample size (AICc) for each model using the AICc model property in Mathematica. AICc is a measure of goodness of fit that takes into account model complexity [106], with lower values representing better models. We recursively tested whether removing any one term improved the AICc for the model; this procedure allowed us to ensure that simpler models did not provide as proportionally adequate of a fit with fewer parameters.

Biocrude Property	Set 10 (Biochemical)		Set 11 (Biochemical + Species)					
	$R_{adj}^2$	ESS %	$R_{adj}^2$	ESS %	PSS %		Model Sensitivities	
					Biochemical	Species	Biochemical	Species
H/C	0.62	67	0.76	80	70	30	0.40 n/n	0.05 n/n
N	0.87	88	0.90	90	71	29	1.1 wt%	0.4 wt %
O	0.68	71	0.77	80	58	42	4.2 wt%	1.7 wt%
HHV	0.46	50	0.50	55	86	14	1.8 MJ kg <sup>-1</sup>	0.2 MJ kg <sup>-1</sup>
Yield	0.97	97	0.98	98	86	14	12.6 wt%	1.9 wt%

Table 3.3: Summary of the best models for correlating biocrude properties based on only biochemical composition (Set 10) and based on biochemical composition and species identity (Set 11). Model Sensitivities show the differences between the maximum and minimum possible model-predicted values due to either biochemical composition or species identity terms.

Out of the twelve model types considered, Set 11, comprising the second-order models based on biochemical composition with fatty acid subgroups and species identity as nominal variables, was always the type with the lowest AICc for all biocrude properties, shown in Table 3.3. Moreover, Set 10, comprising the second-order models based on biochemical composition with fatty acid subgroups, was always the best variant with no species incorporation for all biocrude properties, shown in Table 3.3. Set 11 also had a higher explained sum of squares (ESS) than Set 10, although by varying degrees for each biocrude property; N content, HHV, and yield all saw marginal improvement in ESS for models in Set 11, while H/C and O content saw at least 9 % (absolute) improvement in ESS. The partial sum of squares (PSS) owed to species identity terms in Set 11 models ranged from minimally (HHV and yield) to moderately (H/C and N content) to significantly contributing (O content).

All of the Set 10 and 11 models showed at least 50 % ESS, however only the models for biocrude N content and yield explained enough variation to be considered to be reasonable correlations, with  $R_{adj}^2$  of at least 0.87. The two right-most columns in Table 3.3 quantify how sensitive the Set 11 models are to either biochemical content or species identity. More specifically, we determined the two biochemical profiles that maximized and minimized each biocrude property, respectively, and calculated the sensitivity to biochemical composition as the difference between those values; this procedure followed similarly for species identity. The Set 11 models were all less sensitive to species identity than biochemical composition, ranging from 60 to 89 % lower. The calculated Set 10 and 11 model coefficients are listed in Tables C.1 to C.5 in Appendix C.

Based on this analysis, we conclude that biochemical composition best correlates biocrude H/C, N and O content, HHV, and yield, as previous studies have suggested [13, 40, 48]. However, we also show that the inclusion of species identity as nominal variables provides more information than biochemical composition alone, even after adjusting for the increase in parameters via AICc. Moreover, for the first time, we have quantified the effect of species identity on biocrude properties and compared it to that of biochemical composition. The sensitivity of the models with respect to biochemical composition and species identity suggests that, in terms of feedstock characteristic considerations, the former should be the focus of any process modeling efforts; however, the latter should be considered as well for the highest model accuracy.

The effects of species identity could very well be linked to cell morphology, which varied considerably between each species in the present study. That of *A. falcatus* is thin and rod-like, while that of *C. sorokiniana* is fairly spherical. *Chlorella* exists in colonies of dozens or more cells with “tooth-like” morphologies. *S. acuminatus* and *S. ecorinis* both exist in small (4 to 10) clusters of rod-like cells, with the former exhibiting cells with much thinner and narrower morphology. Finally, the cells of *S. capricornutum* are crescent-shaped. These different morphologies likely influence the reactivity of the cells during HTL, which could

ultimately affect the yield and quality of the biocrude produced. Future studies designed to decouple the effects of biochemical composition and species identity are necessary to further substantiate the results presented here.

### 3.3.7 Trade-offs between product quality and quantity

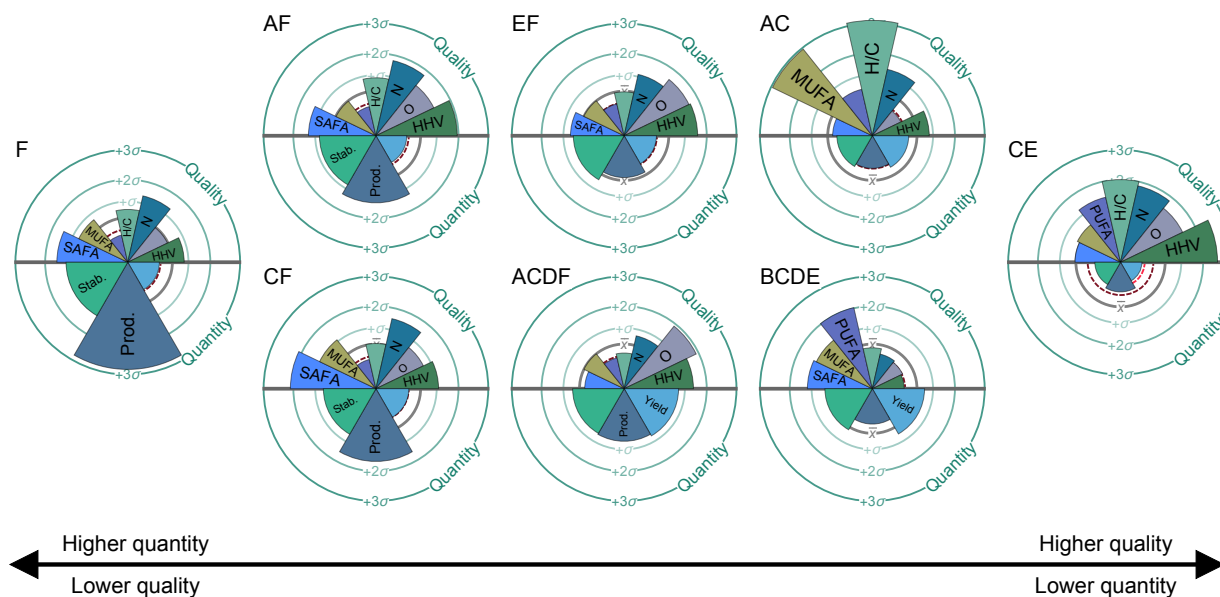


Figure 3.6: Quality (top half of each circle) vs. quantity (bottom half of each circle) sector charts for selected species combinations of *Ankistrodesmus falcatus* (A), *Chlorella sorokiniana* (B), *Pediastrum duplex* (C), *Scenedesmus acuminatus* (D), *Scenedesmus ecornis* (E), and *Selenastrum capricornutum* (F). Combinations on the right exhibited higher product quality but lower quantity; the reverse is true for the left. Wedge lengths indicate number of SDs  $((x_i - \bar{x})/\sigma_i)$  away from the mean (averaged over all 37 species combinations) for each metric. SAFA, MUFA, and PUFA represent yields present in microalgal feedstocks. H/C, N<sup>a</sup>, O<sup>a</sup>, HHV, Yield, Prod., and Stab. represent biocrude hydrogen-to-carbon atomic ratio, nitrogen content, oxygen content, higher heating value, yield, productivity, and stability, respectively. <sup>a</sup>Denotes metrics multiplied by -1 so that larger wedges correspond to more favorable outcomes.

In evaluating which polycultures were the top performers with respect to product quality, it becomes clear that any gains in quality are at the direct expense of quantity. As an example, across all species combinations, biocrude yield and HHV were significantly, strongly, and negatively correlated ( $\rho = -0.57$ ,  $p = 0.0001$ ). In our earlier study [6], we found that the monoculture of *S. capricornutum* (F) was the single most productive and stable culture. As a result, the present discussion of the best species combinations for product quality should include comparisons against this monoculture. Figure 3.6 presents these comparisons as a

summary of the performance of the top species combinations for product quality (sector charts for every species combination can be found in Figure B.5 in Appendix B). Each sector chart is divided such that the top half shows metrics related to product quality (SAFA, MUFA, PUFA, H/C, N, O, and HHV), while the bottom half shows those related to product quantity (Stability, Production, and Yield). Recall that we define biocrude yield as the mass of biocrude produced per unit mass dry algae, production as the mass of dry algae per unit volume growth media multiplied by biocrude yield, and stability as the mean biocrude production (averaged over all seven sampling weeks) divided by the SD. Each combination lies along a spectrum of higher production (but lower quality) to lower production (but higher quality), with the monoculture of *S. capricornutum* representing the extreme of high production.

From left to right, each polyculture sacrifices incrementally more biocrude production and stability in exchange for more favorable biocrude properties compared to the monoculture of *S. capricornutum*, including higher biomass fatty acid content and higher H/C, lower N and O content, and higher HHV in the biocrude. These trade-offs show that there is no single species combination that performed the best for all metrics of interest, in contrast to the conclusion from our earlier study, which only considered aspects of biocrude quantity and not quality [6]. Based on these results, the addition of another species, such as *A. falcatus*, *Chlorella*, or *S. ecorinis*, to a culture of the most productive and stable species, *S. capricornutum*, may be the most optimal trade-off due to the enhanced quality afforded by a modest decrease in production. Ultimately a quantitative optimization function that appropriately weights each of the quality and quantity metrics will be necessary to evaluate the holistic performance of each species combination. For example, the 3 % lower N content and 5 % lower O content afforded by the AF polyculture could represent significant cost savings for catalytic upgrading that may or may not outweigh the cost of additional raceway ponds necessary to reach the same level of total biocrude production.

### 3.4 Conclusion

In this chapter, we examined the performance of algal polycultures and monocultures in terms of feedstock characteristics and quality of biocrude oil produced from HTL. We found that, on average, the 2-species cultures produced biomass and biocrude of a quality that matched the average monoculture, while the 4- and 6-species cultures were worse on average. Specific species combinations met or exceeded the best monoculture for each metric presented; however, no one species combination was the best for all metrics considered. Several species, including *Chlorella* in particular, as well as *A. falcatus* and *S. ecornis* were present in 2-species combinations that demonstrated the greatest extent of favorable instances of TO and TU with respect to product quality. When considered together, biochemical composition and species identity best explained the variation in biocrude properties compared to biochemical composition alone. We also quantify this species identity effect for the first time and show that its maximum effect on modeled biocrude properties is 11 to 40 % of that of biochemical composition. We suggest that biocrude productivity is inversely related to product quality by comparing the most productive monoculture (*S. capricornutum*) to the polycultures producing the highest quality products. These polycultures may offer potentially compelling advantages, including higher lipid content and lower biocrude N and O content, over their monoculture counterparts at the direct expense of quantity. Such advantages, however, will likely be found only on a combination-specific basis, rather than as a general trend with respect to species richness.

## CHAPTER IV

# The effects of biochemical composition, microalgal species, concentration, temperature, and time on biocrude production by hydrothermal liquefaction

This chapter contains results that were submitted for publication in *Applied Energy* written along with co-authors Casey M. Godwin, Bradley J. Cardinale, and Phillip E. Savage [107]. Herein, we sought to examine the effects of HTL reaction conditions and feedstock characteristics on biocrude production in a more comprehensive and systematic manner based on observations from results presented in Chapters II and III and including previously unexplored variable combinations. Specifically, we examined the effects of temperature (150 to 350 °C), reaction time (1 to 100 min), slurry concentration (30 and 120 g L<sub>rxn</sub><sup>-1</sup>), biochemical composition (5.2 to 28.5 wt% lipid, 14.7 to 50.9 wt% protein), and species identity (*Nannochloropsis*, *Chlorella*, and *Spirulina*) on biocrude oil properties. Measured properties included gravimetric yield, elemental (CHNSOP) composition and recovery, HHV, energy recovery (ER), and fatty-acid profile, content, and recovery. All examined factors affect the yield and composition of the biocrude, with biochemical composition and temperature exhibiting the greatest impacts. The effects of slurry concentration and species identity were of the same order of magnitude as reaction time and have not been scrutinized in detail in the literature until now. We show evidence of increased slurry concentration promoting Maillard

reactions that result in increased biocrude yield, C content, and N content and decreased O content. Moreover, the extent of these Maillard reactions appears to be affected by the ratio of proteins to carbohydrates, with carbohydrates serving as the limiting reactant. High-lipid, 30 g L<sub>rxn</sub><sup>-1</sup> slurries reacted at 300 °C for 3.2 min (including 1 min heat-up) generally yielded more biocrude with higher C and H content and lower N, S, and O content than did their high-protein, 120 g L<sub>rxn</sub><sup>-1</sup>, 200 °C, or 31.6 min counterparts. This condition also provided recoveries of saturated, monounsaturated, and polyunsaturated fatty acids in the biocrude of up to 89.3, 80.1, and 64.7 wt%, respectively. These novel findings and expansive experimental data further expand our understanding of microalgal HTL and provide the basis for developing a new quantitative kinetic model in Chapter VI.

## 4.1 Introduction

Biocrude yield and the extent of catalytic upgrading required depend on factors such as temperature and time [21–25, 27, 29, 34], concentration [21, 23, 24, 38], biochemical composition [13, 15, 29, 39, 40, 42–44], and species identity [39, 42]. Many previous studies of these factors have various limitations. Generally no more than one or two factors are considered at a time, and there are regions of the reaction domain that are relatively unexplored, particularly at low and mild reaction severities. Furthermore, factors such as slurry concentration [21, 23, 24, 38] and species identity [39] have received little scrutiny to date, especially in terms of actually quantifying their effects in the context of other factors. No previous study has examined all of these factors together and how they may dynamically synergize or antagonize over regions of the reaction domain. There may be unexplored yet desirable relationships between these variables that reduce the extent of catalytic upgrading required downstream, thus improving overall process EROI and sustainability.

In this study, we employ fast-heating batch reactors (1-min heat-up) to establish a wide-ranging set of experimental data for microalgal HTL that establish and corroborate the individual and dynamic impacts of several types of reaction conditions and feedstock charac-

teristics. These experiments span reaction times logarithmically ( $10^{0.0}$ ,  $10^{0.5}$ ,  $10^{1.0}$ ,  $10^{1.5}$ , and  $10^{2.0}$  min) over a large range of temperatures (150, 200, 250, 300, and 350 °C) for six biomass types with different biochemical profiles (5.2 to 28.5 wt% lipid, 14.7 to 50.9 wt% protein) at two different slurry concentrations (30 and 120 g L<sub>rxn</sub><sup>-1</sup>). We chose three of these biomass feedstocks, including a high-lipid *Nannochloropsis*, high-lipid *Chlorella*, and high-protein *Spirulina*, to exhibit different proximate biochemical compositions to assess the effects of different lipid, protein, and carbohydrate contents at different reaction severities and slurry concentrations. We chose the other three, including a high-protein *Nannochloropsis*, a high-protein *Chlorella*, and a mixture of high-protein *Spirulina* and high-lipid *Chlorella*, to exhibit similar proximate biochemical composition, allowing assessment of the variability between different species over different reaction conditions and slurry concentrations while controlling for biochemical composition. Similarly, the two variants of *Nannochloropsis* and *Chlorella* allow evaluation of the effects of biochemical composition while controlling for species identity. We also compare and contrast the measured and predicted effects of the two-species mixture, respectively, to help illuminate how the different proportions of biochemical components in high-protein *Spirulina* and high-lipid, high-carbohydrate *Chlorella* interact with each other over different reaction severities and slurry concentrations, compared to how they react individually. We report herein on the impact of these inputs on the yield and composition of the biocrude oil, with that of the ACP, solid, and gas fractions documented in Chapter V, Appendix F, and Appendix G, respectively. These data serve as the foundation for the creation of a unique, quantitative kinetic model for the HTL of microalgae in Chapter VI.

## 4.2 Materials and methods

### 4.2.1 Microalgae feedstocks

We obtained preservative-free high-protein *Nannochloropsis oculata* (Nan-1) as a slurry, high-lipid *Nannochloropsis salina* (Nan-2) as a dry powder, and *Spirulina platensis* (Spi-1)

as a dry powder from commercial sources. We grew *Chlorella sorokiniana* as 12-L batch cultures in a temperature-controlled room (20 °C). We cultivated algae in Bold-3N medium (Bold 1949), containing either replete nitrogen (8.82 mmol L<sup>-1</sup> as nitrate) or limiting nitrogen (0.882 mmol L<sup>-1</sup> as nitrate). We chose these conditions based on preliminary growth experiments showing that the replete- and limiting-nitrogen treatments produced a high-protein *Chlorella* (Chl-1) and a high-lipid *Chlorella* (Chl-2), respectively. We maintained cultures in polyethylene buckets with a capacity of 20 L and fluorescent lights delivered 300  $\mu\text{mol photon m}^{-2} \text{ s}^{-1}$  at the surface of the water (18 h light and 6 h dark). A single air diffuser continuously mixed and aerated the cultures. We monitored algal growth using in vivo fluorescence of chlorophyll *a* as a proxy for algal biomass. We measured fluorescence in microtiter plates using a Biotek Synergy H1 plate reader (excitation at 435 nm and emission at 685 nm). We computed the maximum exponential growth rate of each culture using all consecutive fluorescence measurements in a similar manner as our previous work [84]. We harvested the algae after 19 days by centrifuge and decanting. Upon harvest, we measured the algal biomass by collecting samples onto pre-weighed filters (Millipore AP40), drying the biomass at 60 °C for 48 h, then weighing the filters again [6]. These measurements demonstrate N-limitation for high lipid production and are presented in Figure D.1 in Appendix D. While it is widely recognized that even mild N-limitation can lead to increased lipid content in algae [91, 108], balancing the benefits of increased lipid content against the costs of lower biomass density and growth rate remains an area of interest, including for this study. Severe N-limitation may lead to even greater lipid content in biomass, but, by definition, the total amount of biomass and the rate at which it is produced will decrease further with the severity of N-limitation.

#### 4.2.2 Slurry preparation

We diluted and pre-mixed each biomass type with deionized water to prepare slurries at a variety of mass percentages such that their concentrations were either 30 or 120 g L<sub>rxn</sub><sup>-1</sup> at

reaction conditions (150 to 350 °C), calculated based on the density of pure, saturated, liquid water at those conditions. The solids content of those slurries ranged from 3.2 to 5.0 wt% and 11.6 to 17.3 wt%, respectively; see Table D.1 in Appendix D for exact solids contents used. We chose a mass per volume-at-reaction-condition basis for slurry concentration to allow for orthogonal comparison of temperature effects holding all else constant, which would not be possible using a wt% basis due to the expansion of water with increasing temperature. Moreover, a mass-per-volume basis is more relevant for characterizing reaction systems that deviate from first-order behavior. We note that all references to concentration herein, including those from the literature, are on this mass per volume-at-reaction-condition basis, *not* at ambient conditions. We prepared the two-species mixture slurries (Mix-m) by mixing roughly three parts low-protein *Chlorella* (Chl-2) with seven parts *Spirulina* (Spi-1) for an average Chl-2 content of 30.1 wt%. We calculated the predicted two-species mixture slurry (Mix-p) behavior based on the weighed average of the behavior of Spi-1 (69.9 wt%) and Chl-2 (30.1 wt%).

We re-measured the solids content of slurries each instance they were used for reactions to control for any possible evaporative losses of water during storage. We accomplished this by pre-weighing four aluminum weigh boats, filling two of them with roughly 500 mg of slurry each, and leaving the other two to serve as controls. We placed all four into an oven set to 70 °C for 24 h and then placed them inside a dessicator for approximately 1 h. We then re-weighed each weigh boat and calculated the solids content as the mass of dry algae (subtracting out the average loss in mass from drying the control weigh boats) divided by the initial mass of slurry and then averaged across both replicates.

### 4.2.3 Hydrothermal liquefaction

We reacted slurries of all biomass types at 200 and 300 °C for 3.2 ( $10^{0.5}$ ) and 31.6 min ( $10^{1.5}$ ), a subtotal of 24 conditions. We also reacted slurries of Nan-1 and Chl-2 at 150, 250, and 350 °C for  $10^{0.0}$ ,  $10^{1.0}$ , and  $10^{2.0}$  min, a subtotal of 18 reaction conditions. Moreover, we

reacted slurries of Nan-2 and Spi-1 at 150 °C for 1 min and at 350 °C for 100 min, a subtotal of 4 reaction conditions. Finally, all reactions were run for both 30 and 120 g L<sub>rxn</sub><sup>-1</sup> loadings with the exception of Spi-1 at 350 °C, 100 min, which would have required a slurry that was too viscous to pipette for the 120 g L<sub>rxn</sub><sup>-1</sup> concentration. We conducted HTL at a total of 91 unique sets of reaction conditions in at least duplicate, and in some cases triplicate or more to generate enough product mass for subsequent analysis. All reactions were conducted in a completely random order.

We built each 1.30 mL batch reactor using 1/4-in. o.d., 0.049 in. thick Swagelok tubing cut to 10.5 cm lengths and two caps, all made of 316 stainless steel. We loaded each reactor with enough of the appropriate pre-mixed slurry such that the entire control volume would be occupied at reaction conditions from thermal expansion under autogenous pressure. We sealed reactors to 20 ft-lbs. using a torque wrench.

We constructed additional 1.16 mL proxy reactors for temperature measurements using the same 10.5 cm lengths of tubing as the main reactors, a cap, and a 1/4-in.-to-1/16-in. bored-through reducing union. We fitted the reactors with an Omega Engineering 1/16-in.-diameter 18-in.-long stainless-steel-clad K-type thermocouple (TJ36-CASS-18U-18-CC-SB) such that the tip of the thermocouple resided 6 cm away from the opening of the tubing. We bent the thermocouple in a 90° angle at a 1/4-in. rounding radius so that reactors could be oriented flat for maximum heat transfer, relative to the thermocouple wire which extended upward. We loaded proxy reactors with enough deionized water to match the same ratio of total-loaded-mass to-control-volume as the primary reactors. We used an Omega Engineering UWBT-TC-UST-NA Datalogger to record the temperature measured by the proxy reactor thermocouples every 1 s.

We conducted reactions individually by immersing both a slurry-loaded reactor and proxy reactor horizontally into a metal basket residing within a Techne IFB-51 fluidized sand bath, preheated to the specified temperature. Usually, set-point temperatures of 150, 200, 250, 300, and 350 °C resulted in average heating rates of 155, 250, 300, 365, and 450 °C min<sup>-1</sup>,

respectively. We calculated these rates as linear averages over the time it took reactors to achieve 95% of the maximum temperature change relative to ambient conditions, on average about 43 s. It typically took reactors about 58 s to achieve 98% of the maximum temperature change. At a set-point temperature of 250 °C, for example, this is a temperature change of change of 220.5 °C, or when the reactor reaches 245.5 °C. See Table D.2 in Appendix D for average temperature profiles. At the end of the holding time ( $10^{0.0}$ ,  $10^{0.5}$ ,  $10^{1.0}$ ,  $10^{1.5}$ , or  $10^{2.0}$  min), we quenched the reactors in a cold water bath. We define this holding time as the time from the moment the reactor starts to heat up to the moment the reactor starts to cool down. After about 1 min, we dried the exterior of the reactors with paper towels and placed the primary reactor into an acetone bath for 10 min to displace any residual water. We then briefly air dried the reactor to evaporate the acetone and allowed it to equilibrate at room temperature for 10 min.

We weighed the reactor and tapped it forcefully on the benchtop three times before slowly opening the reactor in a vice grip to release gas. Once the gas escaped, we re-weighed the reactor to estimate the mass of gas evolved by difference from the pre-opened mass of the reactor. We note that in some instances, especially for the  $120 \text{ g L}_{\text{rxn}}^{-1}$  slurries at high reaction severity, gas bubbled out so vigorously that a small aliquot of reaction mixture escaped. In these instances, we omitted the gas measurement and instead recovered the escaped mixture. We measured 5.5 mL of DCM (>99.9% optima grade, Fisher Scientific) and enough deionized water (4.3 to 4.9 mL) such that the total volume of water (in the reaction mixture and added water) was approximately 5.5 mL to facilitate product collection. We then used a glass pipette to collect as much of the reaction mixture as possible into a glass conical tube, washing the reactor walls using aliquots of solvent. For low-severity reactions (250 °C, 10 min and lower) we used the water first and then the DCM; for more severe reactions, we reversed the order. This was done to more effectively recover products by matching the polarity of the solvent with the more dominant polarity in the reaction mixture. In some instances, particularly with both types of *Chlorella*, the total 11 mL of solvent was insufficient

to collect all of the reaction mixture. In those situations, we washed the reactor walls with aliquots of additional solvent, primarily acetone and sometimes including additional DCM or deionized water (depending on reaction severity), into a secondary glass conical tube kept out of contact with the first. This procedure continued until the reactor was clean (rinsings were clear and colorless).

Following product recovery, we vortexed the primary-reaction-mixture conical tube at 3000 rpm for 15 s. We then centrifuged this conical tube at 1000 rcf for 1 min and subsequently collected the organic (DCM-soluble) phase into a separate glass tube. We once again vortexed and centrifuged (1500 rcf, 3 min) the remaining mixture of ACP and solid products, and then collected the ACP into an additional glass tube, with the solid phase remaining in the original conical tube. Generally the separation between phases during these steps was excellent for reactions at moderate to high reaction severity, although for milder reactions, sometimes additional centrifugation at higher rcf for longer amounts of time was required to fully separate the phases.

We dried the tubes containing the DCM-dissolved organics, remaining solids, ACP, and additional acetone-dissolved products (if present) under nitrogen (99.998%, Metro Welding Supply Corp.) using a Labconco RapidVap Vertex Dry Evaporator with a solid aluminum heating block at 35 °C for 1 h. We then capped tubes containing the dried organic phase, or biocrude oil, and allowed them to cool overnight before weighing them. This process of drying at 35 °C for 1 h, cooling, and weighing continued cyclically until consecutive measurements differed by less than 1.5 % of the initial dry algae mass loaded. We dried the other tubes containing the solids, ACP, and acetone-dissolved products under nitrogen at 70 °C for 1 h or until phases appeared dried. We similarly followed a cycle of allowing tubes to cool overnight, reweighing, and re-drying for 1 h until measurements differed by less than 1.5 % of the initial dry algae mass loaded. Note that we used a set of four empty, capped glass tubes as a control for mass change due to temperature and humidity, among other possible environmental factors, which was factored into this 1.5 % difference threshold.

In cases where acetone was used to collect additional reaction products, we added the same 11 mL of 1:1 DCM/water mixture to the dried tubes and followed the same steps as above, including vortexing, centrifuging, collecting products into additional glass tubes, drying, and weighing. We calculated the biocrude mass as the total dried masses of the DCM-soluble phase(s) and calculated the solid and aqueous-phase product masses similarly. In all cases, we set aside only the original, non-acetone-exposed fractions for further characterization and assumed those analyses are representative of each total product fraction. In this manner, each characterized fraction from each set of experimental conditions underwent roughly the same conditions during product collection. We combined and homogenized replicate non-acetone-exposed solid and biocrude product fractions before measuring their fatty-acid profile and elemental content.

#### 4.2.4 Fatty-acid esterification

We adapted the procedure used to extract, esterify, and quantify fatty acids from the method developed by Levine et al. [94]. We pre-weighed approximately 10 mg of dried biocrude, algal biomass, or solid residue into 10-mL glass round-bottom tubes and added a Teflon-coated micro-stir bar and 2 mL of acidified methanol (Fisher Scientific, HPLC grade) containing 5 % acetyl chloride (ACROS Organics, ACS reagent grade) by volume into each tube. We capped all vials tightly and placed them in a preheated Fisher Scientific Isotemp Dynabloc on a hot plate maintained at 100 °C and 800 rpm for 90 min. Every 30 min, we agitated the vials to ensure sample remained immersed in solution. After 90 min, we removed the vials and allowed them to cool to room temperature for about 10 min. Once the vials reached room temperature, we added 1 mL of deionized water and 3 mL of a 250 mg L<sup>-1</sup> solution of tricosanoic methyl ester (C23:0, Sigma-Aldrich, ≥99.0%) in n-heptane (ACROS Organics, ≥99.0%) to each vial. We then vortexed each vial for 2 min, centrifuged at 2000 rpm for 10 min, and then transferred the heptane layers into GC vials for subsequent analysis.

We quantified FAMEs using an Agilent 7890A GC-FID and an Agilent Biodiesel GC column (1909BD-113). Helium was the carrier gas at a flow rate of 1 mL min<sup>-1</sup>. We held the oven temperature at 150 °C for 3 min, then ramped at 4 °C min<sup>-1</sup> to 240 °C, ramped at 2 °C min<sup>-1</sup> to 260 °C, and finally held at 260 °C for 10 min for a total run time of 45.5 min. The FID temperature was 300 °C with nitrogen as the make-up gas. We identified compounds by comparing retention times with those produced by a Supelco 37 Component FAME mix. We identified an additional four compounds not present in this standard mixture by running representative samples on the same column through an Agilent 6890N gas chromatograph with mass spectrophotometer (GC-MS) and the same column. These compounds were identified either by high-quality (> 97%) matches with known compounds from the Wiley mass spectral library or by comparing the  $m/z$  ratio of the parent ion to other fatty acids. We quantified compound masses by two methods to control for injection-volume variability and ensure calibration linearity. The first was through relating each peak area to the known concentration and peak area of the internal standard, adjusting for carbon number and molar mass. The second was through comparing peak areas to an external standard calibration curve, also adjusting for carbon number and molar mass. We averaged these two calculations together, converted FAME masses into fatty-acid masses, and normalized by the mass of dry sample used.

Although acid-catalyzed transesterification is advantageous for quantifying total fatty-acid content in the biomass because of its ability to capture free fatty acids, we confirmed experimentally that this method is also capable of converting fatty-acid amides to FAMEs. Therefore the values reported herein may include both fatty acids and their derivatives, such as fatty-acid amides and alkanoamides, which still retain the same chain structure and terminating carbonyl group as their fatty-acid counterparts.

#### 4.2.5 Elemental content

Elemental Microanalysis Ltd measured C, H, N, and S content via the Dumas combustion method in duplicate on dry biomass feedstocks and as a single replicate on all other samples, as mass permitted. Elemental Microanalysis Ltd also directly measured biomass feedstocks for O content in duplicate via the Unterzaucher pyrolysis method, and we calculated O content for all other samples by difference. We used the reported measurement uncertainties for biomass C, H, N, S, and O content. For all other samples, given that replicate samples were mixed together, we assumed the uncertainties in elemental contents were equivalent to the standard, reported uncertainties of 0.25, 0.05, and 0.1 wt% for C, H, and N, respectively. We assumed a 1.5 % relative error for S content based on the average relative error for biomass S measurements. We measured total P in the algal biomass using persulfate digestion and the ascorbic acid molybdenum method [7, 96]. We measured P content in the solids and biocrude by combusting the samples at 550 °C for 4 h, dissolving the ash in hot 0.5 normal sulfuric acid for 8 h, and then using the ascorbic acid molybdenum method [109]. We measured absorbance using a Biotek Synergy H1 plate reader. We used a relative error of 3.3 % for solids and biocrude P content based on the average relative error for P measurements. Biomass and biocrude HHV calculations followed the formula developed by Channiwala and Parikh [99].

#### 4.2.6 Biomass biochemical content

We estimated biomass lipid content as the total fatty-acid content of the biomass (see Section 4.2.4) averaged over five replicates, with the acknowledgement that unsaponifiable lipids and minor components derived from the lipid structures, such as phosphate and glycerol, will be neglected. We estimated biomass protein content by multiplying biomass N content by 4.78, a standard multiplication factor averaged over all growth phases for a wide variety of types of microalgae [110]. We measured biomass ash content by combusting the samples at 550 °C for 30 h and calculating the percentage of mass retained, minus biomass

P content, averaged over five replicates. We calculated biomass carbohydrate content by difference from unity and the sum of lipid, protein, and ash content.

#### 4.2.7 Statistical analysis

All statistical analyses on subsets of the data used the function `LocationTest` in Mathematica 11.1, which chooses the most powerful test to apply among the following: t-test, paired t-test, z-test, paired z-test, sign test, signed-rank test, and Mann-Whitney U test. When comparing two sets of data spanning two or more sets of reaction conditions, this tested the null hypothesis that the difference in those two sets had a true population mean or median of zero, and alternative hypothesis that they are nonzero. When comparing data collected at just two different sets of reaction conditions, this tested whether the means or medians of the two sets of replicate data (which could be unequal in length if more than two replicates were run) were equal. All comparisons between subsets of the data are on an absolute deviation basis, not relative, unless otherwise stated.

### 4.3 Results and discussion

Table 4.1 summarizes the microalgal species and their biochemical profiles, shorthand identifiers, and symbols used in figures. Ternary diagrams (Figure 4.1) show these biochemical profiles (dry, ash-free basis) color-coded with red, green, and blue intensity mapped to lipid, protein, and carbohydrate contents, respectively. We use this color scheme for each type of biomass throughout this dissertation to facilitate evaluation of biochemical composition effects. Tables D.3 and D.4 in Appendix D also enumerate the elemental composition and fatty-acid profile for each biomass sample.

#### 4.3.1 Biocrude yield

Herein we describe the effects of temperature, time, slurry concentration, biochemical composition, and species identity in addition to observations about the measured and pre-

ID	Symbol	Genus	Biochemical Composition [wt%]			
			Lipid	Protein	Carb.	Ash
Nan-1	●	<i>Nannochloropsis</i>	11.6 ± 0.1	41.8	43.7	2.8 ± 0.6
Nan-2	●		28.5 ± 0.5	20.1	44.7	6.7 ± 0.9
Chl-1	■	<i>Chlorella</i>	9.4 ± 0.3	43.3	42.5	4.8 ± 0.9
Chl-2	■		19.9 ± 0.1	14.7	61.9	3.4 ± 0.5
Spi-1	◆	<i>Spirulina</i>	5.2 ± 0.1	50.9	31.4	12.5 ± 1.3
Mix-m	▼	Mixture	9.6 ± 0.1	40.0	40.6	9.7 ± 1.1
Mix-p	▲		9.6 ± 0.1	40.0	40.6	9.7 ± 1.1

Table 4.1: Biomass type legend. Mix-m and Mix-p represent the measured and predicted values for the two-species mixture, respectively, and were calculated as an abundance-weighted average of Chl-2 and Spi-1. Uncertainty denotes SE.

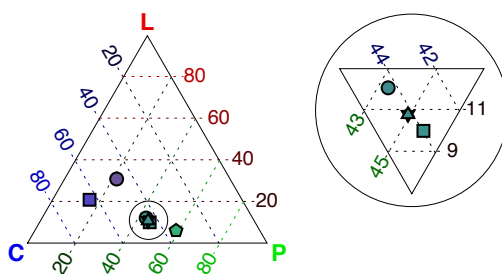


Figure 4.1: Biochemical profile ternary diagrams (dry, ash-free basis) of six different microalgal feedstocks presented in Table 4.1. L (red), P (green), and C (blue) denote color-shaded profile of lipids, proteins, and carbohydrates, respectively.

dicted biocrude yields of the two-species mixture.

#### 4.3.1.1 Temperature and time

Biocrude yield generally increased monotonically with increasing temperature and time, shown in Figure 4.2, consistent with a vast number of previous findings [21–25, 27, 29, 34]. Nonetheless, this trend plateaued or reversed from 10 to 100 min at 350 °C; over this range, the biocrude yield from both concentrations of Chl-2 decreased by on average 3.3 wt% ( $p < 0.06$ ), and that of the 120 g L<sub>rxn</sub><sup>-1</sup> slurry of Nan-1 decreased by 4.1 wt% ( $p < 0.09$ ). Several studies have shown similar decreases in biocrude yield at high severity [25, 34, 111], suggesting that 350 °C and 100 min is around the point at which hydrothermal gasification begins to occur to a significant extent.

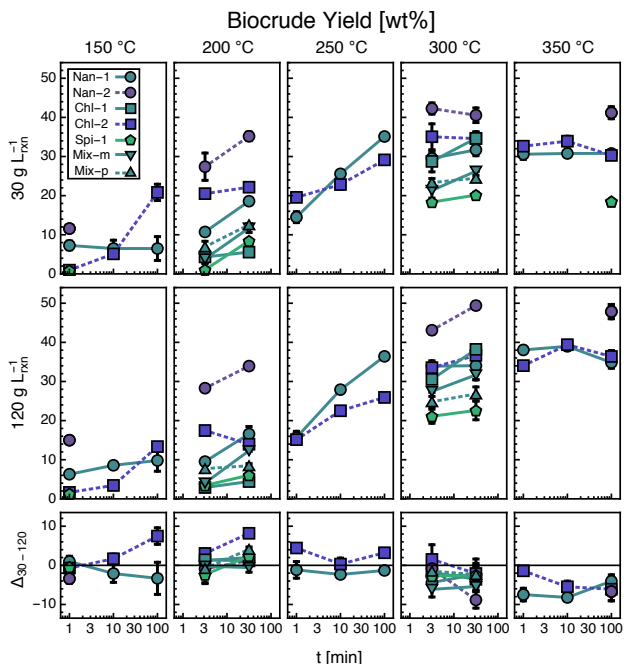


Figure 4.2: Biocrude yield versus reaction time grouped by temperature and initial concentration. See Table 4.1 for microalgae types. The bottom row depicts the first row ( $30 \text{ g L}_{\text{rxn}}^{-1}$ ) minus the second row ( $120 \text{ g L}_{\text{rxn}}^{-1}$ ). Error bars indicate SE.

#### 4.3.1.2 Slurry concentration

At several low-severity conditions (from  $150 \text{ }^\circ\text{C}$ , 100 min to  $250 \text{ }^\circ\text{C}$ , 1 min), the  $30 \text{ g L}_{\text{rxn}}^{-1}$  slurries of Chl-2 yielded on average  $5.8 \text{ wt}\%$  ( $p < 0.02$ ) more biocrude than the  $120 \text{ g L}_{\text{rxn}}^{-1}$  slurries. Moreover, this difference in biocrude yield was not accompanied by a statistically significant difference in mass closure, which varied by only  $2.5 \text{ wt}\%$  ( $p < 0.45$ ) on average. To the authors' knowledge, this effect of increased biocrude yield with decreasing concentration has not been demonstrated previously for microalgae, likely because it occurs at much lower reaction severities than those used by previous concentration studies [21, 23, 24, 38]. One possible explanation is that during product recovery, centrifugation extracted fatty acids from the degraded algal solids more efficiently for the less concentrated slurries. However, biocrude fatty-acid yields in that range were only on average  $1.8 \%$  higher ( $p < 0.06$ ) for  $30 \text{ g L}_{\text{rxn}}^{-1}$  slurries, so the increase in biocrude yield cannot be explained by fatty-acid yield alone. All elemental recoveries were higher, including N and S, suggesting that protein contributed as well, and perhaps carbohydrates. Given that Chl-1 did not

experience the same magnitude of effect, it seems to be a result of biochemical differences rather than cell morphology.

At temperatures of 300 °C and higher, all biomass types generally trend toward significantly increased biocrude yield with increasing initial concentration, a finding which has been documented previously at these reaction conditions [21, 24, 38]. The absolute magnitude of this effect from 30 to 120 g L<sub>rxn</sub><sup>-1</sup> is on average (across all species) about 3.4 wt% ( $p < 0.006$ ) at 300 °C and 5.6 wt% ( $p < 0.0007$ ) at 350 °C, with increases of up to  $8.8 \pm 2.1$  wt% (Nan-2, 300 °C, 31.6 min).

#### 4.3.1.3 Biochemical composition

Increases in biomass lipid content generally were associated with increased biocrude yield (color-coded in Figure 4.2; see Figure E.1 in Appendix E for explicit yield vs. lipid content plots), which has been widely documented [13, 15, 29, 39, 40, 42, 44]. Controlling for reaction conditions and species identity, this was an increase of 11.1 wt% ( $p < 10^{-6}$ ) on average (i.e., comparing the average difference in Nan-1 vs. Nan-2 and Chl-1 vs. Chl-2 across all reaction conditions). However, in several instances, the biocrude yields from the high-protein Nan-1 and Chl-1 matched or exceeded those of the low-protein Chl-2. Although the latter contained more lipids than the other two, it also contained more carbohydrates as well, which individually contributes much less to biocrude formation than the other biochemical fractions [13, 48].

#### 4.3.1.4 Species identity

Despite featuring similar biochemical compositions, Mix-m, Nan-1, and Chl-1 yielded significantly different amounts of biocrude after controlling for reaction conditions (Figure 4.2). Even at high severity (300 °C and 31.6 min), where biocrude yield tends to plateau, the variability in yields from these biomass samples was on average  $\pm 3.7$  wt% across both concentrations. López Barreiro et al. [39] found that biochemical composition alone was

insufficient for correlating the biocrude yield from HTL of eight different types of microalgae at two sets of reaction conditions similar to those employed in this study. They proposed that species identity played a nontrivial role in affecting biocrude yield predictability. The information presented here supports the claim that species identity induces variability, however we demonstrate that biochemical composition could predict biocrude yield to within  $\pm 3.7$  wt% at high severity. It is expected that morphological differences between species would play less of a role at high reaction severity, so the source of the variation would most likely be explained by more granular differences in biochemical composition, such as polar, non-polar, and unsaponifiable lipids for example. In Chapter III we quantified the relative effects of species identity and biochemical composition on biocrude yield to be at most 1.9 and 12.6 wt%, respectively, for the HTL of 30 g  $L_{\text{rxn}}^{-1}$  slurries of six different species of microalgae at 350 °C, 20 min. At 300 °C and 31.6 min in the present study, variability in biocrude due to species identity ( $\pm 3.7$  wt%) is about twice as large that the value presented in Chapter III, while the variability due to biochemical composition in the present study is on average  $\pm 11.8$  wt%, similar to our previous results.

#### 4.3.1.5 Two-species mixture interactions

The measured (Mix-m) and predicted (Mix-p) biocrude yields for the 30 g  $L_{\text{rxn}}^{-1}$  two-species mixture agreed across all four reaction conditions (Figure 4.2). However, the measured biocrude yields for the 120 g  $L_{\text{rxn}}^{-1}$  slurry were on average 3.8 wt% higher than predicted ( $p < 0.03$ ) for all but the 200 °C and 3.2 min condition. This was especially the case at 300 °C and 31.6 min, with a measured biocrude yield of  $31.7 \pm 1.2$  wt% compared to a predicted value of  $26.8 \pm 1.8$  wt%. These data suggest that reactions between the biochemical components of the two different species form additional and/or higher-molecular-weight biocrude components in the bulk high-temperature water; moreover, these reactions are likely occurring between the relatively higher concentration of lipids and/or carbohydrates in Chl-2 and the relatively higher concentration of protein in Spi-1. Higher-than-predicted biocrude

yield from mixtures of feedstocks (including various biomass types and model compounds) with differing biochemical composition has been reported previously [43, 48, 112] and will be discussed further in Section 4.3.4.

## 4.3.2 Carbon content and recovery

### 4.3.2.1 Temperature, time, slurry concentration, and biochemical composition

C content in the biocrude ranged from 62.4 to 76.8 wt%, shown in Figure 4.3a. It monotonically increased with increasing reaction severities at temperatures of 250 °C and higher, consistent with findings from previous studies at comparable reaction conditions [22–24, 27, 39]. Slurry concentration affected biocrude C content only on reaction-condition- and feedstock-specific bases. C content generally increased with increasing lipid content (and decreasing protein content), consistent with previous work [15, 40]. Controlling for species identity, the C content in the biocrude from higher-lipid microalgae was on average 3.8 wt% higher ( $p < 0.0005$ ) than that of the lower-lipid microalgae in the 200 to 300 °C range, for all holding times and slurry concentrations. Notably, at 350 °C and 100 min, the C content of Nan-1, Nan-2, and Chl-1 varied by only 1.3 wt%, despite differing initial concentrations and biochemical compositions (in the case of Nan-2); this result is in line with some previous results [39]. In contrast, Biller and Ross [13] found that biocrude C content decreased from 73.3 to 68.1 wt % with increasing lipid content for 64 g L<sub>rxn</sub><sup>-1</sup> slurries of four different species of microalgae (including *Nannochloropsis*, *Chlorella*, and *Spirulina*) at 350 °C and approximately 90 min total holding time. The *Nannochloropsis* and *Chlorella* in that study contained significantly less carbohydrate content than the four types used in this study, which could explain the differences, although we note that they measured carbohydrates directly while in the present study we estimated them by difference. However, the biochemical compositions for *Spirulina* in both studies were very similar and so were the C contents in the biocrude at those reaction conditions (73.3 vs. 73.2 wt%). These results together suggest that biochemical composition affects C content at all reaction conditions and that

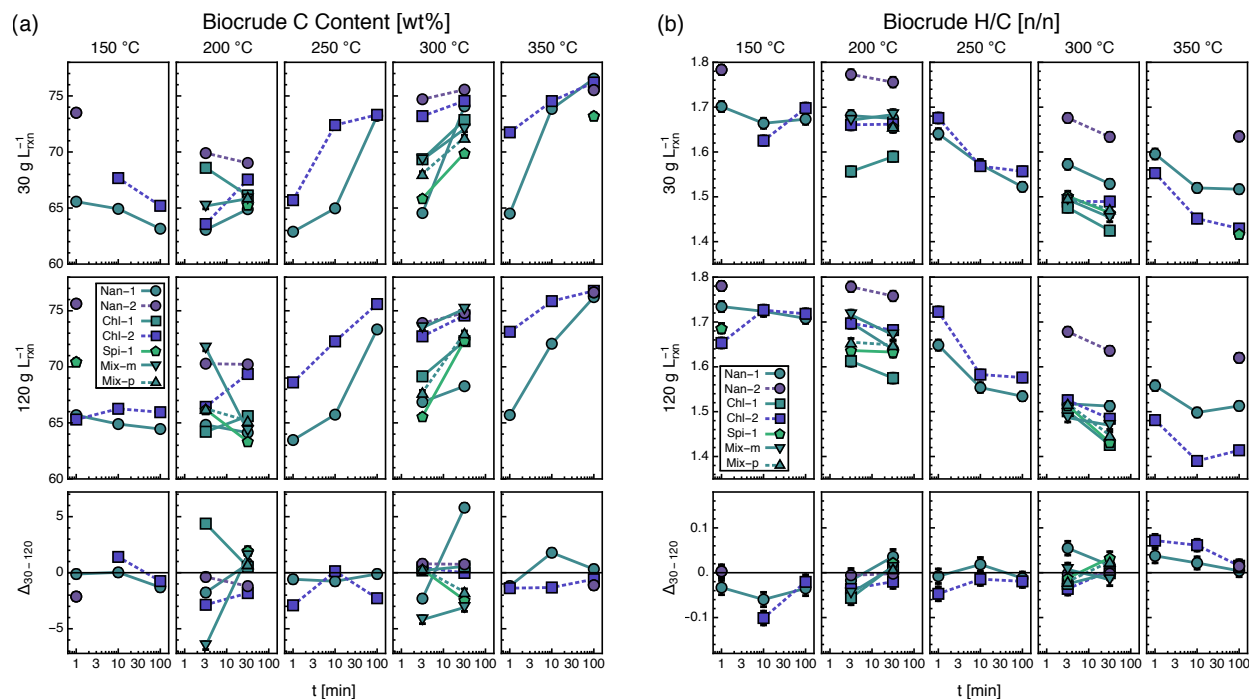


Figure 4.3: Biocrude (a) carbon content and (b) H/C ratio versus reaction time grouped by temperature and initial concentration. See Table 4.1 for microalgae types. The bottom row depicts the first row ( $30 \text{ g L}_{\text{rxn}}^{-1}$ ) minus the second row ( $120 \text{ g L}_{\text{rxn}}^{-1}$ ). Error bars indicate SE.

the magnitude of this effect changes at different reaction conditions depending on the relative proportions of each biochemical class.

#### 4.3.2.2 Species identity and two-species mixture interactions

Biocrude C content varied significantly between Nan-1, Chl-1, and Mix-m—the three biomass types with similar biochemical composition—for low-severity ( $200 \text{ }^{\circ}\text{C}$ , 3.2 min) and high-severity ( $300 \text{ }^{\circ}\text{C}$ ) conditions. At  $300 \text{ }^{\circ}\text{C}$  across both reaction times and concentrations, the two-species mixture produced biocrude with C content that was on average 2.5 wt% higher ( $p < 0.12$ ) than expected. This was especially true for the  $120 \text{ g L}_{\text{rxn}}^{-1}$  slurry, which produced biocrude with C content that was on average 3.6 wt% higher ( $p < 0.10$ ) than that of the  $30 \text{ g L}_{\text{rxn}}^{-1}$  slurry. Remarkably, the  $120 \text{ g L}_{\text{rxn}}^{-1}$  slurry featured biocrude C recovery, shown in Figure E.2, which was 8.1 % higher ( $p < 0.08$ ) than predicted and 11.0 % higher ( $p < 0.04$ ) than that of the  $30 \text{ g L}_{\text{rxn}}^{-1}$  slurry. These observations together suggest that reactions between the different biochemical components (and their degradation products) of

the lipid- and carbohydrate-rich *Chlorella* and protein-rich *Spirulina* are actually improving carbon partitioning into the biocrude oil by forming more and/or higher-molecular-weight, carbon-containing, organic-phase-soluble compounds than predicted by reacting the equivalent proportion of both species individually. Madsen et al. [43] also observed increased biocrude C content for several 64 g L<sub>rxn</sub><sup>-1</sup> biomass mixtures at 350 °C, 20 min, including a mixture of high-protein *Spirulina* and high-carbohydrate poplar wood with roughly the same overall biochemical composition as the mixture employed in this study.

### 4.3.3 Hydrogen content and recovery

H content in the biocrude, shown in Figure E.3a, did not follow any global trends with respect to changing temperature, time, and concentration. However, biocrude H recovery did generally increase with increasing temperature and time, shown in Figure E.3b, following the same general trends reported for biocrude yield in Section 4.3.1. Controlling for species identity and reaction conditions, increased biomass lipid content (and decreased protein content) resulted in an average of 1.1 wt% higher ( $p < 0.0002$ ) H content across all reaction conditions, a trend similar to ones reported previously [15, 40]. Similar to C content, the 120 g L<sub>rxn</sub><sup>-1</sup> two-species mixture produced biocrude with 0.5 wt % higher H content ( $p < 0.1$ ) than expected at 300 °C.

Biocrude H/C (molar ratio of H to C), depicted in Figure 4.3b, generally decreased with increasing temperature and time, similar to previous reports [22]. Given that C and H recovery (Figure E.2 and E.3a) both increase with increasing reaction severity, the decrease in H/C suggests that the ratio of the net rates of partitioning of H and C into the biocrude also decreases with increasing reaction severity. This could be due to an increase in H leaving the biocrude and/or a decrease in H entering the biocrude, relative to the rate of C flux. There were no global effects of initial concentration on biocrude H/C, although it did increase on average by 0.09 ( $p < 10^{-9}$ ) with increasing biomass lipid content, after controlling for species identity and reaction conditions, which corroborates prior findings [15, 40].

### 4.3.4 Nitrogen content

#### 4.3.4.1 Temperature and time

Across the entire data set, biocrude N content varied from 0.3 to 8.4 wt%, shown in Figure 4.4a. It generally increased with increasing temperature and time, which is consistent with previous reports [21–24, 38]. Although at 300 °C and higher, there was no overall trend with respect to temperature and time, but there were trends within different biochemical profiles (see Section 4.3.4.3). Regardless of biomass type, at 200 °C and higher, the 120 g  $L_{\text{rxn}}^{-1}$  slurries produced biocrude with on average 0.47 wt% higher ( $p < 10^{-9}$ ) N content than their 30 g  $L_{\text{rxn}}^{-1}$  counterparts. From 200 °C, 3.2 min to 300 °C, 3.2 min, this effect was only significant for the higher-protein biomass types and not the higher-lipid biomass samples, on average 0.64 ( $p < 0.00003$ ) and 0.07 wt% ( $p < 0.17$ ) higher, respectively. However, at 300 °C, 31.6 min and higher, the average effects were the same regardless of biochemical composition, at 0.56 ( $p < 0.004$ ) and 0.55 wt% ( $p < 0.001$ ) for higher-protein and higher-lipid biomass, respectively. It is not immediately clear why increased concentration promotes N partitioning into the biocrude, however one possibility is that it promotes the formation of DCM-soluble N-containing compounds via Maillard reactions, or reactions between carbohydrate and protein degradation products. Maillard reactions have been demonstrated to occur in high-temperature water [46, 52] and increase biocrude nitrogen content [43, 112, 113]. These reactions could be first order in both amino acids and saccharides (second order overall), so concentration increases would increase their selectivity during HTL.

#### 4.3.4.2 Slurry concentration

To the authors' knowledge there is only one previous study that presented elemental content of biocrude oils as a function of slurry concentration [38]. It showed that at 300 °C and 3 min, biocrude N content increased from 7.2 to 7.8 wt% with an increase in slurry concentration from 37 to 79 g  $L_{\text{rxn}}^{-1}$  for a high-protein *Chlorella*, which is in line with the

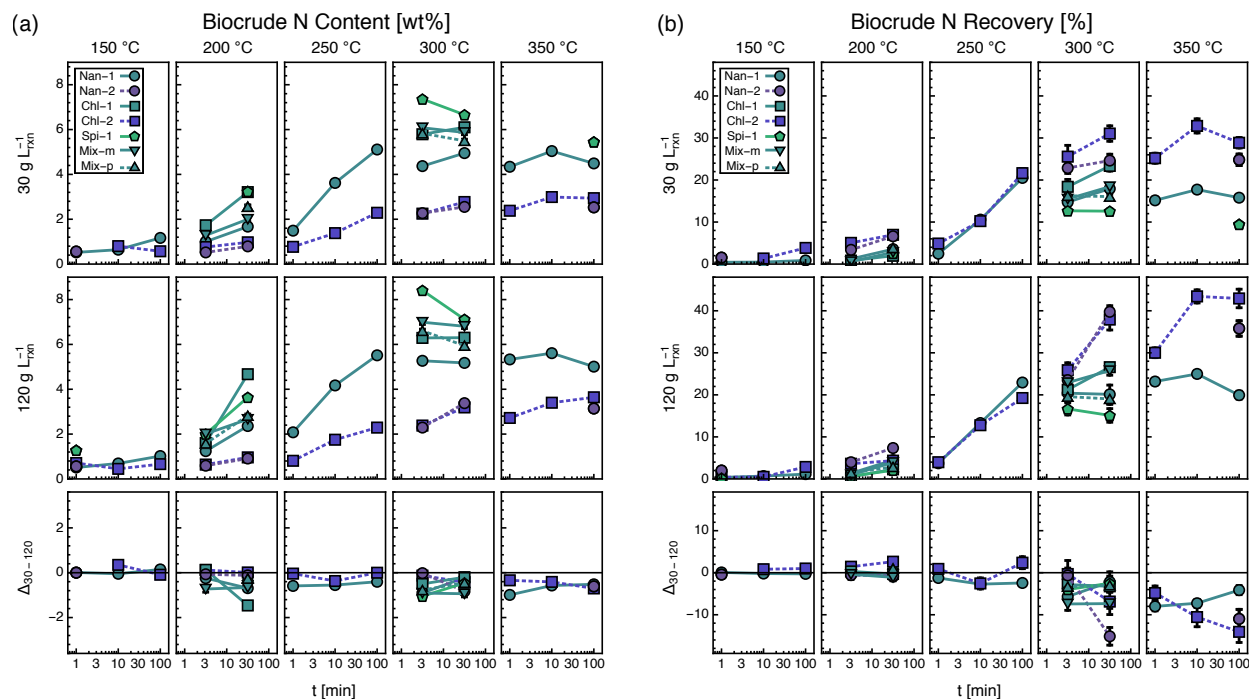


Figure 4.4: Biocrude nitrogen (a) content and (b) recovery versus reaction time grouped by temperature and initial concentration. See Table 4.1 for microalgae types. The bottom row depicts the first row ( $30 \text{ g L}_{\text{rxn}}^{-1}$ ) minus the second row ( $120 \text{ g L}_{\text{rxn}}^{-1}$ ). Error bars indicate SE.

average increase observed in our study. However, at  $350 \text{ }^\circ\text{C}$  they reported a slight decrease in biocrude N of 7.9 to 7.7 wt% with concentration increasing from 30 to  $64 \text{ g L}_{\text{rxn}}^{-1}$ , which we did not observe. We note however that at that temperature, our concentration change was approximately double that of theirs (30 to 120 vs. 30 to  $64 \text{ g L}_{\text{rxn}}^{-1}$ ), so it is possible that a fourfold increase in concentration, as was the case in our study, is necessary to observe a significant concentration effect at  $350 \text{ }^\circ\text{C}$ .

#### 4.3.4.3 Biochemical composition

Biomass biochemical composition significantly affected biocrude N content (color-coded in Figure 4.4a; see Figure E.4a in Appendix E for explicit N content vs. protein content plots), which for example ranged from 2.3 to 8.4 wt% for  $120 \text{ g L}_{\text{rxn}}^{-1}$  slurries at  $300 \text{ }^\circ\text{C}$  and 3.2 min. Controlling for species identity and reaction conditions, biocrude N content was on average 2.2 wt% higher ( $p < 10^{-5}$ ) for higher-protein biomass types compared to lower-protein biomass samples at  $200 \text{ }^\circ\text{C}$  and higher. Leow et al. [40] and Li et al. [15] showed that, when

controlling for species identity, biocrude N content increased linearly with increasing biomass protein content for 178 g L<sub>rxn</sub><sup>-1</sup> slurries at 300 °C, 30 min, which is consistent with the results presented here (Figure E.4a). The levels of reaction severity at which biocrude N content plateaued and then decreased appears to have increased with decreasing protein content. For example, biocrude N content for the highest-protein-content type, Spi-1, decreases with increasing time at 300 °C; however, N content in biocrude from biomasses that are lower, but still high in protein content, including Nan-1, Chl-1, and Mix-m, generally plateau at 300 °C, and that of the lowest in protein content, including Nan-2 and Chl-2, actually increases with increasing time at 300 °C. Therefore the reaction conditions for maximum N content in the biocrude appear to be a function of biochemical composition as well.

#### 4.3.4.4 Species identity

Biocrude N content varied by as much as 2.3 wt% and as little as 0.7 wt% between the three biomass types with similar biochemical composition after controlling for reaction conditions. The measured two-species mixture biocrude N content was on average 0.47 wt% higher ( $p < 0.10$ ) than predicted for all times and concentrations at 300 °C. The mixture contains both a high-protein *Spirulina* (Spi-1) and a high-carbohydrate *Chlorella* (Chl-2), which suggests that Maillard reactions are likely to account for the difference between measured and predicted values. The presence of both protein- and carbohydrate-degradation products together has been shown to shift selectivities toward nitrogen-containing ring structures over cyclic oxygenates [43] to the point where a 1:1 mixture of protein and carbohydrate model compounds, the latter of which contains no N, produces biocrude with nearly the same N content as that of pure protein. These cross reactions can also form N- and O-containing structures that are unique from those present in biocrude from pure feedstocks [112].

### 4.3.5 Nitrogen recovery

N recovery in the biocrude, shown in Figure 4.4b, followed trends with respect to temperature, time, and concentration that are similar to those of N content, consistent with previous reports [63, 114]. We observed a maximum biocrude N recovery of 43.4 % for the 120 g L<sub>rxn</sub><sup>-1</sup> slurry of Chl-2 at 350 °C and 10 min. At 250 °C and higher, biocrude N recovery was on average 4.6 % higher (absolute,  $p < 10^{-5}$ ) for the 120 g L<sub>rxn</sub><sup>-1</sup> slurries than the 30 g L<sub>rxn</sub><sup>-1</sup> slurries; the largest absolute increase in biocrude N recovery due to increasing concentration was 15.1 %, in the case of Nan-2 at 300 °C and 31.6 min. The more highly concentrated (120 g L<sub>rxn</sub><sup>-1</sup>) slurries of Mix-m at 300 °C also recovered 5.0 % ( $p < 0.21$ ) more N in the biocrude than predicted; whereas this effect was absent or significantly reduced for the 30 g L<sub>rxn</sub><sup>-1</sup> slurries. Given that Maillard reactions between sugars and amino acids likely proceed by an overall second order reaction mechanism, we propose that the four-fold increase in concentration likely promoted these reactions and the higher biocrude N recovery observed for the 120 g L<sub>rxn</sub><sup>-1</sup>.

Notably, the trends in N recovery in the biocrude due to changing biochemical composition are the opposite of those of N content (color-coded in Figure 4.4b; see Figure E.4b in Appendix E for explicit N recovery vs. protein content plots). In fact, after controlling for species identity, biocrude N recovery increased by 5.8 % (absolute,  $p < 0.0005$ ) on average with decreasing protein content (and increasing lipid content) at 200 °C and higher. This is to say that although the mass percentage of N in biocrude is lower for lower-protein species, that N constitutes a higher percentage of the total N in the starting biomass than does the N from higher-protein species, an effect previously observed at 300 °C [40, 115]. This is significant because higher N recovery in the biocrude directly translates to lower N recovery in the ACP for recycling. Amide derivatives have also been reported to increase with increasing lipid content and were in the range of 1.4 to 3.0 wt% of the biocrude [115, 116], which likely explains at least part of the increase in biocrude N recovery.

Another explanation is that the protein concentrations in slurries of Nan-1, Chl-1, Spi-1,

and Mix-m are high enough to be in excess compared to carbohydrate concentrations for Maillard reactions, or, in other words, that carbohydrates could be the limiting reactant. In fact, Peterson et al. [46] found exactly that when examining hydrothermal degradation of glycine (an amino acid) and glucose (a sugar) alone and together; when glycine was in excess, increases in initial glucose concentration led to proportionally greater glycine destruction. Such behavior in the present study would lead to a less-than-expected increase in the rate of N-cyclic formation from Maillard reactions due to increased protein content, allowing a greater proportion of the N in the protein to degrade to ammonium compared to the more protein-deficient and/or carbohydrate-rich biomass samples (Nan-2 and Chl-2). In fact, we observe such differences in ammonium liberation later in Chapter V. A third possibility is that the proportion of biomass N representing protein changes with increasing N-limitation (decreasing proteins and increasing lipids), which would obfuscate whether the changes in biocrude N recovery are due to protein or other, generally less abundant sources of N such as DNA and RNA. Regardless of the biochemical source, biocrude N recovery increases with decreasing biomass N content.

### **4.3.6 Sulfur content**

#### **4.3.6.1 Temperature, time, and slurry concentration**

S content in the biocrude, depicted in Figure 4.5a, increases with increasing temperature and time until 300 °C and 3.2 min, at which point it plateaus (in the case of the higher-lipid species) or decreases, similar to the trends for N content and consistent with previous reports [21, 24, 27, 38]. There was no apparent global effect of initial concentration; however at 300 °C, 120 g L<sub>rxn</sub><sup>-1</sup> slurries of Spi-1, Chl-1, and Chl-2 on average produced biocrude with 0.10 wt% ( $p < 0.03$ ) lower S content than the 30 g L<sub>rxn</sub><sup>-1</sup> slurries, while those of Nan-1 and Nan-2 showed no effect or in some cases a slight increase for the 120 g L<sub>rxn</sub><sup>-1</sup> slurries.

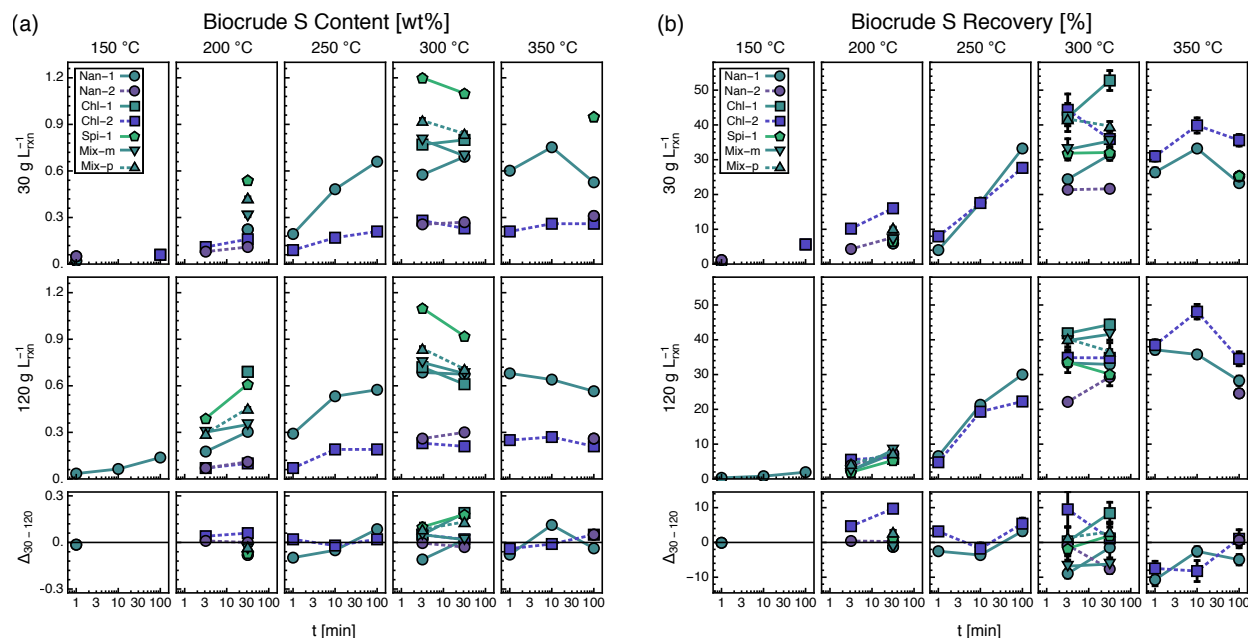


Figure 4.5: Biocrude sulfur (a) content and (b) recovery versus reaction time grouped by temperature and initial concentration. See Table 4.1 for microalgae types. The bottom row depicts the first row ( $30 \text{ g L}_{\text{rxn}}^{-1}$ ) minus the second row ( $120 \text{ g L}_{\text{rxn}}^{-1}$ ). Error bars indicate SE.

#### 4.3.6.2 Biochemical composition and species identity

Similar to N content, S content is a strong function of biochemical composition, with high-protein biomass producing biocrude with higher S content (color-coded in Figure 4.5a; see Figure E.5a in Appendix E for S content vs. protein content plots). Controlling for species identity, biocrude S content was on average 0.37 wt% ( $p < 10^{-5}$ ) higher for higher-protein biomass than their lower-protein counterparts, an effect demonstrated previously [43]. The three feedstocks with similar biochemical composition, Nan-1, Chl-1, and Mix-m, produced biocrude with significantly varied S content at low-to-moderate reaction severities, although at 300 °C, 31.6 min, these differences reduced to no more than 0.11 and 0.07 wt% for the 30 and 120  $\text{g L}_{\text{rxn}}^{-1}$  slurries, respectively. This suggests that biochemical composition is a good predictor of biocrude S content at high reaction severity and that species identity is a significant factor at low severity only, which could be due to morphological differences between biomass types affecting the rate of S partitioning to the biocrude.

### 4.3.6.3 Two-species mixture interactions

At 200 °C, 31.6 min and higher reaction severities, measured S content was always lower than predicted in the two-species mixture by 0.10 wt% ( $p < 0.002$ ) on average across those six different sets of conditions. It is not immediately clear why this would occur, but this effect was also previously observed by Madsen et al. [43] in various mixtures of biomass feedstocks, some of which similarly featured a high-protein feedstock paired with a high-carbohydrate feedstock. The trend points to reactions occurring in the bulk high-temperature water between compounds originating from both the high-protein *Spirulina* and high-lipid, high-carbohydrate *Chlorella* that inhibit some of the S from partitioning into the biocrude.

### 4.3.7 Sulfur recovery

S recovery in the biocrude usually increased with increasing temperature and time, shown in Figure 4.5b, similar to S content. However, on average S recovery did decrease by 8.8 % ( $p < 0.03$ ) from 10 to 100 min at 350 °C for both initial concentrations of Nan-1 and Chl-2. There were no consistent global trends as a function of initial concentration, although certain types of biomass in particular showed consistent differences; for example, biocrude S recovery for the 30 g  $L_{\text{rxn}}^{-1}$  slurry of Chl-2 was on average 8.0 % ( $p < 0.05$ ) higher than the 120 g  $L_{\text{rxn}}^{-1}$  slurry for 300 °C, 3.2 min and milder reaction severities. In contrast to N recovery, there were also no globally consistent trends with respect to biochemical composition (Figure E.5b); however, when controlling for species identity, we did observe an average increase in biocrude S recovery of 10 % ( $p < 0.04$ ) as a function of increasing protein content across both initial concentrations at 300 °C and 31.6 min. The variability in biocrude S recovery due to species identity was at least 8.5 % and at most 21.3 % at 300 °C. This wide range in S recoveries suggests that more information, such as the abundance of specifically S-containing amino acids, is required to adequately predict S partitioning into the biocrude. The predicted S recoveries for the two-species mixture matched the measured values for the 120 g  $L_{\text{rxn}}^{-1}$  across all conditions, but were predicted on average 5.5 % ( $p < 0.09$ ) higher than

measured for the 30 g L<sub>rxn</sub><sup>-1</sup> slurry.

### 4.3.8 Oxygen content and recovery

#### 4.3.8.1 Temperature and time

Biocrude O content ranged from 8.1 to 29.2 wt%, shown in Figure 4.6a. Starting at 200 °C, increasing reaction severity decreased biocrude O content, consistent with prior studies [21, 22, 24, 27, 38]. From 200 °C, 3.2 min to 300 °C, 31.6 min, for example, this reduction was on average about 10.6 wt% ( $p < 10^{-6}$ ), a relative decrease of about 47 %. We note however that over this same range of conditions, the recovery of O in the biocrude, depicted in Figure 4.6b, increases on average by 5.7 % ( $p < 0.02$ ), indicating that there is actually a net influx of O into the biocrude over these conditions, but that the higher influx of other elements, primarily C and H, is diluting the overall O content. At higher reaction severities however, the average decrease in O content of 6.1 wt% ( $p < 0.009$ ) is accompanied by a significant average reduction in O recovery of 7.3 % ( $p < 0.03$ ), suggesting that deoxygenation is occurring.

#### 4.3.8.2 Slurry concentration

We did not observe a global effect of slurry concentration on O content, however there was a small, yet statistically significant average decrease in O recovery of 1.9 % ( $p < 0.01$ ) with increasing slurry concentration at 200 °C for both reaction times. There is little information in the literature about the effect of concentration on biocrude O content, however Jazrawi et al. [38] found that increasing concentration (7 to 79 g L<sub>rxn</sub><sup>-1</sup>) of a high-protein *Chlorella* slurry decreased biocrude O content at 300 and 350 °C for 3 min reaction time. In the present study, at 300 °C and 3.2 min, all four high-protein biomass types produced biocrude with on average 2.5 wt% ( $p < 0.13$ ) lower O content with increasing initial concentration, which is comparable in magnitude to the study by Jazrawi et al. [38]. Jena et al. [21] also showed a slight decrease in biocrude O content from 64 to 144 g L<sub>rxn</sub><sup>-1</sup> at 350 °C and

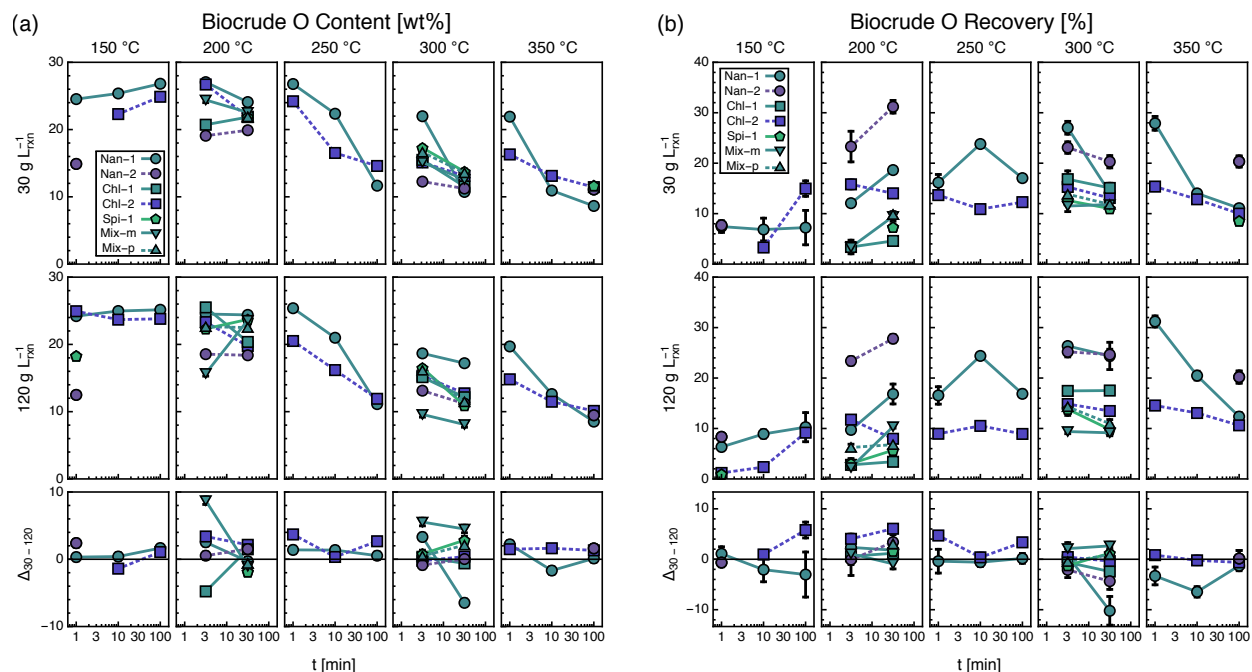


Figure 4.6: Biocrude oxygen (a) content and (b) recovery versus reaction time grouped by temperature and initial concentration. See Table 4.1 for microalgae types. The bottom row depicts the first row ( $30 \text{ g L}_{\text{rxn}}^{-1}$ ) minus the second row ( $120 \text{ g L}_{\text{rxn}}^{-1}$ ). Error bars indicate SE.

60 min holding time.

#### 4.3.8.3 Biochemical composition and species identity

There similarly was no consistent overall trend in O content with respect to changing biochemical composition, although for specifically the two *Nannochloropsis* feedstocks, O content was on average 6.6 wt% higher ( $p < 0.0002$ ) in the higher-protein strain (Nan-1) than the lower-protein strain (Nan-2) for reaction severities of 300 °C, 31.6 min and lower. Li et al. [15] showed a relatively weak trend of increasing biocrude O content with increasing biomass carbohydrate content, however we did not observe this trend (Figure E.6a). Nan-1, Chl-1, and Mix-m produced biocrude with widely varying O content and recovery despite their similar biochemical profiles. After controlling for reaction conditions, the differences in O content and recovery ranged from 1.9 to 9.8 wt% and 3.3 to 17.0 %, respectively. These differences highlight the limit of proximate biochemical composition as a predictor for O partitioning in the biocrude.

#### 4.3.8.4 Two-species mixture interactions

At 300 °C across both reaction times, the measured two-species mixture biocrude O contents and recoveries were on average 5.0 wt% higher ( $p < 0.07$ ) and 2.4 % higher ( $p < 0.08$ ), respectively, for the 30 g L<sub>rxn</sub><sup>-1</sup> slurry compared to the 120 g L<sub>rxn</sub><sup>-1</sup> slurry. Moreover, biocrude O contents for the 120 g L<sub>rxn</sub><sup>-1</sup> slurry were actually lower than those of the component species with the lowest O content (i.e., Chl-2 at 3.2 min and Spi-1 at 31.6 min) by on average at least 4.3 wt%, and the same was true for O recovery, which was 2.6 % lower (absolute). These observations for a single initial concentration across two time points were not enough to demonstrate statistical significance, however at these conditions across both concentrations, the measured two-species mixture O contents and recoveries were lower than predicted by an average of 3.1 wt% ( $p < 0.10$ ) and 2.3 wt% ( $p < 0.11$ ), respectively. In other words, we measured lower O content in the biocrude from the two-species mixture than expected at 300 °C (possibly even lower than any component species), and this effect is magnified by increasing initial concentration. This finding corroborates the results of Madsen et al. [43], which found that mixtures of high-protein and high-carbohydrate feedstocks led to decreased O content and increased N content in the biocrude oil. Increased N content was also observed in this study, discussed in Section 4.3.4. The reaction mechanism identified in that study, whereby nitrogen degradation products shift reaction selectivities toward nitrogen-containing ring structures away from cyclic oxygenates, is therefore very likely to be occurring in the present study as well.

#### 4.3.9 Phosphorus content and recovery

At a temperature of 300 °C and lower, biocrude P content and recovery, (Figure E.7), stayed below 0.10 wt% and 2.3 %, respectively, for all samples measured; however, we note that these measurements were over a smaller subset of conditions than the other elemental analyses due to sample mass constraints. At 350 °C, some of the higher-lipid biomass samples produced biocrude with higher P content and recovery, although the highest observed were

only 0.20 wt% and 8.3 %, respectively, in the case of Nan-2 at 100 min, 30 g L<sub>rxn</sub><sup>-1</sup>. These values were lower than reported by Valdez et al. [24] for similar experimental conditions but comparable to that of Jiang and Savage [37]. These data confirm that the majority of the phosphorus does not partition into the biocrude, especially at 300 °C and below; however, at 350 °C, a non-trivial amount of P (relative to the biomass P) may partition into the biocrude.

#### 4.3.10 Higher-heating value

Biocrude HHV varied from 29.3 to 38.4 MJ kg<sup>-1</sup> across all reaction conditions and feedstock characteristics, shown in Figure 4.7a. HHV increased monotonically with increasing reaction severity at 250 °C and higher for all biomass types, consistent with previous studies [21, 22, 24, 27]. There were no significant global trends in HHV with respect to initial concentration. Controlling for species identity and reaction conditions, biocrude HHV was on average 3.0 MJ kg<sup>-1</sup> higher ( $p < 0.00003$ ) for the higher-lipid strains compared to the lower-lipid strains, across all reaction conditions (color-coded in Figure 4.7a; see Figure E.8a in Appendix E for explicit HHV vs. lipid content plots). Even without controlling for species identity, biocrude HHV generally increased with increasing biomass lipid content, although at high reaction severities, the low-lipid Nan-1 matched or exceeded the HHV of the high-lipid Chl-2. Li et al. [15] similarly found that biocrude HHV increased with increasing lipid content, but there was no clear association with protein content.

Biocrude HHV varied widely among Nan-1, Chl-1, and Mix-m, although the average spread in values, across all reaction conditions, for the 30 g L<sub>rxn</sub><sup>-1</sup> slurries ( $\pm 1.0$  MJ kg<sup>-1</sup>) was lower than that of the 120 g L<sub>rxn</sub><sup>-1</sup> slurries ( $\pm 1.8$  MJ kg<sup>-1</sup>). At 300 °C across both reaction times, biocrude HHV for the two-species mixture was substantially higher for the 120 g L<sub>rxn</sub><sup>-1</sup> slurry than the 30 g L<sub>rxn</sub><sup>-1</sup> slurry, on average by about 2.3 MJ kg<sup>-1</sup> ( $p < 0.07$ ). Moreover, the HHV for the 120 g L<sub>rxn</sub><sup>-1</sup> slurry of the two-species mixture was 0.6 MJ kg<sup>-1</sup> higher ( $p < 0.02$ ) than that of Chl-2, the highest of the two component species, which follows a similar observation for O content in Section 4.3.8. These deviations from the expected values for

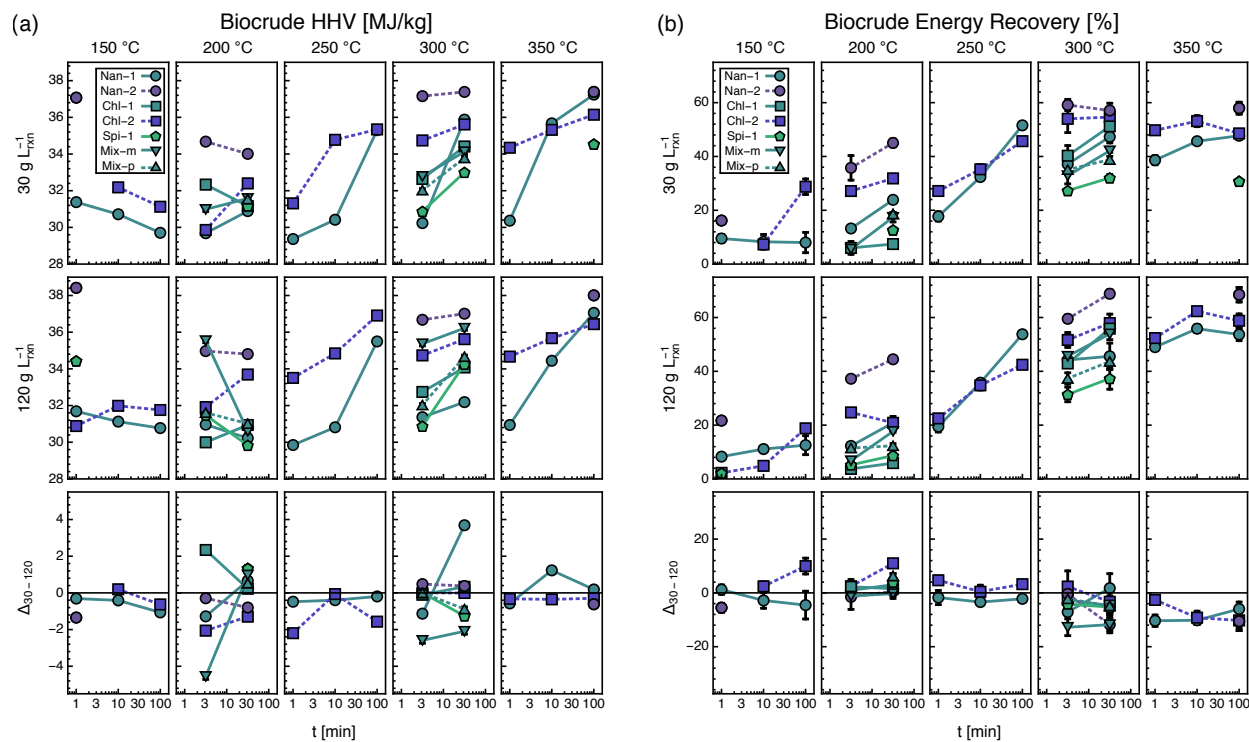


Figure 4.7: Biocrude (a) HHV and (b) ER versus reaction time grouped by temperature and initial concentration. See Table 4.1 for microalgae types. The bottom row depicts the first row ( $30 \text{ g L}_{\text{rxn}}^{-1}$ ) minus the second row ( $120 \text{ g L}_{\text{rxn}}^{-1}$ ). Error bars indicate SE.

HHV were largely due to significant increases in C content and decreases in O content.

#### 4.3.11 Energy recovery

Biocrude ER, or the percentage of energy in the biocrude (biocrude HHV multiplied by yield) relative to the biomass HHV, followed the same general trends as biocrude yield (Figures 4.7b and E.8b). Notably, the higher-lipid  $30 \text{ g L}_{\text{rxn}}^{-1}$  slurries reached a maximum ER at just  $300 \text{ }^{\circ}\text{C}$  and 3.2 min, while the higher-protein slurries continued to increase in ER with increasing reaction severity. The  $120 \text{ g L}_{\text{rxn}}^{-1}$  slurries, however, exhibited largely the same trends with changing reaction severity, regardless of biochemical composition. For each biomass type at  $300 \text{ }^{\circ}\text{C}$  and higher, the maximum ER achievable was always higher for the  $120 \text{ g L}_{\text{rxn}}^{-1}$  slurries than their  $30 \text{ g L}_{\text{rxn}}^{-1}$  counterparts due to increased C recovery (Figure E.2) and H recovery (Figure E.3a).

### 4.3.12 Mass balances, solid characteristics, and gas yield

The total mass balances, including the biocrude, solid, and aqueous fractions, are reported both without and with gas yields in Figures D.2a and b, respectively, in Appendix D. Mass closure was generally very good at 150 and 200 °C, but decreases with increasing reaction severity. We expect that a large portion of the lost mass is comprised of volatile compounds in the ACP. At high reaction severity (300 to 350 °C), some of the lost mass may be due to coke formation on the reactor walls as well. Data for solid yields and elemental content and recoveries are presented in Appendix F. Data for gas yields are presented in Appendix G. These data were not the primary focus of this dissertation but we report them in the Appendices because they are important for quantifying the distribution of elements between the different phases produced during HTL. Moreover, those data are integral for the development of the kinetic model presented in Chapter VI.

### 4.3.13 Fatty-acid recovery

Figure 4.8 depicts SAFA, MUFA, and PUFA recoveries in the solid (green, bottom) and biocrude (brown, top) phases as functions of reaction temperature and time for the 120 g  $L_{\text{rxn}}^{-1}$  slurries of Nan-1 and Chl-2. As described in Section 4.2.4, these recoveries comprise fatty acids and their derivatives, such as fatty-acid amides, that retain the same chain structure and terminating carbonyl group. Plots for the 120 g  $L_{\text{rxn}}^{-1}$  slurries of other biomass types as well as data for the 30 g  $L_{\text{rxn}}^{-1}$  slurries are shown in Figures E.9 and F.8. Fatty-acid recoveries in the biocrude and solids are shown in Figures E.9 and F.8, respectively.

#### 4.3.13.1 Saturated fatty acids

SAFAs begin partitioning into the biocrude at conditions as mild as 150 °C and 10 min, and possibly even lower than that (there was insufficient biocrude generated by the 150 °C, 1 min reactions for analysis). In the case of the 120 g  $L_{\text{rxn}}^{-1}$  slurry of Nan-1, SAFA recovery reaches a maximum of 93.8 wt% at 250 °C and 10 min (with similar recovery at comparable

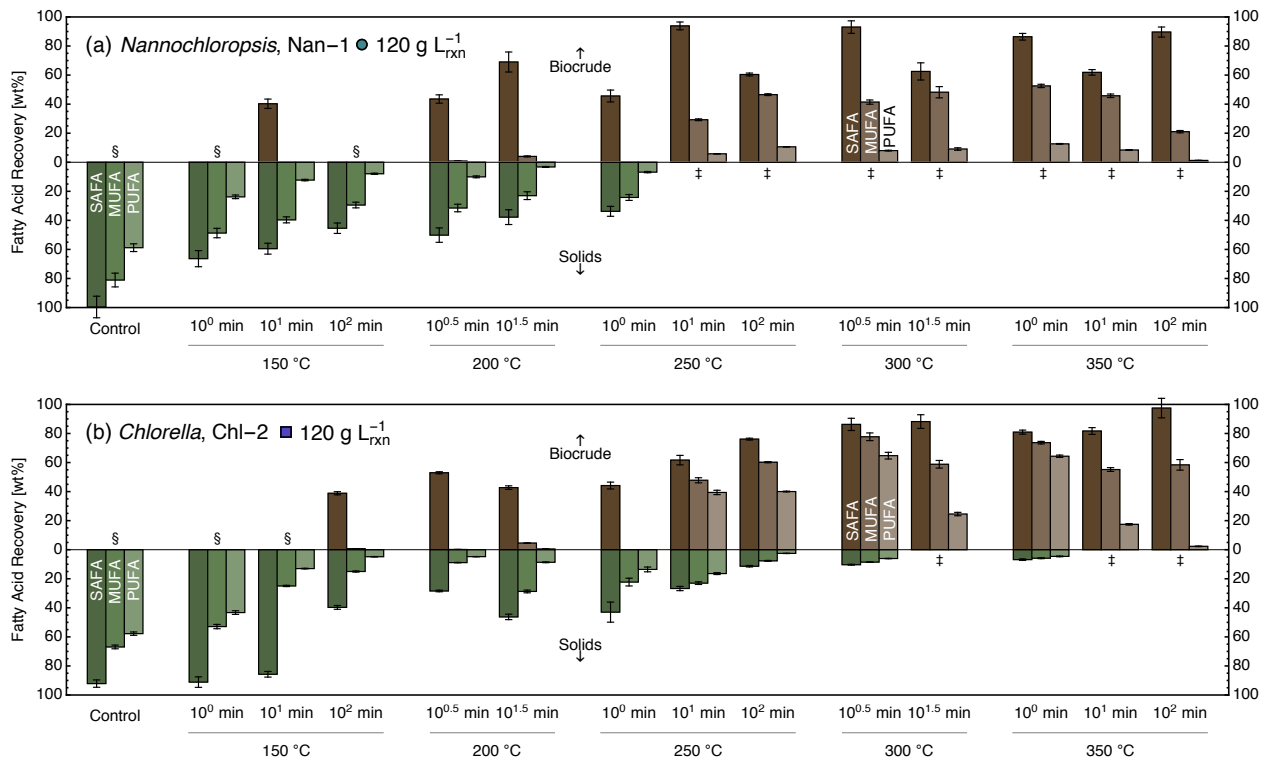


Figure 4.8: SAFA, MUFA, and PUFA recoveries in the biocrude (brown, top) and solids (green, bottom) as functions of temperature and time for (a) low-lipid *Nannochloropsis* (Nan-1) and (b) high-lipid *Chlorella* (Chl-2). § and ‡ denote insufficient biocrude and solid mass for FAMES analysis, respectively. Error bars indicate SE.

reaction severities), but then decreases with increasing reaction time. From 10 to 100 min at 350 °C, however, it actually increases back up to a recovery comparable to the maximum. In fact, when considering the 30 g L<sup>-1</sup> slurries of Nan-1 and Chl-2 shown in Figure E.9a, SAFA recovery increased by on average 16.2 wt% ( $p < 0.053$ ) from 10 to 100 min at 350 °C. Closer inspection reveals that this increase was partially due to an average absolute increase of 140 % ( $p < 0.05$ ) in C18:0 recovery in the biocrude, shown in Figure E.10a, far more C18:0 than measured in the starting biomasses. Relative to all C18 fatty acids (including unsaturated), its recovery is still no greater than 12 wt%, shown in Figure E.10b. This suggests that unsaturated C18 fatty acids are hydrogenating to form C18:0 at 350 °C on the order of tens of minutes. This phenomenon has been suggested previously for similar HTL reaction conditions [117] due to the ability of high-temperature water to facilitate hydrogen production [11]. The extent of this hydrogenation of unsaturated C18 fatty acids to C18:0

increased with increasing slurry concentration as well, with C18:0 recovery increasing on average by about 78 % (absolute,  $p < 0.02$ ). We also note that there was a large increase in C16:0 recovery at 350 °C, 100 min as well, but it was generally not enough to exceed 100 %, possibly because C16:0 is much more abundant in the original biomass.

#### 4.3.13.2 Unsaturated fatty acids

In contrast, MUFAs and PUFAs were measured in the biocrude to a significant extent only at 250 °C, 10 min and higher reaction severities, significantly more severe than the mildest conditions for appreciable SAFA detection. Moreover, at mild reaction severities (below 250 °C, 10 min), these classes of fatty acids were not measured in either the solids or the biocrude phases; however, at higher reaction severities we measured appreciable amounts of both which were higher than the total sum of their presence in the solids and biocrude at mild reaction severity. There are two possible explanations for this phenomenon.

The first explanation is that MUFAs and PUFAs enjoy more stability in biocrude oil generated at reaction severities of at least 250 °C and 10 min than they do in the solid phase or in biocrude generated at milder temperatures. This hypothesis is supported by the reduction of MUFAs and PUFAs measured in the control experiments (left-most group of bars in Figure 4.8), which were performed along with the actual reactions, but with no temperature treatment, and subsequently measured for fatty-acid content with the rest of the reaction products. This reduction highlights that some of the MUFAs and PUFAs degrade in the solids naturally over time, rather than purely through hydrothermal treatment. It is possible that this trend holds for the biocrude perhaps as a function of the amount of other light-absorbing molecules in the oil which could protect the light-sensitive unsaturated fatty acids [118] from degrading as quickly. An additional explanation is that an intermediate reaction product is formed at mild conditions which reverts back to the original unsaturated fatty acid at moderate conditions. In our view, the former explanation is more likely than the latter, and further studies focusing on characterizing fatty-acid kinetics in high-temperature

water would be needed to qualify the existence of an intermediate reaction product.

Notably, we observed MUFA and PUFA recoveries as high as 80.1 and 64.7 wt%, respectively, at 300 °C and 3.2 min for Nan-2 and Chl-2, shown in Figures E.9b and c, which includes Chl-2 in Figure 4.8b. At this reaction condition, across both slurry concentrations for both the high-lipid Nan-2 and Chl-2, these recoveries were on average 76.4 and 53.3 wt% for MUFAs and PUFAs, respectively. To the authors' knowledge, no study of microalgal HTL has demonstrated such high recovery of both MUFAs and PUFAs in the biocrude at those conditions.

Several recent studies reported MUFA and PUFA recovery in the biocrude at temperatures in the range of 225 to 240 °C and 20 to 30 min holding time (not including heat up), but they were not reported in excess of 35 wt% [36, 119]. Another showed appreciable MUFA (14.1 wt%) and PUFA (20.7 wt%) content in the biocrude produced from a high-lipid *Chlorella* at 260 °C, 60 min holding time which was comparable to that at similar conditions presented herein [116]; however, initial biomass MUFA and PUFA content were not provided for determination of recovery. Several other studies conducted at higher reaction severity, including 300 °C (or higher) and at least 30 min total reaction time (including heat up), observed MUFA and PUFA recoveries of up to 85 and 9 wt%, respectively [40, 120, 121]. The MUFA recoveries reported therein are comparable to those presented here, but the reported PUFA recoveries were all significantly lower. We believe this is a result of longer total reaction times employed in these studies, either by design or necessity due to longer heat up times, because our own PUFA recoveries at 300 °C and 31.6 min are substantially lower than at 3.2 min.

Our results show that high PUFA recoveries are only achievable with higher-lipid microalgae. These findings suggest that fast HTL (300 °C and 3.2 min total reaction time) is an effective method for extracting all types of fatty acids without significantly degrading their structure, especially for high-lipid microalgae. Preserving the structure of the unsaturated fatty acids is of particular interest for downstream upgrading (more double bonds allows for

more types of upgrading chemistries) as well for sale as high-value nutraceutical compounds, particularly omega-3 PUFAs [122].

At reaction times longer than 3.2 and 1 min at temperatures of 300 °C and 350°C, respectively, MUFA recovery generally decreased and PUFA recovery monotonically decreased for all biomass types and concentrations (Figures 4.8 and E.9). Fatty acids exhibit lower hydrothermal stability with increasing degrees of unsaturation, due to the increase in reactivity afforded by the additional double bonds [100]. Johnson and Tester [123] calculated kinetic parameters for triglyceride hydrolysis and subsequent unsaturated-fatty-acid degradation at comparable HTL conditions; they proposed that the time scale for degradation suggests reaction times of 30 min or less at temperature of 300 to 350 °C are optimal for maximizing unsaturated-fatty-acid yields. In the present study, reaction severities above the range of 300 °C, 3.2 min and 350 °C, 1 min resulted in lower MUFA and especially lower PUFA recoveries in the biocrude. Therefore we can conclude that the timescale is actually on the order of just minutes, much shorter than proposed by Johnson and Tester [123] and a novel finding arising from the use of reactors that fully heat up in just 1 min.

#### 4.3.13.3 Total fatty acids

Total fatty-acid recovery, depicted in Figure E.9d, followed the same trends with respect to temperature and time reported above for all biomass types, and was not globally affected by initial concentration. It did however increase on average by 26.2 wt% ( $p < 10^{-5}$ ) with increasing lipid content, across all reaction conditions after controlling for species identity. This trend was true for each class of fatty acid as well, with an increase of 8.1 wt% ( $p < 0.04$ ), 28.5 wt% ( $p < 0.0004$ ), and 14.0 wt% ( $p < 0.007$ ) for SAFA, MUFA, and PUFA recoveries, respectively. Those trends highlight that not only do higher-lipid biomass samples produce biocrude oil with higher fatty-acid content, but actually recover higher percentages of all classes of fatty acids than their higher-protein counterparts. This could be due to an increased prevalence of side reactions between protein degradation products and the fatty

acids in the high-protein strains. The higher magnitudes of increases for MUFA and PUFA recoveries suggests it could be due to the inhibition of side reactions with the double bonds, likely in addition to reactions with the carboxyl group.

## 4.4 Further discussion and conclusion

Table 4.2 presents a summary of the impacts of changing reaction time, slurry concentration, lipid content, protein content, species, and reaction temperature on the yield and properties of the biocrude oil. These changes control for all other factors and occur from two reference points at 200 and 300 °C, respectively, for 30 g L<sub>rxn</sub><sup>-1</sup> slurries and 3.2 min reaction time.

### 4.4.1 Mild-reaction-severity reference point

At the 200 °C, 3.2 min, and 30 g L<sub>rxn</sub><sup>-1</sup> reference point, biocrude properties are most sensitive to changing lipid content and temperature. In fact, an average increase from 10.5 to 24.2 wt% lipid content resulted in very similar increases in biocrude yield, C recovery, and ER as did an increase in temperature from 200 to 300 °C, all of which were statistically significant. Linear approximation reveals that a 1 wt% increase in lipid content produces an equivalent increase in biocrude C recovery (+1.5 %) as does a 5.8 °C increase in reaction temperature. Notably however, increasing temperature also resulted in statistically significant increases in N content (+3.1 wt%) and N recovery (+17 %) in the biocrude whereas increasing lipid content decreased N content (-0.7 wt%) and slightly increased N recovery (+3 %).

The effect of increasing protein content was (necessarily) of equal magnitude but opposite sign of that of increasing lipid content, but over about twice as wide of a range in protein content (25.2 wt%) than lipid content (13.7 wt%). In general, increasing protein content negatively affected the yield and composition of the biocrude oil at this reference point, however it did decrease both N (-3%) and O (-12%) recovery. The variabilities in biocrude properties induced by different microalgae species were similar in magnitude to the effects of

Ref. Point	Independent Variable	Change	Sensitivity Scale	Yield [wt%]	Content [wt%]					HHV [kJ/g]	Recovery [%]									
					C	H	N	S	O		C	H	N	S	O	ER	SA	MU	PU	TF
200 °C 3.2 min 30 g L <sub>rxn</sub> <sup>-1</sup>	Temperature:	200 → 300 °C	██████	18*	4	-0.2	3.1*	0.2*	-8*	2	26*	22*	17*	26	7	27*	11	37	26	26
	Lipid Content:	10.5 → 24.2 wt%	██████	16*	1	0.7	-0.7	- <sup>a</sup>	-1	1	21*	21	3	-	12*	22*	-	-	-	-
	Protein Content:	17.4 → 42.6 wt%	██████	-16*	-1	-0.7	0.7	-	1	-1	-21*	-21	-3	-	-12*	-22*	-	-	-	-
	Species:	Nan-1, Chl-1, Mix-m	██	4	3	0.1	0.4	-	3	1	4	5	0	-	5	4	-	-	-	-
	Time:	3.2 → 31.6 min	█	6*	1	0.1	0.7*	0.0	-2	1	7*	7*	2*	3	4	8*	5	5	0	4
	Concentration:	30 → 120 g L <sub>rxn</sub> <sup>-1</sup>	█	0	1	0.4	0.2	0.0	-2	1	-1	-1	0	-2	-2	-1	-2	-1	0	-1
300 °C 3.2 min 30 g L <sub>rxn</sub> <sup>-1</sup>	Lipid Content:	10.5 → 24.2 wt%	██████	10	7	1.3	-2.8	-0.4	-5	5	16	15	8*	0	-3	18	-4	61	52	46
	Protein Content:	17.4 → 42.6 wt%	██████	-10	-7	-1.3	2.8	0.4	5	-5	-16	-15	-8*	0	3	-18	4	-61	-52	-46
	Species:	Nan-1, Chl-1, Mix-m	██	5	3	0.1	0.9	0.1	4	1	4	4	2	9	8	4	21	30	21	18
	Time:	3.2 → 31.6 min	██	2	4*	0.3	0.1	0.0	-4*	2	5	4	3*	2	-3	6	-8	-9	-22	-12
	Concentration:	30 → 120 g L <sub>rxn</sub> <sup>-1</sup>	█	2	1	0.1	0.6*	0.0	-1	1	4	3	3*	1	0	4	2	6	9	7

Table 4.2: Summary of differences in biocrude properties as a result of changing six different independent variables from two different reference points. Sensitivity Scale qualitatively denotes the sensitivity of biocrude properties to each independent variable at a given reference point. SA, MU, PU, and TF indicate SAFA, MUFA, PUFA, and total FA recovery in the biocrude, respectively. Yellow and blue intensity denote increases and decreases in the associated property, respectively. Changes in temperature, time, and concentration are the average of the differences in the six different types of biomass (see Table 4.1). Changes in biochemical composition show the average of differences in the two different types of *Nannochloropsis* and *Chlorella*, respectively. Changes in species denote the SD of values from Nan-1, Chl-1, and Mix-m. <sup>a</sup>Denotes no data available. \*Denotes statistically significant difference at the 0.05 level.

increasing reaction time from 3.1 to 31.6 min. Finally, a four-fold increase in concentration at this reference point did not affect biocrude properties to a significant extent.

#### 4.4.2 High-reaction-severity reference point

At the 300 °C, 3.2 min, and 30 g L<sub>rxn</sub><sup>-1</sup> reference point, the characteristics of the biocrude are most sensitive to changing biochemical composition. Increased lipid content produced similar trends in biocrude properties as at 200 °C; however, the increases to yield, C content and recovery, H content and recovery, and ER were lower, and the decreases to N and O content were higher. Increased protein content was again detrimental to the yield and composition of the biocrude, although it decreased N recovery (-8%) to a statistically significant extent, greater than that at 200 °C.

Species identity, reaction time, and slurry concentration demonstrated around the same magnitude of effects on biocrude yield and properties. Increased time and concentration both induced similar changes in biocrude yield and elemental content and recovery; although, increased time substantially reduced fatty-acid recovery while increased concentration slightly increased it.

### 4.4.3 Additional conclusions

In addition to the aforementioned effects, there were several other key takeaways from this chapter. Maillard reactions explained observed increases in biocrude yield, C recovery, and N recovery and associated decreases in O recovery. Moreover, the selectivity of these reactions were promoted by increases in concentration, as evidenced by the differences between the measured and observed values for a two-species mixture of a high-protein biomass (Spi-1) and a high-carbohydrate biomass (Chl-2). Furthermore, carbohydrates may act as the limiting reactant in an excess of protein for these reactions, causing a greater proportion of N recovery in the biocrude for biomass samples with higher carbohydrate-to-protein ratios (e.g., Chl-2 and Nan-1). Additionally, we found that fast HTL (300 °C, 3.2 min) of more dilute slurries of high-lipid biomass is an effective method for recovering up to 89.3, 80.1, and 64.7 wt% of SAFAs, MUFAs, and PUFAs, respectively. These results together suggest that high-lipid and low-carbohydrate biomass may be optimal for producing high-quality biocrude and limiting the extent of Maillard reactions, although future work is needed to optimize the relative proportions of proteins and carbohydrates for the minimization of Maillard reactions during HTL.

## CHAPTER V

# The impacts of temperature, time, concentration, biochemical composition, and microalgal species on the aqueous co-product from hydrothermal liquefaction

This chapter contains results that were in preparation for submission to *Applied Energy* written along with co-authors Casey M. Godwin, Bradley J. Cardinale, and Phillip E. Savage [124]. In this chapter, we expand on the work presented in Chapter IV to include the individual and dynamic impacts of reaction conditions and feedstock characteristics on the ACP. Explicitly, we measured the effects of temperature (150 to 350 °C), reaction time (1 to 100 min), slurry concentration (30 and 120 g L<sub>rxn</sub><sup>-1</sup>), biochemical composition (5.2 to 28.5 wt% lipid, 14.7 to 50.9 wt% protein), and species identity (*Nannochloropsis*, *Chlorella*, and *Spirulina*) on ACP characteristics. Measured properties included gravimetric yield, elemental (CHNSOP) recovery, NH<sub>4</sub><sup>+</sup>-N and PO<sub>4</sub><sup>3-</sup>-P recovery, and pH. The impacts of slurry concentration and species identity on ACP properties are examined in depth for the first time, with all probed variables affecting ACP yield and composition. Temperature exhibited the most influence, followed by microalgal species (at 200 °C) and biochemical composition (at 300 °C). Lower slurry concentration led to increased ACP yields and recovery of NH<sub>4</sub><sup>+</sup>-N, total nitrogen, PO<sub>4</sub><sup>3-</sup>-P, total phosphorus, and sulfur; in fact, we report evidence that increased slurry concentration promotes Maillard reactions that inhibit NH<sub>4</sub><sup>+</sup>-N recovery in

the ACP and promote N recovery in the biocrude. Low-protein biomass liberated nitrogen as ammonium more efficiently at lower temperature (200 °C); however, high-protein biomass did so more efficiently at higher temperature (300 °C) and with significantly higher  $\text{NH}_4^+ - \text{N}$  recovery. We identified high-lipid, 30 g  $\text{L}_{\text{rxn}}^{-1}$  slurries reacted at 200 °C for 31.6 min as ideal for both maximizing ACP recyclability while limiting N and S recovery in the biocrude to less than 5 and 8 %, respectively. The unique results and expansive experimental data reported herein expand our understanding of microalgal HTL and provide the foundation for constructing a new quantitative kinetic model in Chapter VI.

## 5.1 Introduction

The ACP is of great importance for overall process sustainability because it contains high concentrations of nutrients required for microalgal growth, including N, P, and S [18, 19] and their bioavailable forms  $\text{NH}_4^+ - \text{N}$ ,  $\text{PO}_4^{3-} - \text{P}$ , and  $\text{SO}_4^{2-} - \text{S}$  [3], all of which enhance ACP recyclability. ACP can be directly recycled both with or without dilution to grow microalgae with positive, synergistic effects on algal growth rates and biomass productivity, most notably with polycultures [84], although also with some monocultures under certain conditions [33, 125]. In addition to high nutrient abundance, there are also organic compounds in the ACP that inhibit growth [47] (thus lowering recyclability). These compounds represent up to 38 % of the biomass C [24, 27] and possess energy content that could be recovered. Therefore, another route of ACP utilization is through hydrothermal gasification to convert these organics to fuel gases, such as methane, before recycling the N, P, and S for algal growth [20]. The most optimal process in terms of maximizing EROI and minimizing environmental impacts likely requires a combination of direct recycling and indirect recycling via hydrothermal gasification that balances nutrient recycling with energy recovery via methane formation from aqueous C.

Aqueous-phase-product yield and recyclability depend on variables such as HTL temperature and time [22, 24, 26–28, 30–37], concentration [32, 37, 38], feedstock biochemical

composition [15, 28, 36, 40, 41, 44, 45], and microalgal species [28, 39]. Previous examinations of the impacts of these variables have various shortcomings, however. Often only one or two variables are examined, and there are some combinations of variables that are yet to be scrutinized in detail, particularly at low to mild reaction severities. Often overlooked factors, such as slurry concentration and species identity have yet to be rigorously quantified in terms of their impact on ACP yield and properties. Furthermore, no previous study has probed all of these factors together when examining the ACP. There could, therefore, be previously unexamined synergistic or antagonistic effects between different feedstock characteristics and reaction conditions.

In this study, we use fast-heating batch reactors (1-min heat-up) to conduct a broad set of microalgal HTL experiments that establish and corroborate the individual and dynamic effects of a variety of reaction conditions and feedstock characteristics. We probe reaction times logarithmically ( $10^{0.0}$ ,  $10^{0.5}$ ,  $10^{1.0}$ ,  $10^{1.5}$ , and  $10^{2.0}$  min) over a large range of temperatures (150, 200, 250, 300, and 350 °C) for six microalgal feedstocks with different biomolecule distributions (5.2 to 28.5 wt% lipid, 14.7 to 50.9 wt% protein) at two different slurry concentrations (30 and 120 g L<sub>rxn</sub><sup>-1</sup>). We chose three of these microalgae, including a high-lipid *Nannochloropsis*, high-lipid *Chlorella*, and high-protein *Spirulina*, to contain different proximate biochemical compositions to evaluate the impacts of different lipid, protein, and carbohydrate contents at different reaction severities and slurry concentrations. We selected the other three, including a high-protein *Nannochloropsis*, a high-protein *Chlorella*, and a mixture of high-protein *Spirulina* and high-lipid *Chlorella*, to contain a similar proximate biomolecule distribution, enabling quantification of the variability between different species over different reaction conditions and slurry concentrations after controlling for biochemical composition. Likewise, the two variants of *Nannochloropsis* and *Chlorella* enable examination of the effects of biochemical composition while controlling for microalgal species. Additionally, we juxtapose the two-species-mixture measured and predicted effects to elucidate how the different allotments of biomolecule components in high-protein *Spirulina* and

high-lipid, high-carbohydrate *Chlorella* react dynamically at different reaction severities and slurry concentrations, compared to how they react alone. These experimental results, along with those presented in Chapter IV, provide the basis for developing a novel mathematical model of microalgal HTL in Chapter VI.

## 5.2 Materials and methods

We describe experimental methods in great detail in Chapter IV and therefore limit the information presented here to the most important details, many of which are reproduced from earlier.

### 5.2.1 Microalgae feedstocks and slurry preparation

Microalgal species for this study include a high-protein *Nannochloropsis oculata* (Nan-1), high-lipid *Nannochloropsis salina* (Nan-2), high-protein *Spirulina platensis* (Spi-1), high-protein *Chlorella sorokiniana* (Chl-1), and high-lipid *Chlorella sorokiniana* (Chl-2). We pre-mixed slurries of each biomass type such that their concentrations were either 30 or 120 g L<sub>rxn</sub><sup>-1</sup> at reaction conditions (150 to 350 °C) and froze them prior to each reaction (upon which they were thawed at room temperature). See Appendix D for the equivalent solids contents and calculation of the concentrations on a g L<sub>rxn</sub><sup>-1</sup> basis. We prepared the two-species mixture slurries (Mix-m) by combining roughly three parts low-protein *Chlorella* (Chl-2) with seven parts *Spirulina* (Spi-1) for an average Chl-2 content of 30.1 wt%.

### 5.2.2 Hydrothermal liquefaction

We conducted HTL in 1.30 mL stainless-steel batch reactors using <sup>1</sup>/<sub>4</sub>-in. o.d., 0.049 in. thick Swagelok tubing. We constructed additional 1.16 mL proxy reactors fitted with a K-type thermocouple for temperature measurements. Individual reactions proceeded by immersing both a slurry-loaded reactor and proxy reactor into a Techne IFB-51 fluidized sand bath, preheated to the specified temperature. It typically took reactors about 58 s to

achieve 98% of the maximum temperature change relative to ambient conditions. At the end of the holding time ( $10^{0.0}$ ,  $10^{0.5}$ ,  $10^{1.0}$ ,  $10^{1.5}$ , or  $10^{2.0}$  min), we quenched the reactors in a cold water bath. We define this holding time as the time from the moment the reactor starts to heat up to the moment the reactor starts to cool down.

We measured 5.5 mL of DCM (>99.9% optima grade, Fisher Scientific) and enough deionized water (4.3 to 4.9 mL) such that the total volume of water was approximately 5.5 mL to facilitate product collection via pipette. Following product recovery, we vortexed and centrifuged the product mixture twice to separate out the biocrude (DCM-soluble products), aqueous phase, and solid products into separate glass tubes. We transferred a 500  $\mu$ L aliquot of aqueous phase into a small plastic vial to be frozen for subsequent ammonium and phosphate analyses. We measured the pH of the aqueous phase using a Fisher Scientific accumet 0.25-in. diameter electrode calibrated using pH 4, 7, and 10 buffer solutions. We dried the ACP under nitrogen at 70 °C for 1 h or until dry. We calculated the ACP mass as the measured dried mass, adjusted to account for the 500  $\mu$ L aliquot set aside for further characterization.

### 5.2.3 Elemental content, ammonium, and phosphate

We report elemental contents (C, H, N, O, S, and P) for biomass samples in Table D.3. We combined and homogenized replicate dried ACP fractions before Elemental Microanalysis Ltd measured their C, H, N, and S content. We measured total P in the ACP using persulfate digestion and the ascorbic acid molybdenum method [7, 96]. We measured ACP ammonium and phosphate also using this ascorbic acid molybdenum method. To quantify any ammonium that may not have evaporated from the ACP during the drying step, we also rehydrated an aliquot of dried sample with deionized water and measured ammonium that remained in the ACP after initially drying (likely as a salt). We subtracted the yield and N content of this residual ammonium from the dried aqueous phase yield and N content, respectively, to obtain the ammonia-free aqueous yield and organic N content, respectively.

We previously showed that other forms of aqueous N, such as  $\text{NO}_2^-$  and  $\text{NO}_3^-$ , are below detection limits for ACP generated at 350 °C, and 20 min, so we assume them to be negligible here [7].

#### 5.2.4 Biomass biochemical content

We approximated biomass lipid content as the total fatty acid content of the biomass averaged over five replicates, with the acknowledgement that unsaponifiable lipids and minor components derived from the lipid structures, such as phosphate and glycerol, will be neglected. We estimated biomass protein content by multiplying biomass N content by 4.78 [110]. We measured biomass ash content by combusting the samples at 550 °C for 30 h and calculating the percentage of mass retained, minus biomass P content, averaged over five replicates. We calculated biomass carbohydrate content by difference from unity and the sum of lipid, protein, and ash content.

#### 5.2.5 Statistical analysis

We performed all statistical analyses on subsets of the data using the function `LocationTest` in Mathematica 11.1. All comparisons between subsets of the data are on an absolute deviation basis, not relative, unless otherwise stated.

### 5.3 Results and discussion

Table 4.1 summarizes the microalgal species and their biochemical profiles, shorthand identifiers, and symbols used in figures. Ternary diagrams (Figure 4.1) show these biochemical profiles (dry, ash-free basis) color-coded with red, green, and blue intensity mapped to lipid, protein, and carbohydrate contents, respectively. We use this color scheme for each type of biomass throughout this dissertation to facilitate evaluation of biochemical composition effects. We report data for aqueous-phase elemental recoveries graphically in the following sections and refer the reader to Appendix H for supplemental figures and information.

### 5.3.1 Aqueous-phase-product yield

#### 5.3.1.1 Temperature and time

The yield of non-volatile aqueous-phase products (hereafter referred to as aqueous yield) is shown in Figure 5.1 and includes ammonia-free products retained after drying under nitrogen at 70 °C. Aqueous yield increased with increasing temperature and time until a maximum was reached at low-to-moderate reaction severity (200 °C, 31.6 min to 250 °C, 10 min). Other studies have shown a maximum to occur at similar conditions [22, 34, 36]. This maximum appears to be a function of biochemical composition, with the high-protein Nan-1 reaching a maximum later than the low-protein Chl-2 at 250 °C. Beyond this point, aqueous yield decreased monotonically with increasing reaction severity, a trend consistent with numerous previous studies [22, 24, 27, 28, 34, 36]. The magnitudes of aqueous yields in the present study were also generally consistent with these studies from the literature, with some variability due to differences in drying conditions for the aqueous phase (e.g., temperature).

#### 5.3.1.2 Slurry concentration

Across all temperatures and times, decreasing slurry concentration led to an average increase in aqueous yield of 3.9 wt% ( $p < 10^{-8}$ ). This effect is largest between 200 and 300 °C (4.9 wt%,  $p < 10^{-5}$ ), and is lower but still statistically significant at 350 °C, 10 min and higher (1.4 wt%,  $p < 0.02$ ). One explanation for this effect is that the more dilute slurry facilitates hydrolysis of proteins and carbohydrates into smaller peptides/amino acids and saccharides, respectively, which as a general rule become increasingly soluble in water with decreasing size. We posit that this hydrolysis facilitation could occur due to shifts in the relative proportions of conjugate acids and bases of compounds in solution owed to the four-fold difference in slurry concentration that in turn affect the relative amounts of  $H^+$  and  $OH^-$  ions that catalyze hydrolysis. This explanation is supported by the variability in aqueous

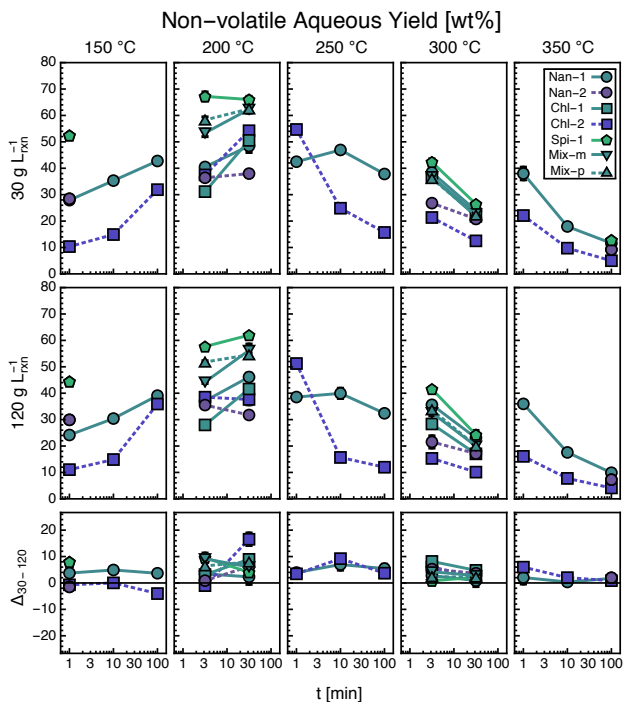


Figure 5.1: Non-volatile aqueous-phase-product yield versus reaction time grouped by temperature and initial concentration. See Table 4.1 for microalgae types. The bottom row depicts the first row ( $30 \text{ g L}_{\text{rxn}}^{-1}$ ) minus the second row ( $120 \text{ g L}_{\text{rxn}}^{-1}$ ). Error bars indicate SE.

pH as a function of slurry concentration discussed later in Section 5.3.6, which shows that at room temperature, the ACP is significantly more basic for the  $30 \text{ g L}_{\text{rxn}}^{-1}$  slurries than the  $120 \text{ g L}_{\text{rxn}}^{-1}$  slurries. This may suggest that the perceived increase in hydrolysis rate is due to base-catalysis, however without knowing the pH of the mixture at reaction temperature this categorization is tentative. Another possibility is that the more concentrated slurry significantly increases the rates of reaction between biomolecule-degradation products at the expense of hydrolysis with the bulk high-temperature water.

It is also possible that the  $120 \text{ g L}_{\text{rxn}}^{-1}$  slurries produced ACP that was saturated with certain compounds that possess limited solubility in water. All product mixtures were dissolved in approximately the same volume of water (including fresh DI-water diluent to facilitate with product recovery), so theoretically, a solubility limitation for the more concentrated slurries would result in higher per-unit-biomass yields for the lower concentrations. However, we would expect to see this concentration effect predominantly at the points of maxi-

imum aqueous yield, where the amount of dissolved material is the greatest, but instead we see it throughout the dataset. This suggests that solubility limitations are unlikely to be systematically affecting this trend.

### 5.3.1.3 Biochemical composition

Aqueous yield generally increased with increasing protein content (color-coded in Figure 5.1; see Figure H.1 in Appendix H for explicit yield vs. protein plots); however, there were several exceptions at temperatures of 250 °C and lower. This trend was more consistent at 300 °C and higher, a finding that has been seen previously [15, 36, 40] and would be expected due to the high aqueous solubility of protein-degradation products, including most peptides and amino acids. Controlling for species identity (i.e., comparing effects of biochemical composition between *Nannochloropsis* and *Chlorella*, respectively) at 300 °C, higher biomass-protein content led to an average aqueous yield increase of 9.9 wt% ( $p < 0.0004$ ).

### 5.3.1.4 Species identity

Despite comparable biochemical profiles, the aqueous yields of Nan-1, Chl-1, and Mix-m varied considerably due to species identity at 200 °C. However, complete separation of the solid and aqueous phase for samples produced from Spi-1 (the primary constituent of the two-species mixture Mix-m) was difficult at 200 °C and lower, so aqueous yields for those samples (which were generally higher than other biomass types at those temperatures) may contain solids. Excluding Mix-m, the average difference between Nan-1 and Chl-1 was only significant at 3.2 min (9.2 wt%,  $p < 0.01$ ) rather than at 31.6 min (1.2 wt%,  $p < 0.78$ ). At 300 °C, variability due to species identity between Nan-1, Chl-1, and Mix-m was on average only  $\pm 1.0$  wt% for the 30 g L<sub>rxn</sub><sup>-1</sup> slurries, whereas it was  $\pm 3.3$  wt% for the 120 g L<sub>rxn</sub><sup>-1</sup> slurries. López Barreiro et al. [39] reported aqueous yield variabilities of  $\pm 6.2$  and  $\pm 2.4$  wt % for 50 g L<sub>rxn</sub><sup>-1</sup> slurries at 250 °C, 9 min and for 30 g L<sub>rxn</sub><sup>-1</sup> slurries at 375 °C, 11 min, respectively, for

five different species with similar biochemical composition ( $52 \pm 2$  wt % protein content, dry ash-free basis). Those variabilities are comparable in magnitude and trend with increasing temperature as those of the present study. Both the data in the present study and that of López Barreiro et al. [39] demonstrate that biochemical composition is a reasonable predictor of aqueous yield at reaction severities of 300 °C and higher, especially for dilute slurries.

### 5.3.1.5 Two-species mixture interactions

The measured aqueous yield for the two-species mixture (Mix-m) only deviated from predicted (Mix-p) at 200 °C, 3.2 min ( $-6.2$  wt%,  $p < 0.14$ ), although not with statistical significance. There was no difference at all other reaction conditions ( $0.3$  wt%,  $p < 0.52$ ), suggesting that there are no significant interactions between the protein-degradation products of Spi-1 and carbohydrate- and lipid-degradation products of Chl-2 affecting aqueous yield.

## 5.3.2 Nitrogen recovery

### 5.3.2.1 Temperature and time

$\text{NH}_4^+$ -N recovery (Figure 5.2a), or the percentage of biomass N recovered as aqueous  $\text{NH}_4^+$ , monotonically increased with increasing reaction severity for all biomass types and slurry concentrations, reaching a maximum of 81.2% ( $30 \text{ g L}_{\text{rxn}}^{-1}$  slurry of Spi-1 at 350 °C, 100 min). In contrast, organic N recovery (Figure 5.2b) followed a similar trend as that of aqueous yield, increasing to a maximum at moderate severity (200 °C, 31.6 min to 250 °C, 10 min) before decreasing thereafter. Total N recovery (Figure 5.2c) shows that at 300 °C and above, any decrease in organic N recovery with increasing severity is matched with an approximately equivalent increase in  $\text{NH}_4^+$ -N recovery. Magnitudes and trends with respect to reaction severity for total N recoveries are comparable to other reports [22, 24, 26, 28, 30, 33, 35], with some variation due to differences in measurement technique (namely dry oxidation versus digestion, the latter of which can underestimate organic N content). The percentage

of ACP N as  $\text{NH}_4^+$  (Figure 5.2d) followed the same trend as  $\text{NH}_4^+$ -N recovery, reaching a maximum of 97.0 %. At high reaction severity, these percentages were somewhat higher than some other studies [24, 36, 40] but equivalent to others [28, 35], although less severe conditions were more comparable. At high reaction severity, other sources of volatile N, such as methylamine and ethylamine, have been reported as degradation products of amino acids [126]; however, most of these compounds are likely lost during the drying step and would be unaccounted for in the aqueous total N, which may explain the higher percentages of aqueous N as ammonium. We note that with the exception of Chl-2, N mass closure (from all products) was 80 % or higher at 300 °C and higher (Figure 5.7, discussed in Section 5.3.7).

Notably, the ACP total N recovery produced by Chl-2 reaches a maximum at 200 °C and 31.6 min before decreasing at higher reaction severity, while all other biomass types continue to increase or plateau in N recovery through 300 °C and 31.6 min. In Chapter IV, we showed that, for Chl-2, this N is recovered in both the biocrude (Figure 4.4) and solid (Figure F.4) phases to a greater extent than the other biomass types; however, the N recovery in the solid fraction monotonically decreased with reaction severity (albeit slowly), so the decrease in ACP total N recovery corresponds directly with an increase in biocrude N recovery.

At 350 °C for Nan-1, aqueous total N recovery increased by 9.2 % ( $p < 0.03$ ) from 10 to 100 min despite having decreased from 1 to 10 min by 6.3 % ( $p < 0.18$ ). Figure 5.2a and 5.2b show that this increase is entirely due to increasing  $\text{NH}_4^+$ -N recovery. Moreover, we previously found that biocrude N recovery for Nan-1 decreases in this range as well (Figure 4.4). Therefore we conclude that at these reaction conditions (350 °C, 10 to 100 min), N-containing biocrude-soluble compounds are losing N to the ACP in the form of ammonium, possibly through deamination reactions. This result suggests that for higher-protein biomass, extended reaction times at 350 °C could both improve ACP recyclability and reduce biocrude heteroatom content, a trend demonstrated previously [24].

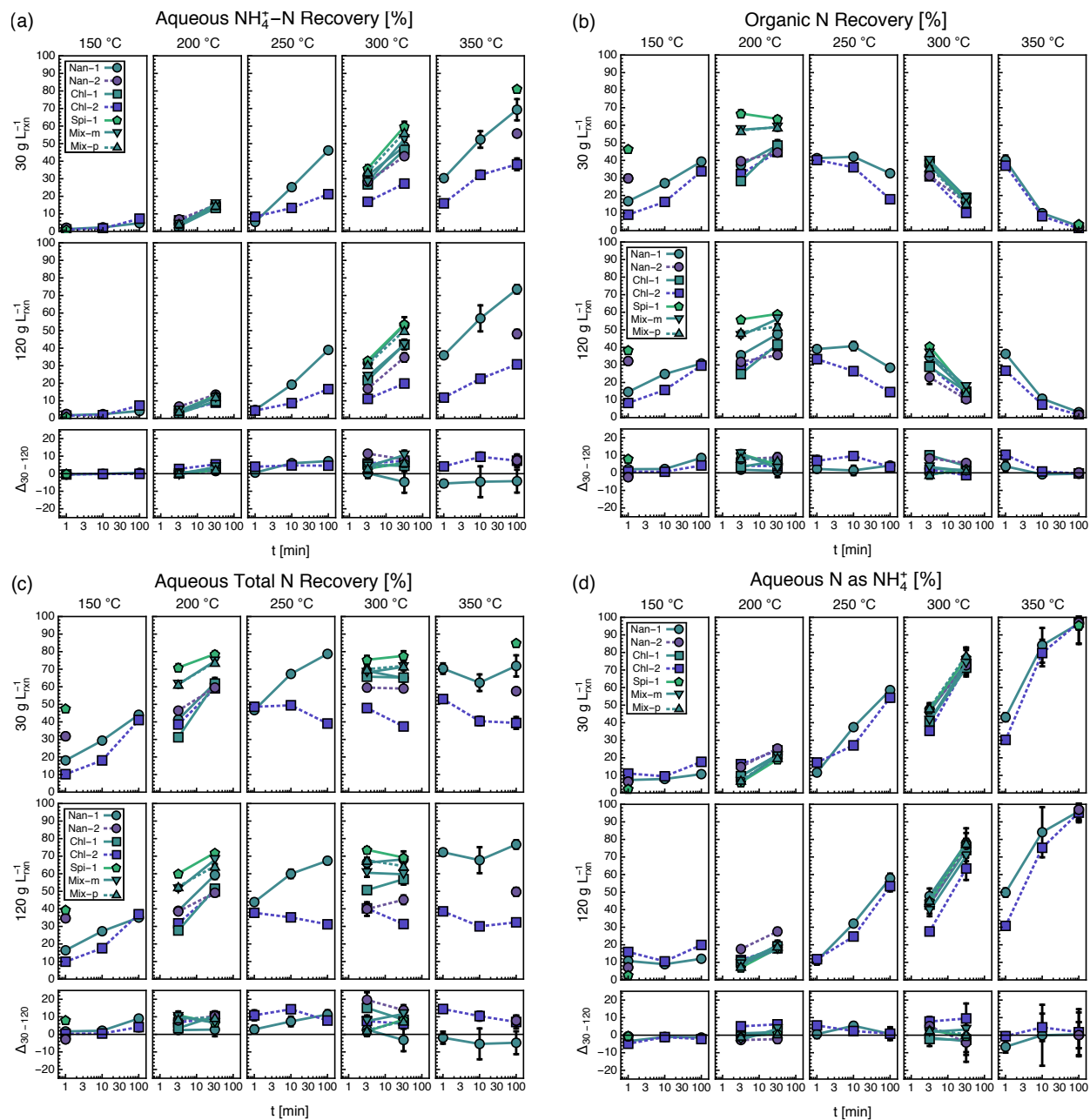


Figure 5.2: Aqueous-phase-product nitrogen recovery (a) as ammonium ( $\text{NH}_4^+ - \text{N}$ ), (b) as organic nitrogen, (c) in total, and (d) as ammonium relative to total aqueous nitrogen versus reaction time grouped by temperature and initial concentration. See Table 4.1 for microalgae types. The bottom row depicts the first row ( $30 \text{ g L}_{\text{rxn}}^{-1}$ ) minus the second row ( $120 \text{ g L}_{\text{rxn}}^{-1}$ ). Error bars indicate SE.

### 5.3.2.2 Slurry concentration

At  $200 \text{ }^\circ\text{C}$  and higher, regardless of biomass type, the  $30 \text{ g L}_{\text{rxn}}^{-1}$  slurries led to on average 3.3 % higher ( $p < 0.0001$ )  $\text{NH}_4^+ - \text{N}$  recovery, 3.9 % higher ( $p < 10^{-6}$ ) organic N recovery, and

as a result 7.3 % higher ( $p < 10^{-5}$ ) total N recovery. This trend coincides with a previously reported 4.6 % decrease in biocrude N recovery at 250 °C and higher for the 30 g  $L_{\text{rxn}}^{-1}$  slurries relative to that of the 120 g  $L_{\text{rxn}}^{-1}$  slurries (Figure 4.4). The data in Figure 5.2 reveal that this decrease in biocrude N recovery directly benefits both  $\text{NH}_4^+ - \text{N}$  and organic N recovery in the ACP.

### 5.3.2.3 Biochemical composition

$\text{NH}_4^+ - \text{N}$  recovery (Figure 5.2a) is a strong function of biochemical composition at 250 °C and higher; for example, it increases by on average 13.0 % ( $p < 0.001$ ) with increasing protein content at 300 °C (see Figure H.3 in Appendix H for explicit N recovery vs. protein plots). These data support the assertion in Chapter IV that carbohydrates are the limiting reactant in the Maillard reaction. A greater proportion of proteins to carbohydrates would enable more of the protein fraction to degrade autogenously into products such as ammonium, as is observed here with the more protein-rich biomass samples. In contrast, for the biomass samples with higher proportions of carbohydrates to proteins, such as Chl-2 and Nan-2, relatively more protein-degradation products, such as amino acids, would participate in Maillard reactions rather than undergo deamination.

Organic N recovery (Figure 5.2b) generally increased with increasing protein content at all reaction conditions but not universally and to a lesser extent than that of  $\text{NH}_4^+ - \text{N}$ . This effect was low and statistically insignificant (+1.8 %,  $p < 0.3$ ) at 200 °C, but greater and statistically significant (+5.3 %,  $p < 0.01$ ) at 300 °C. As a result, total N recovery generally increased with increasing biomass protein content at 200 °C and lower. This trend was more significant at 250 °C and higher, a result corroborated by previous work [40, 41, 44, 45]. Notably, the proportion of total N owed to ammonium (Figure 5.2d) was on average 4.3 % lower ( $p < 0.01$ ) with increasing protein content at 200 °C, but 4.6 % higher ( $p < 0.07$ ) with increasing protein content at 300 °C. This suggests that low-protein biomass liberates ammonium more efficiently (per unit biomass N) at low severity (200 °C) than high-protein

biomass, while the opposite is true at high severity (300 °C). Shakya et al. [44] showed similar trends at high reaction severity, albeit with even larger increases than we observed; however in contrast, Leow et al. [40] found no clear trend in the percentage of total N as ammonium with increasing protein content at 300 °C.

#### 5.3.2.4 Species identity

Between Nan-1, Chl-1, and Mix-m,  $\text{NH}_4^+$ -N recovery varied by  $\pm 1.0$  % and  $\pm 4.3$  % at 200 and 300 °C, respectively. Previous work has demonstrated similar  $\text{NH}_4^+$ -N recovery variability due to species identity [28], indicating that biochemical composition is a reasonable predictor of  $\text{NH}_4^+$ -N within those uncertainties. Variability in organic ( $\pm 2.1$  %) and total N ( $\pm 4.8$  %) recoveries were similarly low at 300 °C for these three biomass types with similar biochemical composition.

#### 5.3.2.5 Two-species mixture interactions

At 300 °C, the measured (Mix-m)  $\text{NH}_4^+$ -N recovery in the 120 g  $\text{L}_{\text{rxn}}^{-1}$  slurries was 7.4 % ( $p < 0.06$ ) lower than predicted (Mix-p). This trend is partially explained in Section 4.3.4, where we showed that biocrude N recovery at these conditions was on average 5.0 % ( $p < 0.21$ ) higher than predicted (Figure 4.4). We proposed that Maillard reactions between the degradation products from the carbohydrate-rich Chl-2 and protein-rich Spi-1 in the two-species mixture were the most likely explanation for the increased N recovery. The data presented here suggest that this increased N recovery in the biocrude is directly related to reduced  $\text{NH}_4^+$ -N recovery in the aqueous phase. We note that although the increase in biocrude N recovery was not statistically significant, the associated decrease in  $\text{NH}_4^+$ -N recovery was statistically significant. This effect was absent or significantly reduced at 200 °C and/or for the 30 g  $\text{L}_{\text{rxn}}^{-1}$  slurries. These data demonstrate that the Maillard reactions are favored by concentration increases and likely proceed by an overall reaction order greater than one.

### 5.3.3 Phosphorus recovery

#### 5.3.3.1 Temperature and time

Increasing temperature and time increased  $\text{PO}_4^{3-}$ -P recovery (Figure 5.3a) until a maximum was reached at moderate reaction severity (around 250 °C, 10 min). Notably the reaction conditions that maximized  $\text{PO}_4^{3-}$ -P recovery were essentially the same for all biomass types, similar to  $\text{NH}_4^+$ -N recovery. We do however report significantly higher total P recovery (Figure 5.3c) at this maximum than one previous study [35]. Further increases in temperature and time led to decreasing  $\text{PO}_4^{3-}$ -P recovery, in some cases down to single-digit recoveries by 350 °C, 100 min. This reduction in P recovery has been documented before [22, 24, 27, 33, 35, 37], and is likely due to the formation of highly insoluble phosphate precipitates in the solid phase [27], including calcium phosphates like hydroxyapatite [127]. In Appendix F, we showed an increase in P recovery in the solid phase at these conditions (Figure F.7). These precipitates likely form as a function of pH, which itself is a function of reaction conditions and feedstock characteristics (discussed later in Section 5.3.6); pH and  $\text{PO}_4^{3-}$ -P recovery were strongly and significantly correlated ( $\rho = -0.47$ ,  $p < 10^{-10}$ ).

Non-phosphate P recovery (Figure 5.3b) was significant at low reaction severities, similar to that of Ekpo et al. [35], but generally decreased with increasing reaction severity. At 250 °C, 10 min and above, the vast majority of P was present as phosphate (Figure 5.3d), consistent with some prior findings [22, 24] although others showed 15 to 35 % non-phosphate P recovery at these conditions for a strain of *Chlorella vulgaris* [35]. We also observed non-phosphate P recoveries as high as 18.3 % at 300 °C, 31.6 min and 350 °C, 10 min for our high-lipid *Chlorella* (Chl-2), but only for the 30 g  $\text{L}_{\text{rxn}}^{-1}$  slurries. The absolute concentrations of non-phosphate were comparable between the two different slurry concentrations, however, so this discrepancy in non-phosphate P recovery may be attributed to solubility limitations and also possibly equilibria between phosphate and other soluble phosphorus forms such as polyphosphate. Ekpo et al. [35] proposed that phospholipids in the aqueous phase could be

the reason, however they are unlikely to remain unhydrolyzed at those conditions.

### 5.3.3.2 Slurry concentration

At moderate reaction severity (200 to 300 °C), decreased slurry concentration (30 g  $L_{\text{rxn}}^{-1}$ ) led to on average 10.2 % higher ( $p < 10^{-7}$ )  $\text{PO}_4^{3-}$ -P recovery and 10.3 % higher ( $p < 10^{-6}$ ) total P recovery, but no difference in non-phosphate P recovery. This effect was significant enough to increase  $\text{PO}_4^{3-}$ -P recovery to >95 % for Chl-2 in two separate instances (Figure 5.3a). This trend was previously shown to hold for even higher ranges of slurry concentrations (126 to 422 g  $L_{\text{rxn}}^{-1}$ ) [32]. One explanation is that algal slurries in the range of 30 to 120 g  $L_{\text{rxn}}^{-1}$  may produce ACP that quickly saturates with  $\text{PO}_4^{3-}$ , which would allow a greater proportion of the  $\text{PO}_4^{3-}$  from the 30 g  $L_{\text{rxn}}^{-1}$  slurry to dissolve, thus increasing its recovery. If solubility is the limiting factor, pH would be the dominant factor controlling  $\text{PO}_4^{3-}$ -P recovery. Given that hydrolysis is the mechanism by which  $\text{PO}_4^{3-}$  is liberated from the phospholipids, DNA, and RNA (the three main phosphate-containing compounds in microalgae [108]), it is also possible that the 30 g  $L_{\text{rxn}}^{-1}$  slurries experience improved rates of hydrolysis compared to those of the 120 g  $L_{\text{rxn}}^{-1}$  slurries through the same mechanism we suggested in Section 5.3.1 for aqueous yields. Notably, at 350 °C and 100 min,  $\text{PO}_4^{3-}$  and total P recovery are higher for the 120 g  $L_{\text{rxn}}^{-1}$  slurries than those of the 30 g  $L_{\text{rxn}}^{-1}$  slurries. Slurries of both concentrations experience decreasing P recovery with increasing reaction time at 350 °C, but it appears that the 30 g  $L_{\text{rxn}}^{-1}$  slurries precipitate P in the solids faster than the 120 g  $L_{\text{rxn}}^{-1}$  slurries, again possibly due to differences in pH.

### 5.3.3.3 Biochemical composition

$\text{PO}_4^{3-}$ -P and total P recoveries generally decreased with increasing ash content (Figures H.4b and d in Appendix H) and generally increased with increasing lipid content (color-coded in Figure 5.3a and c; explicitly in Figure H.4a and c). The concentration of metal cations in solution (originating from the ash fraction), is known to affect phosphate recovery due

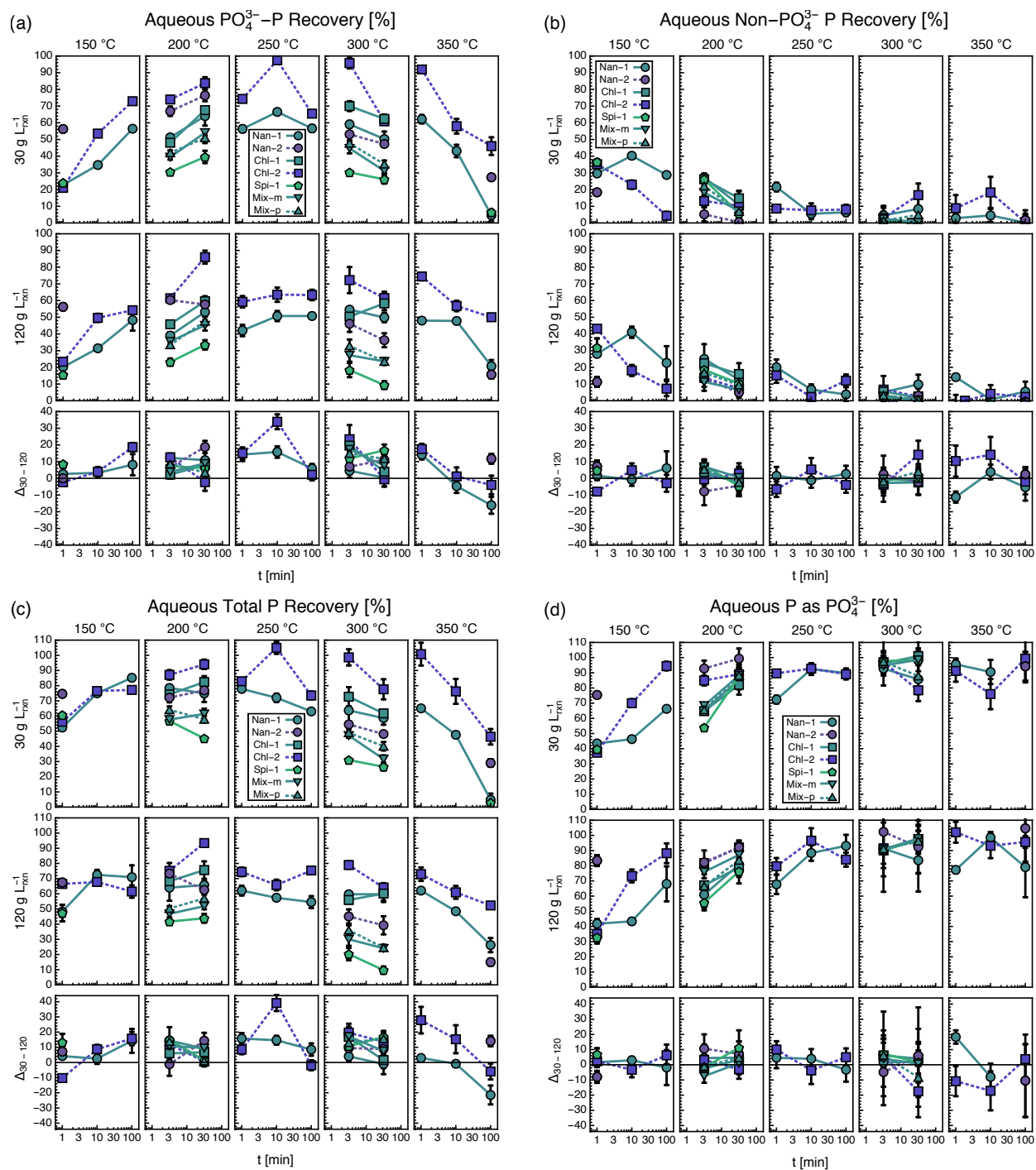


Figure 5.3: Aqueous-phase-product phosphorus recovery (a) as phosphate ( $\text{PO}_4^{3-} - \text{P}$ ), (b) as non-phosphate, (c) in total, and (d) phosphate relative to total aqueous phosphorus versus reaction time grouped by temperature and initial concentration. See Table 4.1 for microalgae types. The bottom row depicts the first row ( $30 \text{ g L}_{\text{rxn}}^{-1}$ ) minus the second row ( $120 \text{ g L}_{\text{rxn}}^{-1}$ ). Error bars indicate SE.

to precipitation into the solid phase [128]. The data reported herein support this notion, especially at 300 °C. Between the two types of *Chlorella*, the higher-lipid sample (Chl-2) demonstrated 21.9 % higher  $\text{PO}_4^{3-}$ -P recovery ( $p < 0.001$ ) at 300 °C, 3.2 min and milder severities compared to Chl-1. Non-phosphate recovery showed the opposite effect (Figure 5.3b), decreasing with increasing lipid content by on average 20.7 % ( $p < 0.0001$ ) at 200 °C and lower severities, for both types of *Nannochloropsis* and *Chlorella*.

### 5.3.3.4 Species identity and two-species mixture interactions

Variability in  $\text{PO}_4^{3-}$ -P recovery due to species identity was on average  $\pm 6.4$  % and  $\pm 15.3$  % at 200 and 300 °C, respectively. Although the proximate biochemical compositions of Nan-1, Chl-1, and Mix-m were similar, their P contents were relatively different (Table D.3; 0.94, 1.03, and 1.21 wt %, respectively). Additional information, such as phospholipid and/or DNA content, may be necessary to correlate  $\text{PO}_4^{3-}$ -P recovery with greater precision. There was no significant difference between the measured (Mix-m) and predicted (Mix-p) P recoveries for the two-species mixture. This suggests that there are likely no significant interactions between degradation products of the composite Chl-2 and Spi-1 affecting P recovery in the aqueous phase.

## 5.3.4 Sulfur recovery

### 5.3.4.1 Temperature and time

S recovery in the aqueous phase ranged from 7.7 to 75.5 %, shown in Figure 5.4. It generally increased with increasing reaction severity to a maximum between 200 °C, 31.6 min and 250 °C, 10 min. At 250 °C, this maximum occurred at 1 min for Chl-2, but at 10 min for Nan-1, the same conditions maximizing aqueous yield and organic N recovery for those respective biomass types. Beyond this maximum, S recovery generally decreased with increasing reaction severity, as has been reported previously [27]. In contrast, Jiang and Savage [37] did not observe a monotonic decrease in aqueous S recovery at 350 °C with

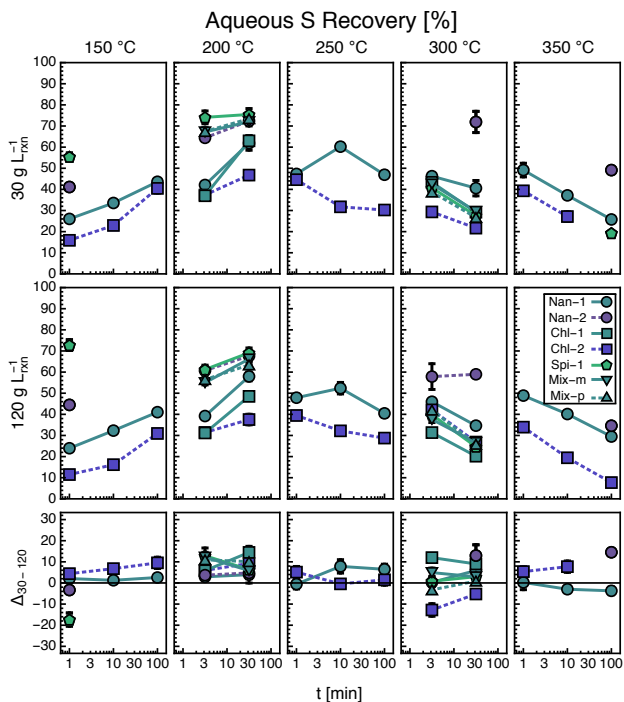


Figure 5.4: Aqueous-phase-product sulfur recovery versus reaction time grouped by temperature and initial concentration. See Table 4.1 for microalgae types. The bottom row depicts the first row ( $30 \text{ g L}_{\text{rxn}}^{-1}$ ) minus the second row ( $120 \text{ g L}_{\text{rxn}}^{-1}$ ). Error bars indicate SE.

increasing time for a  $101 \text{ g L}_{\text{rxn}}^{-1}$  slurry of *Nannochloropsis*; instead it decreased from an initial maximum and varied by only  $\pm 3 \%$  from 2 to 60 min reaction time. Crucially, they did not analyze the elemental content of the dried aqueous phase, but rather of the undried aqueous phase via inductively coupled plasma optical emission spectrometry (ICP-OES). This suggests that volatile forms of S, for example hydrogen sulfide or methanethiol, could be formed at these conditions and would be lost during the drying of the aqueous phase at  $70 \text{ }^\circ\text{C}$ .

### 5.3.4.2 Slurry concentration

At reaction conditions preceding the maximum aqueous S recovery, decreasing slurry concentration led to an average of  $5.4 \%$  higher S recovery ( $p < 10^{-5}$ ). Beyond that point, there was no universal trend with respect to changing concentration, however certain biomass types showed large, but statistically insignificant differences with decreasing slurry concen-

tration, such as Chl-1 (+10.5 %,  $p < 0.09$ ) and Chl-2 (−9.0 %,  $p < 0.26$ ) at 300 °C. At 350 °C, 30 min for a strain of *Nannochloropsis*, Jiang and Savage [37] observed a decrease in aqueous S recovery of 8 % from 30 to 64 g L<sub>rxn</sub><sup>−1</sup>, but no change from 64 to 101 g L<sub>rxn</sub><sup>−1</sup>, which is comparable in magnitude to the differences reported herein at similar reaction severities.

#### 5.3.4.3 Biochemical composition and species identity

There were no clear trends in aqueous S recovery with respect to changing biochemical composition. Additionally, the three biomass types with comparable biochemical composition demonstrated high variability in aqueous S recovery at both 200 °C ( $\pm 10.7$  %) and 300 °C ( $\pm 5.7$  %) López Barreiro et al. [28] presented similar variability ( $\pm 6.9$  %) from 300 to 350 °C. Moreover, there were no clear trends with respect to changing biomass S content (Figure H.5). The reason for the variability could therefore lie with sulfates precipitating in the solids phase as a function of aqueous pH and cation availability. Additionally, further study of the behavior of S-containing compounds in microalgae, such as the amino acids methionine and cysteine [129], as well as some lipids [108] could be useful for understanding S partitioning.

#### 5.3.4.4 Two-species mixture interactions

Similar to aqueous P recoveries, the measured and predicted two-species mixture aqueous S recoveries were in agreement at both 200 and 300 °C. These data provide no evidence of any reactions between the protein-degradation products (some of which contain S) of Spi-1 and the carbohydrate-degradation products of Chl-2.

### 5.3.5 Carbon recovery

#### 5.3.5.1 Temperature and time

Aqueous C recovery ranged from 1.3 to 60.8 % (Figure 5.5a). Trends with changing reaction severity were similar to those of S recovery. C recovery increased with increasing

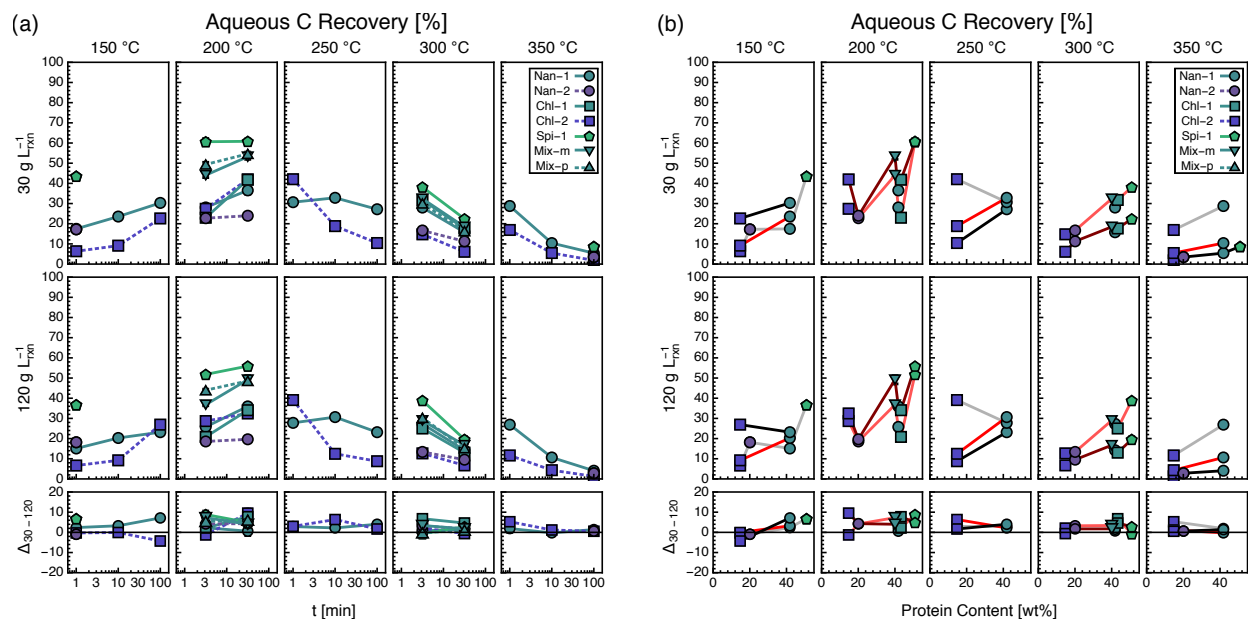


Figure 5.5: Aqueous-phase-product carbon recovery (a) versus reaction time and (b) versus protein content grouped by temperature and initial concentration. Gray, pink, red, dark red, and black lines represent 1.0, 3.2, 10.0, 31.6, and 100.0 min reaction time, respectively. See Table 4.1 for microalgae types. The bottom row depicts the first row ( $30 \text{ g L}_{\text{rxn}}^{-1}$ ) minus the second row ( $120 \text{ g L}_{\text{rxn}}^{-1}$ ). Error bars indicate SE.

temperature and time, reaching a maximum at moderate reaction severity (200 °C, 31.6 min to 250 °C, 10 min) before decreasing with further increases in severity. Both the initial increases [30] and subsequent decreases [24, 27, 28, 32, 35] in aqueous C recovery are consistent with prior studies. We note that Garcia-Moscoso et al. [26] demonstrated that with just 9 s of residence time, aqueous total organic carbon generally increases with increasing temperature from 205 to 325 °C, so it is likely that at temperatures above 250 °C, the maximum is achieved on the order of seconds rather than minutes.

### 5.3.5.2 Slurry concentration

The ACP of the  $30 \text{ g L}_{\text{rxn}}^{-1}$  slurries recovered on average 2.9 % more C ( $p < 10^{-6}$ ) than the  $120 \text{ g L}_{\text{rxn}}^{-1}$  slurries at HTL temperatures of 200 °C and higher. This effect was more pronounced at lower temperature (e.g., 200 °C, +4.5 %,  $p < 0.001$ ) than at higher temperature (e.g., 300 °C, +2.3 %,  $p < 0.01$ ). Other studies have shown this trend over both relatively dilute (7 to  $70 \text{ g L}_{\text{rxn}}^{-1}$ ) [38] and concentrated ranges (126 to  $422 \text{ g L}_{\text{rxn}}^{-1}$ ) [32], respectively.

Jazrawi et al. [38] posed that equilibrium limitations, particularly carbon solubility in the aqueous phase, could be a factor. Given that organic N recovery (Figure 5.2b) and S recovery (Figure 5.4) are also higher for the 30 g L<sub>rxn</sub><sup>-1</sup> slurries, we suspect that this increased C recovery is due to higher concentrations of peptides and amino acids liberated from the protein fraction via hydrolysis.

### 5.3.5.3 Biochemical composition

At 250 °C and lower, higher protein content resulted in generally higher aqueous C recovery, however with a significant amount of variability (Figure 5.5b). However, at 300 °C, there was a strong, positive correlation between C recovery and biomass protein content. For example, the correlation coefficient,  $\rho$ , was 0.98 for the 30 g L<sub>rxn</sub><sup>-1</sup> slurries at 3.2 min ( $p < 10^{-4}$ ), similar to the data for 120 g L<sub>rxn</sub><sup>-1</sup> slurries and at 31.6 min. This correlation provides strong evidence that the protein fraction of the biomass is the primary source of C in the aqueous phase at temperatures of 300 °C and higher, corroborating similar results from previous studies at these conditions [15, 40, 41, 44, 45].

### 5.3.5.4 Species identity

Variability in aqueous C recovery between Nan-1 and Chl-1 was  $\pm 3.0$  % at 200 °C. At 300 °C, variability between Nan-1, Chl-1, and Mix-m was slightly lower at  $\pm 1.9$  % (we excluded Mix-m at 200 °C for the reasons discussed in Section 5.3.1). López Barreiro et al. [28] similarly found that C recovery variability due to species identity was  $\pm 2.4$  % from 300 to 350 °C. Collectively, these data demonstrate that biochemical composition predicts aqueous C recovery with reasonable precision.

### 5.3.5.5 Two-species mixture interactions

The two-species mixture measured and predicted aqueous C recoveries were generally in agreement. One exception was on average 6.2 % lower C recovery ( $p < 0.10$ ) at 200 °C, 3.2

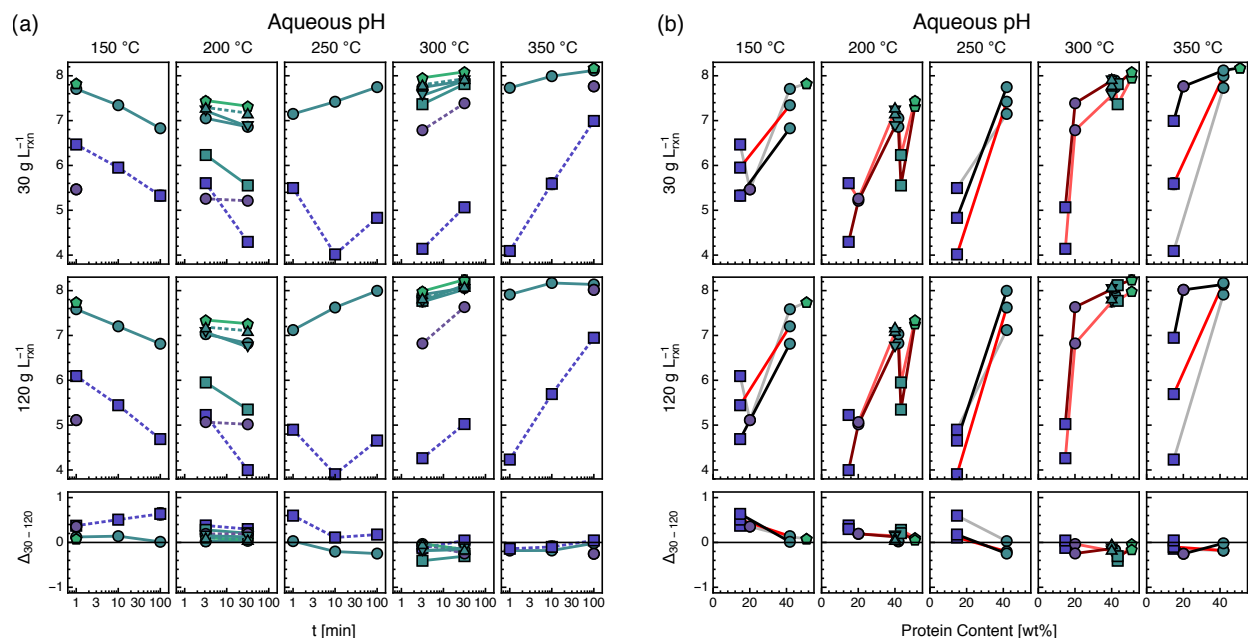


Figure 5.6: Aqueous phase pH (a) versus reaction time and (b) versus protein content grouped by temperature and initial concentration. Gray, pink, red, dark red, and black lines represent 1.0, 3.2, 10.0, 31.6, and 100.0 min reaction time, respectively. See Table 4.1 for microalgae types. The bottom row depicts the first row ( $30 \text{ g L}_{\text{rxn}}^{-1}$ ) minus the second row ( $120 \text{ g L}_{\text{rxn}}^{-1}$ ). Error bars indicate SE.

min. Given that total N recovery measured and predicted values were equivalent here, this suggests that the carbohydrate fraction may be the source of this discrepancy.

### 5.3.6 pH

Aqueous-phase pH (Figure 5.6) varied dramatically depending on biomass type and reaction conditions, ranging from 3.90 to 8.24. We note that this pH measurement occurred after the addition of deionized water during product recovery, which represents a 4.7x to 9.1x dilution factor, depending on reaction temperature and concentration.

#### 5.3.6.1 Temperature and time

Aqueous pH decreased (became more acidic) with increased reaction severity to a minimum in the range of 200 °C, 31.6 min to 250 °C, 10 min (Figure 5.6a). Garcia-Moscoso et al. [26] similarly observed this minimum to be at 240 °C, 9 s over a temperature range of 205 to 325 °C. Beyond this maximum acidity, the aqueous phase becomes monotonically more

basic with increasing reaction severity, a trend demonstrated previously [21, 26, 31, 35].

### 5.3.6.2 Slurry concentration

At reaction severities of 250 °C, 1 min and lower, the ACP was more basic for the 30 g L<sub>rxn</sub><sup>-1</sup> slurries than the 120 g L<sub>rxn</sub><sup>-1</sup> slurries by an average of 0.22 ( $p < 10^{-6}$ ). This could be explained by the increased NH<sub>4</sub><sup>+</sup>-N recovery (Section 5.3.2) at those conditions. At 300 °C and higher however, the trend reversed with the less concentrated slurries producing more acidic aqueous phase by an average of 0.52 ( $p < 0.01$ ). At these conditions, NH<sub>4</sub><sup>+</sup>-N is generally still favored with decreasing slurry concentration, and would push the pH in the opposite direction of this trend (toward more basic). This suggests that compounds other than the ammonium seem to be responsible for this pH trend. Previous studies have shown these increases in basicity with increasing slurry concentration at high reaction severity [21, 32].

### 5.3.6.3 Biochemical composition

In general, pH significantly increased (became more basic) with increasing biomass protein content (Figure 5.6b), a trend also observed previously [41, 44, 45, 130]. Between the two types of both *Nannochloropsis* and *Chlorella*, higher protein content led to an average increase of 2.91 ( $p < 0.01$ ) across all reaction conditions. The increased ammonia ( $K_b = 1.8 \times 10^{-5}$ ) generated from deamination of amino acids liberated from protein likely explains this sharp increase in pH.

### 5.3.6.4 Species identity

Nan-1 and Mix-m produced aqueous phases with nearly identical pH values regardless of concentration, temperature, or time, an average difference of just 0.03 ( $p < 0.47$ ). However, the pH for Chl-1 was on average 0.64 lower ( $p < 0.03$ ) than that of Nan-1 and Mix-m at 200 °C. It is not immediately clear why the Chl-1 aqueous phase was more acidic, given that

ammonium and phosphate recoveries were similar to at least one of the other two biomass types. However, at 300 °C, variability between the three species was just  $\pm 0.09$ , indicating that at high reaction severity, biochemical composition is a strong predictor of aqueous-phase pH.

### 5.3.6.5 Two-species mixture interactions

There was a small but significant decrease in pH ( $-0.16$ ,  $p < 0.01$ ) for Mix-m compared to Mix-p across all reaction conditions. This difference was largest ( $-0.33$ ,  $p < 0.07$ ) at 200 °C, 31.6 min. We demonstrated earlier (Section 5.3.2) that at 300 °C, there was less ammonium recovery than expected in the aqueous phase from Mix-m, which could explain why its pH is lower (more acidic) than expected. At 200 °C however, there was no such difference in ammonium recovery and there are no other trends concurrent with the increase in pH there.

### 5.3.7 Engineering nutrient recovery and recycling

In this section, we describe particular sets of reaction conditions and feedstock characteristics that tend to maximize aqueous phase recyclability, while also considering other factors such as the minimization of heteroatoms in the biocrude (discussed in Chapter IV). We remind the reader that, in general, the most optimal aqueous phase is one that maximizes recovery of key elements required for microalgal growth, such as N, P, and S [18, 19], while minimizing recovery of C. In addition, bioavailable forms of these elements, such as  $\text{NH}_4^+$  and  $\text{PO}_4^{3-}$ , are preferred to other forms, as they can be directly used during growth [3, 84]. Figure 5.7 demonstrates how these key elements partition into the different product fractions with respect to changing reaction conditions for the  $120 \text{ g L}_{\text{rxn}}^{-1}$  slurries of Nan-1 and Chl-2. We chose these two biomass types because we analyzed them over the most temperatures and times and the  $120 \text{ g L}_{\text{rxn}}^{-1}$  slurries provided sufficient mass for characterizing most product fractions. We note that not only are N, P, and S beneficial to the ACP for recycling, they are also undesirable in the biocrude, as they must be removed through catalytic upgrading

prior to traditional refining processes [16].

Figures 5.7a and b show that there is a trade-off between maximizing  $\text{NH}_4^+$ -N recovery (at 350 °C, 100 min), and limiting biocrude N recovery, for example to less than 5 % (around 200 °C, 31.6 min or 250 °C, 1 min).  $\text{PO}_4^{3-}$ -P recovery (Figures 5.7c and d) tends to be maximized at moderate reaction severity (e.g., 200 °C, 31.6 min or 300 °C, 3.2 min), although total P recovery in the ACP decreases with increasing reaction severity thereafter; at such high severities, P is either precipitated as a solid or incorporated into the biocrude phase. Aqueous S recovery (Figures 5.7e and f) is maximized at several moderately severe conditions; however, at 200 °C, 31.6 min, biocrude S recovery is additionally limited to less than 8 % and further increases to reaction severity dramatically increase S partitioning to the biocrude. Aqueous C recovery (Figures 5.7g and h) is maximized at moderate reaction severity and minimized at the highest reaction severity examined (350 °C, 100 min), whereas biocrude C recovery is maximized at 300 °C, and changes very little with increasing reaction severity.

In terms of maximizing aqueous phase recyclability while minimizing heteroatom incorporation into the biocrude, a reaction condition such as 200 °C and 31.6 min appears to achieve both. This condition generally maximizes aqueous  $\text{PO}_4^{3-}$ -P, total P, and S recoveries while limiting biocrude N and S recoveries to less than 5 and 8 %, respectively. This condition does, however, only recover 50 to 60 % of the N in the aqueous phase, with just 20 % of that in the bioavailable form of  $\text{NH}_4^+$ . In practice, if the aqueous phase at this reaction condition were recycled continuously, a steady-state amount of organic N in the aqueous phase would be achieved [131]. This steady-state amount will also depend on the extent that algae or heterotrophic bacteria can directly consume the organic C or use extracellular enzymes to liberate the amine groups; such a phenomenon occurs frequently in aquatic environments [132]. Further research and process modeling would be necessary to determine the approximate amount of organic N in this theoretical recycle loop [133]. It is possible that at steady-state, enough ammonium would be liberated to fully replenish the

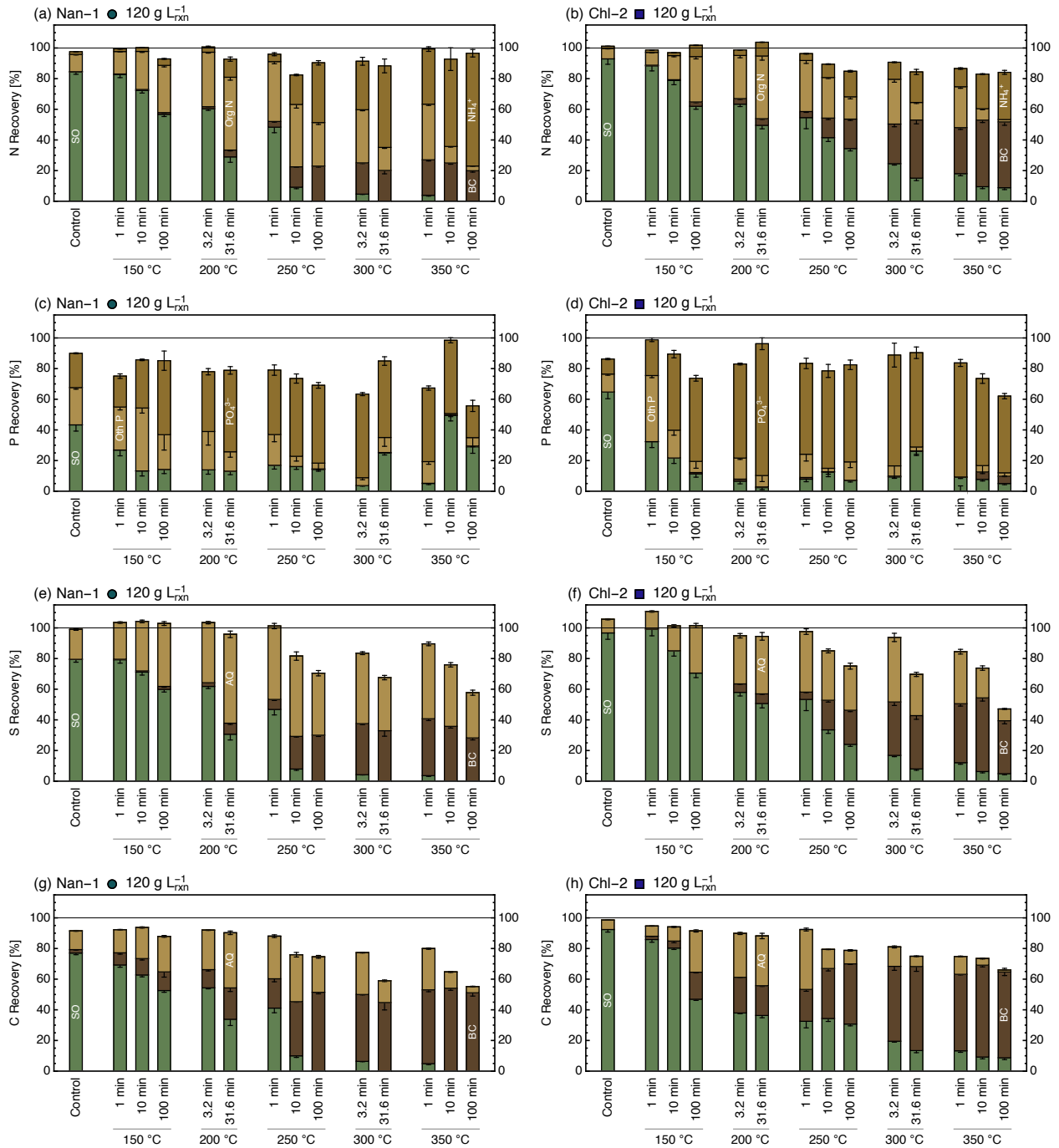


Figure 5.7: (a,b) Nitrogen, (c,d) phosphorus, (e,f) sulfur, and (g,h) carbon recoveries in the aqueous (AQ), biocrude (BC), and solid (SO) phases versus reaction severities. Control represents the same experimental procedure applied with no reaction time. Org N and Oth P represent organic nitrogen and other phosphorus, respectively. See Table 4.1 for microalgae types. Error bars indicate SE.

spent media for each cycle. The solids remaining at this condition could also be recycled or reacted at higher severity conditions; this latter scenario has been referred to as two-step HTL, and is a subject of ongoing research [30, 119, 134].

Another possibility is to operate HTL at very high reaction severity, such as 350 °C, 100 min or higher. This condition maximized ammonium recovery, and higher reaction severities approaching hydrothermal gasification are likely to liberate N from the biocrude (Section 4.3.4). P at these conditions has been demonstrated to form solid precipitates [27, 127], and could be a side product used as fertilizer for other applications. It is not immediately clear where the rest of the P partitions, however there are a few possibilities. The most plausible one is that the remaining P exists as a solid precipitate lost during the product recovery step. We believe that the majority of solids were recovered at these conditions, but because P content in the solid phase is high at high reaction severity (Figure F.7), small losses in solids result in relatively larger losses in P. Another possibility is that our method for total P measurement in the aqueous phase is not sensitive to certain forms of P. A final possibility is that some of the P is present in more volatile forms, such as phosphine, which could be lost in the gas phase. High-temperature water at those conditions can serve as a hydrogen source [11], for example for reduction of phosphate to phosphine. S recovery at high severity is similarly low, and it is possible that hydrogen sulfide or similarly volatile compounds are similarly unaccounted for there, as we suggested earlier in Section 5.3.4. Further research at higher reaction severities aimed at fully recovering and characterizing the more volatile components produced during HTL is necessary to compare the aqueous phase recyclability at these conditions.

## 5.4 Further discussion and conclusion

Table 5.1 summarizes how the yield, elemental recoveries, and pH of the ACP are affected by manipulating reaction time, slurry concentration, lipid content, protein content, microalgal species, and reaction temperature. These changes each occur with all other factors fixed

Ref. Point	Independent Variable	Change	Sensitivity Scale	Yield [wt%]	Recovery [%]								pH
					NH <sub>4</sub> <sup>+</sup> -N	ON	TN	PO <sub>4</sub> <sup>3-</sup> -P	OP	TP	S	C	
200 °C 3.2 min 30 g L <sub>rxn</sub> <sup>-1</sup>	Temperature:	200 → 300 °C	██████	-10	23*	-7	16*	7	-17*	-10	-11	-7	0.5
	Species:	Nan-1, Chl-1, Mix-m	██████	11	1	15	15	6	5	11	16	11	0.5
	Time:	3.2 → 31.6 min	██████	9*	10*	8	18*	13*	-11*	1	12*	9*	-0.4
	Lipid Content:	10.5 → 24.2 wt%	██████	1	3*	3	6	21	-18	3	11	0	-1.2
	Protein Content:	17.4 → 42.6 wt%	██████	-1	-3*	-3	-6	-21	18	-3	-11	0	1.2
	Concentration:	30 → 120 g L <sub>rxn</sub> <sup>-1</sup>	██████	-4	0	-6	-7	-8	-2	-10	-7	-4	-0.2
300 °C 3.2 min 30 g L <sub>rxn</sub> <sup>-1</sup>	Lipid Content:	10.5 → 24.2 wt%	██████	-14	-7	-7	-14	10	-2	8	-14	-14	-2.1
	Protein Content:	17.4 → 42.6 wt%	██████	14	7	7	14	-10	2	-8	14	14	2.1
	Time:	3.2 → 31.6 min	██████	-13*	18*	-20*	-2	-12*	2	-11*	-11	-12*	0.4*
	Concentration:	30 → 120 g L <sub>rxn</sub> <sup>-1</sup>	██████	-4*	-5*	-4	-9*	-14*	1	-13*	-1	-3	0.2*
	Species:	Nan-1, Chl-1, Mix-m	██████	1	3	1	2	13	1	13	2	2	0.2

Table 5.1: Summary of differences in ACP properties as a result of changing six different independent variables from two different reference points. Sensitivity Scale qualitatively denotes the sensitivity of aqueous phase properties to each independent variable at a given reference point. ON, TN, OP, and TP represent organic nitrogen, total nitrogen, other phosphorus, and total phosphorus recoveries, respectively. Yellow and blue intensity denote increases and decreases in the associated property, respectively. Changes in temperature, time, and concentration are the average of the differences in the six different types of biomass (see Table 4.1). Changes in biochemical composition show the average of differences in the two different types of *Nannochloropsis* and *Chlorella*, respectively. Changes in species denote the standard deviation of values from Nan-1, Chl-1, and Mix-m. \*Denotes statistically significant difference at the 0.05 level.

from two reference points at 200 and 300 °C, respectively, for 30 g L<sub>rxn</sub><sup>-1</sup> slurries and 3.2 min reaction time.

#### 5.4.1 Mild-reaction-severity reference point

At the 200 °C, 3.2 min, and 30 g L<sub>rxn</sub><sup>-1</sup> reference point, temperature is the most influential input variable affecting ACP properties. An increase of 100 °C led to significantly higher NH<sub>4</sub><sup>+</sup>-N (+23 %) and total N (+16 %) recoveries in addition to 7 % higher PO<sub>4</sub><sup>3-</sup>-P recovery and 7 % lower C recovery, all of which are improvements in recyclability. However, at the same time, total P and S recoveries decreased by 10 and 11 %, respectively. Reaction time was nearly as broadly significant as temperature and species identity at this mild reference point, although crucially, increased time led to nearly universal improvements in aqueous phase recyclability. The recoveries of NH<sub>4</sub><sup>+</sup>-N (+10 %), organic N (+8 %), P-PO<sub>4</sub><sup>3-</sup> (+13 %), and S (+12 %) all increased with increasing time, albeit with a 9 % increase in C recovery. Increased biomass lipid content only affected PO<sub>4</sub><sup>3-</sup>-P recovery

(+21 %), S recovery (+11 %), and pH (−1.2) to a significant extent at this reference point, although it did also provide a small (+3 %) but statistically significant boost to  $\text{NH}_4^+$ -N recovery. Notably, higher lipid content improved ACP recyclability unilaterally, albeit to a slightly lesser extent than did reaction time, but also without increasing C recovery. We previously showed that at this reference point, increased lipid content also increases C and H recovery to the biocrude by 21 % (Section 4.4). HTL of high-lipid microalgae at this reference point is a “win-win,” improving nutrient partitioning to the aqueous phase while also increasing yield of high-quality biocrude.

Slurry concentration was less influential than the aforementioned independent variables at this reference point; however, increased concentration led to universal decreases in nutrient recovery to the aqueous phase, likely through promotion of Maillard reactions between protein- and carbohydrate-degradation products discussed in Section 5.3.2. Variability due to species identity was generally the least influential variable, although aqueous yields and organic N recoveries varied by  $\pm 7$  wt% and  $\pm 6$  %, respectively. We assumed that all biomass N resided in the protein fraction, although it is possible that these differences in aqueous yield and organic N recovery could be explained by the true distribution of N between biomass protein and DNA in each of the microalgae. The incorporation of N on a molecular level is generally different in protein and DNA, for example within an amino-acid-linking peptide bond for the former and within a cyclic or polycyclic nitrogenous base structure for the latter. Therefore the total rate of liberation of the N into the aqueous phase could be expected to be different based on the relative abundances of those two biochemical classes. A more granular accounting of biochemical composition may be required to reduce this variability between microalgae that are expected to behave similarly during HTL on these grounds.

### 5.4.2 High-reaction-severity reference point

At the 300 °C, 3.2 min, and 30 g L<sub>rxn</sub><sup>-1</sup> reference point, biochemical composition is the most influential variable, with approximately as much influence as that of temperature from 200 to 300 °C. Increased protein content improved some key recyclability metrics, such as NH<sub>4</sub><sup>+</sup>-N (+7 %), total N (+14 %), and S (+14 %) recoveries; however, it also decreased PO<sub>4</sub><sup>3-</sup>-P (-10 %) and total P (-8 %) recoveries and increased C recovery (+14 %). Increasing lipid content (necessarily) demonstrated the opposite effect.

Aqueous phase characteristics and elemental recoveries were nearly as sensitive to increasing reaction time as biochemical composition. Increasing time at this reference point had mixed effects on aqueous phase recyclability, with decreases to PO<sub>4</sub><sup>3-</sup>-P (-12 %), total P (-11 %), and S (-11 %) recoveries, but increases to NH<sub>4</sub><sup>+</sup>-N recovery (18 %) and decreases to C recovery (-12 %). Notably, reaction time, lipid content, and protein content all demonstrated different combinations of effects on N, P and S recoveries. These different combinations could enable optimization of specific nutrient recycling metrics at the expense of others. For example, if N recovery were prioritized, followed by P and S, then high lipid content and longer reaction times could be used together to improve NH<sub>4</sub><sup>+</sup>-N recovery (net +11 %) and maintain PO<sub>4</sub><sup>3-</sup>-P recovery (net -2 %) at the expense of S recovery (net -25 %).

Increased slurry concentration led to widespread reductions in aqueous-phase-recyclability metrics which were comparable in magnitude to those at the previous reference point. At the high-reaction-severity reference point, species identity did not affect ACP properties or elemental recovery, with the lone exception of PO<sub>4</sub><sup>3-</sup>-P recovery ( $\pm 13$  %), and as a result total P recovery, indicating that proximate biochemical composition is a reasonable predictor of ACP properties around this reference point.

### 5.4.3 Additional conclusions

In addition to the aforementioned effects, there were several other key takeaways from this chapter. The tendency for higher protein-to-carbohydrate biomass to produce ACP with higher  $\text{NH}_4^+ - \text{N}$  recovery corroborated the claim in Chapter IV that carbohydrates are the limiting reactant for Maillard reactions. More dilute slurries also tended to recover more N as  $\text{NH}_4^+$  (plausibly due to less Maillard reaction products formed), suggesting that the overall reaction order for the Maillard reaction is greater than one. We illuminated additional benefits of employing dilute slurries of high-lipid biomass for HTL, including enhanced ACP recyclability. These results demonstrate that high-lipid and low-carbohydrate biomass could be ideal for maximizing ACP recyclability in addition to maximizing biocrude yield and quality, as discussed in Chapter IV.

## CHAPTER VI

# A gravimetric, elemental, and multiphase kinetic model for the hydrothermal liquefaction of microalgae

In this chapter, we leverage the vast experimental dataset presented in Chapters IV and V to build a novel gravimetric, elemental, and multiphase kinetic model for microalgal HTL. Specifically, we proposed a reaction network comprising 16 reaction pathways based on known classes of reactions that occur during HTL, including hydrolysis, repolymerization, cyclodehydration, retro-aldol condensation, Maillard reactions, deamination, and decarboxylation. We utilize these pathways with 22 unique lumped-product components to construct a system of coupled, first-order ODEs governing the rate of evolution of each total, carbon, and nitrogen yield. We evaluate the accuracy of model solutions over the entire range of experimental conditions, including over specific subsets therein, highlighting their relative strengths and areas to expand upon for future iterations. The model describes many empirical trends from Chapters IV and V, including the effects of slurry concentration and Maillard reactions, which until now were never modeled for this system. The model captures the biocrude and ammonia quantities most accurately, substantiating the utility of the model for optimizing important HTL process metrics, such as biocrude C recovery and aqueous ammonia recovery, that could help enhance overall process sustainability and EROI.

## 6.1 Introduction

Herein we use the results presented in Chapters IV and V to develop a comprehensive kinetic model capable of quantifying yields and elemental contents for a variety of HTL products. We propose a reaction network that merges the complexity of molecular reaction pathways that were previously documented from model compound reactions with the tractability afforded by lumped products. These pathways enable proximate biochemical components, including lipids, proteins, and carbohydrates, to degrade into their respective secondary products, such as fatty acids, peptides, and smaller polysaccharides. These products can then further degrade into tertiary products, including amino acids and saccharides, that also degrade into ammonia and gases, as well as additional ACP and biocrude compounds. The objective is to produce a sophisticated microalgal HTL kinetic model that enables optimization of key process metrics, such as biocrude C recovery and aqueous ammonium recovery, with respect to reaction temperature, time, slurry concentration, and microalgal biochemical composition. Such a model would significantly advance the state of quantitative kinetic modeling for HTL, ultimately facilitating improvement of algal biorefining sustainability and EROI.

## 6.2 Methods and model development

### 6.2.1 Reaction network development

The kinetic model calculates the temporal evolution of 40 unique quantities, including 22 total yields, 6 carbon yields, 6 nitrogen yields, and 6 average molar masses. The carbon contents, nitrogen contents, and molar masses of the other 16 components are assumed to be constant, obviating the need to calculate their rates of change explicitly. The following sections introduce those components and their reaction pathways, with summaries of them appearing in Tables 6.1 and 6.2. We note that each pathway and associated rate equations are modeled on a per-mole-reaction basis; however, all components are calculated in units

of  $\text{g L}_{\text{rxn}}^{-1}$ , or grams of component per liter at reaction conditions. We use square brackets,  $[\ ]$ , to denote this  $\text{g L}_{\text{rxn}}^{-1}$  basis. This conversion is possible only through incorporation of the average molar mass of each component and is discussed further below. We describe the contribution of each pathway toward the total rate of change of each component, which is calculated as the sum of the contributing pathways.

### 6.2.1.1 Hydrolysis and repolymerization

Hydrolysis is the first major reaction pathway involved during microalgal HTL and is the primary means by which the large biomacromolecules degrade into smaller polymers and monomers [12]. This class of reaction affects all three major biochemical classes, including lipids, proteins, and carbohydrates. We describe each hydrolysis pathway and associated equations, starting with lipids.

**Pathway 1: Lipid (LIP) hydrolysis to fatty acid (FA)** We model the hydrolysis of LIP to FA using the following reaction pathway:



Assuming a constant-volume, well-mixed, closed system, and that this pathway follows pseudo-first-order kinetics, we model the rate of reaction due to Pathway 1,  $r_1$  ( $\text{g L}_{\text{rxn}}^{-1} \text{ s}^{-1}$ ), as follows:

$$r_1 = k_1[\text{LIP}] \quad (6.2)$$

Here  $k_1$  ( $\text{s}^{-1}$ ) is the temperature-dependent rate constant for Pathway 1. Given that we define this rate on a mass-per-volume-per-time basis, we introduce a mass-conversion factor,  $f_1$ , which represents the mass fraction of the total rate,  $r_1$ , attributed to the rate of consumption of LIP. Similarly,  $(1 - f_1)$  represents the mass fraction of  $r_1$  attributed to the rate of consumption of  $\text{H}_2\text{O}$ . Given that FA is the only product formed via this pathway, its rate of formation is equal to  $r_1$ , with no mass-conversion factor needed. We can then write the rates of change for LIP,  $\text{H}_2\text{O}$ , and FA with respect to Pathway 1 (denoted using  $|_1$ ) using

the following equations:

$$\left. \frac{d[\text{LIP}]}{dt} \right|_1 = -f_1 k_1 [\text{LIP}] \quad (6.3)$$

$$\left. \frac{d[\text{H}_2\text{O}]}{dt} \right|_1 = -(1 - f_1) k_1 [\text{LIP}] \quad (6.4)$$

$$\left. \frac{d[\text{FA}]}{dt} \right|_1 = k_1 [\text{LIP}] \quad (6.5)$$

To calculate  $f_1$ , we introduce the average molar mass of lipids,  $M_{\text{LIP}}$ . For the purposes of this model, we treat  $M_{\text{LIP}}$  as the average unhydrolyzed molar mass of a fatty acid, rather than as the molar mass of an entire lipid compound, such as a phospholipid. For the lipid profiles of the six biomass types presented in Table 4.1, this average molar mass was  $269.3 \pm 2.1 \text{ g mol}^{-1}$  (SD). Constants such as this one are listed in Table I.1 in Appendix I. We assume this value to be representative for the purposes of allocating mass within the kinetic model and use it as a fixed constant henceforth. Using  $M_{\text{LIP}}$  with  $M_{\text{H}_2\text{O}}$  and employing an implicit per-mole-reaction basis, we can calculate  $f_1$  as follows:

$$f_1 = \frac{M_{\text{LIP}}}{M_{\text{LIP}} + M_{\text{H}_2\text{O}}} \quad (6.6)$$

**Pathways 2 and 3: Protein (PRO) and polypeptide (PPE) hydrolysis to peptide (PEP) and PEP repolymerization to PPE** We model the hydrolysis of PRO to PEP similar to that of LIP; however, we allow PEP to repolymerize to insoluble polypeptides (PPE), based on empirical results from a recent study [54]. We then enable PPE to subsequently hydrolyze according to the same reaction kinetics as PRO. These reactions can be modeled according to the following reaction pathways:



The associated equations for Pathway 2 are similar to those of Pathway 1, assuming that PRO and PPE hydrolyze additively:

$$\left. \frac{d[\text{PRO}]}{dt} \right|_2 = -f_2 k_2 [\text{PRO}] \quad (6.9)$$

$$\left. \frac{d[\text{PPE}]}{dt} \right|_2 = -f_2 k_2 [\text{PPE}] \quad (6.10)$$

$$\left. \frac{d[\text{H}_2\text{O}]}{dt} \right|_2 = -(1 - f_2) k_2 ([\text{PRO}] + [\text{PPE}]) \quad (6.11)$$

$$\left. \frac{d[\text{PEP}]}{dt} \right|_2 = k_2 ([\text{PRO}] + [\text{PPE}]) \quad (6.12)$$

$$f_2 = \frac{M_{\text{PEP}} - M_{\text{H}_2\text{O}}}{M_{\text{PEP}}} \quad (6.13)$$

Here, we again assume a representative average molar mass of a peptide,  $M_{\text{PEP}}$ , to be that of a typical dipeptide (two amino acids linked by a peptide bond) in microalgae based on an average of reported amino acid profiles [110, 129, 135]. We model this component as a dipeptide to allow it to undergo cyclodehydration, presented later in Section 6.2.1.3. We found that PEP repolymerization to PPE followed first-order kinetics, which can be described by the following sets of equations that use the same mass conversion factor,  $f_2$ , as the last pathway:

$$\left. \frac{d[\text{PEP}]}{dt} \right|_3 = -k_3 [\text{PEP}] \quad (6.14)$$

$$\left. \frac{d[\text{PPE}]}{dt} \right|_3 = f_2 k_3 [\text{PEP}] \quad (6.15)$$

$$\left. \frac{d[\text{H}_2\text{O}]}{dt} \right|_3 = (1 - f_2) k_3 [\text{PEP}] \quad (6.16)$$

**Pathway 4: Peptide (PEP) hydrolysis to amino acid (AA)** PEP can continue to hydrolyze into AA:



These amino acids feature at least one amine group and one carboxyl group, which can

be subsequently liberated through deamination and decarboxylation reactions presented in Sections 6.2.1.6 and 6.2.1.7. However, some of the amino acids in microalgae feature more than one amine or carboxyl group. To account for these functional groups, we introduce a new notation for amino acids,  $AA_i$ , where  $i$  indicates the number of amine groups in the amino acid. We have grouped the various microalgal amino acids into two subclasses, including  $AA_1$  and  $AA_2$ , and a summary of the types of amino acids in those classes can be found in Table I.3. The hydrolysis of peptides can then be modeled according to the following equations:

$$\left. \frac{d[\text{PEP}]}{dt} \right|_4 = -f_4 k_4 [\text{PEP}] \quad (6.18)$$

$$\left. \frac{d[\text{H}_2\text{O}]}{dt} \right|_4 = -(1 - f_4) k_4 [\text{PEP}] \quad (6.19)$$

$$\left. \frac{d[AA_i]}{dt} \right|_4 = w_{AA_i} k_4 [\text{PEP}] \quad (6.20)$$

$$f_4 = \frac{M_{\text{PEP}}}{M_{\text{PEP}} + M_{\text{H}_2\text{O}}} \quad (6.21)$$

Here  $w_{AA_i}$  is the weight fraction abundance of each subclass of amino acid in microalgae, a constant calculated based on an average of reported amino acid profiles [110, 129, 135]. Values for these abundances are listed in Table I.2 in Appendix I.

**Pathways 5, 6, and 7: Carbohydrate (CAR) and biochar (BCH) hydrolysis to polysaccharide (PSA), PSA repolymerization to BCH, and PSA hydrolysis to saccharide (SAC)** The pathways for the degradation of carbohydrates (CAR) and assumptions therein are analogous to those of PRO. In summary, carbohydrates (CAR) hydrolyze into PSAs, which can repolymerize to insoluble BCH via a second-order reaction rate or further hydrolyze into SAC. The BCH is also capable of hydrolyzing back to PSA via the same rate constant governing CAR hydrolysis. The following equations describe those reaction pathways:

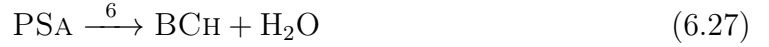


$$\left. \frac{d[\text{CAR}]}{dt} \right|_5 = -k_5[\text{CAR}] \quad (6.23)$$

$$\left. \frac{d[\text{BCH}]}{dt} \right|_5 = -k_5[\text{BCH}] \quad (6.24)$$

$$\left. \frac{d[\text{PSA}]}{dt} \right|_5 = k_5([\text{CAR}] + [\text{BCH}]) \quad (6.25)$$

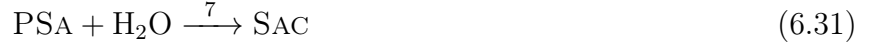
$$(6.26)$$



$$\left. \frac{d[\text{PSA}]}{dt} \right|_6 = -k_6[\text{PSA}]^2 \quad (6.28)$$

$$\left. \frac{d[\text{BCH}]}{dt} \right|_6 = k_6[\text{PSA}]^2 \quad (6.29)$$

$$(6.30)$$



$$\left. \frac{d[\text{PSA}]}{dt} \right|_7 = -f_7 k_7 [\text{PSA}] \quad (6.32)$$

$$\left. \frac{d[\text{H}_2\text{O}]}{dt} \right|_7 = -(1 - f_7) k_7 [\text{PSA}] \quad (6.33)$$

$$\left. \frac{d[\text{SAC}]}{dt} \right|_7 = k_7 [\text{PSA}] \quad (6.34)$$

$$f_7 = \frac{M_{\text{SAC}} - M_{\text{H}_2\text{O}}}{M_{\text{SAC}}} \quad (6.35)$$

We note that, although water participates in Pathways 5 and 6, we do not involve it in those calculations to avoid making assumptions about their average molar masses that would govern the rates of mass of water consumed. Instead, we account for the consumption of water in Pathway 7, so that, overall, water loss remains accounted for as each monomer saccharide is liberated from the polysaccharides.

### 6.2.1.2 Dissolution

**Pathway 8: Ash (ASH) dissolution to dissolved ash (DAs)** Previous kinetic models have assumed that the ash fraction of the microalgae resides primarily in the solid phase; however, at high reaction severity, the observed solid yields (Figure F.1) were often lower than the biomass ash content (Table 4.1). Therefore, we introduce a first-order pathway for the solid ash fraction to dissolve into the aqueous phase:

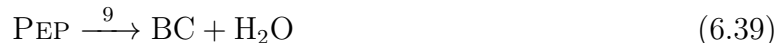


$$\left. \frac{d[\text{ASH}]}{dt} \right|_8 = -k_8[\text{ASH}] \quad (6.37)$$

$$\left. \frac{d[\text{DAs}]}{dt} \right|_8 = k_8[\text{ASH}] \quad (6.38)$$

### 6.2.1.3 Cyclodehydration

**Pathway 9: Peptide (PEP) cyclodehydration to biocrude (BC)** Recently, Sheehan and Savage [54] demonstrated that cyclodipeptides, a specific class of diketopiperazines, are a significant reaction product from the HTL of bovine serum albumin, a model compound for microalgal protein. In fact, these compounds represented over half of the GC-elutable components in the biocrude formed via HTL at 350 °C and 10 min. The formation of cyclodipeptides proceeds via the cyclodehydration of dipeptides [136–138]:



We assume that the abundance of each type of dipeptide,  $w_{\text{PEP}_i}$ , follows a random distribution of amino acid pairs, weighted by the abundances of amino acids,  $w_{\text{AA}_i}$ . We note that for  $w_{\text{PEP}_i}$ , the subscript  $i$  refers to the number of amine groups featured in the resulting cyclodipeptide. Values for these abundances are listed in Table I.2 in Appendix I. We model the cyclodipeptides from this pathway as general biocrude compounds that fall into each of the different biocrude subclasses,  $\text{BC}_i$ . These subclasses also use an  $i$  subscript to account

for amine groups able to be subsequently removed. With these quantities, we can readily write the rate equations governing Pathway 9:

$$\left. \frac{d[\text{PEP}]}{dt} \right|_9 = -k_9[\text{PEP}] \quad (6.40)$$

$$\left. \frac{d[\text{BC}_i]}{dt} \right|_9 = w_{\text{PEP}_i} f_2 k_9 [\text{PEP}] \quad (6.41)$$

$$\left. \frac{d[\text{H}_2\text{O}]}{dt} \right|_9 = (1 - f_2) k_9 [\text{PEP}] \quad (6.42)$$

Note that these use the same mass conversion factor,  $f_2$ , as the PEP hydrolysis pathway. We can also obtain the rates of partitioning of carbon and nitrogen into each biocrude subcomponent by multiplying the right-hand side of Equation (6.41) by the weight fraction of carbon ( $w_{\text{PEP}}^{\text{C}}$ ) and nitrogen ( $w_{\text{PEP}}^{\text{N}}$ ) in the average peptide, respectively:

$$\left. \frac{d[\text{BC}_i^{\text{C}}]}{dt} \right|_9 = w_{\text{PEP}}^{\text{C}} w_{\text{PEP}_i} k_9 [\text{PEP}] \quad (6.43)$$

$$\left. \frac{d[\text{BC}_i^{\text{N}}]}{dt} \right|_9 = w_{\text{PEP}}^{\text{N}} w_{\text{PEP}_i} k_9 [\text{PEP}] \quad (6.44)$$

$$(6.45)$$

Finally, given that each  $\text{BC}_i$  will contain a variety of types of compounds, it is necessary to introduce the average molar mass for each biocrude subclass,  $M_{\text{BC}_i}$ .  $M_{\text{BC}_i}$  changes as a function of the amount of new  $\text{BC}_i$  formed, relative to the amount of existing  $\text{BC}_i$  and the difference between the molar mass of the new components,  $M_{\text{PEP}} - M_{\text{H}_2\text{O}}$ , and that of the existing biocrude,  $M_{\text{BC}_i}$ :

$$\left. \frac{dM_{\text{BC}_i}}{dt} \right|_9 = \frac{(M_{\text{PEP}} - M_{\text{H}_2\text{O}} - M_{\text{BC}_i})}{[\text{BC}_i]} \left. \frac{d[\text{BC}_i]}{dt} \right|_9 \quad (6.46)$$

#### 6.2.1.4 Retro-aldol condensation

**Pathways 10 and 11: Saccharide (SAC) retro-aldol condensation to aqueous-phase products (AQ) and biocrude (BC)** There are several major pathways for saccharide

degradation in the hydrothermal environment, including retro-aldol condensation to aldehydes and ketones and dehydration to furans and their derivatives. Without more detailed information about the composition of the biocrude and aqueous phase, it is difficult to determine which pathway is more prevalent. We therefore chose retro-aldol condensation reactions as a basis for modeling the degradation of individual saccharides:



The products are grouped as either  $\text{AQ}_0$  or  $\text{BC}_0$  because many of these compounds are capable of subsequent decarboxylation and decarbonylation. Given that the majority of gas formed during HTL is  $\text{CO}_2$ , either directly or through the water-gas shift reaction, we model these subsequent reactions as decarboxylation. The following equations describe the rates of reaction, partitioning of carbon and nitrogen, and rate of change of the average molar masses of  $\text{AQ}_0$  and  $\text{BC}_0$ :

$$\left. \frac{d[\text{SAC}]}{dt} \right|_{10} = -k_{10}[\text{SAC}] \quad (6.49)$$

$$\left. \frac{d[\text{AQ}_0]}{dt} \right|_{10} = k_{10}[\text{SAC}] \quad (6.50)$$

$$\left. \frac{d[\text{AQ}_0^{\text{C}}]}{dt} \right|_{10} = w_{\text{SAC}}^{\text{C}} k_{10}[\text{SAC}] \quad (6.51)$$

$$\left. \frac{dM_{\text{AQ}_0}}{dt} \right|_{10} = \frac{(\frac{1}{2}M_{\text{SAC}} - M_{\text{AQ}_0})}{[\text{AQ}_0]} \left. \frac{d[\text{AQ}_0]}{dt} \right|_{10} \quad (6.52)$$

$$\left. \frac{d[\text{SAC}]}{dt} \right|_{11} = -k_{11}[\text{SAC}] \quad (6.53)$$

$$\left. \frac{d[\text{BC}_0]}{dt} \right|_{11} = k_{11}[\text{SAC}] \quad (6.54)$$

$$\left. \frac{d[\text{BC}_0^{\text{C}}]}{dt} \right|_{11} = w_{\text{SAC}}^{\text{C}} k_{11}[\text{SAC}] \quad (6.55)$$

$$\left. \frac{dM_{\text{BC}_0}}{dt} \right|_{11} = \frac{(\frac{1}{2}M_{\text{SAC}} - M_{\text{BC}_0})}{[\text{BC}_0]} \left. \frac{d[\text{BC}_0]}{dt} \right|_{11} \quad (6.56)$$

### 6.2.1.5 Maillard

**Pathway 12: Amino acid (AA) and saccharide (SAC) Maillard reaction to biocrude (BC)** The Maillard reaction between amino acids and reducing sugars is a major reaction pathway affecting the HTL product distribution, especially biocrude and aqueous yields, C recovery, and N recovery. There are a couple of linear regression models of biocrude yield that incorporate interaction pathways between proteins and carbohydrates [48, 139]; however, the coefficients for those terms were either negative (i.e., suggesting that they suppress biocrude formation) or insignificant (i.e., the uncertainty in the coefficient overlapped with zero). In Chapter IV, we showed that the Maillard reaction likely led to increased biocrude yield with increased C and N recovery, and in Chapter V we showed that these effects led to reduced  $\text{NH}_4^+ - \text{N}$  recovery in the aqueous phase. Moreover we observed that this effect was more pronounced for the higher concentration slurries. Therefore, we propose the following reaction pathway which is first order in both  $\text{AA}_i$  and SAC, for an overall second-order mechanism:



We assume that all Maillard reaction products are DCM-phase soluble (biocrude); however, in practice they could be aqueous-phase soluble depending on functional groups. This reaction is modeled such that one free amine group is “consumed” and unable to undergo subsequent deamination, which follows our experimental observations in Chapter V. This pathway is governed by the following sets of equations:

$$\left. \frac{d[AA_i]}{dt} \right|_{12} = -f_{12,i}k_{12}[AA_i][SAC] \quad (6.58)$$

$$\left. \frac{d[SAC]}{dt} \right|_{12} = -(1 - f_{12,i})k_{12}[AA_i][SAC] \quad (6.59)$$

$$\left. \frac{d[BC_{(i-1)}]}{dt} \right|_{12} = f'_{12,i}k_{12}[AA_i][SAC] \quad (6.60)$$

$$\left. \frac{d[H_2O]}{dt} \right|_{12} = (1 - f'_{12,i})k_{12}[AA_i][SAC] \quad (6.61)$$

$$f_{12,i} = \frac{M_{AA_i}}{M_{AA_i} + M_{SAC}} \quad (6.62)$$

$$f'_{12,i} = \frac{M_{AA_i} + M_{SAC} - M_{H_2O}}{M_{AA_i} + M_{SAC}} \quad (6.63)$$

$$\left. \frac{d[BC_{(i-1)}^C]}{dt} \right|_{12} = (f_{12,i}w_{AA_i}^C + (1 - f_{12,i})w_{SAC}^C) k_{12}[AA_i][SAC] \quad (6.64)$$

$$\left. \frac{d[BC_{(i-1)}^N]}{dt} \right|_{12} = f_{12,i}w_{AA_i}^N k_{12}[AA_i][SAC] \quad (6.65)$$

$$\left. \frac{dM_{BC_{(i-1)}}}{dt} \right|_{12} = \frac{(M_{AA_i} + M_{SAC} - M_{H_2O} - M_{BC_{(i-1)}})}{[BC_{(i-1)}]} \left. \frac{d[BC_{(i-1)}]}{dt} \right|_{13} \quad (6.66)$$

### 6.2.1.6 Deamination

**Pathways 13, 14, and 15: Deamination of amino acid (AA) to aqueous-phase product (AQ) and NH<sub>3</sub>, AQ to AQ and NH<sub>3</sub>, and biocrude (BC) to BC and NH<sub>3</sub>** The liberation of ammonium from amino acids and associated degradation products is of great importance because ammonium is a bioavailable source of nitrogen for algal cultivation. To accurately model this product, we incorporated the  $i$  subscript notation to track amine groups across each component. The following pathways enable AA, AQ, and BC components to undergo deamination:



Here we assume that the removal of an amine group does not change the lumped product

solubility for the compound. In practice, some deamination of AQ compounds may yield relatively more non-polar components that are DCM-soluble, but for simplicity we ignore those situations. These pathways follow the following sets of equations that follow a similar notation and style as those presented earlier:

$$\left. \frac{d[\text{AA}_i]}{dt} \right|_{13} = -k_{13}[\text{AA}_i] \quad (6.70)$$

$$\left. \frac{d[\text{AQ}_{(i-1)}]}{dt} \right|_{13} = f_{13,i} k_{13}[\text{AA}_i] \quad (6.71)$$

$$\left. \frac{d[\text{NH}_3]}{dt} \right|_{13} = (1 - f_{13,i}) k_{13}[\text{AA}_i] \quad (6.72)$$

$$f_{13,i} = \frac{M_{\text{AA}_i} - M_{\text{NH}_3}}{M_{\text{AA}_i}} \quad (6.73)$$

$$\left. \frac{d[\text{AQ}_{(i-1)}^{\text{C}}]}{dt} \right|_{13} = w_{\text{AA}_i}^{\text{C}} k_{13}[\text{AA}_i] \quad (6.74)$$

$$\left. \frac{d[\text{AQ}_{(i-1)}^{\text{N}}]}{dt} \right|_{13} = (w_{\text{AA}_i}^{\text{N}} - w_{\text{NH}_3}^{\text{N}}(1 - f_{13,i})) k_{13}[\text{AA}_i] \quad (6.75)$$

$$\left. \frac{dM_{\text{AQ}_{(i-1)}}}{dt} \right|_{13} = \frac{(M_{\text{AA}_i} - M_{\text{NH}_3} - M_{\text{AQ}_{(i-1)}})}{[\text{AQ}_{(i-1)}]} \left. \frac{d[\text{AQ}_{(i-1)}]}{dt} \right|_{13} \quad (6.76)$$

$$\left. \frac{d[\text{AQ}_i]}{dt} \right|_{14} = -k_{14}[\text{AQ}_i] \quad (6.77)$$

$$\left. \frac{d[\text{AQ}_{(i-1)}]}{dt} \right|_{14} = f_{14,i} k_{14}[\text{AQ}_i] \quad (6.78)$$

$$\left. \frac{d[\text{NH}_3]}{dt} \right|_{14} = (1 - f_{14,i}) k_{14}[\text{AQ}_i] \quad (6.79)$$

$$f_{14,i} = \frac{M_{\text{AQ}_i} - M_{\text{NH}_3}}{M_{\text{AQ}_i}} \quad (6.80)$$

$$\left. \frac{d[\text{AQ}_i^{\text{C}}]}{dt} \right|_{14} = -k_{14}[\text{AQ}_i^{\text{C}}] \quad (6.81)$$

$$\left. \frac{d[\text{AQ}_{(i-1)}^{\text{C}}]}{dt} \right|_{14} = k_{14}[\text{AQ}_i^{\text{C}}] \quad (6.82)$$

$$\left. \frac{d[\text{AQ}_i^{\text{N}}]}{dt} \right|_{14} = -k_{14}[\text{AQ}_i^{\text{N}}] \quad (6.83)$$

$$\left. \frac{d[\text{AQ}_{(i-1)}^{\text{N}}]}{dt} \right|_{14} = k_{14} \left( [\text{AQ}_i^{\text{N}}] - w_{\text{NH}_3}^{\text{N}} (1 - f_{14,i}) [\text{AQ}_i] \right) \quad (6.84)$$

$$\left. \frac{dM_{\text{AQ}_{(i-1)}}}{dt} \right|_{14} = \frac{(M_{\text{AQ}_i} - M_{\text{NH}_3} - M_{\text{AQ}_{(i-1)}})}{[\text{AQ}_{(i-1)}]} \left. \frac{d[\text{AQ}_{(i-1)}]}{dt} \right|_{14} \quad (6.85)$$

$$\left. \frac{d[\text{BC}_i]}{dt} \right|_{15} = -k_{15}[\text{BC}_i] \quad (6.86)$$

$$\left. \frac{d[\text{BC}_{(i-1)}]}{dt} \right|_{15} = f_{15,i} k_{15}[\text{BC}_i] \quad (6.87)$$

$$\left. \frac{d[\text{NH}_3]}{dt} \right|_{15} = (1 - f_{15,i}) k_{15}[\text{BC}_i] \quad (6.88)$$

$$f_{15,i} = \frac{M_{\text{BC}_i} - M_{\text{NH}_3}}{M_{\text{BC}_i}} \quad (6.89)$$

$$\left. \frac{d[\text{BC}_i^{\text{C}}]}{dt} \right|_{15} = -k_{15}[\text{BC}_i^{\text{C}}] \quad (6.90)$$

$$\left. \frac{d[\text{BC}_{(i-1)}^{\text{C}}]}{dt} \right|_{15} = k_{15}[\text{BC}_i^{\text{C}}] \quad (6.91)$$

$$\left. \frac{d[\text{BC}_i^{\text{N}}]}{dt} \right|_{15} = -k_{15}[\text{BC}_i^{\text{N}}] \quad (6.92)$$

$$\left. \frac{d[\text{BC}_{(i-1)}^{\text{N}}]}{dt} \right|_{15} = k_{15} \left( [\text{BC}_i^{\text{N}}] - w_{\text{NH}_3}^{\text{N}} (1 - f_{15,i}) [\text{BC}_i] \right) \quad (6.93)$$

$$\left. \frac{dM_{\text{BC}_{(i-1)}}}{dt} \right|_{15} = \frac{(M_{\text{BC}_i} - M_{\text{NH}_3} - M_{\text{BC}_{(i-1)}})}{[\text{BC}_{(i-1)}]} \left. \frac{d[\text{BC}_{(i-1)}]}{dt} \right|_{15} \quad (6.94)$$

### 6.2.1.7 Decarboxylation

**Pathway 16: Decarboxylation of amino acid (AA) to aqueous-phase product (AQ) and CO<sub>2</sub>** The final class of reaction incorporated in the model is decarboxylation, which we model using the following reaction pathway that is analogous to that of deamination:



We assume that the entire gas phase produced by HTL is CO<sub>2</sub>, which in practice has been reported to represent about 90 % of the gas produced by HTL at 300 °C and lower [10]. Moreover we only consider the gas produced through decarboxylation of AA; there are also significant gas contributions from decarbonylation and decarboxylation of SAC degradation products, however those reactions were out of scope for the purposes of the present model.

$$\left. \frac{d[AA_i]}{dt} \right|_{16} = -k_{16}[AA_i] \quad (6.96)$$

$$\left. \frac{d[AQ_i]}{dt} \right|_{16} = f_{16,i}k_{16}[AA_i] \quad (6.97)$$

$$\left. \frac{d[CO_2]}{dt} \right|_{16} = (1 - f_{16,i})k_{16}[AA_i] \quad (6.98)$$

$$f_{16,i} = \frac{M_{AA_i} - M_{CO_2}}{M_{AA_i}} \quad (6.99)$$

$$\left. \frac{d[AQ_i^C]}{dt} \right|_{16} = (w_{AA_i}^C - w_{CO_2}^C(1 - f_{16,i})) k_{16}[AA_i] \quad (6.100)$$

$$\left. \frac{d[AQ_i^N]}{dt} \right|_{16} = w_{AA_i}^N k_{16}[AA_i] \quad (6.101)$$

$$\left. \frac{dM_{AQ_i}}{dt} \right|_{16} = \frac{(M_{AA_i} - M_{CO_2} - M_{AQ_i})}{[AQ_i]} \left. \frac{d[AQ_i]}{dt} \right|_{16} \quad (6.102)$$

## 6.2.2 Summary of governing equations and system components

The full equation for the rate of change of each component sums all of the contributions from each pathway (Table 6.1). For example, the rate of change of AA<sub>1</sub> is explicitly affected

Path	Reaction	Reactant(s)	Product(s)
(1)	Hydrolysis	LIP, H <sub>2</sub> O	FA
(2)	Hydrolysis	PRO, PPE, H <sub>2</sub> O	PEP
(3)	Repolymerization	PEP	PPE, H <sub>2</sub> O
(4)	Hydrolysis	PEP, H <sub>2</sub> O	AA
(5)	Hydrolysis	CAR, BCH, H <sub>2</sub> O	PSA
(6)	Repolymerization	PSA	BCH, H <sub>2</sub> O
(7)	Hydrolysis	PSA, H <sub>2</sub> O	SAC
(8)	Dissolution	ASH	DAS
(9)	Cyclodehydration	PEP	BC, H <sub>2</sub> O
(10)	Retro-aldol Condensation	SAC	AQ
(11)	Retro-aldol Condensation	SAC	BC
(12)	Maillard	SAC, AA	BC, H <sub>2</sub> O
(13)	Deamination	AA	AQ, NH <sub>3</sub>
(14)	Deamination	AQ	AQ, NH <sub>3</sub>
(15)	Deamination	BC	BC, NH <sub>3</sub>
(16)	Decarboxylation	AA	AQ, CO <sub>2</sub>

Table 6.1: Reaction pathways incorporated in the kinetic model.

by Pathways 4, 12, 13, and 16 as follows:

$$\begin{aligned}
\frac{d[\text{AA}_1]}{dt} &= \left. \frac{d[\text{AA}_1]}{dt} \right|_4 + \left. \frac{d[\text{AA}_1]}{dt} \right|_{12} + \left. \frac{d[\text{AA}_1]}{dt} \right|_{13} + \left. \frac{d[\text{AA}_1]}{dt} \right|_{16} \\
&= w_{\text{AA}_1} k_4 [\text{PEP}] - f_{12,1} k_{12} [\text{AA}_1] [\text{SAC}] - k_{13} [\text{AA}_1] - k_{16} [\text{AA}_1]
\end{aligned}$$

The total rates of change for the other components follow similarly. We refer the reader to Tables 6.1 and 6.2 for summaries of the reaction pathways and components in the system. Each of the rate constants,  $k_p$ , presented in Section 6.2.1 follows Arrhenius kinetics, where  $p$  is the pathway number:

$$k_p(t) = A_p \exp\left(\frac{-E_p}{RT(t)}\right) \quad (6.103)$$

Here,  $A_p$  is the pre-exponential factor,  $E_p$  is the activation energy,  $R$  is the gas constant,

ID	Component	Product Fraction	Pathways Involved
AA	Amino acid	Aqueous	4, 12, 13, 16
AQ	Aqueous-phase product	Aqueous	10, 13, 14, 16
ASH	Ash	Solid	8
BC	Biocrude	Biocrude	9, 11, 12, 15
BCH	Biochar	Solid	5, 6
CAR	Carbohydrate	Solid, Aqueous	5
CO <sub>2</sub>	Carbon dioxide	Gas, Volatile	16
DAS	Dissolved ash	Aqueous	8
H <sub>2</sub> O	Water	Water	1, 2, 3, 4, 7, 9, 12
FA	Fatty acid	Biocrude	1
LIP	Lipid	Solid, Biocrude	1
NH <sub>3</sub>	Ammonia	Gas, Volatile	13, 14, 15
PEP	Peptide	Aqueous	2, 3, 4, 9
PPE	Polypeptide	Solid	2, 3
PRO	Protein	Solid, Aqueous	2
PSA	Polysaccharide	Solid	5, 6, 7
SAC	Saccharide	Aqueous	7, 10, 11, 12

Table 6.2: Component names, product fractions, and participating pathways in the kinetic model.

and  $T(t)$  is the time-dependent temperature. In general, each rate constant and reaction pathway use a unique set of  $A_p$  and  $E_p$  to govern their behavior; however, to simplify the model, we allow some of the pathways within the same type of reaction (e.g., hydrolysis) to share the same activation energy. This simplification greatly reduced computation time required to optimize the kinetic parameters, and we are confident that it was not accompanied by a significant loss in precision or accuracy. The following equations highlight the pathways using this simplification:

$$E_2 = E_4 \tag{6.104}$$

$$E_5 = E_7 \tag{6.105}$$

$$E_{10} = E_{11} \tag{6.106}$$

$$E_{14} = E_{15} \tag{6.107}$$

These equations reduce the number of free parameters governing the system, bringing the total to (16 pathways)(2 Arrhenius parameters) – (4 equations) = 28 total free parameters.

### 6.2.3 Model development in MATLAB

We developed the kinetic model using MATLAB R2017a. We first calculated polynomial coefficients for each empirical temperature profile. We used these polynomials to calculate the time-dependent temperature during heat-up and assumed an isothermal temperature after the first 90 s (we previously reported the heat-up to be on average 58 s in Chapter IV). We used `ode23s` to solve the system of coupled, first-order ODEs listed in Section 6.2.1 using the aforementioned temperature polynomials, subject to a trial set of kinetic parameters,  $A_p$  and  $E_p$ . We used these solutions to calculate the objective function, which consisted of the sum of squared errors (SSE) between calculated and observed values for the components listed in Table 6.3. In general, to obtain the calculated lumped-product quantities (e.g., biocrude N yield), which can consist of multiple individual components in the model, we summed the quantities of all of the model components residing in that fraction based on solubility assumptions (e.g.,  $BC_0^N$ ,  $BC_1^N$ ,  $BC_2^N$ ). This SSE compares 1,067 individual measurements to calculated values, for a data-to-parameter ratio of  $\frac{1067}{28} = 38.1$ .

To obtain appropriate trial sets of Arrhenius parameters, we initially started with only a few pathways in the model and chose broad, yet reasonable boundaries. We randomly chose starting points within those boundaries and calculated the objective function for each trial set. These sets often consisted of  $10^4$  to  $10^7$  subsets of points, so we used FLUX, the high-performance computing cluster at the University of Michigan, to calculate the objective function on hundreds of cores in parallel. We then sorted these points by objective function, and ran `fmincon` on the trial sets with the lowest SSE. We used the AICc metric (discussed in Section 3.3.6) to evaluate the likelihood that different values for the kinetic parameters were better than one another at the  $\alpha = 0.05$  level. These AICc comparisons allowed us to refine the boundaries for the parameters and repeat this process until each boundary contained all solutions with at least a 5 % probability of being optimal. We then added additional pathways to the model and repeated this process until all pathways were added. The optimized kinetic parameters for each pathway are presented in Table 6.4.

Product Fraction	Quantity	Observed, $Y$	Calculated, $\mathcal{Y} = f(\Gamma_i)$	Constraint
Solid	Lipid	$Y_{LIP}$	$\mathcal{Y}_{LIP} = \Gamma_{LIP}^{SO}$	$Y_{LIP} > \mathcal{Y}_{LIP}$
	Total	$Y_{SO}$	$\mathcal{Y}_{SO} = \Gamma_{LIP}^{SO} + \Gamma_{PRO}^{SO} + \Gamma_{PPE}$ $+ \Gamma_{CAR}^{SO} + \Gamma_{PSA} + \Gamma_{ASH}$	-
	Carbon	$Y_{SO}^C$	$\mathcal{Y}_{SO}^C = w_{LIP}^C \Gamma_{LIP}^{SO} + w_{PRO}^C (\Gamma_{PRO}^{SO} + \Gamma_{PPE})$ $+ w_{CAR}^C (\Gamma_{CAR}^{SO} + \Gamma_{PSA})$	-
	Nitrogen	$Y_{SO}^N$	$\mathcal{Y}_{SO}^N = w_{PRO}^N (\Gamma_{PRO}^{SO} + \Gamma_{PPE})$	-
Biocrude	Fatty acid	$Y_{FA}$	$\mathcal{Y}_{FA} = \Gamma_{LIP}^{BC} + \Gamma_{FA}$	$Y_{FA} > \mathcal{Y}_{FA}$
	Total	$Y_{BC}$	$\mathcal{Y}_{BC} = \Gamma_{LIP}^{BC} + \Gamma_{FA} + \Gamma_{BC}$	-
	Carbon	$Y_{BC}^C$	$\mathcal{Y}_{BC}^C = w_{LIP}^C (\Gamma_{LIP}^{BC} + \Gamma_{FA}) + \Gamma_{BC}^C$	-
	Nitrogen	$Y_{BC}^N$	$\mathcal{Y}_{BC}^N = \Gamma_{BC}^N$	-
Aqueous (non-volatile)	Total	$Y_{AQ}$	$\mathcal{Y}_{AQ} = \Gamma_{PRO}^{AQ} + \Gamma_{PEP} + \Gamma_{AA} + \Gamma_{CAR}^{AQ}$ $+ \Gamma_{SAC} + \Gamma_{PSA} + \Gamma_{DAs}$	$Y_{AQ} < \mathcal{Y}_{AQ}$
	Carbon	$Y_{AQ}^C$	$\mathcal{Y}_{AQ}^C = w_{PRO}^C \Gamma_{PRO}^{AQ} + w_{PEP}^C \Gamma_{PEP}$ $+ w_{AA}^C \Gamma_{AA} + w_{CAR}^C \Gamma_{CAR}^{AQ}$ $+ w_{SAC}^C \Gamma_{SAC} + w_{PSA}^C \Gamma_{PSA}$	$Y_{AQ}^C < \mathcal{Y}_{AQ}^C$
	Nitrogen	$Y_{AQ}^N$	$\mathcal{Y}_{AQ}^N = w_{PRO}^N \Gamma_{PRO}^{AQ} + w_{PEP}^N \Gamma_{PEP}$ $+ w_{AA}^N \Gamma_{AA}$	$Y_{AQ}^N < \mathcal{Y}_{AQ}^N$
	Total	$Y_{AQ}$	$\mathcal{Y}_{AQ+} = \mathcal{Y}_{AQ} + \Gamma_{AQ}$	$Y_{AQ} > \mathcal{Y}_{AQ+}$
	Carbon	$Y_{AQ}^C$	$\mathcal{Y}_{AQ+}^C = \mathcal{Y}_{AQ}^C + \Gamma_{AQ}^C$	$Y_{AQ}^C > \mathcal{Y}_{AQ+}^C$
	Nitrogen	$Y_{AQ}^N$	$\mathcal{Y}_{AQ+}^N = \mathcal{Y}_{AQ}^N + \Gamma_{AQ}^N$	$Y_{AQ}^N > \mathcal{Y}_{AQ+}^N$
	Volatile	$NH_3$	$Y_{NH_3}$	$\mathcal{Y}_{NH_3} = \Gamma_{NH_3}$
Gas	$CO_2$	$Y_{CO_2}$	$\mathcal{Y}_{CO_2} = \Gamma_{CO_2}$	$Y_{CO_2} < \mathcal{Y}_{CO_2}$
Aqueous, Gas, and Volatile	Total	$Y_{AGV}$	$\mathcal{Y}_{AQ++} = \mathcal{Y}_{AQ+} + \Gamma_{H_2O} + \Gamma_{NH_3} + \Gamma_{CO_2}$	-
	Carbon	$Y_{AGV}^C$	$\mathcal{Y}_{AQ++}^C = \mathcal{Y}_{AQ+}^C + w_{CO_2}^C \Gamma_{CO_2}$	-
	Nitrogen	$Y_{AGV}^N$	$\mathcal{Y}_{AQ++}^N = \mathcal{Y}_{AQ+}^N + w_{NH_3}^N \Gamma_{NH_3}$	-

Table 6.3: Types of residuals between observed ( $Y$ ) and calculated ( $\Gamma$ ) yields used in calculation of model objective function. All values on a per-unit-algal-mass basis. ‘‘Constraint’’ shows the criteria for calculating the residual, which is otherwise set to zero.

### 6.3 Results and discussion

Herein we evaluate the accuracy of the model relative to observed values documented in Chapters IV and V and Appendix F. We remind the reader that the abbreviations and biochemical profiles for each microalgal feedstock are listed in Table 4.1 in Chapter IV.

Pathway	$\log(A_p)$		$E_p$
	Value	Units	[kJ mol <sup>-1</sup> ]
LIP + H <sub>2</sub> O $\xrightarrow{1}$ FA	10 <sup>10.5</sup>	s <sup>-1</sup>	114
PRO/PPE + H <sub>2</sub> O $\xrightarrow{2}$ PEP	10 <sup>11.2</sup>	s <sup>-1</sup>	125
PEP $\xrightarrow{3}$ PPE	10 <sup>13.7</sup>	s <sup>-1</sup>	151
PEP + H <sub>2</sub> O $\xrightarrow{4}$ 2 AA	10 <sup>10.1</sup>	s <sup>-1</sup>	125
CAR/BCH + H <sub>2</sub> O $\xrightarrow{5}$ PSA	10 <sup>19.8</sup>	s <sup>-1</sup>	187
PSA $\xrightarrow{6}$ BCH	10 <sup>18.2</sup>	L <sub>rxn</sub> g <sup>-1</sup> s <sup>-1</sup>	184
PSA + H <sub>2</sub> O $\xrightarrow{7}$ SAC	10 <sup>14.9</sup>	s <sup>-1</sup>	187
ASH $\xrightarrow{8}$ DAS	10 <sup>25.8</sup>	s <sup>-1</sup>	254
PEP $\xrightarrow{9}$ BC + H <sub>2</sub> O	10 <sup>5.7</sup>	s <sup>-1</sup>	92
SAC $\xrightarrow{10}$ 2 AQ <sub>0</sub>	10 <sup>20.0</sup>	s <sup>-1</sup>	193
SAC $\xrightarrow{11}$ 2 BC <sub>0</sub>	10 <sup>19.2</sup>	s <sup>-1</sup>	193
AA <sub>i</sub> + SAC $\xrightarrow{12}$ BC <sub>(i-1)</sub> + H <sub>2</sub> O	10 <sup>20.5</sup>	L <sub>rxn</sub> g <sup>-1</sup> s <sup>-1</sup>	160
AA <sub>i</sub> $\xrightarrow{13}$ AQ <sub>(i-1)</sub> + NH <sub>3</sub>	10 <sup>16.6</sup>	s <sup>-1</sup>	159
AQ <sub>i</sub> $\xrightarrow{14}$ AQ <sub>(i-1)</sub> + NH <sub>3</sub>	10 <sup>12.8</sup>	s <sup>-1</sup>	175
BC <sub>i</sub> $\xrightarrow{15}$ BC <sub>(i-1)</sub> + NH <sub>3</sub>	10 <sup>17.5</sup>	s <sup>-1</sup>	175
AA <sub>i</sub> $\xrightarrow{16}$ AQ <sub>i</sub> + CO <sub>2</sub>	10 <sup>17.8</sup>	s <sup>-1</sup>	175

Table 6.4: Arrhenius parameters for each pathway in the kinetic model.

### 6.3.1 Parity plots

In this section we discuss the general accuracy of the model for the nine major residuals in Figure 6.1 (listed in Table 6.3) used for calculating the SSE objective function. We discuss each of these in greater detail in Sections 6.3.2 to 6.3.4. Between the solid, biocrude, and the collective aqueous, volatile, and gas products, the model captured biocrude yield most accurately (Figure 6.1b), with a root-mean-square deviation (RMSD) of just  $\pm 4.0$  wt% across all feedstock characteristics and reaction conditions. Notably there were no systematic biases above or below the parity line for any particular biomass type or range of observed biocrude yields, indicating that the model predictions for biocrude yield are fairly robust throughout the reaction domain. Solid yields and the collective aqueous, volatile, and gas yields (Figures 6.1a and c, respectively) were less accurate, but still very reasonable, with RMSDs of  $\pm 6.7$  and  $6.3$  wt%, respectively. A substantial portion of this error originated from the inability to capture the solid yields from Chl-2 at moderate-to-high reaction severity, as discussed later in Section 6.3.2.

About 83 % of the biocrude-yield RMSD can be attributed to error in biocrude C yield (Figure 6.1e). Contrary to biocrude total yield, there were a few systemic biases for biocrude C yield, which tended to be overpredicted for low observed values and underpredicted for high observed values. Moreover, biocrude C yields for high-protein biomass types, such as Nan-1, tended to be underpredicted relative to high-lipid sources, including Chl-2. Despite these biases, the RMSD was just  $\pm 3.3$  wt%. Roughly 57 and 65 % of the RMSD for solids and the aggregate aqueous, volatile, and gas product yields, respectively, is due to C yields, which themselves were both around  $\pm 4$  wt%. The lower attribution of error to C yield for the solid, aqueous, volatile, and gas products compared to that of the biocrude is consistent with their typical elemental compositions; the former contain significant amounts of other heteroatoms, such as N, O, S, and P, whereas the biocrude is predominantly composed of C and H.

The model calculated the N yields of each product fraction generally without systematic

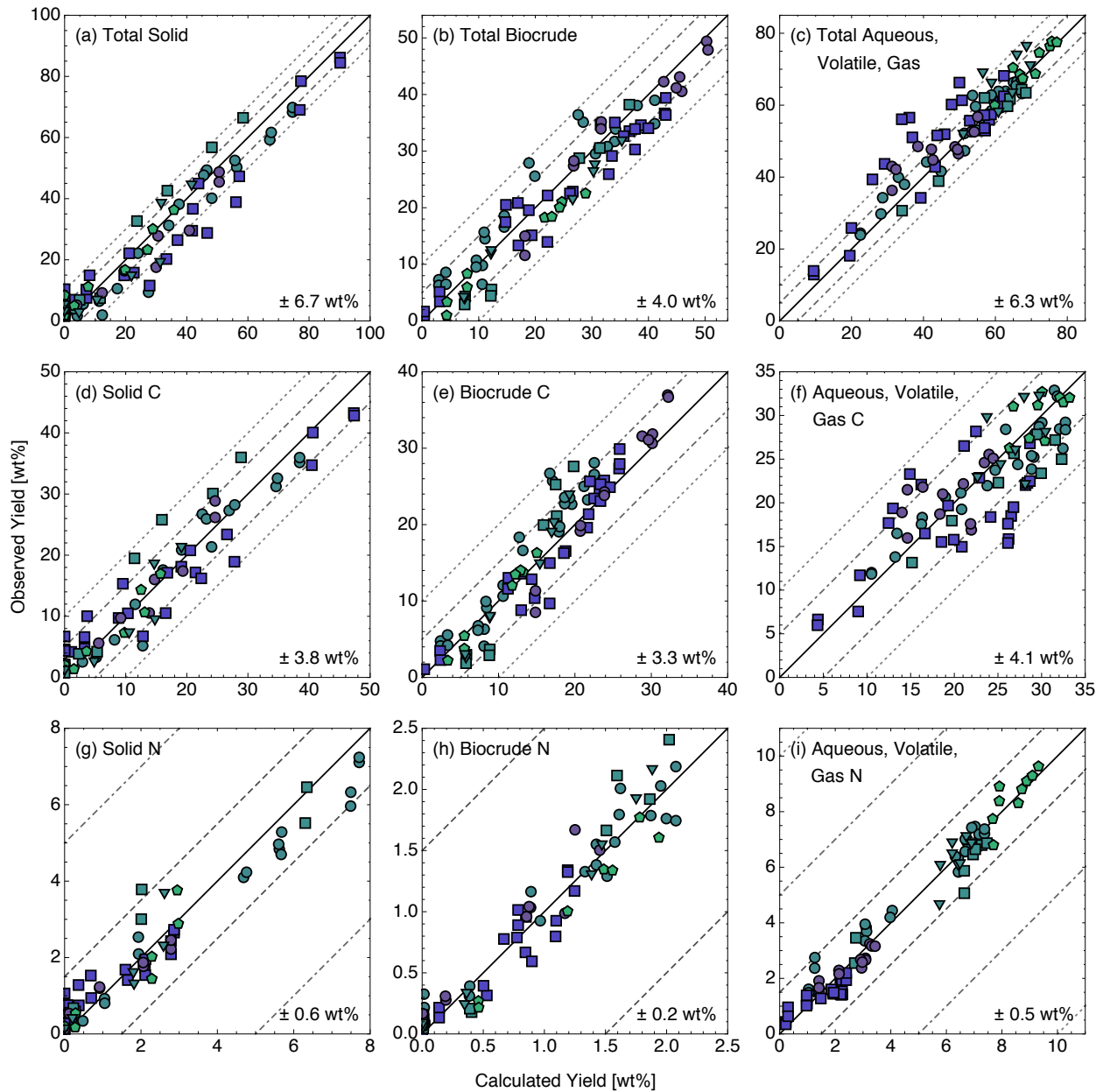


Figure 6.1: Parity plots of observed vs. calculated (a,b,c) total, (d,e,f) carbon, and (g,h,i) nitrogen yields (wt %, dry-algal-mass basis) for (a,d,g) solid, (b,e,h) biocrude, and (c,f,i) the collective aqueous, volatile, and gas products. Dashed (N yields only), dot-dashed, and dotted lines represent residuals of  $\pm 1.5$ , 5, and 10 wt%, respectively. The “ $\pm$ ” value in the bottom right corner of each panel represents the RMSD for that component.

biases with respect to biomass source or range of observed yields. One exception is solid N yield (Figure 6.1g) at high observed values, which tended to be overpredicted by about 1 wt%. Given that product N yields were low in general, due to the lower abundance of N compared to C, the RMSD values were proportionally lower as well, ranging from  $\pm 0.2$  to

$\pm 0.6$  wt%. However, even relative to the respective maximum observed N yields for solid, biocrude, and collective aqueous, volatile, and gas products, the RMSD values were fairly low, at  $\frac{\pm 0.6}{8.7} = 7\%$ ,  $\frac{\pm 0.2}{2.4} = 7\%$ , and  $\frac{\pm 0.5}{9.6} = 5\%$ , respectively.

These parity plots demonstrate that the kinetic model captures a wide variety of trends in total, carbon, and nitrogen yields for solid, biocrude, and the aggregate aqueous, volatile, and gas products with relatively high fidelity. Moreover, there were relatively few systematic biases toward over- or underprediction of yields, suggesting that the model is robust over a wide range of reaction conditions and feedstock characteristics. With the precision of the model in the aggregate established, we can examine specific subsets of reaction conditions and feedstock characteristics where the model performs well and where the model could be improved in future iterations.

### 6.3.2 Product yields

We superimposed model solutions onto various product fraction yields previously reported in Chapters IV and V and Appendix F with RMSD values for each specific subplot to evaluate the utility of the model over different regions of the reaction domain (Figure 6.2). Solid yield accuracy was generally good at 150, 300, and 350 °C, but appreciably lower at moderate reaction severity. As we indicated earlier, the model does not accurately capture solid degradation for Chl-2 in the 200 to 250 °C range, especially for the 120 g L<sub>rxn</sub><sup>-1</sup> slurries. Additional data from other biomass sources at 250 °C, including additional high-carbohydrate sources would facilitate parameter optimization with respect to solid degradation for future attempts. We do however note that the model captures the trends of lower solid yields with decreasing initial concentration, as seen in the third row in Figure 6.2a. This effect was previously undocumented and thus not considered for previous mathematical models of HTL.

Calculated biocrude yields matched observed values with generally high precision across reaction conditions, capturing many of the empirical trends with respect to biochemical

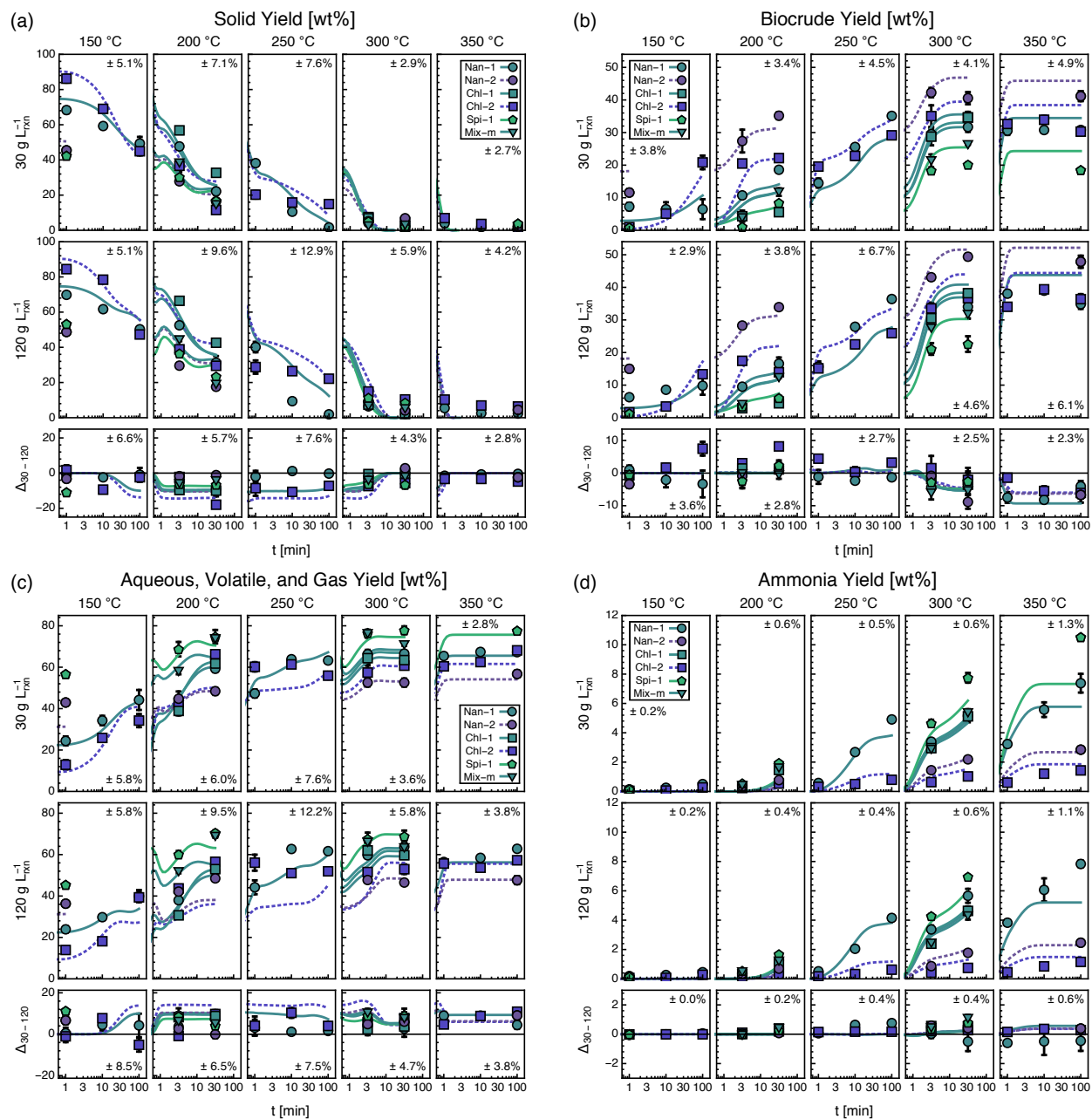


Figure 6.2: Model solutions for HTL product total yields (wt %, dry-algal-mass basis) versus reaction time grouped by temperature and initial concentration. See Table 4.1 for microalgae types. The bottom row depicts the first row ( $30 \text{ g L}_{\text{rxn}}^{-1}$ ) minus the second row ( $120 \text{ g L}_{\text{rxn}}^{-1}$ ). The “ $\pm$ ” value in each panel represents the RMSD for that component and subset of reaction conditions. Error bars indicate SE.

composition. The model correlates biocrude yield with high fidelity at  $300 \text{ }^\circ\text{C}$  and at low reaction severity ( $\leq 200 \text{ }^\circ\text{C}$ ), a first for any HTL kinetic model. The transition from low to high severity is less accurate, which is coupled with some of the error in solid yields in that region. The calculated yields at  $350 \text{ }^\circ\text{C}$  do not account for some of the gasification

occurring after extended reaction time. Those reaction pathways are an area of ongoing optimization; however, it is likely that additional data at even longer reaction times would be necessary to accurately calibrate rate constants for that region. Notably, the trend of increased biocrude yield with increasing concentration at 300 °C and higher is captured well via primarily the Maillard reaction (Pathway 12), which we modeled as second order overall. It appears that such a pathway is sufficient for explaining the observed concentration effect, lending credibility to the usefulness of the model for optimizing biocrude yield with respect to slurry concentration.

The model captured most of the general trends in aqueous, volatile, and gas yields (Figure 6.2c) with respect to changing reaction severity, biochemical composition, and slurry concentration. Calculated yields were also less accurate in the 200 to 250 °C region, but were very accurate at 300 °C and higher. Predictions for the higher-protein biomass types were generally better than those of the higher-lipid biomass at low severity, especially Chl-2 which also contained high carbohydrate content.

Within the aqueous, volatile, and gas group of compounds, we also depict model-calculated ammonia yields (Figure 6.2d), which include both  $\text{NH}_3$  and  $\text{NH}_4^+$  measured in the ACP. The model does an outstanding job of calculating ammonia yields across all biomass types and reaction conditions, with the lone exception of 350 °C, 100 min for the high-protein biomass types. Moreover, the trend of increased ammonia yield with decreasing concentration is also captured at 300 °C and higher. The high fidelity in ammonia yields demonstrates that the amine-group accounting approach we used to develop the model (e.g.,  $\text{AA}_i$  notation) is an excellent method for calculating ammonia yields up to 350 °C, 10 min. Beyond that point, it is likely that the cyclic dipeptides (via Pathway 9) and Maillard reaction products (via Pathway 12) degrade to an extent where ammonia begins to be liberated; therefore, additional degradation pathways would need to be incorporated for those severities. Similar to our observation for biocrude yield in this region, additional experimental data for extended reaction times at 350 °C would likely be needed to accurately model those types of reactions.

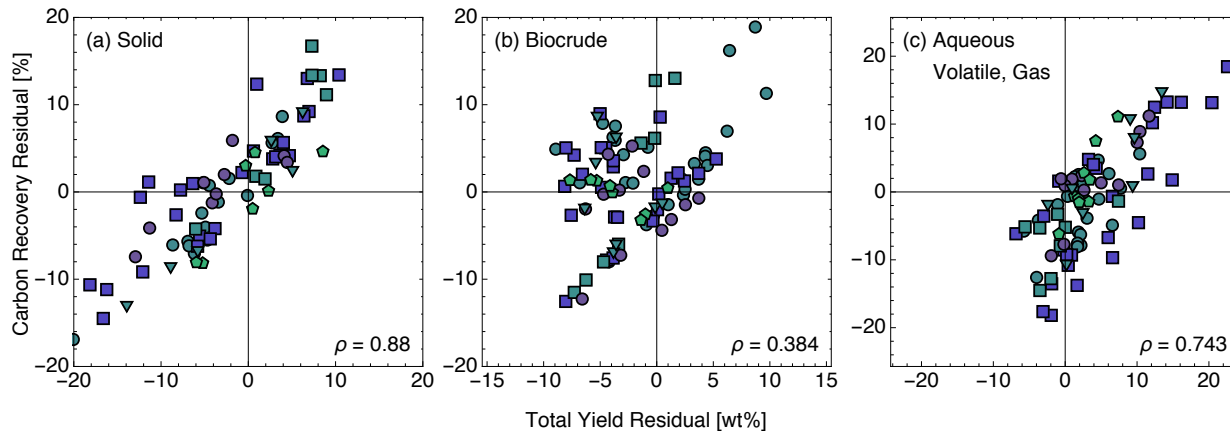


Figure 6.3: Carbon recovery residual versus total yield residual for (a) solid, (b) biocrude, and (c) the collective aqueous, volatile, and gas products. Residuals calculated as the observed minus calculated values. See Table 4.1 for microalgae types.  $\rho$  indicates correlation coefficient.

### 6.3.3 Carbon distribution

The trends in accuracies of calculated C recoveries over different regions of the reaction domain generally mirrored those of yields, shown in Figure I.1. However, it is also worthwhile to understand the extent to which the model faithfully captures product yields and C recoveries simultaneously, or whether there are antagonistic biases affecting one versus the other (i.e., one is overpredicted while the other is underpredicted). Comparing the residuals of C recovery to those of total yield for the solid product fraction (Figure 6.3a), we see that there were only a few instances where solid yields were overpredicted but C recoveries were underpredicted (top left quadrant). For the solid products in general, the residuals (i.e., errors) between yield and C recovery were highly correlated ( $\rho = 0.880$ ).

Although the general trends for biocrude yield (Figure 6.2b) and C recovery (Figure I.1b) are captured well, there were a significant number of points where biocrude yield was overpredicted but C recovery was underpredicted (Figure 6.3b, top left quadrant), but relatively few points vice versa. We remind the reader that the rates of total and carbon mass flows due to reaction were allotted based on assumptions about the molar masses of different components. It is possible that more precise estimates of the various component molar masses would improve the correlation between biocrude yield and C recovery; however, additional data from

analyses such as Fourier-transform ion cyclotron resonance mass spectrometry (FT-ICR MS), which provides measured distributions of molar masses coupled with elemental contents, may be necessary to further improve this relationship. Aside from those points, there was a moderate correlation between biocrude yield residuals and C recovery residuals ( $\rho = 0.384$ ).

The overall patterns for aqueous, volatile, and gas C recoveries (Figure I.1c) were also captured to a reasonable extent, matching many of the trends in yields (Figure 6.2c). Yields and C recoveries were strongly correlated ( $\rho = 0.743$ ), although there were a small number of points where aqueous, volatile, and gas yields were underpredicted but C recoveries were overpredicted.

#### 6.3.4 Nitrogen distribution

Model solutions for solid N recovery (Figure 6.4a) captured experimental trends sufficiently for most biomass types, although recoveries tended to be overpredicted at 150 °C and underpredicted at 200 °C, 31.6 min. Chl-2 was a notable exception, with a significantly slower rate of solid N loss from compared to other biomass types. Notably, Chl-2 possessed a relatively high carbohydrate-to-protein ratio, suggesting that Maillard reactions producing N-containing solid products could be the source of sustained N recovery in the solid fraction. Attempts to incorporate such a pathway in the model were unsuccessful (not including the Maillard reaction pathway to produce biocrude, which was generally successful). It is likely that additional studies of biomass types or model compounds with comparable biochemical profiles are necessary to determine the associated reaction mechanism.

Calculated biocrude N recoveries described observed trends with respect to reaction severity, slurry concentration, and biochemical composition with high fidelity (Figure 6.4b). The effects of increasing reaction severity are captured well, with the exception of decreases observed at 350 °C, 100 min. Moreover, the empirically observed effect of increased biocrude N recovery with increasing slurry concentration is well described via the Maillard reaction (Pathway 12). We proposed in Section 4.3.4 that the prevalence of Maillard reactions could

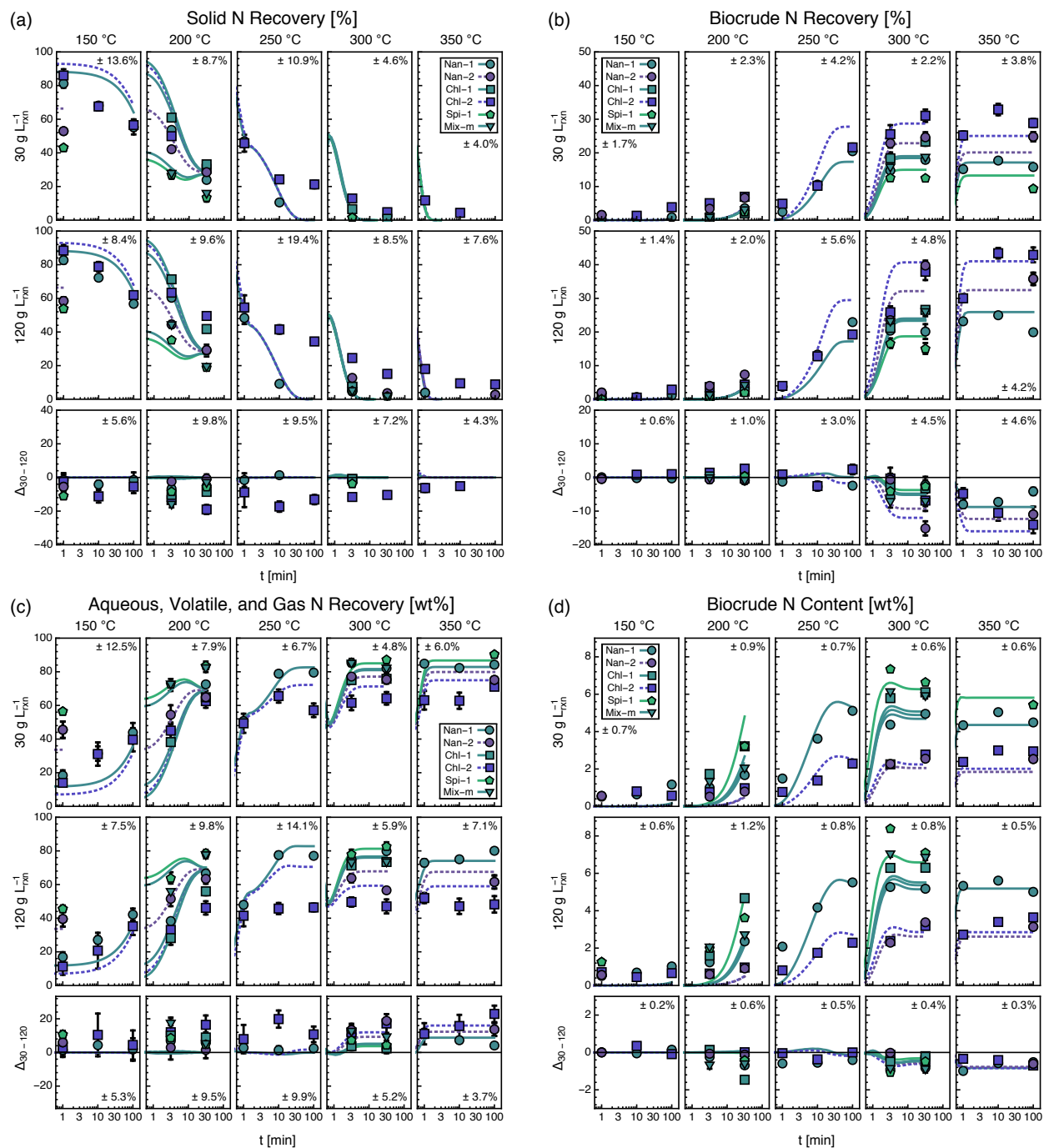


Figure 6.4: Model solutions for HTL product (a,b,c) nitrogen recoveries (% , dry-algal-nitrogen-mass basis) and (d) biocrude nitrogen content (wt % , biocrude-mass basis) versus reaction time grouped by temperature and initial concentration. See Table 4.1 for microalgae types. The bottom row depicts the first row ( $30 \text{ g L}_{\text{rxn}}^{-1}$ ) minus the second row ( $120 \text{ g L}_{\text{rxn}}^{-1}$ ). The “ $\pm$ ” value in each panel represents the RMSD for that component and subset of reaction conditions. Error bars indicate SE.

explain the trend of increasing biocrude N recovery with decreasing protein content, as such reactions may selectively consume free amino acids before they can deaminate. The present

model reflects exactly this sort of behavior, lending credibility to our earlier explanation. Calculated biocrude N recoveries for Chl-2 tended to be overpredicted at 250 °C and underpredicted at 350 °C. Future experimental efforts aimed at further illuminating Maillard reaction kinetics are likely necessary to increase the precision for such biomass types with carbohydrate-to-protein ratios.

The solutions for aqueous, volatile, and gas N recoveries were generally in excellent agreement with observed values for high-protein biomass types. Agreement was relatively good for the 30 g L<sub>rxn</sub><sup>-1</sup> slurries of Nan-2, although less so for the 120 g L<sub>rxn</sub><sup>-1</sup> slurries. Similar to the N recoveries for other product fractions, the model did not capture aqueous, volatile, and gas N recoveries well for Chl-2 for reasons described earlier. Across different reaction severities, model predictions were most accurate at 300 °C, followed by 350 and 150 °C. Slurry concentration effects enabled by the Maillard reaction (Pathway 12) matched reasonably well with experimental data at 300 °C and higher; however, no effects were predicted at 250 °C and lower, even though we generally observed higher N recoveries with lower initial concentration there. Additional or modified reaction pathways with non-unity overall reaction orders would be necessary to capture those effects.

Given the importance of biocrude N content for subsequent catalytic upgrading, we also include model solutions versus experimental data for this dependent variable in Figure 6.4d. At 250 °C and higher, agreement between calculated and observed values was very reasonable. Key trends with respect to biochemical composition and slurry concentration are captured by the model solutions as well, including increased biocrude N content with increasing biomass protein content and increasing slurry concentration. The mathematical descriptions of these trends afforded by the kinetic model demonstrate its utility for the minimization of biocrude N content, a key process metric for optimization.

## 6.4 Conclusion

In this chapter, we proposed an entirely new approach for modeling microalgal HTL via chemical kinetics that blends known molecular reaction pathways with lumped products. The resulting kinetic model is capable of calculating reaction-condition- and biochemical-composition-dependent, gravimetric and elemental yields for the major HTL product fractions with broadly acceptable fidelity. Model calculations for the biocrude and ammonia fractions are particularly accurate, demonstrating the utility of the model for optimization of key metrics like biocrude C recovery and aqueous ammonium recovery. Moreover, the model successfully captures trends with respect to slurry concentration for the first time in addition to expanding predictive capability with changing reaction severity and biochemical composition beyond the scope of previous kinetic models. Such features represent a significant improvement in quantitative models for microalgal HTL that will ultimately facilitate optimization of process sustainability and EROI.

## CHAPTER VII

### Conclusion and recommendations

#### 7.1 Significance of results in algal biofuel production

The viability of renewable fuel production from microalgae via HTL hinges on the minimization of energy and material inputs and costs required for five major process units: (A) algal cultivation and (B) dewatering, (C) HTL, (D) catalytic upgrading, and (E) nutrient recycling. We present hypothetical, yet reasonable, strategies for operating these process units using either a low- or a high-input strategy in Table 7.1, where “input” refers to the amalgamation of energy, materials, and costs. These strategies either minimize the inputs for a process unit locally (assuming that this unit has high input requirements relative to the total process inputs) or employ relatively more inputs locally to reduce inputs for other process units, and thus the process overall (assuming that this unit has lower input requirements relative to the total process inputs.)

An approach often described in the field is to (A) maximize biomass productivity while

Step	Process unit	Low-input strategy	High-input strategy
A	Algal growth	Maximize biomass (high-protein content)	Maximize lipid content (less biomass)
B	Dewatering	Concentrate by 200 to 800x to 4 wt%	Concentrate by 800 to 3200x to 16 wt%
C	Hydrothermal liquefaction	Mild reaction severity (200 °C, 31.6 min)	High reaction severity (350 °C, 100 min)
D	Catalytic upgrading	Upgrade from <3 wt% N content	Upgrade from >5 wt% N content
E	Nutrient recycling	ACP with less fresh media	Upgrading effluent with more fresh media

Table 7.1: Examples for strategies to either minimize process unit inputs locally (low-input strategy; assuming large or many input requirements relative to total process inputs) or employ relatively more inputs locally to reduce inputs of other process units (high-input strategy; assuming small or few input requirements relative to total process inputs). Values chosen represent reasonable examples but are not comprehensive.

minimizing inputs (generating high-protein biomass [91]) and (B) concentrate to high levels (e.g., 16 wt%) to reduce energy spent heating water during (C) HTL at high reaction severity to maximize biocrude yield. Due to the high microalgal-protein content, biocrude N content at these severe reaction conditions is  $> 5$  wt% and must be (D) reduced to lower levels ( $< 0.5$  wt%) via catalytic upgrading before conventional refining [105], thereby (E) liberating nitrogen for nutrient recycling which can be supplemented with fresh media to compensate for losses during upgrading. The crux of this collective approach is the minimization of the inputs for Step A, on a per-unit-biomass basis, while choosing parameters for Steps B and C that maximize biocrude yield, assuming that inputs required in Step D to remove the resulting high-heteroatom content are relatively small, and assuming that most of the nitrogen recovered in the upgrading effluent can be recycled and any deficit met by added fresh media in Step E.

This dissertation provides empirical, quantitative evidence of some of the effects that this approach has on biocrude and ACP yield and properties, enabling quantitative comparison for competing approaches. In Chapter IV, we show that both higher protein content (resulting from low-input growth strategy for Step A) and higher concentration (resulting from biocrude yield-maximizing strategy for Step B) independently lead to higher biocrude N content at nearly all reaction severities (Step C). At 300 °C, these effects are +2.8 wt% and +0.6 wt%, respectively, for a total of +3.4 wt% N content, all of which must be removed via catalytic upgrading (Step D) to produce a viable fuel. It is important to stress that N can be a difficult heteroatom to remove [140] and is often incorporated in heterocyclic saturated or aromatic compounds [43], which themselves are difficult to refine into more useful compounds without expending a relatively large amount of energy. Moreover, higher protein content and higher concentration also result in universal decreases in ACP quality for recycling (Step E) from HTL at 200 °C (Chapter V). For example, increased protein content and slurry concentration lead to  $-6$  and  $-7$  % total N recovery,  $-3$  and  $-10$  % total P recovery, and  $-11$  and  $-7$  % S recovery, respectively. At 300 °C, increased concentration

still negatively affects ACP properties, including  $-9\%$  total N recovery,  $-13\%$  total P recovery, and  $-1\%$  S recovery; however, as stated in Section 5.4.2, biochemical composition could be manipulated to optimize specific nutrient recoveries.

Another strategy is to maximize biomass lipid content (Step A), which requires more time to cultivate and with decreased biomass productivity and protein content compared to high-protein biomass [40, 91]. Per unit biomass, this approach needs additional raceway ponds to compensate for reduced productivity, thus requiring additional inputs beyond those needed for the previous approach. However, we show in this dissertation that high-lipid biomass reacted using a lower slurry concentration (Step B) produces comparatively higher biocrude yields (20 to 35 wt%) with up to 3.4 wt% less N content, higher energy density, and up to 50 % higher fatty acid recovery. When reacted at 200 °C for 31.6 min, these slurries produce ACP with across-the-board boosts to its recyclability (Step E), including up to +13 %  $\text{NH}_4^+ - \text{N}$ , +31 % total N, +42 %  $\text{PO}_4^{3-}$ , +14 % total P, and +30 % S recoveries. These shifts in elemental contents benefit the ease of upgrading the biocrude (Step D) to a more reasonable petroleum substitute, given that the initial heteroatom contents are far lower, while simultaneously bolstering ACP nutrient recovery for direct recycling (Step E).

Approaches for optimizing an algal biorefinery (i.e., maximizing productivity vs. lipid content) are rooted in assumptions about algal growth (Step A), catalytic upgrading (Step D), and nutrient recycling (Step E). The additional inputs needed to grow high-lipid biomass to enable more direct ACP recycling and simultaneously reduce catalytic upgrading inputs must be rigorously evaluated alongside the fewer inputs needed to cultivate high-protein biomass with enhanced productivity but with significantly more inputs required for nutrient recycling and catalytic upgrading. In this dissertation, we further characterize the HTL process unit, and how upstream parameters (algal growth and dewatering) can impact downstream parameters (catalytic upgrading and nutrient recycling). These effects are manifested within a quantitative tool for comparing different HTL approaches in Chapter VI. Our results suggest that modest reductions in biomass productivity in favor of enhanced lipid content

could be more than offset by increases in aqueous nutrient recovery, decreases in biocrude heteroatom content, and increases in biocrude energy density.

## 7.2 Conclusion

This dissertation elucidated many novel individual and dynamic effects of reaction conditions and feedstock characteristics for the hydrothermal liquefaction (HTL) of microalgae. These results served as the foundation for several new mathematical models that quantify the effects of slurry concentration and species identity for the first time while expanding modeling capability for temperature, time, and biochemical composition.

We first quantified the kinetics for algal HTL in Chapter II through an in-depth study of the impacts of reaction conditions, such as temperature, reaction time, and heating rate, on product yields from the HTL of *Nannochloropsis oculata*. These data informed the development of a reaction network and kinetic model valid over a wide range of temperatures (100 – 400 °C) and holding times (10 s – 60 min), including much shorter timescales (10 s – 10 min) than previously established. The incorporation of recorded temperature profiles allowed this model to decouple reactor heat-up from kinetic analysis, enabling more accurate characterization of temperature and time relationships. Calculated yields for this model correlated reasonably well with observed yields, with biocrude yields as high as 46 wt % predicted at 400 °C and 1 min. This model also highlighted possible trade-offs between biocrude quantity and quality via about a 100 °C difference in the conditions maximizing biocrude yields and aqueous-phase product yields, respectively.

In Chapter III we examined the quality of biomass and biocrude oil from the HTL of algal monocultures and polycultures. We sought to determine if there were any advantages for using polycultures in terms of sustainability metrics, as well as whether the identity of the species present in the polycultures affected biocrude quality beyond the effects of biochemical composition. We found that, on average, the 2-species cultures produced biomass and biocrude of a quality that matched the average monoculture, while the 4- and 6-species

cultures were worse on average. Specific combinations of species met or exceeded the best monoculture for each quality metric, offering potentially compelling advantages, although no individual combination of species was superior for all metrics of quality. We posited that biocrude productivity was inversely related to product quality by comparing the most productive monoculture (*S. capricornutum*) to the polycultures producing the highest quality products. Multiple linear regression models of biocrude yield and composition that considered both biochemical composition and species identity explained a greater extent of the variation between samples compared to those employing only biochemical composition. We also quantified this effect of species identity for the first time, showing that its maximum effect on modeled biocrude properties is 11 to 40 % of that of biochemical composition.

These insights into the effects of reaction conditions and feedstock characteristics from Chapters II and III, respectively, along with results from the literature, led to a far more comprehensive study of the effects of temperature, time, slurry concentration, biochemical composition, and species identity on the biocrude and aqueous product fractions in Chapter IV and Chapter V, respectively. Temperature and biochemical composition were the most important factors governing HTL product yields and composition, and we quantified the effects of slurry concentration and species identity in depth for the first time. Increased concentration promoted Maillard reactions between protein- and carbohydrate-degradation products that increased biocrude yield and C content, but also decreased its quality via increased N content. This increase in N corresponded with a decrease in aqueous ammonium recovery, thus decreasing the recyclability of the ACP. We found that less concentrated slurries ( $30 \text{ g L}_{\text{rxn}}^{-1}$ ) of high-lipid microalgae consistently produced higher yields of high-quality biocrude. At  $200 \text{ }^\circ\text{C}$ , 31.6 min, these slurries also maximized nutrients for ACP recycling, including  $\text{NH}_4^+$ , total N,  $\text{PO}_4^{3-}$ , total P, and S while limiting N and S recovery in the biocrude to less than 5 and 8 %, respectively. At a higher temperature ( $300 \text{ }^\circ\text{C}$ ) but with less reaction time (3.2 min), these slurries produced biocrude with high fatty acid recoveries, including 89.3, 80.1, and 64.7 wt% of SAFA, MUFA, and PUFA. Such high recoveries of unsaturated

fatty acids had not been demonstrated before at such severe conditions, suggesting that fast HTL may be an effective means of extracting and preserving unsaturated fatty acids. The trade-offs between high ACP recycling at moderate severity and high biocrude fatty-acid recovery at high severity presented an excellent opportunity for quantitative modeling to maximize both of these metrics.

The empirical observations from previous chapters then led to the development of a gravimetric, elemental, multiphase kinetic model in Chapter VI. The model pioneers a new methodology for modeling HTL via chemical kinetics that combines the sophistication of molecular-level reaction pathways for model compounds with the tractability of lumped product fractions powered by the vast experimental data we presented in Chapters IV and V. This novel quantitative model is capable of calculating total, carbon, and nitrogen yields for the solid, biocrude, ammonia, and collective aqueous, volatile, and gas products as functions of HTL process variables such as temperature, time, concentration, and microalgal biochemical composition. This effort marks the first time that slurry concentration, Maillard reactions, and elemental information have been incorporated into a kinetic model for HTL, in addition to expanding the domain of reaction severities and biochemical profiles beyond the ranges of applicability for previous models. We found that the kinetic model broadly predicts a variety of dependent measurements with reasonable accuracy, and calculations for the biocrude and ammonia fractions are exceptionally accurate. The fidelity of model calculations substantiate the usefulness of the model for optimization of target metrics like biocrude C recovery and aqueous ammonium recovery, which will ultimately help improve the sustainability and EROI for algal biorefining processes.

### **7.3 Recommendations for future research**

In Chapters III to V, we observed some variability in product yields and compositions between different microalgal species even after controlling for proximate biochemical composition (i.e., lipid, protein, and carbohydrate). A significant extent of the variability for

some product characteristics may adequately be explained by a more detailed accounting of the biochemical components. For example, we found significant variability in  $\text{PO}_4^{3-}$ -P that was not explained by similar overall lipid content in Section 5.3.3; however, detailed information about the relative amounts of phospholipids and DNA, for example (among other P-containing biomolecules), could reveal trends explaining these differences in phosphate recovery. Another example was S recovery in the biocrude, which varied significantly between biochemically comparable species, even at high reaction severity (Section 4.3.7). In this case, an accounting of the specific S-containing amino acids, as well as perhaps sulfolipids, may be necessary to explain differences in S recovery. Future studies aimed at understanding how the distributions P, S, and other low-abundance elements are affected by specific biochemical subgroups would help illuminate the discrepancies we observed at the proximate-biochemical-composition level. Such experiments would be necessary to produce an accurate kinetic model describing the partitioning of these elements during HTL.

We presented evidence that the Maillard reaction between sugars and amino acids produced components that increased biocrude yield, C recovery, and N recovery at the expense of aqueous yield and  $\text{NH}_4^+$ -N recovery. Moreover, increased concentration appeared to promote this reaction. Peterson et al. [46] showed that when glycine, a model amino acid, was in excess compared to glucose, a model sugar, the destruction of glycine always increased proportionally with increasing initial concentrations of glucose. However, when glucose was in excess compared to glycine, glucose destruction could be either be increased or decreased by the presence of glycine depending on reaction time and the initial glucose concentration. These results suggest that microalgae with high carbohydrate content relative to protein content may promote Maillard-reaction-product selectivity, as amino acids appear to preferentially participate in the Maillard reaction instead of self-degrading. More interestingly, they also suggest that there may be an optimal ratio of proteins and carbohydrates that inhibits the Maillard reaction, depending on reaction conditions. This dissertation found significant evidence that the Maillard reaction negatively affects the quality of the biocrude

(Section 4.3.4) and the recyclability of the ACP (Section 5.3.2); therefore, the elucidation of an ideal proportion of carbohydrates and proteins, slurry concentration, and reaction conditions that minimizes this Maillard reaction, thereby allowing the amino acids and sugars to break down without reacting together, would be tremendously valuable in advancing the feasibility of producing biofuel from microalgae via HTL. Furthermore, a kinetic analysis that proposes reaction mechanisms and associated Arrhenius parameters would enable the development of more sophisticated quantitative models. These models would greatly facilitate the discovery of optimal conditions for minimizing the extent of the Maillard reaction.

Future HTL modeling efforts that incorporate other feedstocks, such as bacteria, yeast, and food waste, would further expand the applicability and scope of such models. Furthermore, models that account for the distribution of additional elements such as H, S, O, and P, as well as some metals would enable even deeper process optimization. Such models likely would require more granular biochemical data for the biomass, as we explain earlier, in addition to more detailed experimental data. These data could include, among many other possibilities: measured abundances of amino acids and saccharides in the ACP, ash content and/or ICP-OES measurements of the product fractions to reveal metal contents, and high-performance liquid chromatography (HPLC) characterization of the biocrude and ACP to estimate the yield of oligomerization products. However, as we describe in the previous section, quantitative models for HTL are merely one step in the algal biorefinery process. The field currently lacks mathematical models for some important steps in the process, including the effects of steady-state ACP recycling on algal growth and HTL products, as well as the catalytic upgrading of the biocrude. Such steps are important for the overall sustainability of biofuel production from microalgae via HTL, as they dictate the extent of fresh nutrients required for algal growth and the limit of EROI, respectively. Quantitative models for those steps, among others, are needed to characterize the viability of microalgae-based fuels as a competitor to those of conventional petroleum and thus as a driver for reducing anthropogenic emissions of greenhouse gases.

## APPENDICES

## APPENDIX A

### Additional figures and calculations for Chapter II

## A.1 Representative 1.67-mL reactor heat-up temperature profiles

Time [s]	Set-point temperature [°C]								
	200	250	300	350	400	450	500	550	600
0	40.5	40.8	40.3	40.5	40.7	41.7	41.7	41.5	40.5
3	52.8	58.3	56.5	64.9	73.0	85.3	107.7	98.1	107.2
6	66.0	76.5	74.6	98.7	129.0	117.4	163.0	160.9	185.3
9	77.0	93.5	92.2	133.3	164.1	139.7	196.2	211.0	231.8
12	88.1	109.2	110.4	161.8	191.4	175.3	225.6	255.6	272.2
15	96.8	123.9	128.1	181.4	212.3	202.5	249.5	287.5	304.3
18	106.0	136.8	144.8	199.2	231.4	227.0	272.4	316.8	334.4
21	113.8	148.0	157.5	213.1	247.1	246.2	292.2	340.7	358.1
24	121.8	157.5	169.6	226.6	262.3	265.0	310.4	362.7	381.5
27	126.4	166.9	180.7	237.7	275.4	280.7	327.4	381.5	-
30	130.6	175.1	191.3	249.0	286.9	296.3	342.2	398.9	-
33	136.2	183.5	200.2	258.5	297.4	309.4	355.7	-	-
36	142.0	188.0	208.7	267.6	306.8	322.4	368.9	-	-
39	147.0	191.8	215.6	275.0	315.2	333.3	382.3	-	-
42	151.7	197.5	222.3	281.4	322.3	343.9	-	-	-
45	156.0	202.9	227.4	286.2	327.8	353.1	-	-	-
48	160.0	207.5	232.4	291.0	331.1	361.7	-	-	-
51	163.5	211.9	238.6	296.2	338.3	369.4	-	-	-
54	166.9	215.7	242.5	301.5	342.4	375.9	-	-	-
57	169.8	219.3	246.9	305.9	347.3	381.1	-	-	-
60	172.6	222.4	251.6	310.2	352.0	386.1	-	-	-
63	175.0	225.3	255.3	313.9	355.9	392.6	-	-	-
66	177.4	227.8	259.1	317.5	359.9	-	-	-	-
69	179.3	230.1	262.4	320.6	363.2	-	-	-	-
72	181.3	232.2	265.6	323.6	366.6	-	-	-	-
75	182.9	234.1	268.4	326.1	369.5	-	-	-	-
78	184.6	235.8	271.1	328.5	372.4	-	-	-	-
81	185.8	237.4	273.4	330.6	374.8	-	-	-	-
84	187.2	238.7	275.7	332.7	377.3	-	-	-	-
87	188.3	240.0	277.7	334.5	379.2	-	-	-	-
90	189.4	241.1	279.6	336.0	381.2	-	-	-	-
93	190.3	242.1	281.2	337.4	382.8	-	-	-	-
96	191.2	243.1	282.8	338.7	384.4	-	-	-	-
99	192.0	243.9	284.1	339.8	385.8	-	-	-	-
102	192.7	244.7	285.4	340.8	387.1	-	-	-	-
105	193.4	245.4	286.6	341.7	388.2	-	-	-	-
108	194.0	246.0	287.6	342.6	389.3	-	-	-	-
111	194.5	246.5	288.6	343.3	390.2	-	-	-	-
114	195.1	247.0	289.5	344.0	390.9	-	-	-	-
117	195.6	247.5	290.4	344.6	391.7	-	-	-	-
120	196.0	247.8	291.2	345.2	392.3	-	-	-	-
123	196.3	248.2	291.8	345.7	393.0	-	-	-	-
126	196.7	248.5	292.5	346.2	393.6	-	-	-	-
129	197.0	248.8	293.1	346.6	394.1	-	-	-	-
132	197.4	249.1	293.6	347.0	394.6	-	-	-	-
135	197.6	249.3	294.1	347.3	395.1	-	-	-	-
138	197.8	249.5	294.5	347.6	395.5	-	-	-	-
141	198.1	249.7	294.9	347.9	395.9	-	-	-	-
144	198.3	249.9	295.2	348.2	396.2	-	-	-	-
147	198.4	250.1	295.6	348.4	396.5	-	-	-	-
150	198.6	250.3	295.9	348.7	396.8	-	-	-	-
153	198.8	250.4	296.1	348.8	397.0	-	-	-	-
156	199.0	250.5	296.4	349.0	397.2	-	-	-	-
159	199.1	250.5	296.6	349.1	397.4	-	-	-	-
162	199.2	250.7	296.8	349.3	397.6	-	-	-	-
165	199.3	250.7	296.9	349.4	397.7	-	-	-	-

Table A.1: Representative heat-up temperature profiles for 1.67 mL stainless-steel batch reactors filled with deionized water at different set-point temperatures.

## A.2 Applying the Valdez and Savage (2013) model

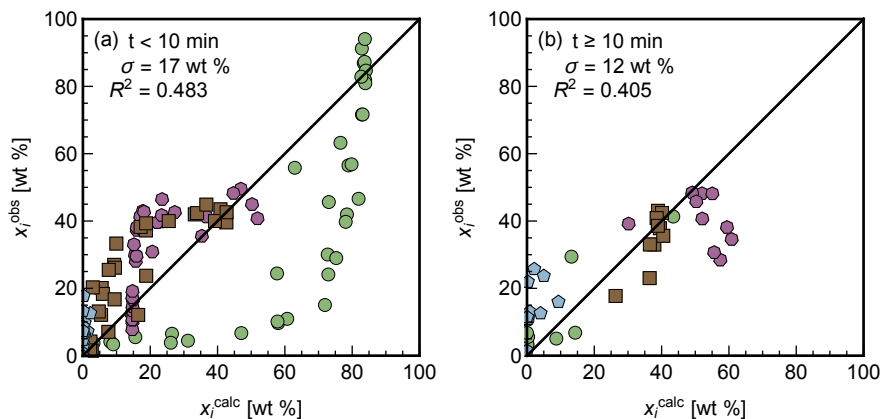


Figure A.1: Parity plots of observed vs. Valdez and Savage [53] model-calculated yields for solids (green circles), aqueous-phase and volatile products (purple heptagons), biocrude (brown squares), and gas (pale blue pentagons).

## A.3 Product fraction yield adjustments

In some instances, we employed corrections to obtain more physically meaningful results for an experiment. Given that we measured the mass of gas evolved by weighing a cooled reactor before and after venting the gas, there was always a possibility of losing small amounts of other material along with the gas. Along with random error, this occasional loss of non-gaseous products led to some “gas” yields being higher than expected based on the data from experiments with similar reaction conditions. In those rare cases, we recalculated the mass of gas evolved by linear interpolation of data points at equivalent set-point temperatures and with holding times immediately preceding and following the one of interest.

For reactions quenched at temperatures above 280 °C, the mass of aqueous phase recovered from the reactor was at least 80 % of the initial water loading. For reactions where the final temperature was below 280 °C, this recovery was sometimes less than 80 wt %, possibly due to the presence of wet, unreacted algae. To close the mass balance for these reactions, we assumed that the “lost” mass was distributed between the solids and wet aqueous phases in a 2:1 ratio. More specifically, we calculated correction factors ( $z$ ) and corrected yields of

product fraction  $i$  ( $x_i$ ) according to Equations (A.1) to (A.4):

$$z = \frac{(m_0 - m_T)}{2m_S + m_A} \quad (\text{A.1})$$

$$x_S = \frac{m_S(1 + 2z)}{m_0} \quad (\text{A.2})$$

$$x_A = \frac{m_A(1 + z)}{m_0} \quad (\text{A.3})$$

$$x_{WA} = \frac{m_{WA}(1 + z)}{m_{W,0}} \quad (\text{A.4})$$

Here  $m_0$  and  $m_{W,0}$  are the initial masses of dry algae and water,  $m_i$  is the recovered mass of product  $i$ ,  $m_{WA}$  is the mass of aqueous phase (before drying), and  $m_T = \sum_i m_i$  is the total mass of dried recovered products, ( $i = G, S, B, A$ ). Furthermore, if applying Equations (A.1) and (A.4) resulted in  $x_{WA} > 80$  wt %, we instead used Equation (A.5) to set  $z$  such that  $x_{WA} = 80$  wt % and recalculated all yields accordingly.

$$z = 0.8 \frac{m_{W,0}}{m_{WA}} - 1 \quad (\text{A.5})$$

This cutoff was implemented to avoid over-allocating unrecovered product to the solid and aqueous phase once recoveries reached those observed typically for reactions above 280 °C; above that threshold, the lost mass was attributed to volatiles. Table A.2 lists both the original and adjusted product yields for all experiments conducted in this study.

Set-point $T$ [°C]	Holding time [s]	Solids		Aqueous-phase products		Biocrude	Gas		Volatiles
		Original	Adjusted	Original	Adjusted		Original	Adjusted	
200	50	91	- <sup>a</sup>	12	-	0	15	0	0
	165	50	63	26	30	7	0	-	0
	410	54	56	30	31	12	1	-	0
	880	38	41	37	39	18	2	-	0
	2380	28	29	43	44	23	2	-	1
250	80	43	57	24	28	12	3	-	0
	135	46	-	35	-	17	0	-	3
	290	24	-	39	-	24	5	-	7
	1185	7	-	36	-	33	12	-	13
	3590	6	-	35	-	41	22	-	0
300	15	94	-	11	-	2	10	1	0
	25	87	-	10	-	2	3	-	0
	35	83	-	17	-	2	7	-	0
	60	46	57	27	30	13	0	-	0
	75	40	-	32	-	18	4	-	6
	105	30	-	32	-	26	6	-	5
	190	10	-	34	-	39	17	9	8
	480	7	-	33	-	42	11	-	7
	890	5	-	28	-	43	11	-	13
	2380	11	-	23	-	38	13	-	16
350	10	76	85	13	14	2	9	0	0
	70	24	-	40	-	27	6	-	4
	125	10	-	35	-	37	13	-	5
	260	4	-	23	-	42	18	-	13
	400	5	-	18	-	40	6	-	31
	540	4	-	19	-	43	7	-	26
	1480	3	-	12	-	42	26	-	17
	3585	7	-	12	-	39	24	-	19
400	15	87	-	8	-	2	6	-	0
	25	61	72	18	19	2	8	-	0
	50	29	-	41	-	25	4	-	0
	90	11	-	38	-	38	11	-	1
	125	7	-	17	-	40	20	11	26
	205	4	-	18	-	45	10	-	23
	350	3	-	14	-	40	7	-	36
	490	4	-	10	-	43	13	-	31
	890	3	-	9	-	36	13	-	39
2390	3	-	10	-	33	16	-	38	
450	35	42	-	32	-	20	1	-	6
	55	15	-	39	-	33	9	-	4
500	10	82	-	13	-	1	8	-	0
	15	78	83	10	11	1	5	-	0
	25	47	-	33	-	20	13	-	0
600	5	81	-	15	-	2	8	-	0
	15	60	72	15	17	4	8	-	0

Table A.2: Original and adjusted product yields (wt %) obtained after hydrothermal liquefaction of *Nannochloropsis oculata*. <sup>a</sup>Indicates no change from original.

## A.4 Product fraction residuals

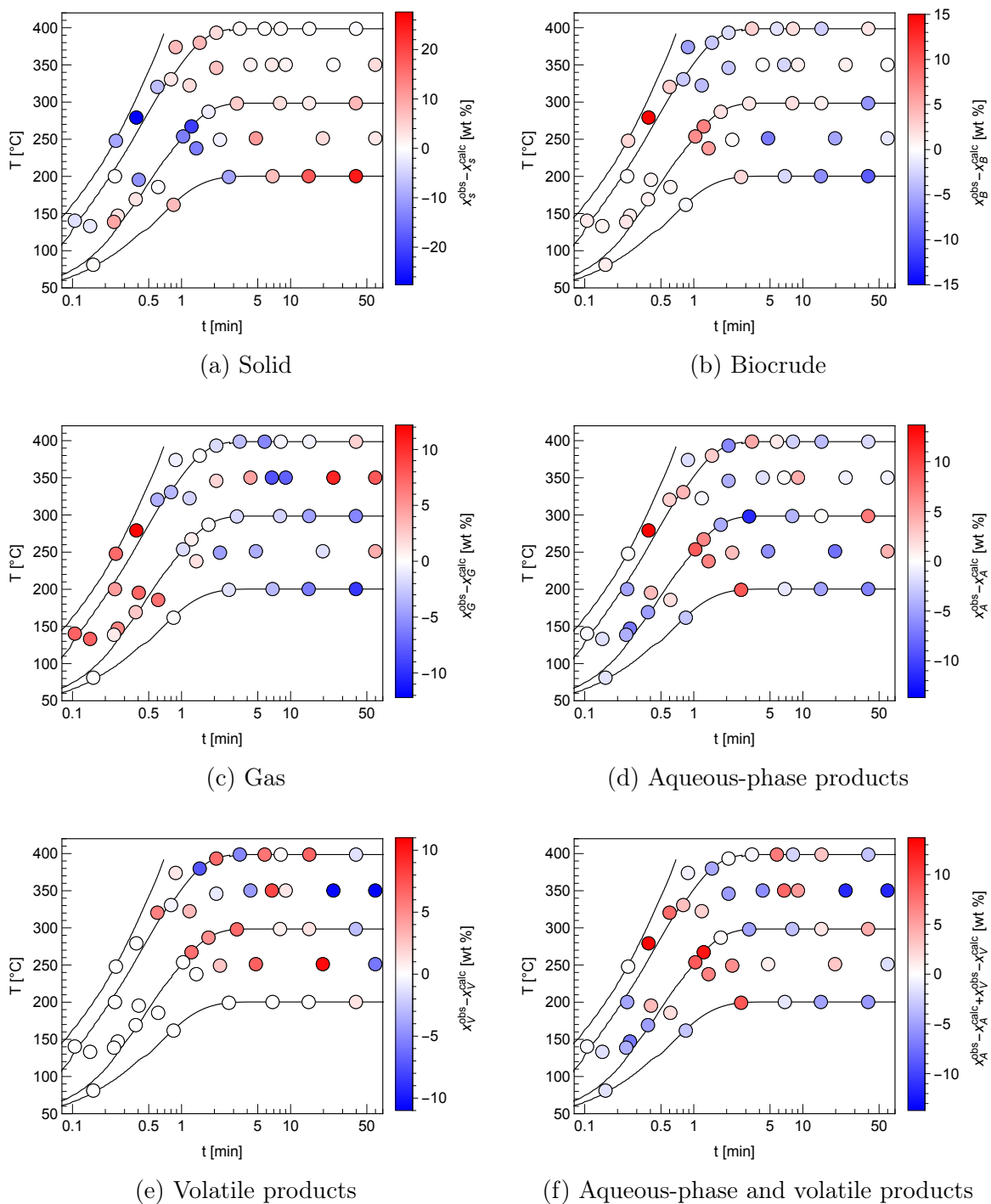


Figure A.2: Product fraction residuals ( $x_i^{obs} - x_i^{calc}$ ) from the HTL of *Nannochloropsis oculata* plotted as functions of final reactor temperature and holding time. Solid lines represent typical temperature profiles based on set-point temperatures of 200, 300, 400, and 500 °C. Red and blue represent values were under-calculated and over-calculated, respectively.

## A.5 Model validation

Table A.3 shows the data used in Figure 2.5 for model validation of biocrude yields. Due to differences in experimental procedures, such as aqueous drying temperature or gas measurement technique, we believe that comparisons of the other product yields are not meaningful.

Study	Isothermal or Profile	Set-point $T$ [°C]	Holding time [min]	Yields [wt %]				
				Solid	Aqueous-phase product	Biocrude	Gas	Volatile
Valdez et al. (2012)	Profile	250	20	20	50	33	0	0
		250	30	12	53	34	1	1
		250	60	8	52	42	0	0
		250	90	6	55	33	1	6
		250	120	5	50	34	2	10
		250	180	5	45	44	1	6
		300	10	5	51	50	1	0
		300	20	4	48	50	1	0
		300	40	3	38	48	7	4
		300	60	3	39	40	2	17
		300	90	2	40	40	3	15
		300	120	3	39	49	4	5
		350	10	5	32	42	2	17
		350	20	2	28	39	2	26
		350	40	4	26	43	3	26
		350	60	2	19	41	6	31
		350	90	2	21	42	0	34
		400	10	4	19	38	11	27
		400	20	3	16	38	10	32
		400	30	2	15	34	9	40
400	40	2	13	32	13	40		
Faeth et al. (2013)	Profile	300	1	62	- <sup>a</sup>	12	-	-
		300	3	14	-	36	-	-
		300	5	7	-	41	-	-
		300	60	-	-	43	-	-
		350	1	67	-	22	-	-
		350	3	6	-	47	-	-
		350	5	5	-	47	-	-
		350	60	-	-	38	-	-
		400	1	35	-	30	-	-
		400	3	4	-	47	-	-
		400	5	4	-	40	-	-
		400	60	-	-	32	-	-
450	1	9	-	49	-	-		
Billar and Ross (2011)	Isothermal	350	60	3	58	35	4	-
López Barreiro et al. (2013)	Isothermal	250	5	25	36	34	7	-
		375	5	6	19	54	20	-
Leow et al. (2015)	Isothermal	300	30	3	29	54	14	-

Table A.3: Product fraction yields used for model validation (reported on a dry wt % basis) [13, 24, 25, 39, 40]. All microalgae used were *Nannochloropsis oculata* or *Nannochloropsis gaditana*. “Isothermal” or “Profile” denote that an isothermal temperature or a temperature profile was used in the calculations, respectively. <sup>a</sup>Denotes datum not provided.

## A.6 Modeling carbon dioxide dissolution into the aqueous phase

In this section we show that measuring the mass of gas evolved during reactions within about 2 h after the reaction was quenched sufficiently limited the extent that  $\text{CO}_2$ , the overwhelmingly principal component of the gas produced from microalgal HTL [10, 21, 22], redissolves into the aqueous phase compared to 24 h.

### A.6.1 Kinetic limitations

To begin this analysis, we first consider the kinetics of the dissolution of  $\text{CO}_2$  into the aqueous phase:



Once dissolved,  $\text{CO}_{2(\text{aq})}$  dissociates to form  $\text{H}_2\text{CO}_3$ ,  $\text{HCO}_3^-$ , and  $\text{CO}_3^{2-}$ . However, the forward and reverse rate constants are reported to both be  $1 \times 10^{10} \text{ s}^{-1}$  [65]. This would lead to instantaneous dissolution kinetics for any reaction condition in our system, therefore we rule out any kinetic limitations of our system.

### A.6.2 Thermodynamic limitations

We next examine the saturation limit of  $\text{CO}_{2(\text{aq})}$  in our system to determine the fraction of  $\text{CO}_{2(\text{g})}$  that could dissolve into the aqueous phase. We measured up to 42 mg of gas evolved out of all reactions conducted; we approximate this to be entirely  $\text{CO}_{2(\text{g})}$ . We filled our 1.67 mL reactors with a range of 0.836 g to 1.076 g of water (assuming the algae contributes a negligible increase to the solution volume), which translates to a headspace range of 0.59 mL to 0.83 mL at 20 °C. Applying the ideal gas law translates the observed mass of gas to a maximum pressure of 3.9 MPa. At 20 °C, the solubility of  $\text{CO}_{2(\text{aq})}$  is 1.72, 36.33 and 59.40 g  $\text{CO}_{2(\text{g})}$   $(\text{kg water})^{-1}$  at pressures of 0.10 MPa, 2.53 MPa and 5.07 MPa, respectively (some values linearly interpolated) [141, 142]. These solubilities allow for a range of saturated  $\text{CO}_{2(\text{aq})}$  masses of 2 mg to 64 mg, depending upon the amount of water

loaded and the pressure of  $\text{CO}_{2(\text{g})}$  produced from the reaction. Our maximum observed mass of gas evolved of 42 mg is well within this range of expected saturated solubilities of  $\text{CO}_{2(\text{aq})}$ , so we therefore rule out any thermodynamic limitations of our system.

### A.6.3 Mass transfer limitations

The final limitation to consider is mass transfer limitations by diffusion. We know that in this system,  $\text{CO}_{2(\text{g})}$  instantaneously dissolves into  $\text{CO}_{2(\text{aq})}$ , and that our reaction conditions and experimental apparatus do not impose an appreciable  $\text{CO}_{2(\text{aq})}$  saturation limit. However, we have not considered how long it takes  $\text{CO}_{2(\text{aq})}$  to diffuse from the vapor-liquid interface. To model  $\text{CO}_{2(\text{aq})}$  diffusion in the aqueous phase of this system, we enlist a few assumptions:

- Aqueous phase may be modeled as pure water.
- The concentration of  $\text{CO}_{2(\text{g})}$  in the headspace,  $c_H$ , can be approximated as constant. In reality, it will decrease as  $\text{CO}_{2(\text{aq})}$  diffuses away from the vapor-liquid interface, thus decreasing the driving force for diffusion. However, we show that diffusion is slow enough that this assumption is reasonable.
- The concentration of  $\text{CO}_{2(\text{g})}$  in the headspace is less than the saturation limit of the pure water. If it were greater, the concentration of  $\text{CO}_{2(\text{aq})}$  would approach the saturation limit rather than the concentration of  $\text{CO}_{2(\text{g})}$  in the headspace.
- The concentration of  $\text{CO}_{2(\text{aq})}$  is  $c_0$  initially.

Applying Fick's Second Law to the geometry of a cylindrical reactor for transient, 1-D diffusion yields the following general equation, initial condition, and boundary conditions:

$$\frac{\partial c}{\partial t} = \mathcal{D} \frac{\partial^2 c}{\partial z^2} \quad (\text{A.7})$$

$$c(0, z) = c_0 \quad (\text{A.8})$$

$$c(t, 0) = c_H \quad (\text{A.9})$$

$$\left. \frac{\partial c}{\partial z} \right|_{t,L} = 0 \quad (\text{A.10})$$

Here  $c$  is the concentration of  $\text{CO}_{2(\text{aq})}$  in pure water,  $\mathcal{D}$  is the diffusivity of  $\text{CO}_{2(\text{aq})}$  in water, and  $L$  is the height of the liquid phase in the reactor. We assume the cylinder is positioned vertically and define  $z = 0$  to be the vapor-liquid interface, with the positive direction pointing down. Non-dimensionalization of the system by  $\Theta = (c - c_0)/(c_H - c_0)$ ,  $\xi = z/L$ , and  $\tau = \mathcal{D}t/L^2$  transforms Equations (A.7) to (A.10) into the following:

$$\frac{\partial \Theta}{\partial \tau} = \frac{\partial^2 \Theta}{\partial \xi^2} \quad (\text{A.11})$$

$$\Theta(0, \xi) = 0 \quad (\text{A.12})$$

$$\Theta(\tau, 0) = 1 \quad (\text{A.13})$$

$$\left. \frac{\partial \Theta}{\partial \xi} \right|_{\tau,1} = 0 \quad (\text{A.14})$$

Applying superposition allows separation of the solution into transient and steady-state components:

$$\Theta(\tau, \xi) = \Theta_{ss}(\xi) + \Theta_t(\tau, \xi) \quad (\text{A.15})$$

Applying Equation (A.15) to Equations (A.11), (A.13) and (A.14) leads to the following set of equations for the steady-state solution:

$$0 = \frac{d^2 \Theta_{ss}}{d\xi^2} \quad (\text{A.16})$$

$$\Theta_{ss}(0) = 1 \quad (\text{A.17})$$

$$\left. \frac{d\Theta_{ss}}{d\xi} \right|_1 = 0 \quad (\text{A.18})$$

Equations (A.16) to (A.18) can be readily solved to provide the steady-state solution:

$$\Theta_{ss}(\xi) = 1 \quad (\text{A.19})$$

Applying Equation (A.15) to Equations (A.11) to (A.14) and (A.19) leads to the following set of equations for the transient solution:

$$\frac{\partial \Theta_t}{\partial \tau} = \frac{\partial^2 \Theta_t}{\partial \xi^2} \quad (\text{A.20})$$

$$\Theta_t(0, \xi) = -1 \quad (\text{A.21})$$

$$\Theta_t(\tau, 0) = 0 \quad (\text{A.22})$$

$$\left. \frac{\partial \Theta_t}{\partial \xi} \right|_{\tau, 1} = 0 \quad (\text{A.23})$$

Applying separation of variables by  $\Theta_t(\tau, \xi) = T(\tau) \Xi(\xi)$  to Equation (A.20) and rearranging terms by independent variable leads to the following general equation:

$$\frac{1}{T} \frac{dT}{d\tau} = \frac{1}{\Xi} \frac{d^2 \Xi}{d\xi^2} = -\lambda^2 \quad (\text{A.24})$$

Equation (A.24) implies:

$$T(\tau) \propto \exp(-\lambda^2 \tau) \quad (\text{A.25})$$

Equations (A.22) to (A.24) allow the spatial component to be recast into the following simplified system of equations:

$$\frac{d^2 \Xi}{d\xi^2} + \lambda^2 \Xi(\xi) = 0 \quad (\text{A.26})$$

$$\Xi(0) = 0 \quad (\text{A.27})$$

$$\left. \frac{d\Xi}{d\xi} \right|_1 = 0 \quad (\text{A.28})$$

The general solution to Equation (A.26) is  $\Xi(\xi) = A \sin(\lambda \xi) + B \cos(\lambda \xi)$ . Applying Equation (A.27) leads to  $B = 0$ . Applying Equation (A.28) leads to  $A \lambda \cos(\lambda) = 0$ , which provides the constraint on eigenvalues for this system,  $\cos(\lambda_n) = 0$ , and implies:

$$\Xi(\xi) \propto \sin(\lambda\xi) \quad (\text{A.29})$$

Examining the eigenvalue constraint leads to the solution for the eigenvalues:

$$\lambda_n = n\pi - \pi/2 \quad n = 1, 2, 3\dots \quad (\text{A.30})$$

The transient solution may then be composed from Equations (A.25) and (A.29):

$$\Theta_t(\tau, \xi) = \sum_{n=1}^{\infty} A_n \sin(\lambda_n \xi) \exp(-\lambda_n^2 \tau) \quad (\text{A.31})$$

Applying Equation (A.21) to Equation (A.31) yields:

$$\Theta_t(0, \xi) = \sum_{n=1}^{\infty} A_n \sin(\lambda_n \xi) = -1 \quad (\text{A.32})$$

The spatial eigenfunction  $\sin(\lambda_n \xi)$  is orthogonal with respect to the inner product with weight function 1. Multiplication by  $\sin(\lambda_m \xi)$  and integration over the domain leads to:

$$\sum_{n=1}^{\infty} A_n \int_0^1 \sin(\lambda_n \xi) \sin(\lambda_m \xi) d\xi = - \int_0^1 \sin(\lambda_m \xi) d\xi \quad (\text{A.33})$$

Orthogonality allows removal of all components where  $n \neq m$  by the Dirac delta:

$$\sum_{n=1}^{\infty} A_n \delta_{nm} \int_0^1 \sin^2(\lambda_m \xi) d\xi = - \int_0^1 \sin(\lambda_m \xi) d\xi \quad (\text{A.34})$$

The Dirac delta removes the summation and allows for direct computation of the Fourier coefficients:

$$A_n = - \frac{\int_0^1 \sin(\lambda_n \xi) d\xi}{\int_0^1 \sin^2(\lambda_n \xi) d\xi} = \frac{\frac{(\cos(\lambda_n) - 1)}{\lambda_n}}{\frac{1}{2} - \frac{\sin(2\lambda_n)}{4\lambda_n}} \quad (\text{A.35})$$

Inspection of the eigenvalue constraint in Equation (A.30) shows that  $\sin(2\lambda_n) = 0$  for all  $n = 1, 2, 3\dots$ , which simplifies Equation (A.35) to:

$$A_n = \frac{2}{\lambda_n} (\cos(\lambda_n) - 1) \quad (\text{A.36})$$

The full non-dimensional solution may then be written by combining Equations (A.15), (A.19), (A.30), (A.31) and (A.36):

$$\Theta(\tau, \xi) = 1 + 2 \sum_{n=1}^{\infty} \frac{\cos(n\pi - \pi/2) - 1}{n\pi - \pi/2} \sin[(n\pi - \pi/2)\xi] \exp[-(n\pi - \pi/2)^2 \tau] \quad (\text{A.37})$$

The full dimensional solution follows from Equation (A.37):

$$\boxed{\frac{c(t, z) - c_0}{c_H - c_0} = 1 + 2 \sum_{n=1}^{\infty} \frac{\cos(n\pi - \pi/2) - 1}{n\pi - \pi/2} \sin\left[(n\pi - \pi/2) \frac{z}{L}\right] \exp\left[-(n\pi - \pi/2)^2 \frac{\mathcal{D}t}{L^2}\right]}$$

(A.38)

Finally, the fractional uptake of CO<sub>2</sub> in the aqueous phase as a function of time,  $\mathcal{F}(t)$ , may be calculated as:

$$\mathcal{F}(t) = \int_0^L \frac{c(t, z)}{c_H} dz \quad (\text{A.39})$$

To apply Equations (A.37) to (A.39) to our system, we employ a diffusion coefficient (at 25 °C and 14.0 MPa) of  $\mathcal{D} = 2.233 \times 10^{-9} \text{ m}^2/\text{s}$  [66] and a minimum and maximum depth of aqueous phase of  $L = 2.6 \text{ cm}$  and  $3.4 \text{ cm}$ , respectively (based on values presented in Section A.6.2 and an inner reactor diameter of 0.64 cm). Cadogan et al. [66] demonstrate that the diffusion coefficient of CO<sub>2(aq)</sub> in water is insensitive to higher pressures at 25 °C, so we expect this value to be close to that in the range of 0.10 MPa to 5.07 MPa. Moreover we also assume that the concentration of CO<sub>2(aq)</sub> initially is 10 % of the initial concentration of CO<sub>2(g)</sub>, or  $c_0 = 0.1c_H$ . This assumes that upon quenching the reaction, 90 % of the carbon dioxide exists in the vapor phase, which is reasonable on the basis that rapid quenching significantly perturbs the system from equilibrium. This assumption leads to an initial fractional uptake of  $\mathcal{F}(0) = 0.12$ . Figure A.3 shows plots of  $c(t, z)/c_H$  at 2 h and 24 h for  $L = 2.6 \text{ cm}$  and  $3.4 \text{ cm}$ . Comparing Figures A.3a and A.3b ( $t = 2 \text{ h}$ ) to Figures A.3c and A.3d ( $t = 24 \text{ h}$ ) shows that, for this reaction system, the fractional uptake of CO<sub>2</sub> in the

aqueous phase,  $\mathcal{F}$ , more than doubles from 0.25 and 0.22 to 0.63 and 0.52, for aqueous phase depths of 2.6 cm and 3.4 cm, respectively.

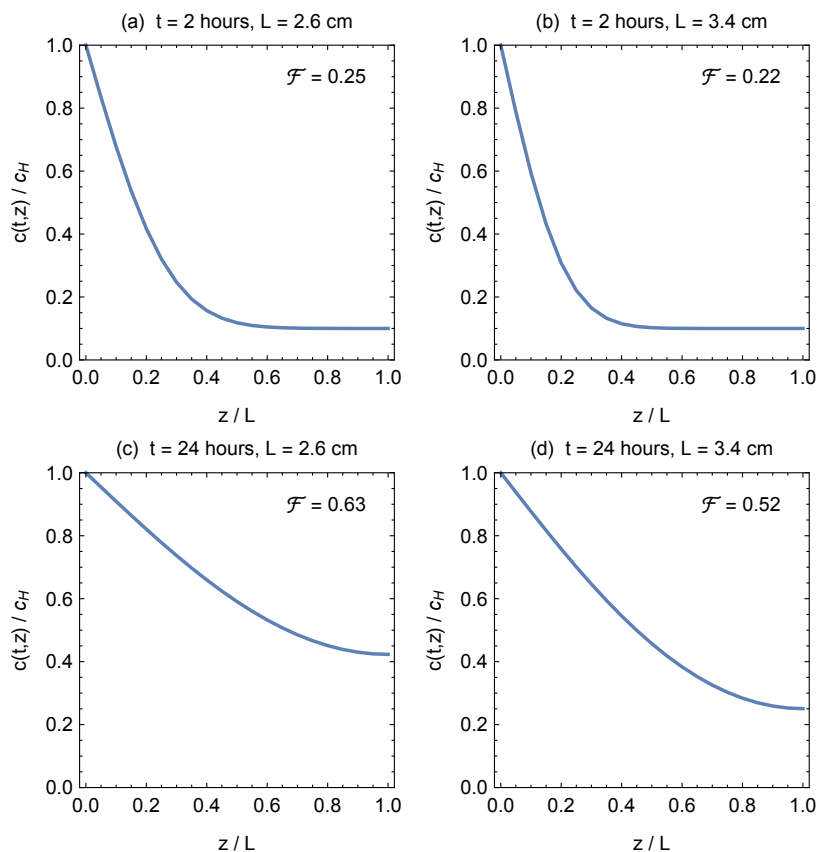


Figure A.3: Relative concentration profiles,  $c(t, z)/c_H$ , of dissolved  $\text{CO}_2(\text{aq})$  with respect to depth of aqueous phase ( $z = 0$  is the vapor-liquid interface) at different times.  $\mathcal{F}$  is the fractional uptake of  $\text{CO}_2$  in the aqueous phase at a given time.

This problem of mitigating  $\text{CO}_2(\text{g})$  dissolution into the aqueous phase to produce a more accurate measurement of gas evolved during the reaction is clearly diffusion limited. Shortening the time from the moment the reaction is quenched to the moment gas is measured to 2 h or less, compared to 24 h, will decrease the fractional uptake of  $\text{CO}_2$  by over a factor of about 2.5. Moreover re-agitating reactors prior to gas measurement may help liberate  $\text{CO}_2(\text{aq})$  back into the vapor phase.

## APPENDIX B

### Constant-growth-temperature figures and tabular data for Chapter III

#### B.1 Figures with constant-growth-temperature data

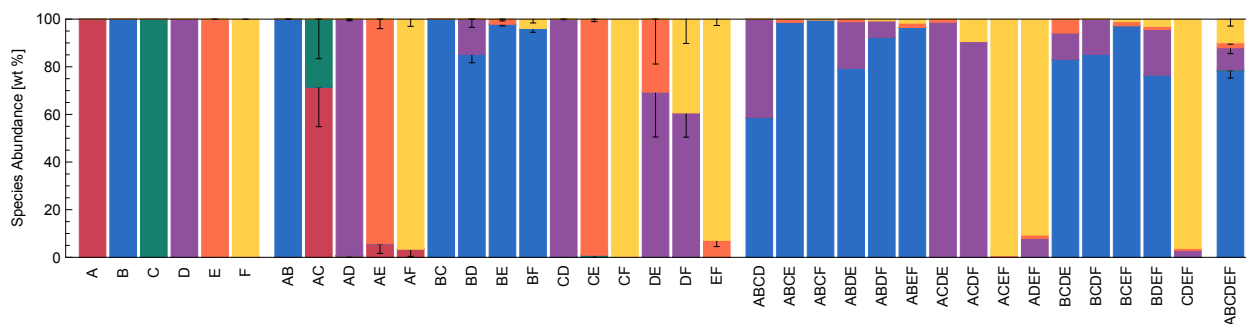


Figure B.1: Species abundance (wt %) for constant-growth-temperature species combinations. *Ankistrodesmus falcatus* (A), *Chlorella sorokiniana* (B), *Pediastrum duplex* (C), *Scenedesmus acuminatus* (D), *Scenedesmus ecornis* (E), and *Selenastrum capricornutum* (F) are indicated as red, blue, green, purple, orange, and yellow, respectively. Only single estimates for species abundance available for 4-species polycultures. Error bars represent SE.

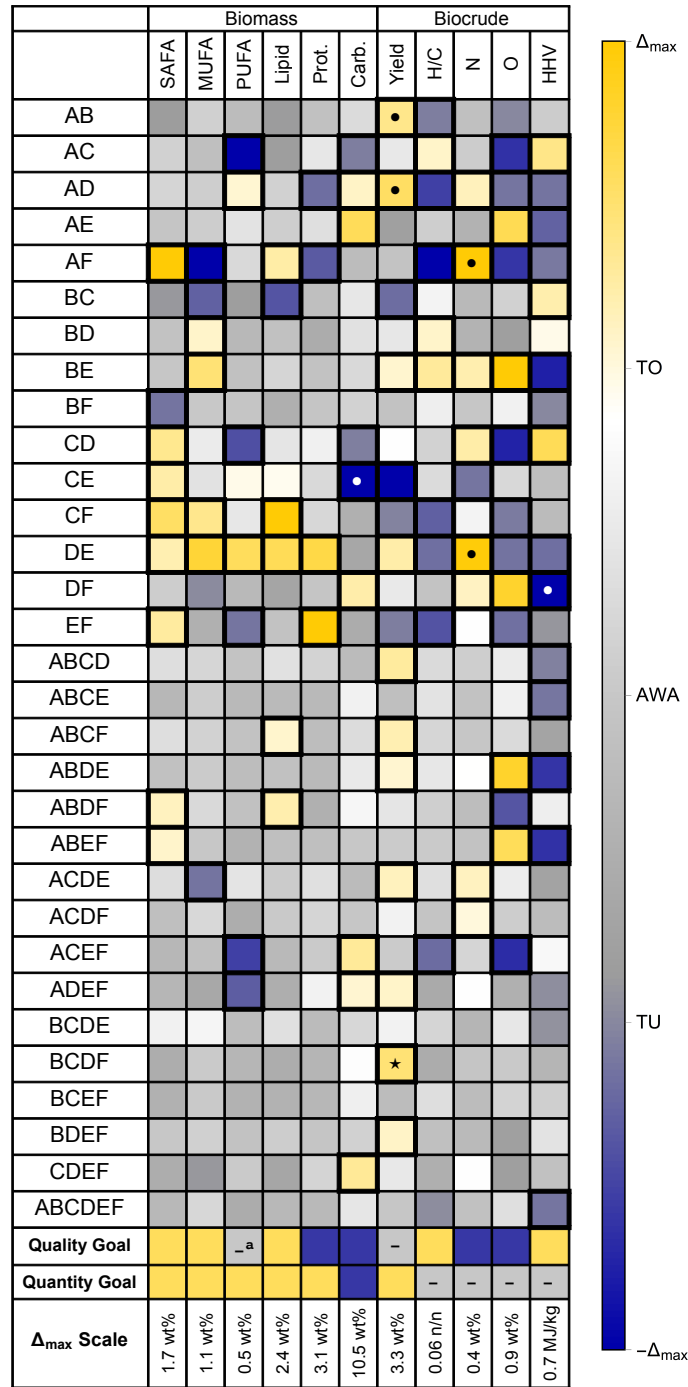


Figure B.2: Polyculture performance relative to thresholds for TO (maize, bold-outline cells), AWA (gray), and TU (blue, bold-outline cells) for SAFA, MUFA, and PUFA yields, lipid, protein, and carbohydrate contents, and biocrude yield, H/C, N content, O content, and HHV under constant growth temperature. Polycultures comprised 2-, 4-, and 6-species combinations of *Ankistrodesmus falcatus* (A), *Chlorella sorokiniana* (B), *Pediastrum duplex* (C), *Scenedesmus acuminatus* (D), *Scenedesmus ecornis* (E), and *Selenastrum capricornutum* (F). ★ and • indicate statistically significant differences with  $\alpha = 0.05$  and  $0.15$ , respectively.  $\Delta_{max}$  corresponds to the highest absolute difference between the value for the polyculture and the threshold for TO or TU for each dependent variable.

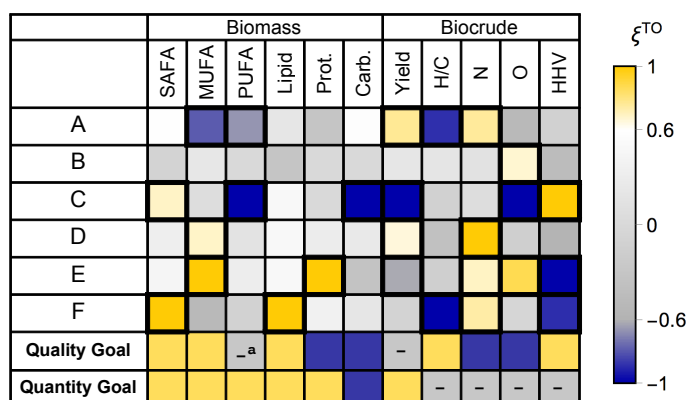


Figure B.3: Relative extent ( $\xi^{\text{TO}}$ ) of net TO (maize) and TU (blue) in bicultures as a function of species inclusion of *Ankistrodesmus falcatus* (A), *Chlorella sorokiniana* (B), *Pediastrum duplex* (C), *Scenedesmus acuminatus* (D), *Scenedesmus ecornis* (E), and *Selenastrum capricornutum* (F) for SAFA, MUFA, and PUFA yields, lipid, protein, and carbohydrate contents, and biocrude yield, H/C, N content, O content, and HHV for constant growth temperature. <sup>a</sup>Denotes goal not applicable for this metric.

## B.2 Properties of biomass and biocrude for constant- and variable-growth-temperature cultures

Species Combination	SAFA [wt%]	MUFA [wt%]	PUFA [wt%]	Lipid [wt%]	Protein [wt%]	Carb. [wt%]
A	3.91 ± 1.43	3.46 ± 0.43	3.62 ± 0.01	11.0 ± 1.9	32.7 ± 3.9	48.7 ± 4.2
B	4.77 ± 1.08	0.68 ± 0.32	6.74 ± 1.12	12.2 ± 2.5	48.4 ± 1.3	34.8 ± 2.9
C	2.68 ± 0.28	1.85 ± 0.09	4.84 ± 0.82	9.4 ± 1.2	38.4 ± 4.3	48.6 ± 3.7
D	2.91 ± 0.46	1.14 ± 0.37	3.61 ± 0.53	7.7 ± 1.2	32.1 ± 1.8	52.6 ± 2.2
E	1.10	0.65	2.7	4.5	30.3 ± 2.3	47.0
F	4.94 ± 0.42	3.69 ± 0.76	2.76 ± 0.19	11.4 ± 0.8	27.1 ± 1.2	50.8 ± 1.8
AB	4.04 ± 0.68	1.05 ± 0.35	6.07 ± 1.00	11.2 ± 1.4	46.6 ± 1.3	39.1 ± 2.0
AC	3.61 ± 0.13	2.82 ± 0.13	3.14 ± 0.60	9.6 ± 0.9	36.3 ± 2.8	47.8 ± 2.3
AD	3.13 ± 0.75	1.43 ± 0.23	3.65 ± 0.60	8.2 ± 1.4	31.5 ± 1.3	53.7 ± 2.7
AE	1.25 ± 0.04	1.07 ± 0.18	3.12 ± 0.20	5.5 ± 0.0	31.2 ± 3.6	55.1 ± 3.6
AF	6.62 ± 1.48	2.37 ± 1.53	3.02 ± 0.60	12.0 ± 2.7	26.0 ± 1.9	50.3 ± 2.2
BC	2.92 ± 0.21	0.36 ± 0.05	5.19 ± 0.46	8.5 ± 0.7	46.7 ± 1.0	41.4 ± 1.1
BD	4.34 ± 0.67	1.25 ± 0.30	5.49 ± 0.48	11.1 ± 1.4	38.6 ± 1.7	43.5 ± 3.0
BE	4.64 ± 0.49	1.21 ± 0.08	6.21 ± 0.32	12.1 ± 0.8	46.3 ± 1.5	38.3 ± 1.7
BF	4.53 ± 1.05	0.86 ± 0.22	6.41 ± 1.01	11.8 ± 2.3	46.7 ± 0.6	37.9 ± 1.7
CD	3.52 ± 0.48	1.53 ± 0.42	3.40 ± 0.28	8.5 ± 1.1	36.0 ± 1.1	47.8 ± 0.2
CE	3.11 ± 0.06	1.16 ± 0.01	4.73 ± 1.27	9.0 ± 1.3	32.5 ± 6.9	36.6 ± 7.5
CF	5.88 ± 1.10	4.10 ± 1.56	3.78 ± 0.73	13.8 ± 3.2	29.8 ± 2.5	49.7 ± 4.6
DE	3.26 ± 0.37	1.99 ± 0.06	3.89 ± 0.73	9.1 ± 1.1	34.3 ± 2.3	48.4 ± 1.9
DF	3.82 ± 0.54	1.17 ± 0.50	3.13 ± 0.42	8.1 ± 0.1	30.0 ± 1.0	55.1 ± 0.9
EF	5.43 ± 1.49	2.18 ± 1.77	2.63 ± 0.05	10.2 ± 0.2	33.4 ± 2.6	48.6 ± 2.6
ABCD	4.27 ± 0.29	1.48 ± 0.24	5.31 ± 0.83	11.1 ± 1.4	42.9 ± 5.0	40.4 ± 4.7
ABCE	3.52 ± 0.29	0.92 ± 0.00	5.59 ± 0.94	10.0 ± 0.7	43.0 ± 2.7	43.7 ± 2.4
ABCF	4.83 ± 0.96	1.20 ± 0.37	6.35 ± 0.98	12.4 ± 2.0	44.0 ± 4.7	40.0 ± 5.0
ABDE	4.00 ± 0.58	0.94 ± 0.30	5.42 ± 0.27	10.4 ± 0.9	41.1 ± 2.9	45.7 ± 2.9
ABDF	5.19 ± 1.06	1.52 ± 0.34	6.01 ± 1.61	12.7 ± 2.3	37.9 ± 4.7	47.8 ± 4.4
ABEF	5.09 ± 0.80	0.75 ± 0.19	4.98 ± 1.20	10.8 ± 1.0	44.5 ± 2.2	35.4 ± 2.1
ACDE	3.22 ± 0.35	0.49 ± 0.07	4.14 ± 0.50	7.8 ± 0.9	34.5 ± 1.8	51.2 ± 1.5
ACDF	3.04 ± 0.70	1.97 ± 0.10	3.12 ± 0.68	8.1 ± 1.4	33.1 ± 3.0	52.3 ± 3.9
ACEF	3.66 ± 0.28	3.24 ± 0.22	2.44 ± 0.13	9.4 ± 0.6	27.7 ± 0.8	54.1 ± 0.6
ADEF	3.52 ± 0.12	1.68 ± 0.69	2.54 ± 0.51	7.7 ± 1.0	30.8 ± 0.6	53.2 ± 1.4
BCDE	4.62 ± 0.53	1.51 ± 0.21	5.46 ± 0.42	11.6 ± 1.2	41.8 ± 3.2	41.0 ± 3.4
BCDF	3.54 ± 1.96	0.90 ± 0.64	5.08 ± 1.73	9.5 ± 4.3	39.3 ± 0.5	49.8 ± 0.9
BCEF	3.08 ± 0.94	0.79 ± 0.26	5.00 ± 0.25	8.9 ± 0.9	41.3 ± 1.5	44.6 ± 1.8
BDEF	4.37 ± 1.06	1.25 ± 0.53	5.66 ± 0.73	11.3 ± 2.3	43.7 ± 2.1	41.0 ± 1.6
CDEF	2.89 ± 0.09	0.99 ± 0.60	2.88 ± 0.69	6.8 ± 1.4	29.4 ± 2.1	56.0 ± 2.6
ABCDEF	3.50 ± 0.62	1.67 ± 0.10	4.17 ± 0.66	9.3 ± 1.2	39.6 ± 0.9	45.0 ± 0.9

Table B.1: Biochemical composition of constant-growth-temperature species combinations. Uncertainty represents SE.

Species Combination	H/C [n/n]	N [wt%]	O [wt%]	HHV [MJ/kg]	Yield [wt%]	Production <sup>a</sup> [mg/L]	Stability <sup>a</sup> ( $\mu/\sigma$ )
A	1.52 ± 0.03	4.74 ± 0.07	12.5 ± 1.1	35.3 ± 0.5	29.6 ± 2.2	13.5 ± 3.4	1.58 ± 0.28
B	1.44 ± 0.03	6.14 ± 0.08	12.2 ± 0.6	34.5 ± 0.4	36.8 ± 0.3	78.3 ± 15.3	3.00 ± 0.51
C	1.50 ± 0.05	5.36 ± 0.27	13.7 ± 1.0	34.3 ± 0.2	36.3 ± 2.2	28.7 ± 12.3	2.07
D	1.40 ± 0.02	5.36 ± 0.13	12.0 ± 0.5	34.8 ± 0.3	34.8 ± 1.0	77.1 ± 8.2	2.42 ± 0.57
E	1.46 ± 0.02	5.41 ± 0.12	12.4 ± 0.5	34.7 ± 0.3	34.4 ± 4.1	12.5 ± 3.8	1.07 ± 0.19
F	1.48 ± 0.00	4.88 ± 0.16	12.6 ± 0.9	35.0 ± 0.5	33.5 ± 0.8	141.0 ± 20.5	1.98 ± 0.65
AB	1.44 ± 0.02	5.94 ± 0.06	12.2 ± 0.1	34.5 ± 0.0	38.1 ± 0.8	81.8 ± 10.1	2.61 ± 0.19
AC	1.53 ± 0.02	4.95 ± 0.23	11.9 ± 0.6	35.6 ± 0.4	33.9 ± 0.7	26.3 ± 4.7	1.40 ± 0.21
AD	1.37 ± 0.02	5.42 ± 0.08	11.8 ± 0.3	34.7 ± 0.2	36.7 ± 0.2	74.7 ± 11.1	2.30 ± 0.41
AE	1.47	5.11	13.1	34.6	30.6	1.4 ± 1.1	3.41 ± 0.92
AF	1.42 ± 0.03	5.27 ± 0.10	11.9 ± 0.2	34.9 ± 0.2	33.0 ± 0.7	113.0 ± 12.8	2.41 ± 0.24
BC	1.48 ± 0.02	5.92 ± 0.04	12.4 ± 1.4	34.6 ± 0.7	35.6 ± 0.9	56.1 ± 14.4	2.29 ± 0.69
BD	1.45 ± 0.01	5.75 ± 0.09	12.0 ± 0.4	34.8 ± 0.3	36.7 ± 0.6	49.7 ± 11.6	2.11 ± 0.41
BE	1.47 ± 0.01	6.22 ± 0.03	13.4 ± 1.0	33.9 ± 0.6	37.1 ± 0.3	50.1 ± 3.4	2.64 ± 0.33
BF	1.46 ± 0.01	6.06 ± 0.03	12.5 ± 0.9	34.5 ± 0.6	36.3 ± 0.7	59.3 ± 4.6	1.90 ± 0.24
CD	1.42 ± 0.01	5.46 ± 0.07	11.3 ± 0.4	35.2 ± 0.3	36.0 ± 1.0	47.1 ± 10.0	1.90 ± 0.29
CE	1.47 ± 0.02	5.31 ± 0.55	12.8 ± 0.0	34.7 ± 0.4	31.1 ± 0.7	15.4 ± 1.6	0.99 ± 0.35
CF	1.46 ± 0.02	5.20 ± 0.19	12.5 ± 0.1	34.8 ± 0.2	33.3 ± 0.9	92.3 ± 6.2	3.05 ± 0.97
DE	1.39 ± 0.02	5.79 ± 0.14	11.8 ± 0.2	34.6 ± 0.2	35.6 ± 1.1	29.8 ± 12.6	1.74 ± 0.48
DF	1.43 ± 0.03	5.41 ± 0.13	13.4 ± 0.7	34.1 ± 0.2	34.6 ± 1.0	100.0 ± 21.8	2.52 ± 0.31
EF	1.43 ± 0.01	5.33 ± 0.17	12.2 ± 0.4	34.8 ± 0.2	33.2 ± 0.8	46.9 ± 10.3	2.03 ± 0.64
ABCD	1.45 ± 0.02	5.85 ± 0.06	13.0 ± 1.0	34.2 ± 0.5	37.8 ± 0.6	53.2 ± 9.1	2.38 ± 0.69
ABCE	1.47 ± 0.01	6.00 ± 0.09	13.1 ± 0.9	34.2 ± 0.5	35.6 ± 0.6	32.6 ± 5.4	1.55 ± 0.31
ABCF	1.46 ± 0.01	6.11 ± 0.07	12.6 ± 0.6	34.3 ± 0.4	37.5 ± 0.2	57.8 ± 13.0	2.33 ± 0.27
ABDE	1.48 ± 0.01	6.12 ± 0.15	13.3 ± 0.9	34.0 ± 0.4	37.0 ± 0.7	40.5 ± 11.3	2.27 ± 0.21
ABDF	1.45 ± 0.01	5.81 ± 0.07	11.6 ± 0.4	35.0 ± 0.1	36.7 ± 1.1	52.9 ± 9.5	2.31 ± 0.71
ABEF	1.45 ± 0.02	5.97 ± 0.24	13.2 ± 0.1	34.0 ± 0.2	36.7 ± 0.6	42.2 ± 4.3	2.69 ± 0.24
ACDE	1.45 ± 0.02	5.47 ± 0.07	13.0 ± 0.4	34.4 ± 0.1	36.8 ± 0.8	36.8 ± 11.8	1.92 ± 0.30
ACDF	1.41 ± 0.02	5.36 ± 0.17	12.2 ± 0.3	34.7 ± 0.3	35.7 ± 0.8	63.2 ± 4.7	1.72 ± 0.27
ACEF	1.44 ± 0.03	5.00 ± 0.25	11.8 ± 0.3	35.2 ± 0.4	33.6 ± 0.4	38.4 ± 5.1	2.17 ± 0.34
ADEF	1.43 ± 0.01	5.33 ± 0.07	12.3 ± 0.1	34.7 ± 0.1	35.2 ± 0.6	37.2 ± 3.7	2.53 ± 0.49
BCDE	1.45 ± 0.02	5.78 ± 0.11	12.9 ± 0.6	34.3 ± 0.3	36.7 ± 0.6	25.7 ± 5.6	1.68 ± 0.20
BCDF	1.42 ± 0.02	5.99 ± 0.10	12.2 ± 0.7	34.4 ± 0.4	38.4 ± 0.3	49.0 ± 3.8	1.87 ± 0.46
BCEF	1.46 ± 0.02	5.84 ± 0.08	12.5 ± 0.3	34.5 ± 0.3	36.0 ± 0.8	38.3 ± 8.3	2.45 ± 0.43
BDEF	1.43 ± 0.01	5.68 ± 0.10	12.0 ± 0.4	34.7 ± 0.3	37.2 ± 0.4	40.7 ± 3.0	1.72 ± 0.68
CDEF	1.44 ± 0.01	5.33 ± 0.04	12.1 ± 0.1	34.9 ± 0.0	34.9 ± 1.2	40.8 ± 6.0	2.47 ± 0.39
ABCDEF	1.41 ± 0.01	5.77 ± 0.19	12.8 ± 0.3	34.2 ± 0.2	36.1 ± 0.3	36.1 ± 4.1	1.70 ± 0.13

Table B.2: Biocrude properties of constant-growth-temperature species combinations. <sup>a</sup>Reproduced from Narwani et al. [6]. Uncertainty represents SE.

Species Combination	SAFA [wt%]	MUFA [wt%]	PUFA [wt%]	Lipid [wt%]	Protein [wt%]	Carb. [wt%]
A	5.11 ± 0.79	3.36 ± 0.55	4.17 ± 1.43	12.6 ± 1.7	30.2 ± 2.5	50.3 ± 2.4
B	3.32 ± 0.25	0.49 ± 0.08	5.68 ± 0.23	9.5 ± 0.3	48.6 ± 0.8	39.2 ± 0.9
C	3.41 ± 1.01	1.18 ± 0.04	4.32 ± 1.22	8.9 ± 2.3	32.7 ± 3.8	52.7 ± 3.8
D	3.78 ± 0.26	1.19 ± 0.29	3.58 ± 0.21	8.5 ± 0.6	31.9 ± 0.8	54.1 ± 1.1
E	1.87 ± 0.65	2.05 ± 0.91	3.35 ± 0.25	7.3 ± 1.8	29.7 ± 2.8	43.6 ± 2.6
F	5.41 ± 0.79	2.01 ± 0.83	2.06 ± 0.24	9.5 ± 0.9	22.9 ± 1.1	59.3 ± 0.6
AB	3.98 ± 1.10	1.06 ± 0.24	5.09 ± 1.45	10.1 ± 2.7	44.0 ± 2.6	45.7 ± 1.7
AC	3.74 ± 0.66	3.74 ± 0.58	4.34 ± 0.60	11.8 ± 1.4	31.7 ± 0.9	50.2 ± 3.3
AD	3.55 ± 0.79	1.86 ± 0.35	3.95 ± 0.45	9.4 ± 1.6	30.6 ± 2.7	54.2 ± 3.1
AE	2.78	1.38	3.40	7.6	27.5	41.6
AF	5.27 ± 1.45	1.51 ± 0.85	2.35 ± 0.40	9.1 ± 1.3	25.5 ± 0.4	58.6 ± 2.2
BC	4.69 ± 1.50	1.25 ± 0.12	6.20 ± 1.36	12.1 ± 3.0	47.3 ± 0.1	37.5 ± 1.0
BD	3.90 ± 0.39	0.98 ± 0.21	5.78 ± 0.90	10.7 ± 1.3	39.2 ± 3.2	45.3 ± 4.1
BE	3.57 ± 0.39	0.66 ± 0.11	5.62 ± 0.48	9.9 ± 0.6	46.4 ± 1.2	40.6 ± 1.5
BF	4.71 ± 1.17	0.56 ± 0.25	3.91 ± 0.97	9.2 ± 0.0	38.8 ± 3.0	49.4 ± 3.0
CD	3.03 ± 0.78	1.69 ± 0.44	3.23 ± 0.20	8.0 ± 1.4	38.6 ± 5.9	47.9 ± 7.1
CE	4.14	1.70	5.77	11.6	22.9 ± 5.7	44.2
CF	5.95 ± 0.95	2.35 ± 1.36	2.36 ± 0.09	10.7 ± 1.1	23.1 ± 0.2	57.1 ± 1.2
DE	3.10 ± 0.63	1.26 ± 0.23	3.86 ± 0.36	8.2 ± 1.1	39.9 ± 2.0	46.1 ± 1.6
DF	4.33 ± 1.15	2.17 ± 1.06	2.90 ± 0.79	9.4 ± 2.7	26.9 ± 1.2	54.6 ± 2.9
EF	4.61 ± 0.62	1.54 ± 0.71	2.74 ± 0.36	8.9 ± 0.6	31.5 ± 3.3	50.8 ± 3.3
ABCD	3.76 ± 1.11	1.89 ± 1.20	4.86 ± 0.58	10.5 ± 2.9	48.0 ± 2.2	38.1 ± 1.4
ABCE	3.81 ± 0.42	0.66 ± 0.11	5.83 ± 0.54	10.3 ± 1.1	45.5 ± 1.6	39.4 ± 1.6
ABCF	3.08 ± 0.79	0.70 ± 0.22	2.27 ± 0.89	6.1 ± 1.3	40.4 ± 4.0	47.2 ± 4.6
ABDE	3.29 ± 0.04	1.22 ± 0.26	4.07 ± 0.48	8.6 ± 0.2	39.0 ± 3.1	46.8 ± 3.2
ABDF	5.01 ± 0.84	2.49 ± 0.71	5.10 ± 1.09	12.6 ± 2.2	38.5 ± 2.1	45.6 ± 1.7
ABEF	3.76 ± 1.32	1.14 ± 0.94	3.38 ± 2.27	8.3 ± 4.5	44.2 ± 4.2	34.6 ± 5.2
ACDE	4.11 ± 0.40	2.18 ± 0.97	4.55 ± 0.31	10.8 ± 0.9	36.4 ± 2.6	44.5 ± 2.2
ACDF	3.72 ± 0.24	1.53 ± 0.71	2.60 ± 0.27	7.9 ± 0.4	30.8 ± 0.6	53.5 ± 0.5
ACEF	5.87 ± 0.14	0.37 ± 0.02	2.44 ± 0.08	8.7 ± 0.0	31.4 ± 2.2	53.5 ± 2.2
ADEF	3.96 ± 0.30	1.49 ± 0.64	2.46 ± 0.11	7.9 ± 0.3	30.3 ± 1.7	53.5 ± 1.6
BCDE	5.16 ± 0.54	2.34 ± 0.28	6.72 ± 0.72	14.2 ± 1.4	36.3 ± 4.1	43.8 ± 4.3
BCDF	4.00 ± 0.79	2.09 ± 1.10	4.37 ± 0.42	10.5 ± 1.4	44.9 ± 2.1	43.1 ± 2.5
BCEF	5.08 ± 2.68	1.61 ± 0.25	5.66 ± 3.57	12.3 ± 6.5	38.7 ± 4.5	41.5 ± 6.0
BDEF	4.18 ± 0.78	1.24 ± 0.15	5.45 ± 0.00	10.9 ± 0.9	38.1 ± 2.2	46.7 ± 2.4
CDEF	4.46 ± 0.64	0.96 ± 0.37	2.59 ± 0.23	8.0 ± 0.2	30.7 ± 0.8	52.9 ± 0.8
ABCDEF	3.51 ± 0.28	0.88 ± 0.18	3.53 ± 0.41	7.9 ± 0.5	38.0 ± 1.7	48.9 ± 1.8

Table B.3: Biochemical composition of variable-growth-temperature species combinations. Uncertainty represents SE.

Species Combination	H/C [n/n]	N [wt%]	O [wt%]	HHV [MJ/kg]	Yield [wt%]	Production <sup>a</sup> [mg/L]	Stability <sup>a</sup> ( $\mu/\sigma$ )
A	1.50 ± 0.02	5.48 ± 0.20	12.4 ± 0.3	34.9 ± 0.3	32.2 ± 1.4	24.2 ± 7.2	1.38 ± 0.45
B	1.45 ± 0.00	6.08 ± 0.05	12.5 ± 0.2	34.4 ± 0.2	37.2 ± 0.3	80.6 ± 12.2	1.74 ± 0.52
C	1.47 ± 0.02	5.46 ± 0.04	12.1 ± 0.2	34.9 ± 0.2	34.4 ± 1.5	16.0 ± 3.0	1.86 ± 0.84
D	1.43 ± 0.01	5.39 ± 0.03	11.7 ± 0.2	35.0 ± 0.1	36.2 ± 0.5	77.0 ± 9.6	1.67 ± 0.20
E	1.42 ± 0.04	5.32 ± 0.06	12.9 ± 0.7	34.4 ± 0.2	31.4 ± 0.1	5.8 ± 2.6	2.21 ± 0.65
F	1.47 ± 0.02	5.01 ± 0.04	12.4 ± 0.3	35.0 ± 0.3	32.2 ± 0.6	140.0 ± 9.9	3.94 ± 0.35
AB	1.46 ± 0.01	6.32 ± 0.23	12.7 ± 0.4	34.2 ± 0.1	38.1 ± 1.1	92.8 ± 4.0	2.91 ± 0.50
AC	1.54 ± 0.04	5.01 ± 0.18	13.0 ± 0.7	35.0 ± 0.2	33.2 ± 0.9	23.9 ± 1.3	1.38 ± 0.53
AD	1.41 ± 0.02	5.40 ± 0.02	12.5 ± 0.7	34.5 ± 0.4	37.1 ± 0.6	86.3 ± 32.4	1.92 ± 0.26
AE	1.42	5.04	11.7	35.1	27.9	33.8	0.57
AF	1.48 ± 0.04	4.86 ± 0.07	11.8 ± 0.6	35.4 ± 0.5	32.0 ± 0.6	94.5 ± 17.8	3.04 ± 0.43
BC	1.45 ± 0.02	5.79 ± 0.03	12.6 ± 0.9	34.4 ± 0.6	35.7 ± 0.5	51.3 ± 20.2	1.77 ± 0.34
BD	1.46 ± 0.02	6.03 ± 0.19	12.4 ± 0.7	34.5 ± 0.5	36.4 ± 0.8	61.0 ± 9.4	1.41 ± 0.24
BE	1.45 ± 0.03	5.90 ± 0.04	12.6 ± 0.3	34.4 ± 0.3	36.2 ± 0.1	34.9 ± 7.1	1.94 ± 0.67
BF	1.45 ± 0.02	5.89 ± 0.04	12.2 ± 0.9	34.6 ± 0.6	35.9 ± 1.2	87.8 ± 24.4	2.77 ± 0.49
CD	1.42 ± 0.03	5.58 ± 0.28	13.2 ± 1.4	34.1 ± 0.5	36.5 ± 0.9	40.8 ± 9.2	2.76 ± 0.45
CE	1.51	4.84	11.6	35.7	29.2	14.7	1.00
CF	1.45 ± 0.03	4.95 ± 0.10	12.1 ± 0.6	35.1 ± 0.5	32.5 ± 0.4	102.0 ± 11.5	2.56 ± 0.70
DE	1.42 ± 0.02	5.46 ± 0.07	12.7 ± 0.7	34.4 ± 0.4	36.5 ± 0.3	32.5 ± 7.9	1.80 ± 0.69
DF	1.43 ± 0.02	5.17 ± 0.13	12.4 ± 0.6	34.7 ± 0.3	33.1 ± 0.8	112.0 ± 14.7	2.62 ± 0.90
EF	1.45 ± 0.00	5.11 ± 0.11	11.6 ± 0.2	35.3 ± 0.1	32.3 ± 0.4	48.2 ± 6.0	2.39 ± 0.23
ABCD	1.48 ± 0.04	5.91 ± 0.08	13.4 ± 0.7	34.1 ± 0.5	36.8 ± 0.4	40.5 ± 9.0	2.29 ± 0.36
ABCE	1.45 ± 0.02	5.97 ± 0.04	12.4 ± 0.7	34.5 ± 0.3	35.6 ± 1.0	34.6 ± 9.3	6.18
ABCF	1.43 ± 0.01	5.79 ± 0.32	12.7 ± 0.5	34.3 ± 0.5	35.3 ± 0.6	54.4 ± 12.8	2.62 ± 0.80
ABDE	1.45 ± 0.01	5.95 ± 0.21	12.4 ± 0.4	34.5 ± 0.2	36.9 ± 0.3	45.7 ± 8.5	2.08 ± 0.30
ABDF	1.42 ± 0.02	5.76 ± 0.63	12.0 ± 1.2	34.7 ± 0.4	36.6 ± 0.4	86.8 ± 22.9	1.77 ± 0.28
ABEF	1.42 ± 0.01	5.56 ± 0.11	11.9 ± 0.5	34.8 ± 0.3	35.6 ± 0.3	43.1 ± 7.3	2.84 ± 0.64
ACDE	1.50 ± 0.02	5.60 ± 0.19	13.4 ± 1.2	34.3 ± 0.6	34.5 ± 0.7	21.5 ± 8.5	1.84 ± 0.43
ACDF	1.43 ± 0.02	5.29 ± 0.14	11.4 ± 0.2	35.2 ± 0.2	36.3 ± 0.7	70.7 ± 9.0	2.46 ± 0.33
ACEF	1.48 ± 0.03	5.15 ± 0.04	13.2 ± 0.5	34.6 ± 0.1	33.8 ± 1.0	45.9 ± 9.9	2.49 ± 0.32
ADEF	1.44 ± 0.01	5.40 ± 0.07	12.4 ± 0.7	34.7 ± 0.4	33.0 ± 0.6	56.4 ± 5.3	2.85 ± 0.21
BCDE	1.44 ± 0.02	5.82 ± 0.14	12.9 ± 0.3	34.3 ± 0.1	36.0 ± 0.6	31.9 ± 2.5	2.09 ± 0.09
BCDF	1.42 ± 0.01	5.76 ± 0.18	12.5 ± 0.5	34.4 ± 0.3	36.6 ± 1.1	56.2 ± 7.9	1.50 ± 0.25
BCEF	1.43 ± 0.02	5.73 ± 0.11	12.1 ± 0.4	34.7 ± 0.3	36.0 ± 0.5	42.2 ± 10.0	1.51 ± 0.40
BDEF	1.45 ± 0.01	5.73 ± 0.07	12.8 ± 0.4	34.4 ± 0.2	36.6 ± 0.7	46.8 ± 7.7	1.98 ± 0.36
CDEF	1.44 ± 0.03	5.35 ± 0.03	12.1 ± 0.8	34.8 ± 0.5	35.5 ± 1.2	48.9 ± 6.6	1.63 ± 0.64
ABCDEF	1.46 ± 0.03	5.88 ± 0.10	11.4 ± 0.1	35.1 ± 0.2	35.7 ± 0.4	36.9 ± 3.1	2.15 ± 0.37

Table B.4: Biocrude properties of variable-growth-temperature species combinations. <sup>a</sup>Reproduced from Narwani et al. [6]. Uncertainty represents SE.

### B.3 Additional quality vs. quantity sector charts

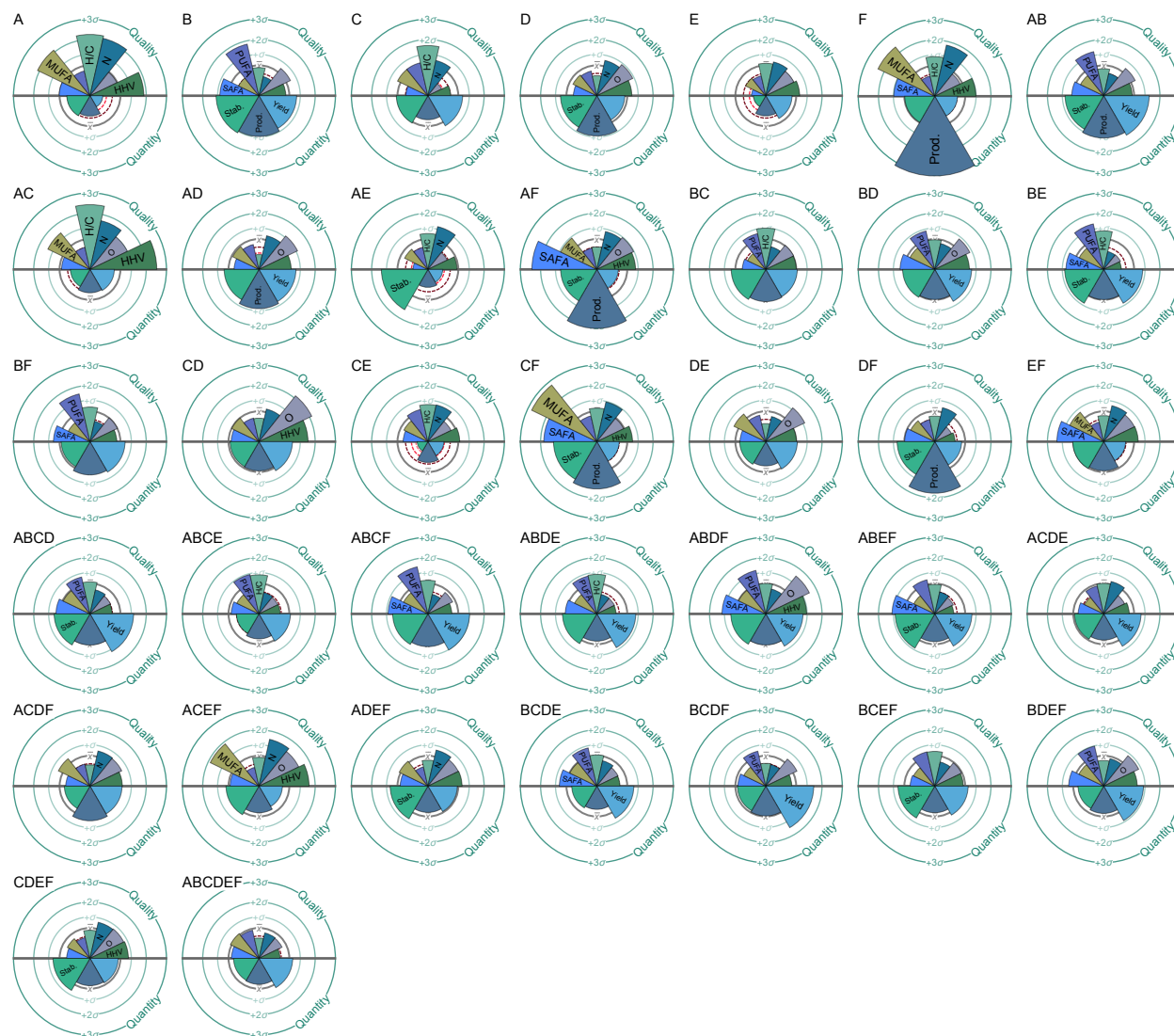


Figure B.4: Quality (top half of each circle) vs. quantity (bottom half of each circle) sector charts for constant-growth-temperature species combinations of *Ankistrodesmus falcatus* (A), *Chlorella sorokiniana* (B), *Pediastrum duplex* (C), *Scenedesmus acuminatus* (D), *Scenedesmus ecornis* (E), and *Selenastrum capricornutum* (F). Wedge lengths indicate number of SDs  $((x_i - \bar{x})/\sigma_i)$  away from the mean (averaged over all 37 species combinations) for each metric. SAFA, MUFA, and PUFA represent yields present in microalgal feedstocks. H/C, N<sup>a</sup>, O<sup>a</sup>, Prod., and Stab. represent biocrude hydrogen-to-carbon atomic ratio, nitrogen content, oxygen content, productivity, and stability, respectively. <sup>a</sup>Denotes metrics multiplied by -1 so that larger wedges correspond to more favorable outcomes.

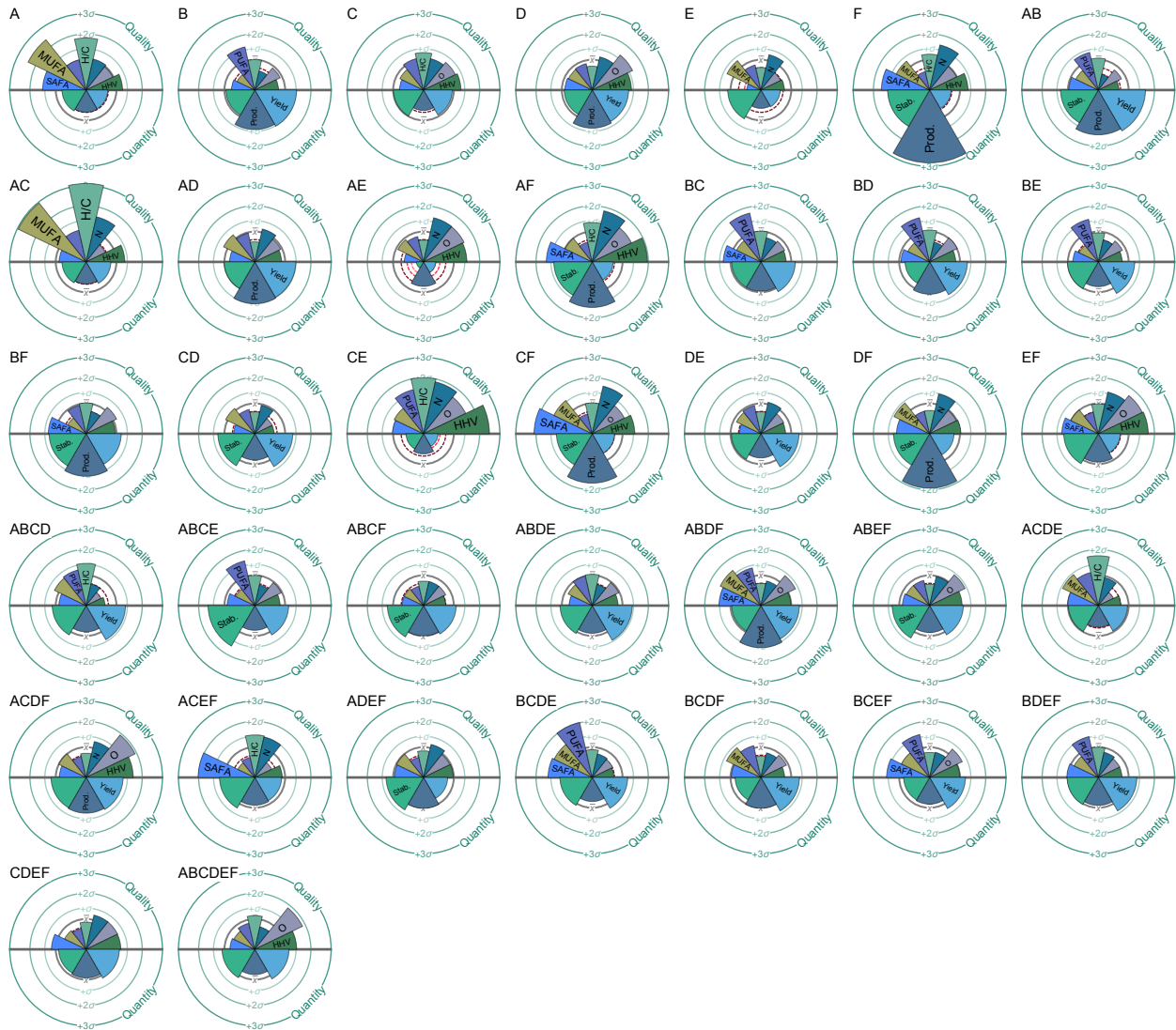


Figure B.5: Quality (top half of each circle) vs. quantity (bottom half of each circle) sector charts for variable-growth-temperature species combinations of *Ankistrodesmus falcatus* (A), *Chlorella sorokiniana* (B), *Pediastrum duplex* (C), *Scenedesmus acuminatus* (D), *Scenedesmus ecornis* (E), and *Selenastrum capricornutum* (F). Wedge lengths indicate number of SDs ( $(x_i - \bar{x})/\sigma_i$ ) away from the mean (averaged over all 37 species combinations) for each metric. SAFA, MUFA, and PUFA represent yields present in microalgal feedstocks. H/C, N<sup>a</sup>, O<sup>a</sup>, Prod., and Stab. represent biocrude hydrogen-to-carbon atomic ratio, nitrogen content, oxygen content, productivity, and stability, respectively. <sup>a</sup>Denotes metrics multiplied by -1 so that larger wedges correspond to more favorable outcomes.

## APPENDIX C

# Parameters for multiple linear regression models in Chapter III

### C.1 Coefficients for Set 10 and 11 models

Model	Biocrude Property	$\beta_0$	$\beta_{Sat}$	$\beta_{Mon}$	$\beta_{Pol}$	$\beta_{Pro}$	$\beta_{Car}$
Set 10	H/C [n/n]	$1.43 \pm 0.01$	-	-	-	-	-
	N content [wt %]	$4.16 \pm 0.19$	-	$87.2 \pm 11.4$	-	-	-
	O content [wt %]	$18.6 \pm 0.8$	-	$-761 \pm 129$	-	-	-
	HHV [ $\text{MJ kg}^{-1}$ ]	$35.8 \pm 0.4$	$49.3 \pm 17.0$	-	$-82.8 \pm 14.9$	-	-
	Yield [wt %]	$10.7 \pm 0.9$	$575 \pm 46$	-	-	-	-
Set 11	H/C [n/n]	$1.43 \pm 0.02$	-	-	-	-	-
	N content [wt %]	$5.11 \pm 0.15$	-	-	-	-	-
	O content [wt %]	$7.58 \pm 0.97$	-	-	$156 \pm 35$	-	-
	HHV [ $\text{MJ kg}^{-1}$ ]	$37.2 \pm 0.4$	-	-	$-99.3 \pm 17.7$	-	-
	Yield [wt %]	$10.8 \pm 2.4$	$468 \pm 64$	$525 \pm 132$	$-265 \pm 51$	$38.5 \pm 4.3$	-

Table C.1: Coefficients for Set 10 and 11 models in Table 3.2 (part 1).  $B_{Sat}$ ,  $B_{Mon}$ ,  $B_{Pol}$ ,  $B_{Pro}$ , and  $B_{Car}$  input as weight fractions.

Model	Biocrude Property	$\gamma_{Sat^2}$	$\gamma_{Mon^2}$	$\gamma_{Pol^2}$	$\gamma_{Pro^2}$	$\gamma_{Car^2}$
Set 10	H/C [n/n]	-	$148 \pm 21$	-	-	$-0.198 \pm 0.039$
	N content [wt %]	-	$-1070 \pm 150$	-	-	$-3.08 \pm 0.40$
	O content [wt %]	-	$2140 \pm 0$	-	-	-
	HHV [ $\text{MJ kg}^{-1}$ ]	$-642 \pm 200$	-	-	$-14.5 \pm 2.8$	-
	Yield [wt %]	-	$-4130 \pm 1070$	-	$65.0 \pm 3.8$	$51.2 \pm 5.0$
Set 11	H/C [n/n]	-	$194 \pm 34$	-	-	-
	N content [wt %]	-	$-348 \pm 47$	-	-	-
	O content [wt %]	-	$387 \pm 77$	-	$48.7 \pm 9.1$	$15.3 \pm 2.9$
	HHV [ $\text{MJ kg}^{-1}$ ]	$-320 \pm 87$	-	-	$-10.7 \pm 2.9$	-
	Yield [wt %]	-	$-4500 \pm 1410$	-	-	$29.0 \pm 6.1$

Table C.2: Coefficients for Set 10 and 11 models in Table 3.2 (part 2).  $B_{Sat}$ ,  $B_{Mon}$ ,  $B_{Pol}$ ,  $B_{Pro}$ , and  $B_{Car}$  input as weight fractions.

Model	Biocrude Property	$\epsilon_{SatMon}$	$\epsilon_{SatPol}$	$\epsilon_{SatPro}$	$\epsilon_{SatCar}$	$\epsilon_{MonPol}$
Set 10	H/C [n/n]	$-134 \pm 22$	-	-	$5.70 \pm 0.90$	-
	N content [wt %]	-	$195 \pm 26$	-	$-11.3 \pm 2.8$	-
	O content [wt %]	-	-	-	-	-
	HHV [MJ kg <sup>-1</sup> ]	-	-	-	-	-
	Yield [wt %]	$223 \pm 77$	-	-	$-1170 \pm 100$	-
Set 11	H/C [n/n]	$-124 \pm 29$	$64.3 \pm 16.3$	$-11.2 \pm 3.1$	$7.18 \pm 1.42$	$-120 \pm 45$
	N content [wt %]	-	$146 \pm 19$	-	$-17.5 \pm 1.7$	-
	O content [wt %]	-	-	-	-	-
	HHV [MJ kg <sup>-1</sup> ]	-	$767 \pm 209$	-	-	-
	Yield [wt %]	-	-	-	$-928 \pm 132$	-

Table C.3: Coefficients for Set 10 and 11 models in Table 3.2 (part 3).  $B_{Sat}$ ,  $B_{Mon}$ ,  $B_{Pol}$ ,  $B_{Pro}$ , and  $B_{Car}$  input as weight fractions.

Model	Biocrude Property	$\epsilon_{MonPro}$	$\epsilon_{MonCar}$	$\epsilon_{PolPro}$	$\epsilon_{PolCar}$	$\epsilon_{ProCar}$
Set 10	H/C [n/n]	-	-	-	-	-
	N content [wt %]	$-183 \pm 24$	-	-	-	$11.4 \pm 1.1$
	O content [wt %]	$912 \pm 167$	$765 \pm 143$	$33.2 \pm 9.9$	-	$-37.5 \pm 4.9$
	HHV [MJ kg <sup>-1</sup> ]	-	-	$208 \pm 41$	-	-
	Yield [wt %]	-	$316 \pm 92$	$-514 \pm 49$	$547 \pm 44$	-
Set 11	H/C [n/n]	$25.2 \pm 7.5$	$-12.1 \pm 4.7$	-	-	-
	N content [wt %]	-	-	-	-	$3.13 \pm 0.81$
	O content [wt %]	-	-	$-338 \pm 93$	-	$-40.3 \pm 6.7$
	HHV [MJ kg <sup>-1</sup> ]	-	-	$154 \pm 42$	-	-
	Yield [wt %]	$-1100 \pm 250$	-	-	$662 \pm 108$	-

Table C.4: Coefficients for Set 10 and 11 models in Table 3.2 (part 4).  $B_{Sat}$ ,  $B_{Mon}$ ,  $B_{Pol}$ ,  $B_{Pro}$ , and  $B_{Car}$  input as weight fractions.

Biocrude Property	$\beta_A$	$\beta_B$	$\beta_C$	$\beta_D$	$\beta_E$	$\beta_F$
H/C [n/n]	-	-	-	$-0.024 \pm 0.004$	$0.012 \pm 0.004$	$-0.013 \pm 0.004$
N content [wt %]	-	$0.275 \pm 0.032$	$-0.077 \pm 0.015$	-	-	-
O content [wt %]	$0.275 \pm 0.067$	$-0.885 \pm 0.134$	-	-	$0.547 \pm 0.078$	-
HHV [MJ kg <sup>-1</sup> ]	-	-	-	-	$-0.187 \pm 0.050$	-
Yield [wt %]	$0.376 \pm 0.140$	-	-	$1.00 \pm 0.20$	$-0.526 \pm 0.128$	-

Table C.5: Coefficients for Set 11 models in Table 3.2 (part 5).  $S_A$ ,  $S_B$ ,  $S_C$ ,  $S_D$ ,  $S_E$ , and  $S_F$  input as weight fractions.

## APPENDIX D

# Additional biomass data and figures, calculations, temperature profiles, and mass balances for Chapter IV

### D.1 Materials and methods

We converted solids contents to slurry concentrations on a  $\text{g L}_{\text{rxn}}^{-1}$  basis using the following equation, which assumes that only water contributes to the volume expansion:

$$c(T) = \frac{x_s}{1 - x_s} \rho_w(T) \quad (\text{D.1})$$

Here  $c(T)$  is the slurry concentration ( $\text{g L}_{\text{rxn}}^{-1}$ ),  $x_s$  is the solids content (wt%), and  $\rho_w(T)$  is the temperature-dependent density of pure, saturated liquid water. The solids contents of the 30 and 120  $\text{g L}_{\text{rxn}}^{-1}$  slurries at various temperatures are presented in Table D.1.

Conc. [ $\text{g L}_{\text{rxn}}^{-1}$ ]	Set-point temperature [ $^{\circ}\text{C}$ ]				
	150	200	250	300	350
30	3.2	3.4	3.6	4.0	5.0
120	11.6	12.2	13.1	14.4	17.3

Table D.1: Target solids content (wt%) for different initial slurry concentrations ( $\text{g L}_{\text{rxn}}^{-1}$ ) as functions of reaction temperature ( $^{\circ}\text{C}$ ).

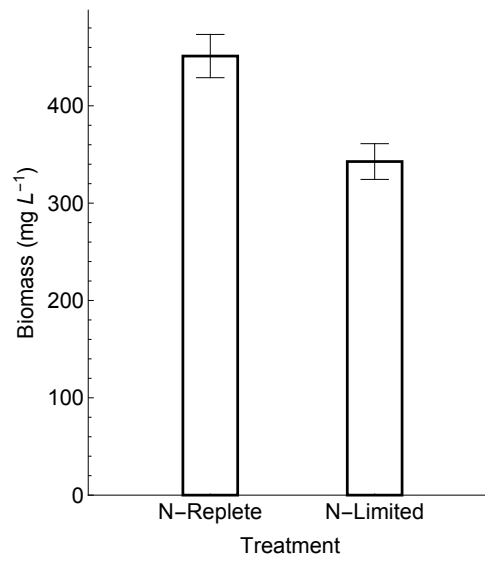
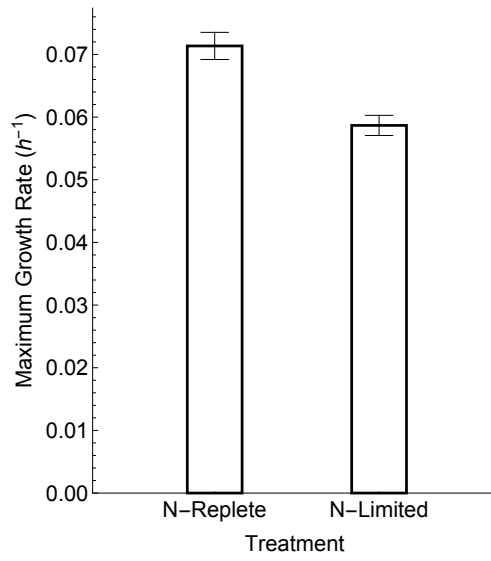


Figure D.1: Maximum growth rate (h<sup>-1</sup>) and biomass productivity (mg L<sup>-1</sup>) for nitrogen-replete and limited cultures of *Chlorella sorokiniana*.

Time [s]	Set-point temperature [°C]				
	150	200	250	300	350
0	44.8	46.6	45.9	52.6	58.3
2	58.2	70.6	78.0	100.2	119.9
4	69.4	92.4	107.6	142.5	168.7
6	79.2	110.5	132.4	171.1	204.5
8	87.2	125.5	152.6	192.8	228.7
10	94.6	138.8	167.6	209.2	247.6
12	101.2	148.1	181.0	220.8	260.9
14	107.1	155.6	191.1	230.4	275.1
16	111.5	161.7	199.0	238.8	284.5
18	115.4	166.4	205.3	246.6	292.1
20	118.6	170.5	211.5	252.3	298.4
22	121.7	173.9	215.6	258.2	304.3
24	124.4	176.6	219.9	262.0	308.9
26	127.5	179.5	222.2	265.4	312.9
28	130.3	182.0	224.6	268.8	315.5
30	132.5	184.1	227.2	271.7	318.7
32	135.4	186.1	229.7	274.7	321.9
34	137.1	187.7	231.7	277.2	324.8
36	138.4	189.3	233.6	279.7	327.8
38	139.8	190.6	235.5	282.0	330.3
40	141.0	<u>191.7</u>	237.0	284.0	332.9
42	142.0	192.7	238.3	285.8	<u>335.3</u>
44	143.0	193.6	<u>239.5</u>	<u>287.4</u>	337.2
46	<u>143.7</u>	194.3	240.5	288.8	338.7
48	144.3	195.0	241.5	290.1	340.0
50	145.0	195.5	242.4	291.2	341.3
52	145.6	195.9	243.2	292.2	342.2
54	146.0	196.4	243.9	293.1	343.2
56	146.6	<b>196.8</b>	244.5	293.9	<b>344.0</b>
58	146.9	197.1	245.0	<b>294.6</b>	344.7
60	147.3	197.4	<b>245.5</b>	295.2	345.3
62	<b>147.6</b>	197.7	245.9	295.8	345.8
64	147.8	198.0	246.2	296.3	346.3
66	148.0	198.1	246.4	296.7	346.7
68	148.2	198.4	246.7	297.1	347.0
70	148.4	198.5	246.9	297.5	347.3
72	148.5	198.6	247.2	297.8	347.6
74	148.7	198.8	247.4	298.0	347.8

Table D.2: Average heat-up temperature profiles for stainless-steel batch reactors (1.30 mL, 386-mm i.d.) filled with deionized water at different set-point temperatures. Underline and **Bold** indicate points where 95 and 98% of maximum temperature change is achieved relative to 25 °C, respectively.

ID	Elemental Composition [wt%]					
	C	H	N	S	O	P
Nan-1	51.9 ± 0.3	7.3 ± 0.1	8.8 ± 0.1	0.70 ± 0.01	24.0 ± 0.4	0.94 ± 0.01
Nan-2	56.2 ± 0.3	8.0 ± 0.1	4.2 ± 0.0	0.51 ± 0.00	22.4 ± 0.3	0.97 ± 0.01
Chl-1	51.0 ± 0.2	7.2 ± 0.1	9.1 ± 0.1	0.53 ± 0.01	26.5 ± 0.4	1.03 ± 0.03
Chl-2	49.9 ± 0.2	7.5 ± 0.1	3.1 ± 0.0	0.22 ± 0.01	34.6 ± 0.5	1.11 ± 0.01
Spi-1	45.6 ± 0.2	6.7 ± 0.1	10.7 ± 0.1	0.69 ± 0.02	25.2 ± 0.4	1.22 ± 0.02
Mix-m	46.9 ± 0.2	6.9 ± 0.1	8.4 ± 0.1	0.52 ± 0.00	28.0 ± 0.4	1.21 ± 0.04

Table D.3: Biomass elemental contents (dry-algal-mass basis). Uncertainty denotes SE.

ID	Content [wt%]														Distribution [wt%]		
	C14:0	C16:0	C16:1n9	C16:1n7	C16:2n6	C17:1n7	C18:0	C18:1n9	C18:1	C18:2n6	C18:3n6	C18:3n3	C20:4n6	C20:5n3	SAFA	MUFA	PUFA
Nan-1	0.49	2.51	0.04	1.35	0.47	0.81	0.14	0.33	0.08	1.62	0.03	1.63	0.26	1.86	3.1	2.6	5.9
Nan-2	0.77	8.43	0.13	5.71	0.27	0.95	0.45	5.63	0.34	1.16	0.05	2.42	0.50	1.70	9.6	12.8	6.1
Chl-1	0.25	1.46	0.08	0.07	0.70	1.94	0.05	0.11	0.09	1.38	0.00	3.29	0.00	0.00	1.8	2.3	5.4
Chl-2	0.14	4.26	0.94	0.05	1.08	2.02	0.37	3.10	0.13	4.79	0.00	3.06	0.00	0.00	4.8	6.2	8.9
Spi-1	0.08	2.53	0.09	0.21	0.00	0.00	0.14	0.15	0.04	1.10	0.83	0.00	0.00	0.00	2.8	0.5	1.9
Mix-m	0.10	3.05	0.34	0.17	0.32	0.61	0.21	1.04	0.06	2.21	0.58	0.92	0.00	0.00	3.4	2.2	4.0

Table D.4: Biomass fatty acid contents and class distributions (dry-algal-mass basis).

## D.2 Mass balance

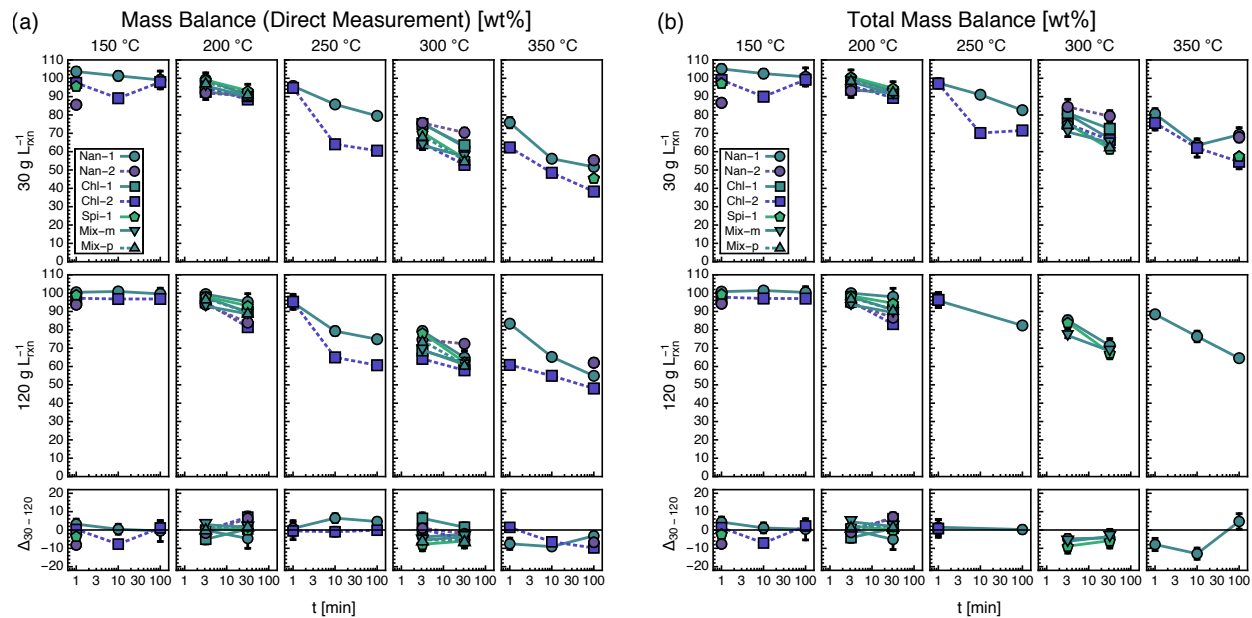


Figure D.2: Mass balances from direct measurements, including (a) solid, biocrude, aqueous, and ammonia yields, and (b) total mass balance, including gas yields, versus reaction time grouped by temperature and initial concentration. See Table 4.1 for microalgae types. The bottom row depicts the first row ( $30 \text{ g L}_{\text{rxn}}^{-1}$ ) minus the second row ( $120 \text{ g L}_{\text{rxn}}^{-1}$ ). Error bars indicate SE.

## APPENDIX E

### Additional biocrude property figures for Chapter IV

#### E.1 Biocrude elemental properties

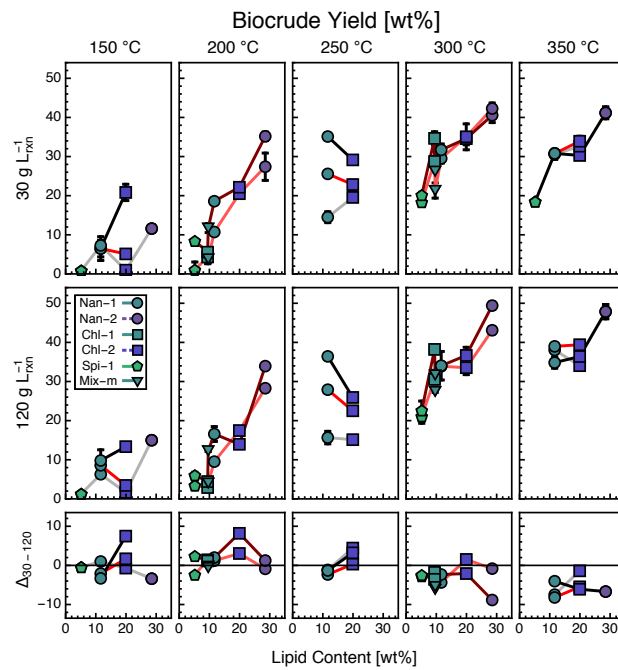


Figure E.1: Biocrude yield versus lipid content grouped by temperature and initial concentration. See Table 4.1 for microalgae types. Gray, pink, red, dark red, and black lines represent 1.0, 3.2, 10.0, 31.6, and 100.0 min reaction time, respectively. The bottom row depicts the first row ( $30 \text{ g L}_{\text{rxn}}^{-1}$ ) minus the second row ( $120 \text{ g L}_{\text{rxn}}^{-1}$ ). Error bars indicate SE.

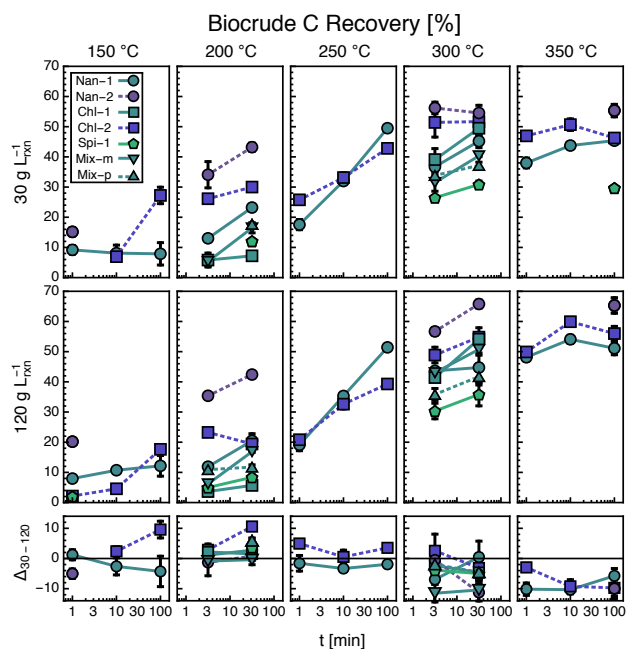


Figure E.2: Biocrude carbon recovery versus reaction time grouped by temperature and initial concentration. See Table 4.1 for microalgae types. The bottom row depicts the first row ( $30 \text{ g L}_{\text{rxn}}^{-1}$ ) minus the second row ( $120 \text{ g L}_{\text{rxn}}^{-1}$ ). Error bars indicate SE.

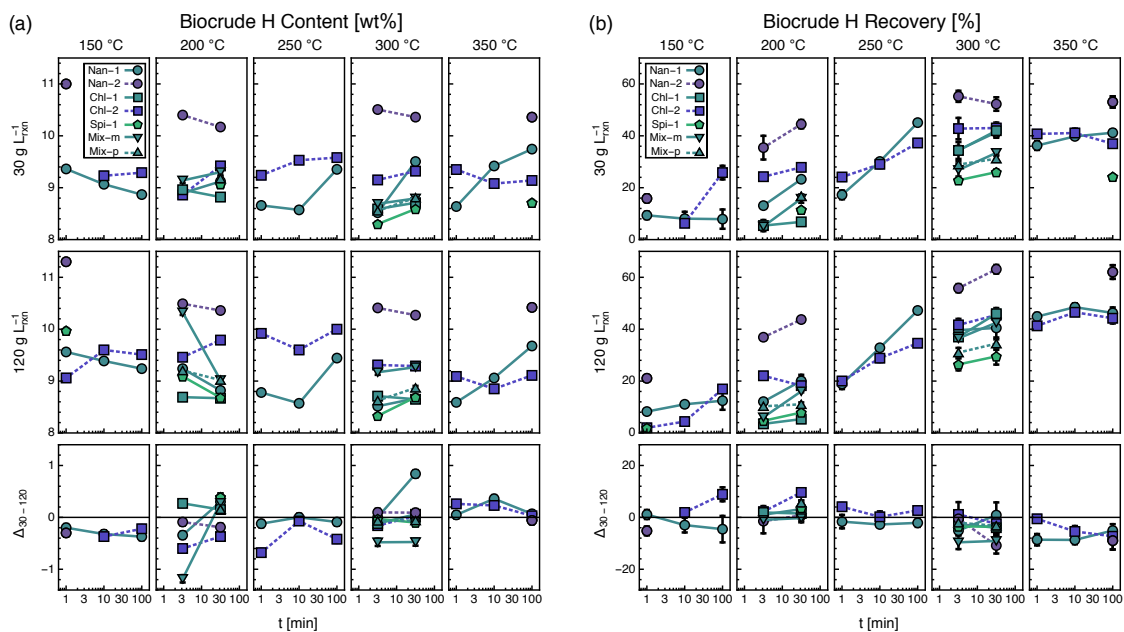


Figure E.3: Biocrude hydrogen (a) content and (b) recovery versus reaction time grouped by temperature and initial concentration. See Table 4.1 for microalgae types. The bottom row depicts the first row ( $30 \text{ g L}_{\text{rxn}}^{-1}$ ) minus the second row ( $120 \text{ g L}_{\text{rxn}}^{-1}$ ). Error bars indicate SE.

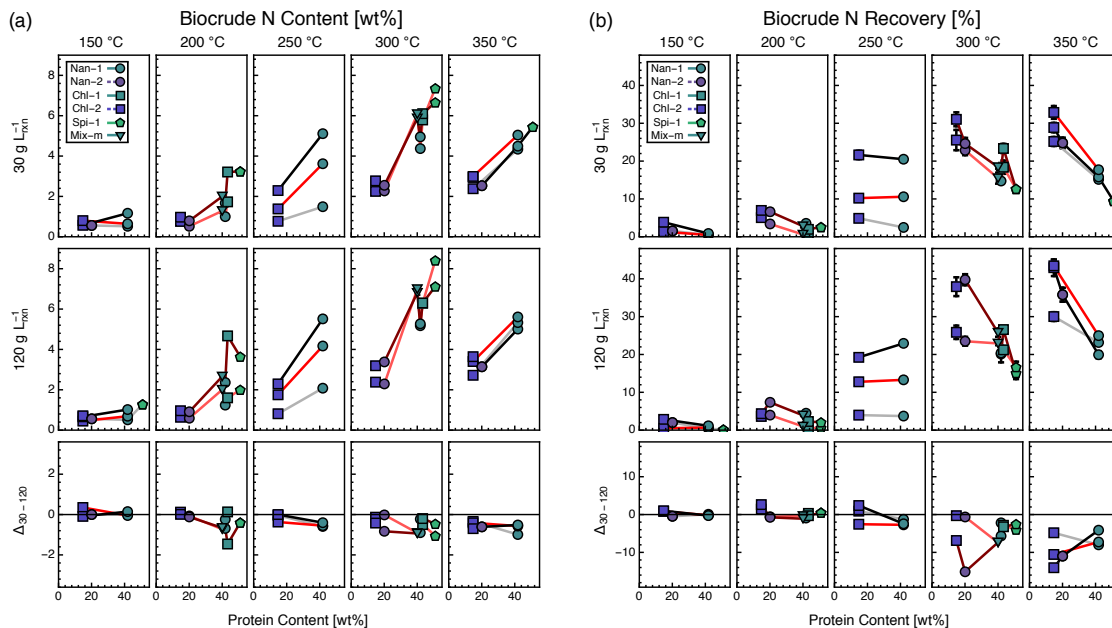


Figure E.4: Biocrude nitrogen (a) content and (b) recovery versus protein content grouped by temperature and initial concentration. See Table 4.1 for microalgae types. Gray, pink, red, dark red, and black lines represent 1.0, 3.2, 10.0, 31.6, and 100.0 min reaction time, respectively. The bottom row depicts the first row ( $30 \text{ g L}_{\text{rxn}}^{-1}$ ) minus the second row ( $120 \text{ g L}_{\text{rxn}}^{-1}$ ). Error bars indicate SE.

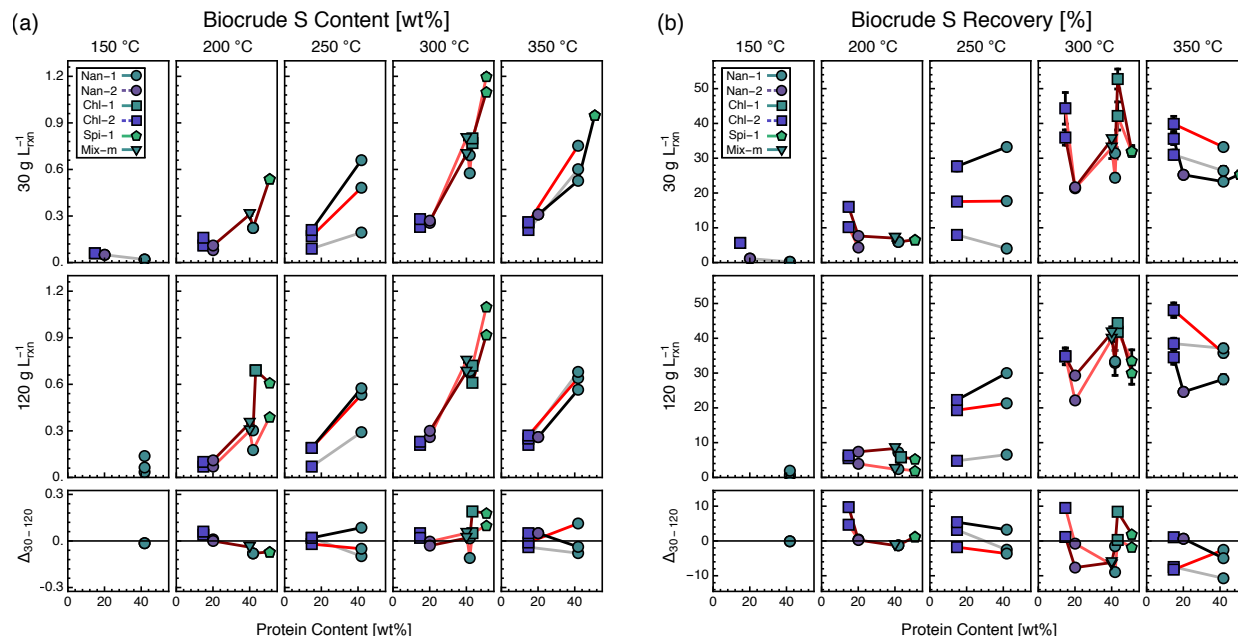


Figure E.5: Biocrude sulfur content (a) and recovery (b) versus protein content grouped by temperature and initial concentration. See Table 4.1 for microalgae types. Gray, pink, red, dark red, and black lines represent 1.0, 3.2, 10.0, 31.6, and 100.0 min reaction time, respectively. The bottom row depicts the first row ( $30 \text{ g L}_{\text{rxn}}^{-1}$ ) minus the second row ( $120 \text{ g L}_{\text{rxn}}^{-1}$ ). Error bars indicate SE.

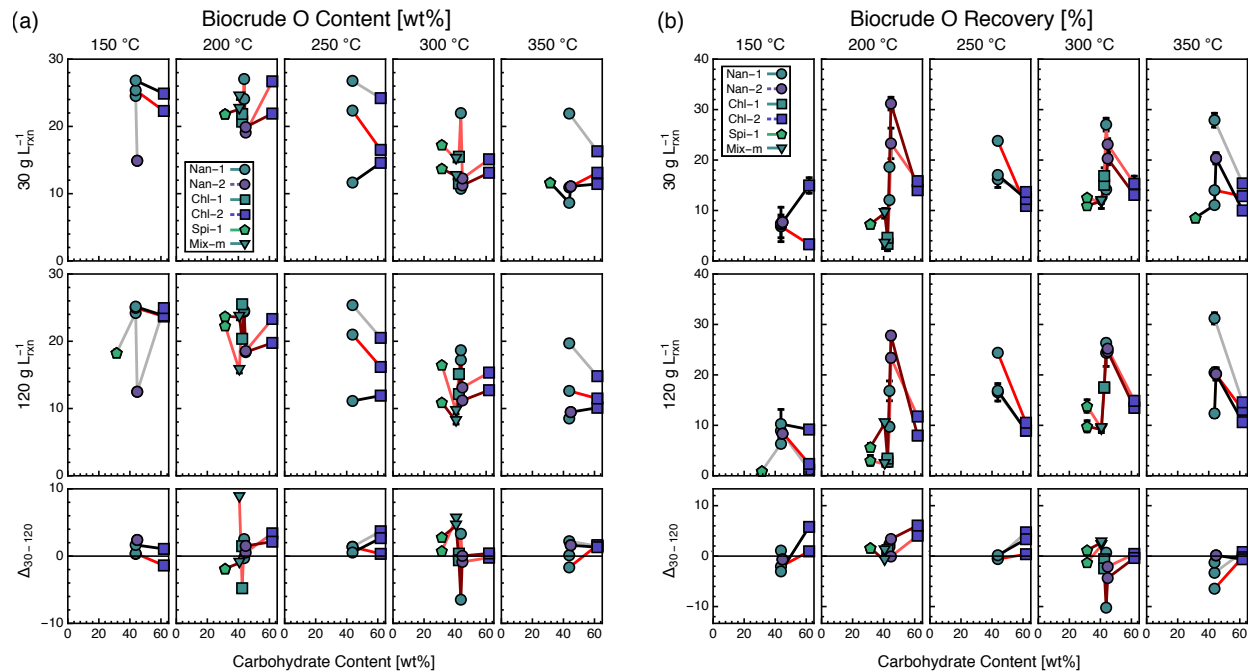


Figure E.6: Biocrude oxygen (a) content and (b) recovery versus carbohydrate content grouped by temperature and initial concentration. See Table 4.1 for microalgae types. Gray, pink, red, dark red, and black lines represent 1.0, 3.2, 10.0, 31.6, and 100.0 min reaction time, respectively. The bottom row depicts the first row ( $30 \text{ g L}_{\text{rxn}}^{-1}$ ) minus the second row ( $120 \text{ g L}_{\text{rxn}}^{-1}$ ). Error bars indicate SE.

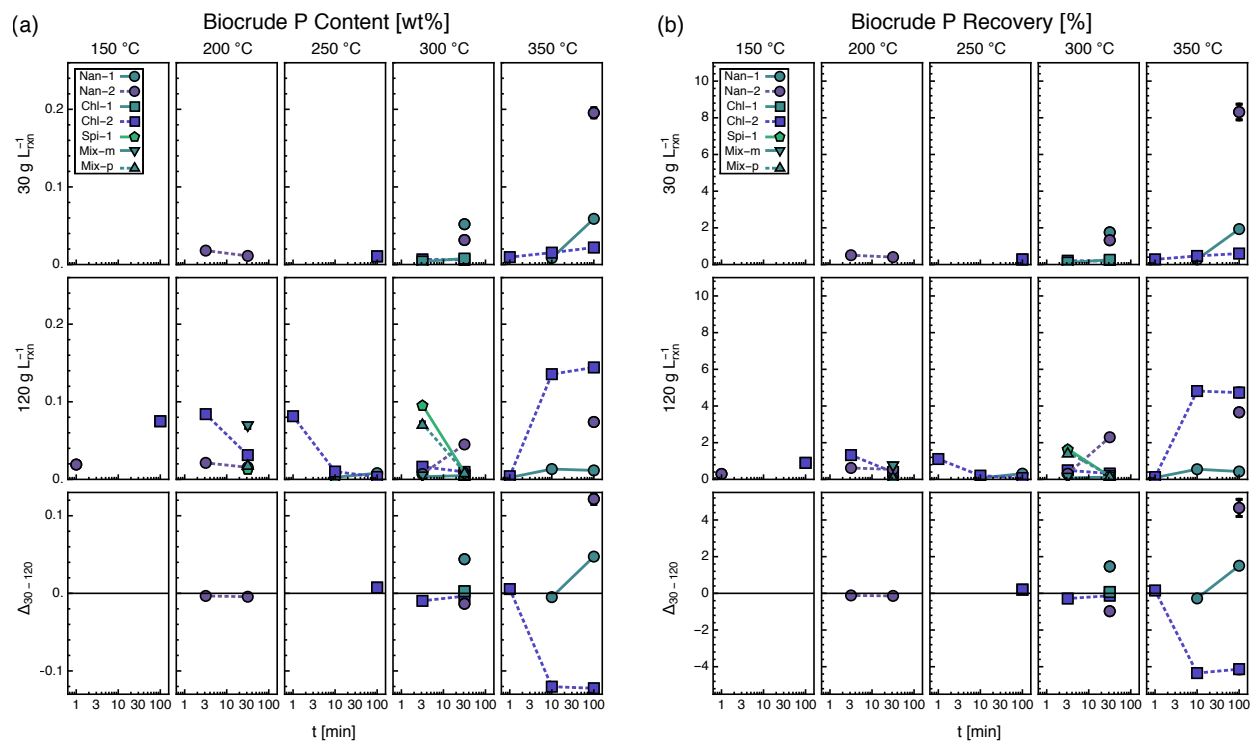


Figure E.7: Biocrude phosphorus (a) content and (b) recovery versus reaction time grouped by temperature and initial concentration. See Table 4.1 for microalgae types. The bottom row depicts the first row ( $30 \text{ g L}_{\text{rxn}}^{-1}$ ) minus the second row ( $120 \text{ g L}_{\text{rxn}}^{-1}$ ). Error bars indicate SE.

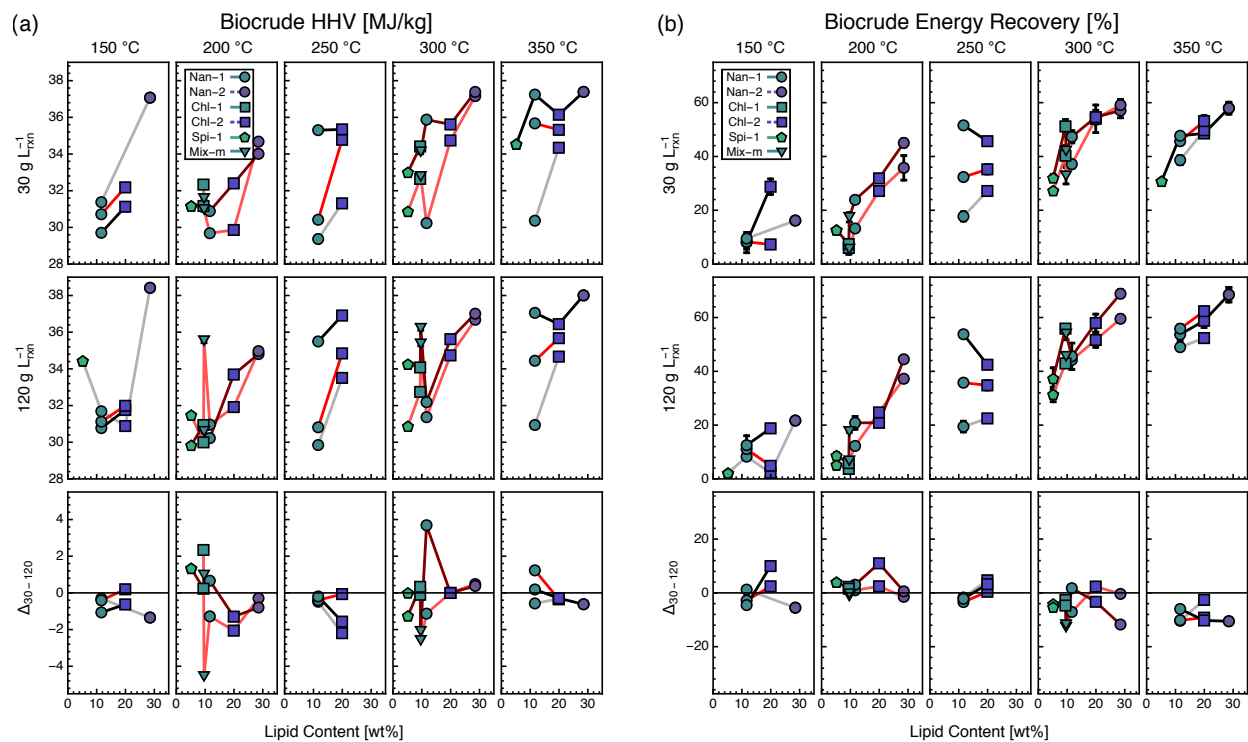


Figure E.8: Biocrude (a) HHV and (b) ER versus lipid content grouped by temperature and initial concentration. See Table 4.1 for microalgae types. Gray, pink, red, dark red, and black lines represent 1.0, 3.2, 10.0, 31.6, and 100.0 min reaction time, respectively. The bottom row depicts the first row ( $30 \text{ g L}_{\text{rxn}}^{-1}$ ) minus the second row ( $120 \text{ g L}_{\text{rxn}}^{-1}$ ). Error bars indicate SE.

## E.2 Biocrude fatty acid data

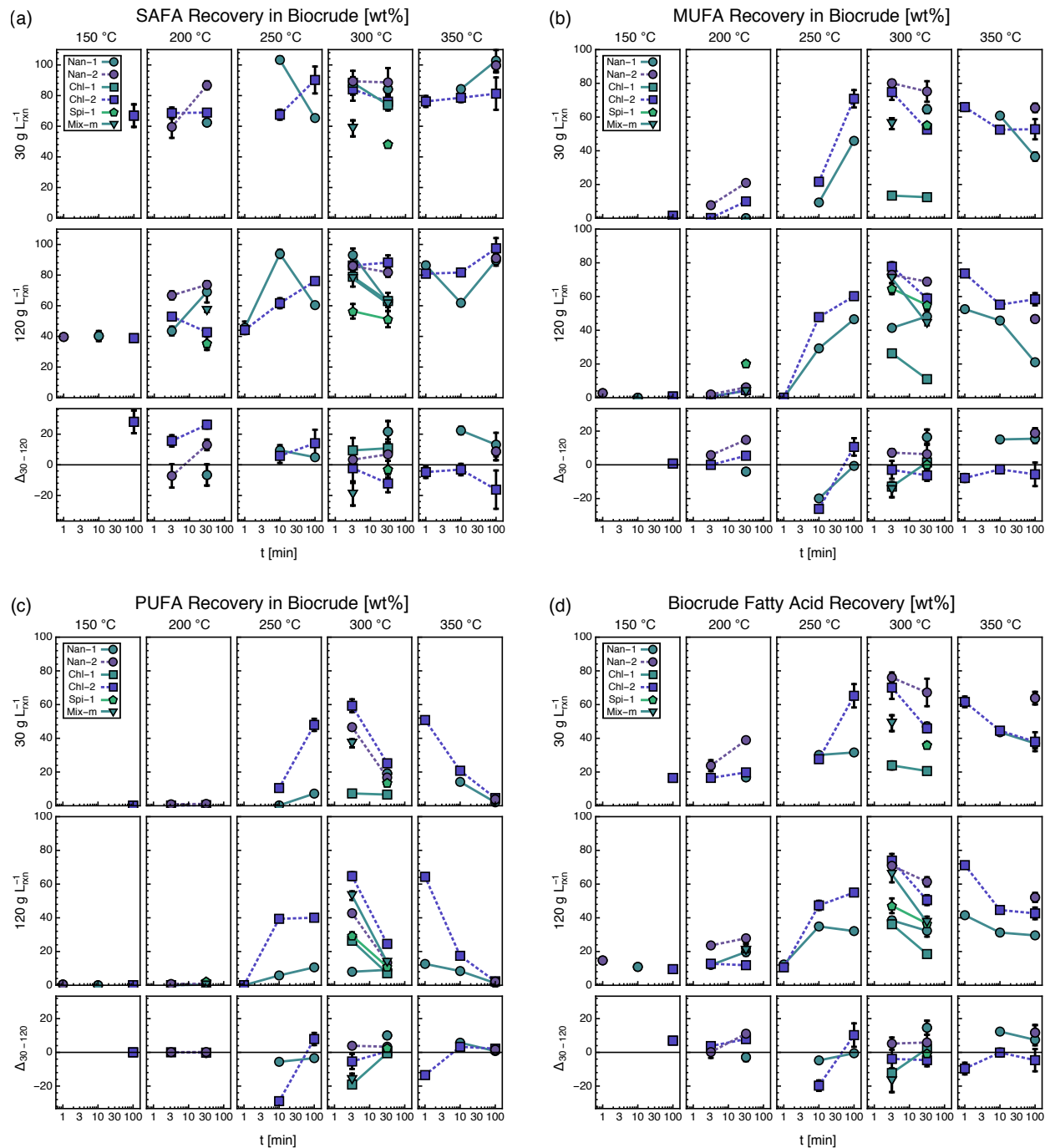


Figure E.9: Biocrude (a) SAFA, (b) MUFA, (c) PUFA, and (d) total FA recovery versus reaction time grouped by temperature and initial concentration. See Table 4.1 for microalgae types. The bottom row depicts the first row ( $30 \text{ g L}_{\text{rxn}}^{-1}$ ) minus the second row ( $120 \text{ g L}_{\text{rxn}}^{-1}$ ). Error bars indicate SE.

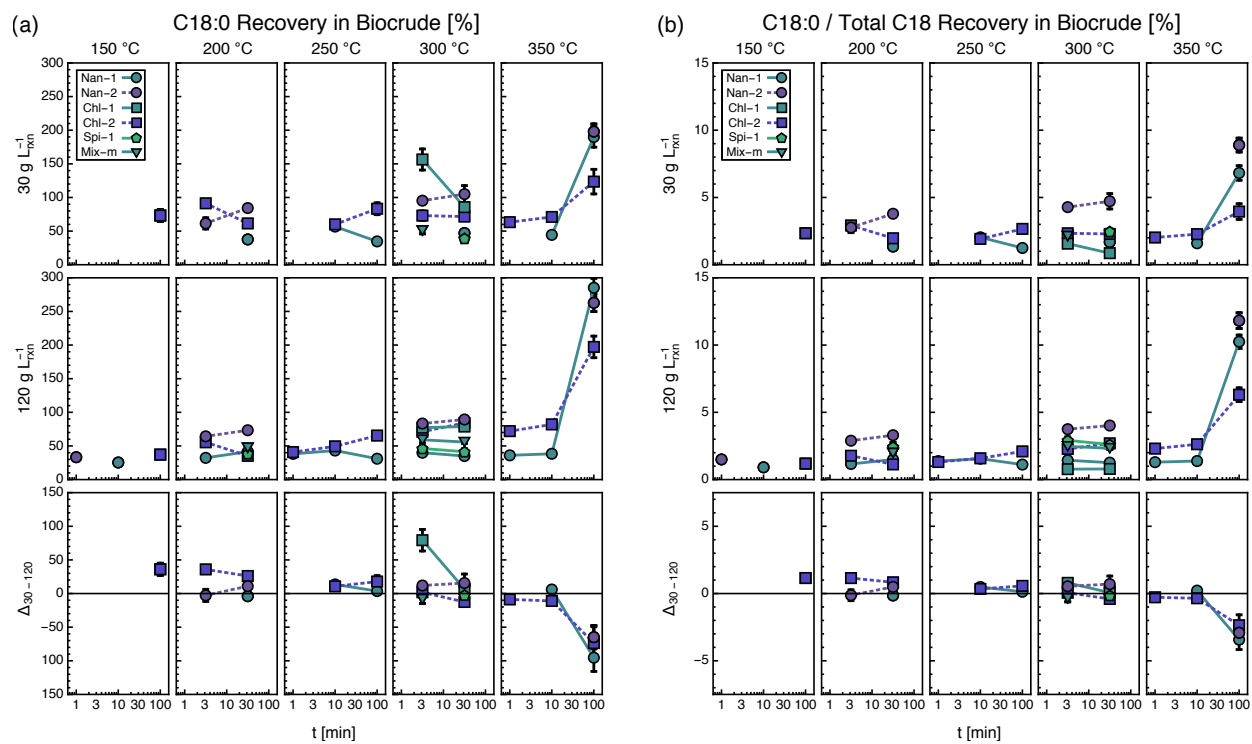


Figure E.10: Biocrude C18:0 recovery relative to (a) biomass C18:0 and (b) total biomass C18 FAs versus reaction time grouped by temperature and initial concentration. See Table 4.1 for microalgae types. The bottom row depicts the first row ( $30 \text{ g L}_{\text{rxn}}^{-1}$ ) minus the second row ( $120 \text{ g L}_{\text{rxn}}^{-1}$ ). Error bars indicate SE.

## APPENDIX F

### Additional solid property data and figures for Chapter IV

#### F.1 Solid yield and elemental properties

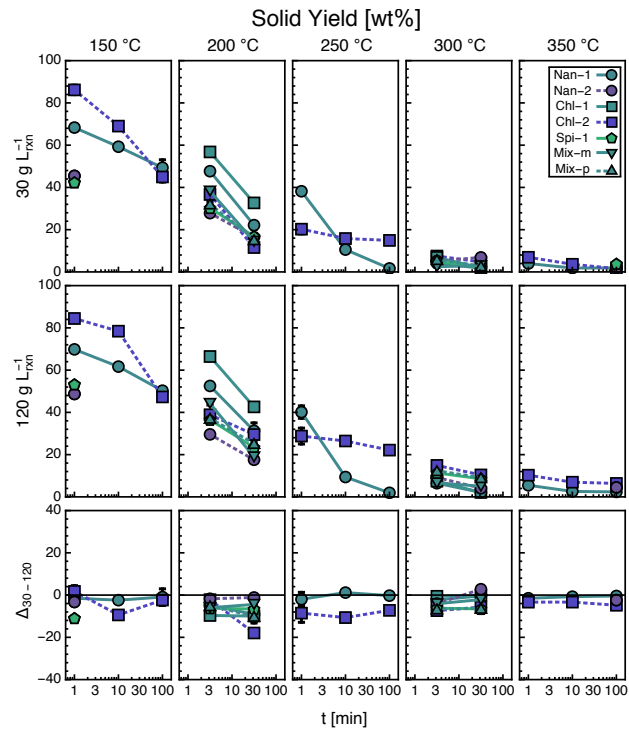


Figure F.1: Solid yields versus reaction time grouped by temperature and initial concentration. See Table 4.1 for microalgae types. The bottom row depicts the first row ( $30 \text{ g L}_{\text{rxn}}^{-1}$ ) minus the second row ( $120 \text{ g L}_{\text{rxn}}^{-1}$ ). Error bars indicate SE.

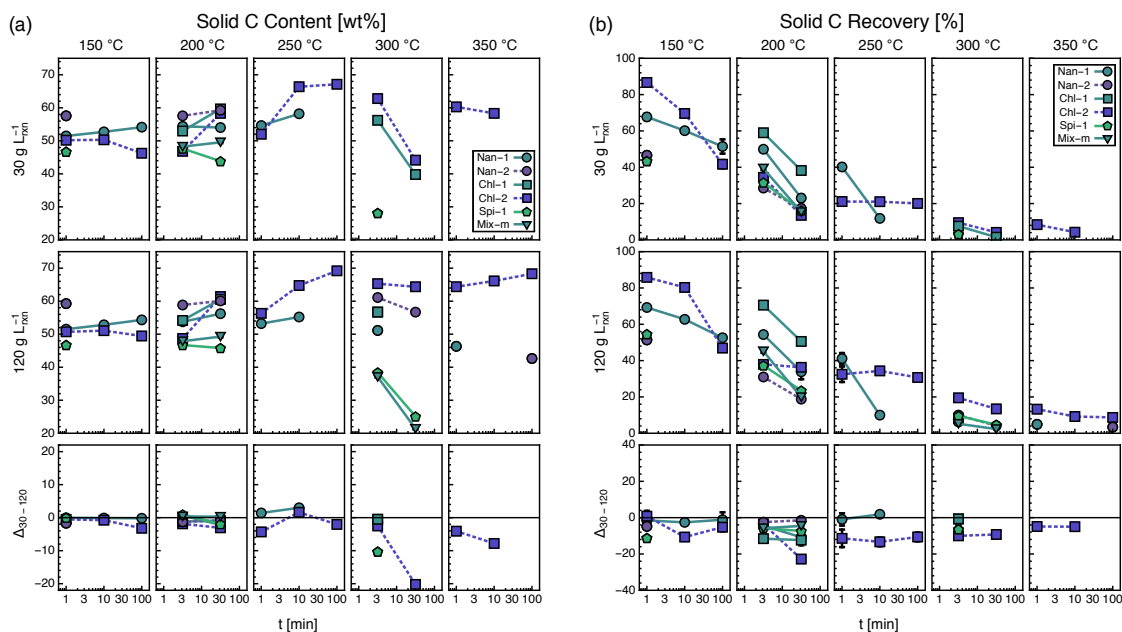


Figure F.2: Solid carbon (a) content and (b) recovery versus reaction time grouped by temperature and initial concentration. See Table 4.1 for microalgae types. The bottom row depicts the first row ( $30 \text{ g L}_{\text{rxn}}^{-1}$ ) minus the second row ( $120 \text{ g L}_{\text{rxn}}^{-1}$ ). Error bars indicate SE.

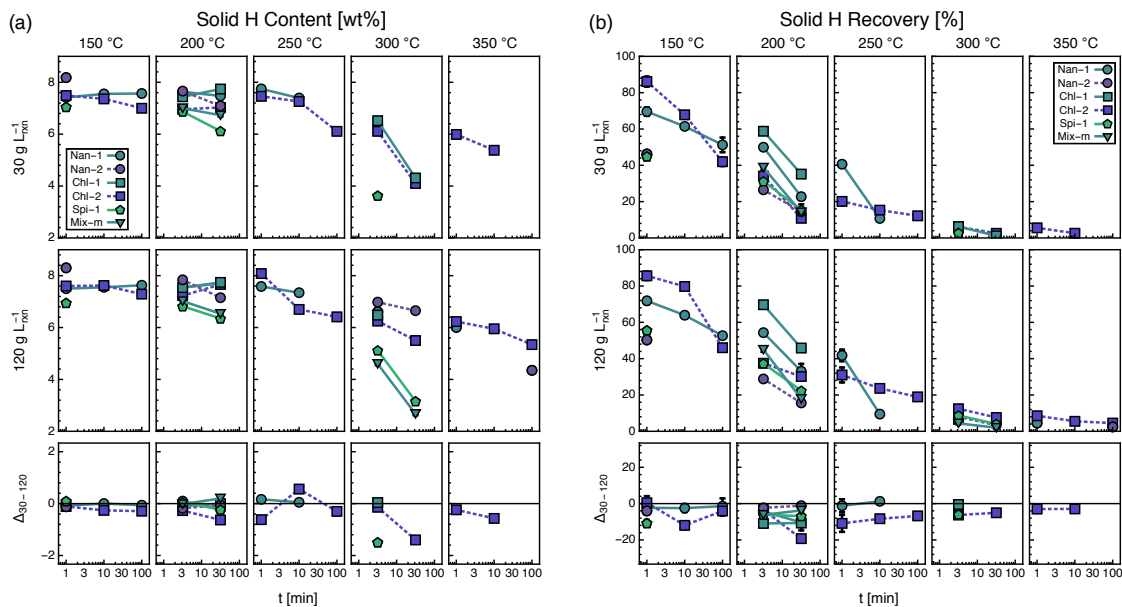


Figure F.3: Solid hydrogen (a) content and (b) recovery versus reaction time grouped by temperature and initial concentration. See Table 4.1 for microalgae types. The bottom row depicts the first row ( $30 \text{ g L}_{\text{rxn}}^{-1}$ ) minus the second row ( $120 \text{ g L}_{\text{rxn}}^{-1}$ ). Error bars indicate SE.

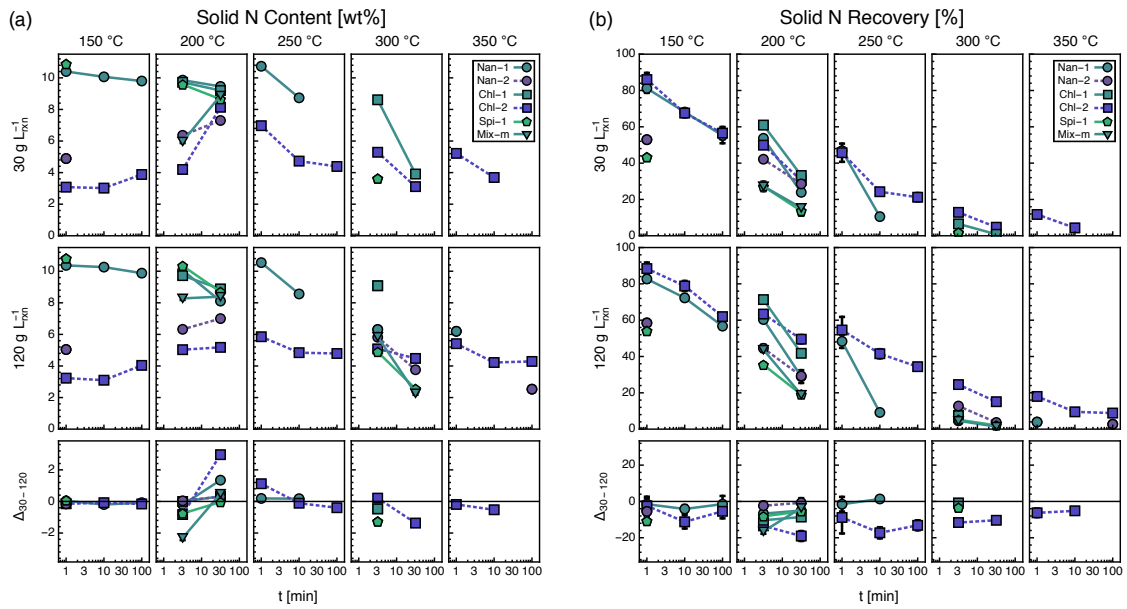


Figure F.4: Solid nitrogen (a) content and (b) recovery versus reaction time grouped by temperature and initial concentration. See Table 4.1 for microalgae types. The bottom row depicts the first row ( $30 \text{ g L}_{\text{rxn}}^{-1}$ ) minus the second row ( $120 \text{ g L}_{\text{rxn}}^{-1}$ ). Error bars indicate SE.

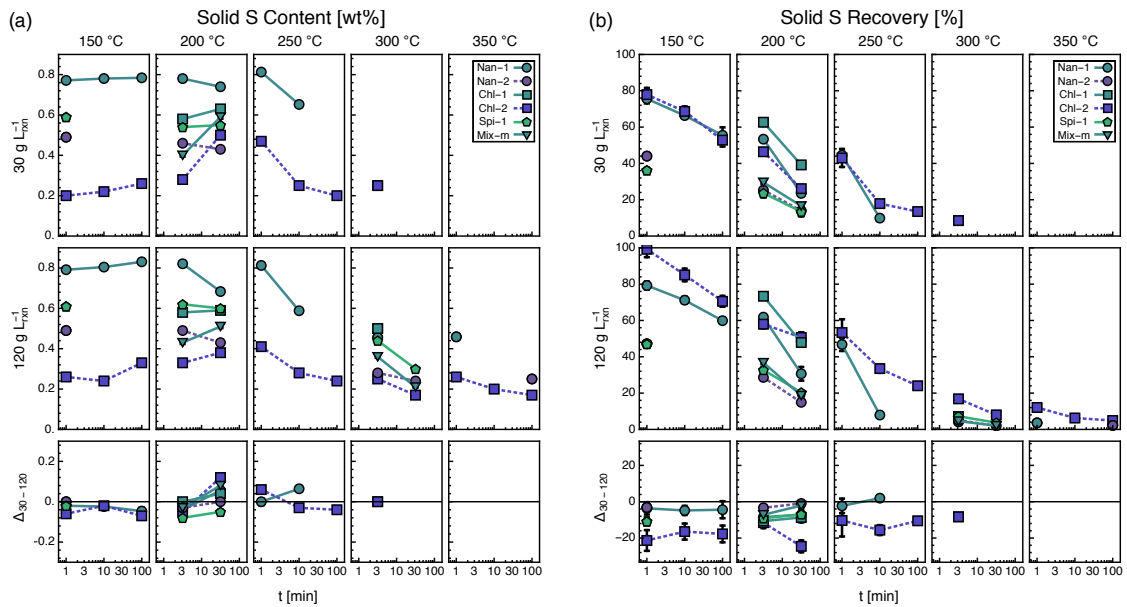


Figure F.5: Solid sulfur (a) content and (b) recovery versus reaction time grouped by temperature and initial concentration. See Table 4.1 for microalgae types. The bottom row depicts the first row ( $30 \text{ g L}_{\text{rxn}}^{-1}$ ) minus the second row ( $120 \text{ g L}_{\text{rxn}}^{-1}$ ). Error bars indicate SE.

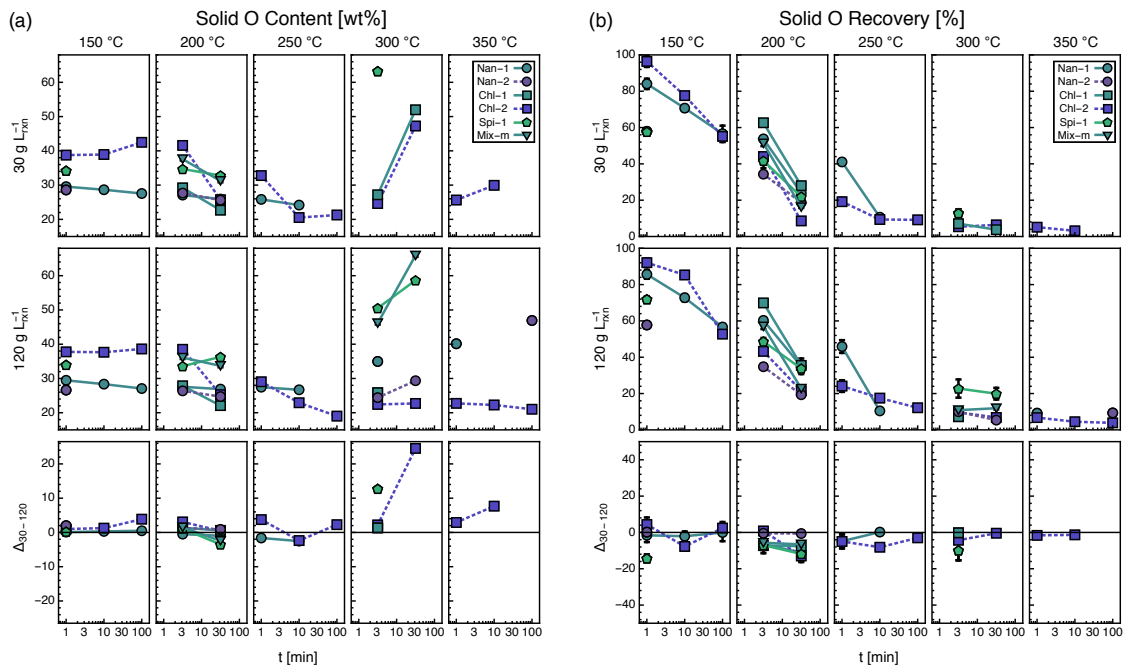


Figure F.6: Solid oxygen (a) content and (b) recovery versus reaction time grouped by temperature and initial concentration. See Table 4.1 for microalgae types. The bottom row depicts the first row ( $30 \text{ g L}_{\text{rxn}}^{-1}$ ) minus the second row ( $120 \text{ g L}_{\text{rxn}}^{-1}$ ). Error bars indicate SE.

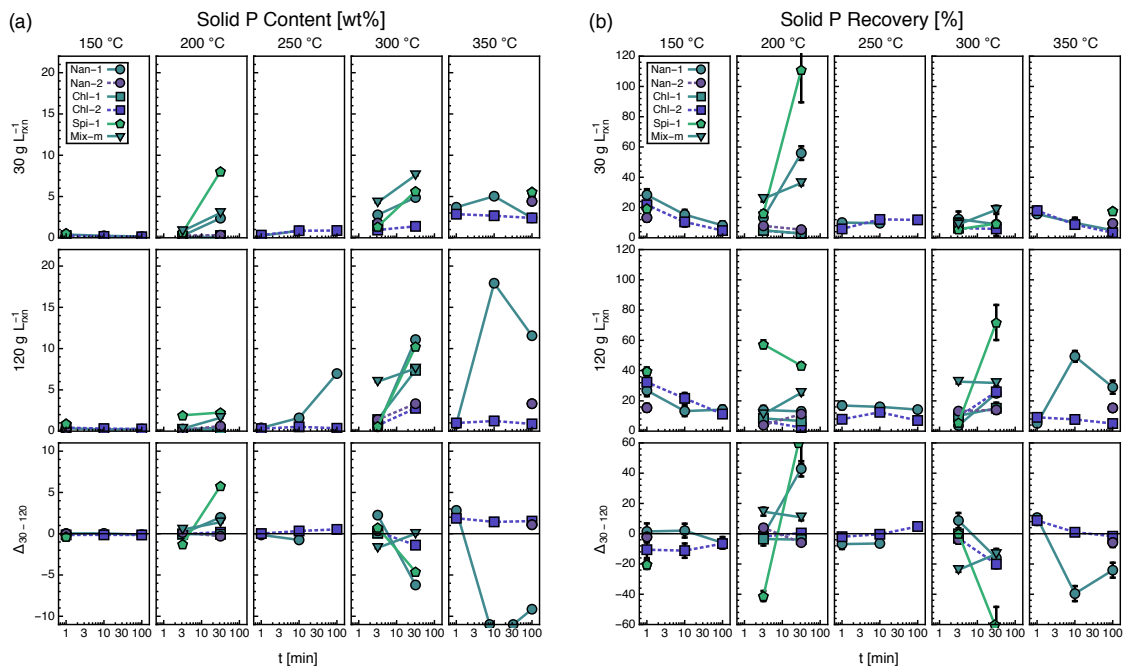


Figure F.7: Solid phosphorus (a) content and (b) recovery versus reaction time grouped by temperature and initial concentration. See Table 4.1 for microalgae types. The bottom row depicts the first row ( $30 \text{ g L}_{\text{rxn}}^{-1}$ ) minus the second row ( $120 \text{ g L}_{\text{rxn}}^{-1}$ ). Error bars indicate SE.

## F.2 Solid fatty acid data

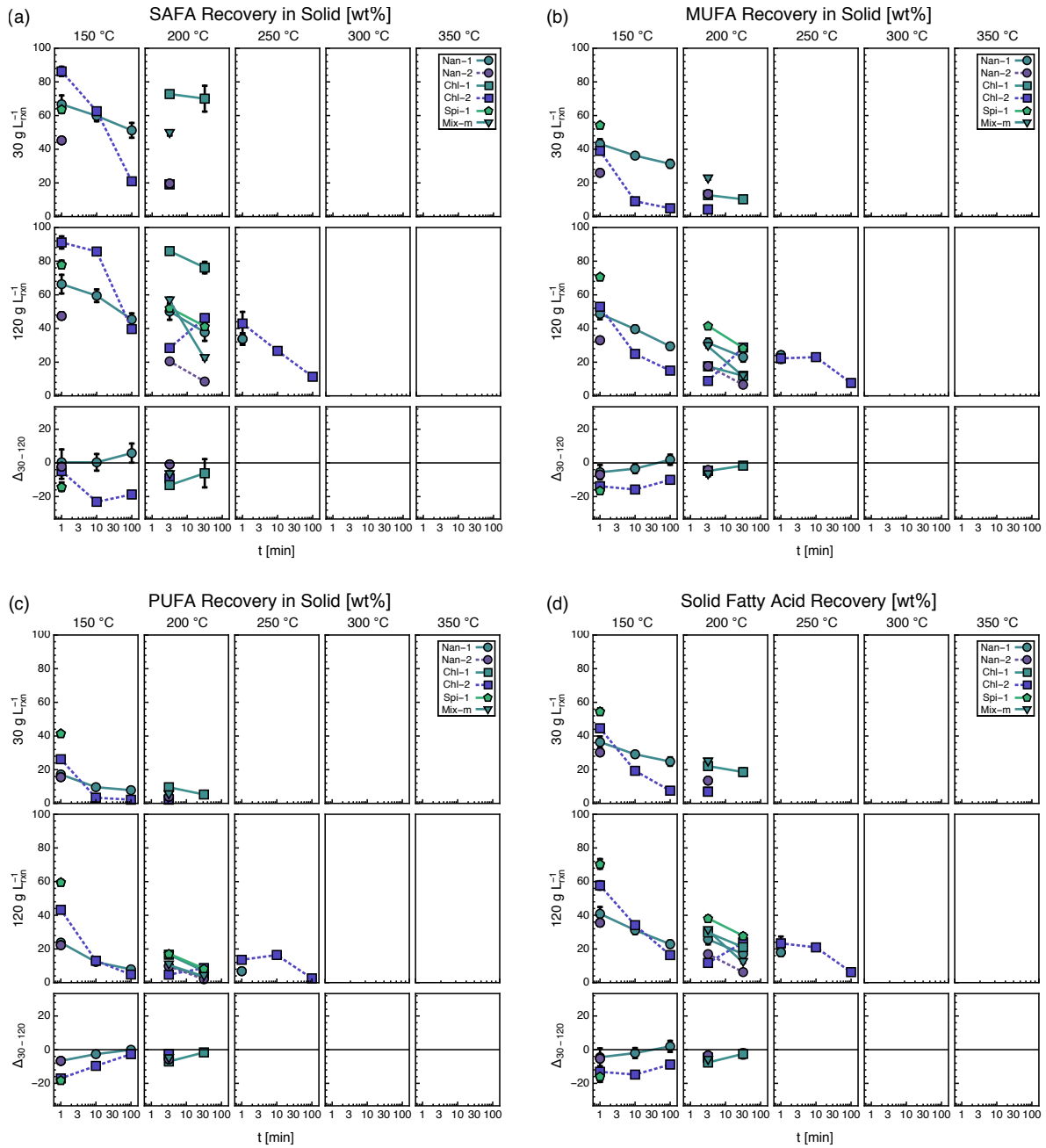


Figure F.8: Solid (a) SAFA, (b) MUFA, (c) PUFA, and (d) total FA recovery versus reaction time grouped by temperature and initial concentration. See Table 4.1 for microalgae types. The bottom row depicts the first row ( $30 \text{ g L}_{\text{rxn}}^{-1}$ ) minus the second row ( $120 \text{ g L}_{\text{rxn}}^{-1}$ ). Error bars indicate SE.

## APPENDIX G

### Additional gas data and figure for Chapter IV

#### G.1 Gas yield

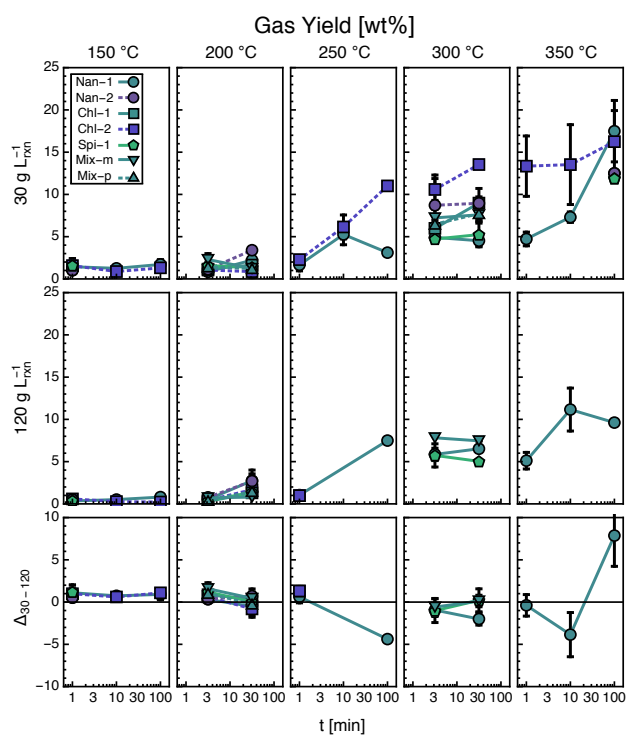


Figure G.1: Gas yields versus reaction time grouped by temperature and initial concentration. See Table 4.1 for microalgae types. The bottom row depicts the first row ( $30 \text{ g L}_{\text{rxn}}^{-1}$ ) minus the second row ( $120 \text{ g L}_{\text{rxn}}^{-1}$ ). Error bars indicate SE.

## APPENDIX H

### Additional aqueous property figures for Chapter V

#### H.1 Aqueous yield

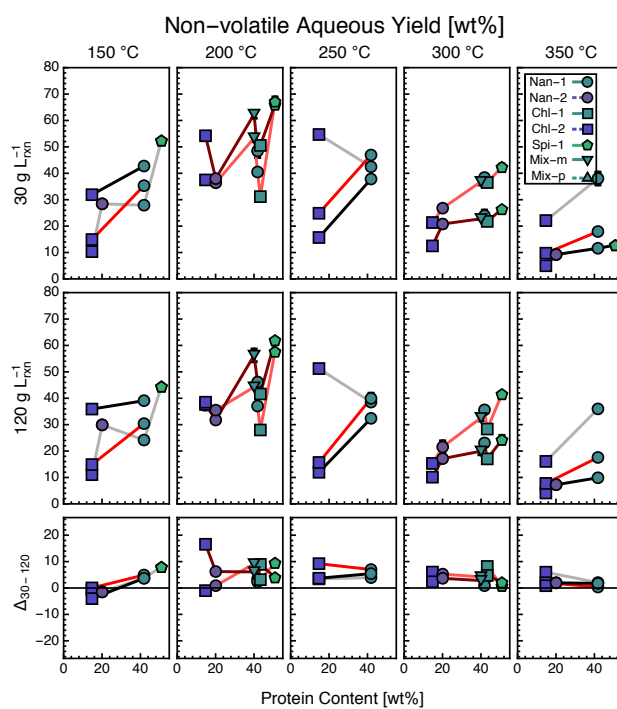


Figure H.1: Non-volatile aqueous-phase-product yield versus protein content grouped by temperature and initial concentration. See Table 4.1 for microalgae types. Gray, pink, red, dark red, and black lines represent 1.0, 3.2, 10.0, 31.6, and 100.0 min reaction time, respectively. The bottom row depicts the top row ( $30 \text{ g L}_{\text{rxn}}^{-1}$ ) minus the second row ( $120 \text{ g L}_{\text{rxn}}^{-1}$ ). Error bars indicate SE.

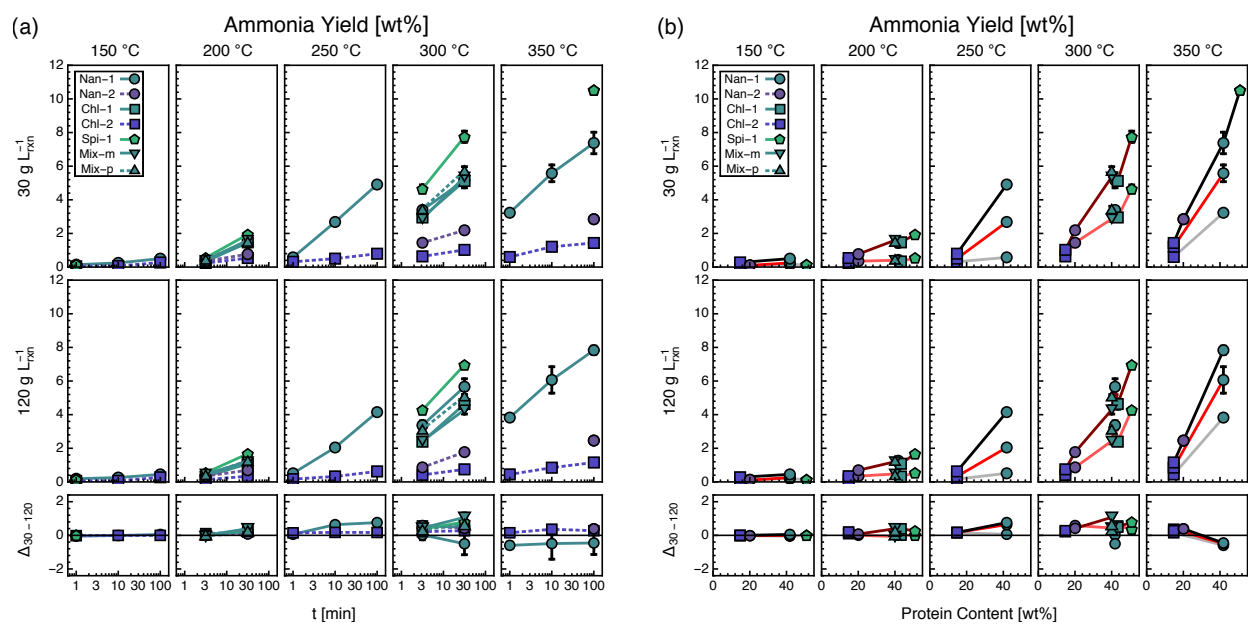


Figure H.2: Ammonia yield (including  $\text{NH}_3$  and  $\text{NH}_4^+$ ) versus (a) reaction time and (b) protein content grouped by temperature and initial concentration. See Table 4.1 for microalgae types. Gray, pink, red, dark red, and black lines represent 1.0, 3.2, 10.0, 31.6, and 100.0 min reaction time, respectively. The bottom row depicts the top row ( $30 \text{ g L}_{\text{rxn}}^{-1}$ ) minus the second row ( $120 \text{ g L}_{\text{rxn}}^{-1}$ ). Error bars indicate SE.

## H.2 Aqueous elemental properties

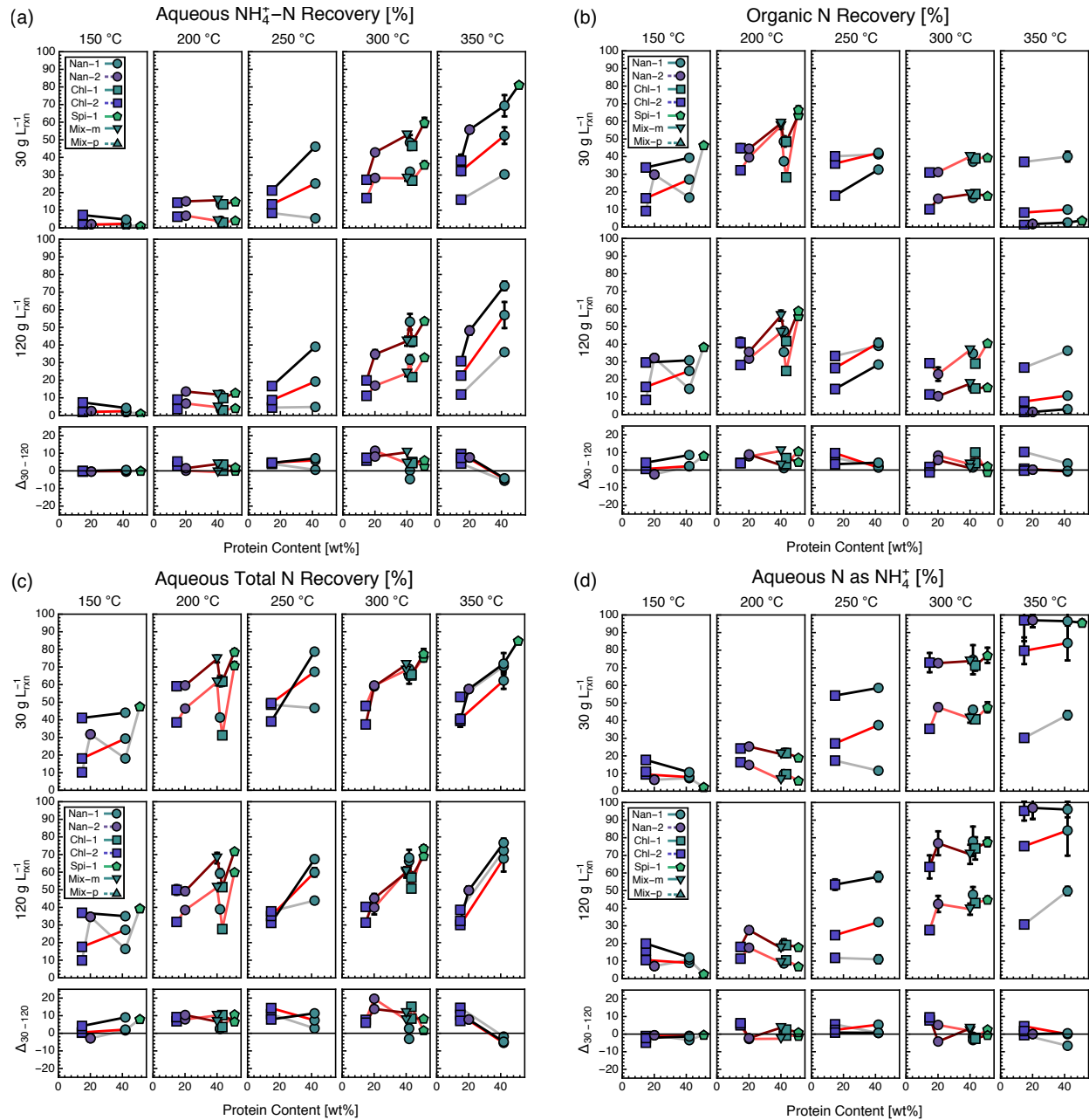


Figure H.3: Aqueous nitrogen recovery (a) as ammonium ( $\text{N-NH}_4^+$ ), (b) as organic nitrogen, (c) in total, and (d) as ammonium relative to total aqueous nitrogen versus protein content grouped by temperature and initial concentration. See Table 4.1 for microalgae types. Gray, pink, red, dark red, and black lines represent 1.0, 3.2, 10.0, 31.6, and 100.0 min reaction time, respectively. The bottom row depicts the top row ( $30 \text{ g L}_{\text{rxn}}^{-1}$ ) minus the second row ( $120 \text{ g L}_{\text{rxn}}^{-1}$ ). Error bars indicate SE.

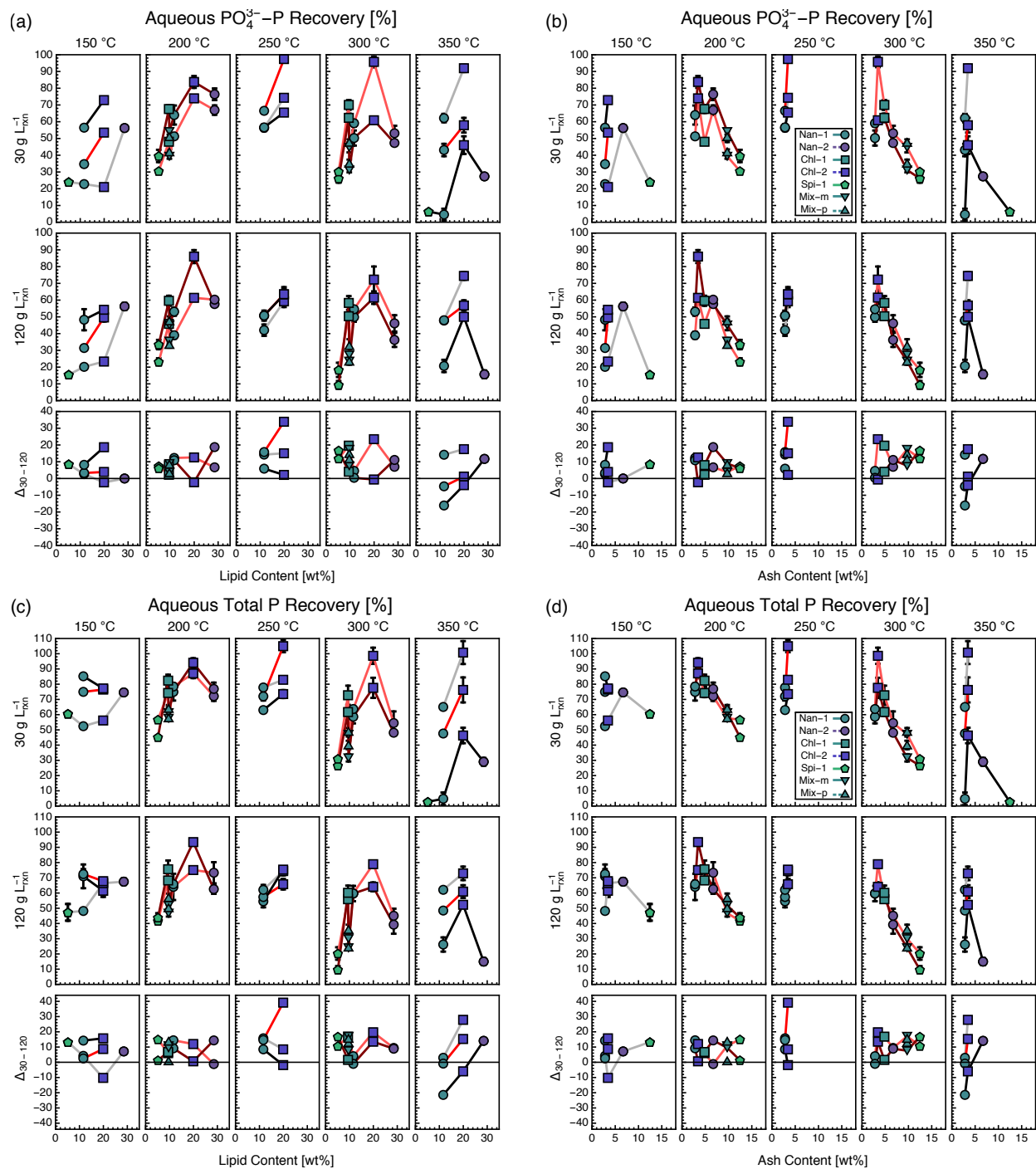


Figure H.4: Aqueous phosphorus recovery (a,b) as phosphate ( $P-PO_4^{3-}$ ) and (c,d) in total versus (a,c) lipid content and (b,d) ash content grouped by temperature and initial concentration. See Table 4.1 for microalgae types. Gray, pink, red, dark red, and black lines represent 1.0, 3.2, 10.0, 31.6, and 100.0 min reaction time, respectively. The bottom row depicts the top row ( $30 \text{ g L}_{\text{rxn}}^{-1}$ ) minus the second row ( $120 \text{ g L}_{\text{rxn}}^{-1}$ ). Error bars indicate SE.

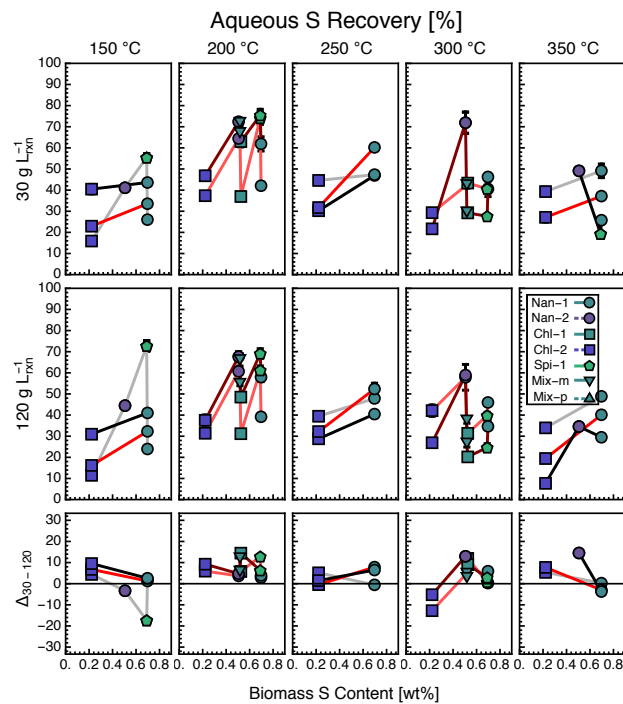


Figure H.5: Aqueous sulfur recovery versus biomass sulfur content grouped by temperature and initial concentration. See Table 4.1 for microalgae types. Gray, pink, red, dark red, and black lines represent 1.0, 3.2, 10.0, 31.6, and 100.0 min reaction time, respectively. The bottom row depicts the top row ( $30 \text{ g L}_{\text{rxn}}^{-1}$ ) minus the second row ( $120 \text{ g L}_{\text{rxn}}^{-1}$ ). Error bars indicate SE.

## APPENDIX I

### Constants and additional figures for Chapter VI

#### I.1 Kinetic model constants and designations

Component	$M$ [g mol <sup>-1</sup> ]	$w^C$ [wt frac]	$w^N$ [wt frac]
AA <sub>1</sub>	128.1	0.460	0.121
AA <sub>2</sub>	159.7	0.449	0.262
CO <sub>2</sub>	44.0	0.273	-
CAR	157.6	0.451	-
H <sub>2</sub> O	18.0	-	-
FA	269.3	0.762	-
LIP	251.3	0.817	-
NH <sub>3</sub>	17.0	-	0.822
PEP	246.8	0.491	0.194
PRO	228.8	0.530	0.209
SAC	175.6	0.405	-

Table I.1: Molar mass, carbon content, and nitrogen constants employed in the kinetic model. Values represent abundance-weighted averages across typical distributions of molecules residing within each lumped-product fraction [110, 129, 135].

Constant	Value [wt frac]
$w_{AA_1}$	0.850
$w_{AA_2}$	0.150
$w_{PEP_0}$	0.722
$w_{PEP_1}$	0.256
$w_{PEP_2}$	0.023

Table I.2: Abundances of amino acids and dipeptides employed in the kinetic model. Values represent abundance-weighted averages of typical amino acid profiles [110, 129, 135].

Lumped product	Constituent amino acids
AA <sub>1</sub>	Alanine, $\Gamma$ -aminobutyric acid, Aspartic acid, Cystine, Glutamic acid, Glycine, Histidine, Hydroxyproline, Isoleucine, Leucine, Methionine, Phenylalanine, Proline, Serine, Threonine, Tryptophan, Tyrosine, Valine
AA <sub>2</sub>	Arginine, Lysine, Ornithine

Table I.3: Group designations for different amino acids present in microalgae.

## I.2 Carbon distribution solutions

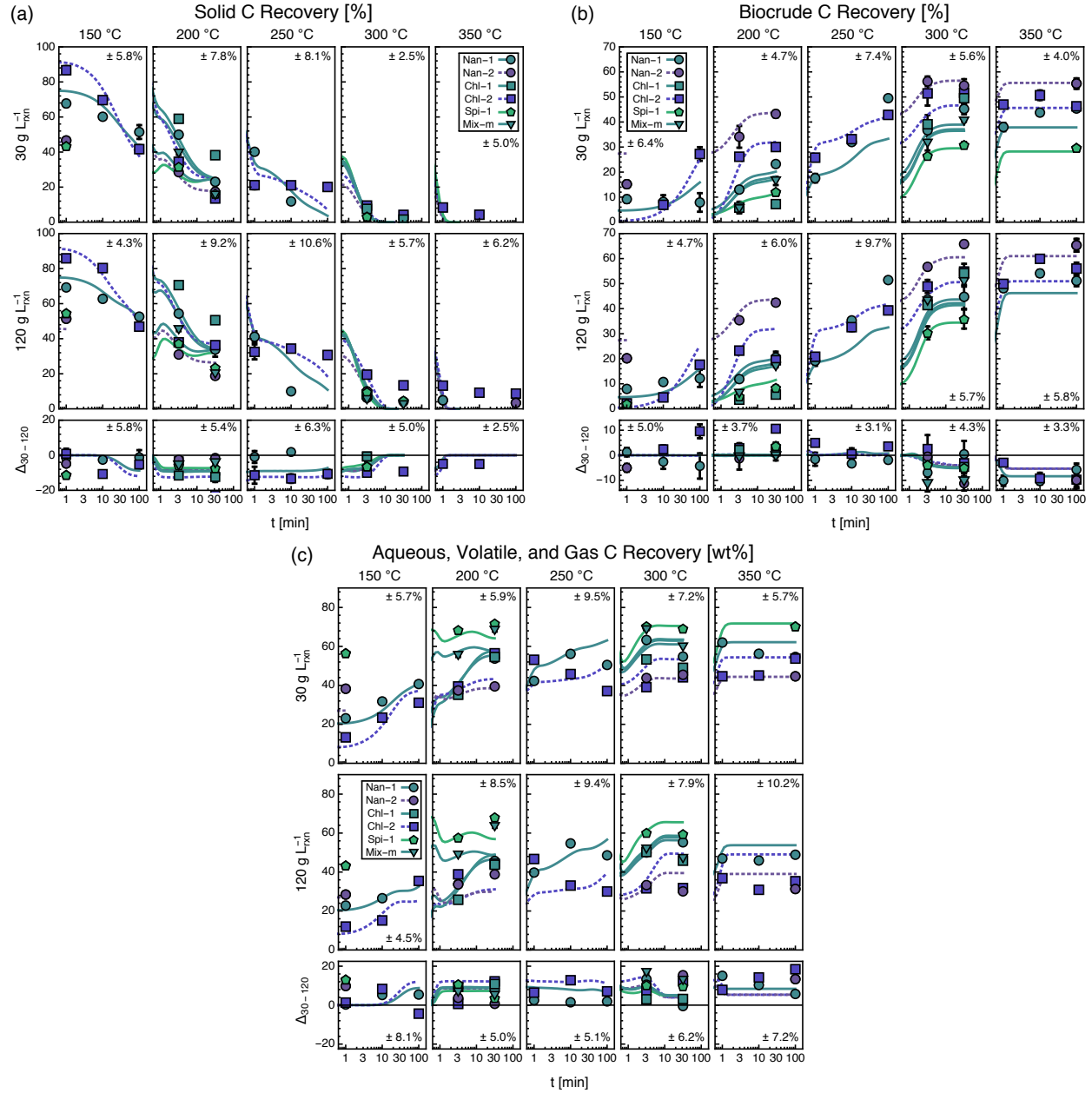


Figure I.1: Model solutions for HTL product carbon recoveries (% , dry-algal-carbon-mass basis) versus reaction time grouped by temperature and initial concentration. See Table 4.1 for microalgae types. The bottom row depicts the first row ( $30 \text{ g L}_{\text{rxn}}^{-1}$ ) minus the second row ( $120 \text{ g L}_{\text{rxn}}^{-1}$ ). The “ $\pm$ ” value in each panel represents the RMSD for that component and subset of reaction conditions. Error bars indicate SE.

## BIBLIOGRAPHY

## BIBLIOGRAPHY

- [1] U.S. EPA. Inventory of U.S. Greenhouse Gas Emissions and Sinks. Technical report, 2018.
- [2] Y. Chisti. Biodiesel from microalgae. *Biotechnology advances*, 25(3):294–306, 2007. doi: 10.1016/j.biotechadv.2007.02.001.
- [3] L. Brennan and P. Owende. Biofuels from microalgae - A review of technologies for production, processing, and extractions of biofuels and co-products. *Renewable and Sustainable Energy Reviews*, 14(2):557–577, 2010. doi: 10.1016/j.rser.2009.10.009.
- [4] P. T. Pienkos and A. Darzins. The promise and challenges of microalgal-derived biofuels. *Biofuels, Bioproducts and Biorefining*, 3(4):431–440, 2009. doi: 10.1002/bbb.159.
- [5] A. Bhatnagar, S. Chinnasamy, M. Singh, and K. C. Das. Renewable biomass production by mixotrophic algae in the presence of various carbon sources and wastewaters. *Applied Energy*, 88(10):3425–3431, 2011. doi: 10.1016/j.apenergy.2010.12.064.
- [6] A. Narwani, A. R. Lashaway, D. C. Hietala, P. E. Savage, and B. J. Cardinale. Power of Plankton: Effects of Algal Biodiversity on Biocrude Production and Stability. *Environmental Science & Technology*, 50(23):13142–13150, 2016. doi: 10.1021/acs.est.6b03256.
- [7] C. M. Godwin, D. C. Hietala, A. R. Lashaway, A. Narwani, P. E. Savage, and B. J. Cardinale. Ecological Stoichiometry Meets Ecological Engineering: Using Polycultures to Enhance the Multifunctionality of Algal Biocrude Systems. *Environmental Science & Technology*, 51(19):11450–11458, 2017. doi: 10.1021/acs.est.7b02137.
- [8] C. M. Godwin, A. R. Lashaway, D. C. Hietala, P. E. Savage, and B. J. Cardinale. Biodiversity improves the ecological design of sustainable biofuel systems. *GCB Bioenergy*, (March):1–14, 2018. doi: 10.1111/gcbb.12524.
- [9] Y. Dote, S. Sawayama, S. Inoue, T. Minowa, and S.-y. Yokoyama. Recovery of liquid fuel from hydrocarbon-rich microalgae by thermochemical liquefaction. *Fuel*, 73(12):1855–1857, 1994. doi: 10.1016/0016-2361(94)90211-9.
- [10] T. M. Brown, P. Duan, and P. E. Savage. Hydrothermal Liquefaction and Gasification of *Nannochloropsis* sp. *Energy & Fuels*, 24(6):3639–3646, 2010. doi: 10.1021/ef100203u.
- [11] N. Akiya and P. E. Savage. Roles of water for chemical reactions in high-temperature water. *Chemical reviews*, 102(8):2725–2750, 2002.

- [12] S. M. Changi, J. L. Faeth, N. Mo, and P. E. Savage. Hydrothermal Reactions of Biomolecules Relevant for Microalgae Liquefaction. *Industrial & Engineering Chemistry Research*, 54(47):11733–11758, 2015. doi: 10.1021/acs.iecr.5b02771.
- [13] P. Biller and A. Ross. Potential yields and properties of oil from the hydrothermal liquefaction of microalgae with different biochemical content. *Bioresource Technology*, 102(1):215–225, 2011. doi: 10.1016/j.biortech.2010.06.028.
- [14] M. Déniel, G. Haarlemmer, A. Roubaud, E. Weiss-Hortala, and J. Fages. Hydrothermal liquefaction of blackcurrant pomace and model molecules: understanding of reaction mechanisms. *Sustainable Energy Fuels*, 2017. doi: 10.1039/C6SE00065G.
- [15] Y. Li, S. Leow, A. C. Fedders, B. K. Sharma, J. S. Guest, and T. J. Strathmann. Quantitative multiphase model for hydrothermal liquefaction of algal biomass. *Green Chem.*, 19(4):1163–1174, 2017. doi: 10.1039/C6GC03294J.
- [16] P. Duan and P. E. Savage. Catalytic hydrotreatment of crude algal bio-oil in supercritical water. *Applied Catalysis B: Environmental*, 104(1-2):136–143, 2011. doi: 10.1016/j.apcatb.2011.02.020.
- [17] D. C. Elliott, T. R. Hart, A. J. Schmidt, G. G. Neuenschwander, L. J. Rotness, M. V. Olarte, A. H. Zacher, K. O. Albrecht, R. T. Hallen, and J. E. Holladay. Process development for hydrothermal liquefaction of algae feedstocks in a continuous-flow reactor. *Algal Research*, 2(4):445–454, 2013. doi: 10.1016/j.algal.2013.08.005.
- [18] R. B. Levine, T. Pinnarat, and P. E. Savage. Biodiesel Production from Wet Algal Biomass through in Situ Lipid Hydrolysis and Supercritical Transesterification. *Energy & Fuels*, 24(9):5235–5243, 2010. doi: 10.1021/ef1008314.
- [19] A. Ross, P. Biller, M. Kubacki, H. Li, A. Lea-Langton, and J. Jones. Hydrothermal processing of microalgae using alkali and organic acids. *Fuel*, 89(9):2234–2243, 2010. doi: 10.1016/j.fuel.2010.01.025.
- [20] D. J. Patzelt, S. Hindersin, S. Elsayed, N. Boukis, M. Kerner, and D. Hanelt. Microalgal growth and fatty acid productivity on recovered nutrients from hydrothermal gasification of *Acutodesmus obliquus*. *Algal Research*, 10:164–171, 2015. doi: 10.1016/j.algal.2015.05.002.
- [21] U. Jena, K. Das, and J. Kastner. Effect of operating conditions of thermochemical liquefaction on biocrude production from *Spirulina platensis*. *Bioresource Technology*, 102(10):6221–6229, 2011. doi: 10.1016/j.biortech.2011.02.057.
- [22] L. Garcia Alba, C. Torri, C. Samorì, J. van der Spek, D. Fabbri, S. R. A. Kersten, and D. W. F. W. Brilman. Hydrothermal Treatment (HTT) of Microalgae: Evaluation of the Process As Conversion Method in an Algae Biorefinery Concept. *Energy & Fuels*, 26(1):642–657, 2012. doi: 10.1021/ef201415s.

- [23] C. Miao, M. Chakraborty, and S. Chen. Impact of reaction conditions on the simultaneous production of polysaccharides and bio-oil from heterotrophically grown *Chlorella sorokiniana* by a unique sequential hydrothermal liquefaction process. *Bioresource Technology*, 110:617–627, 2012. doi: 10.1016/j.biortech.2012.01.047.
- [24] P. J. Valdez, M. C. Nelson, H. Y. Wang, X. N. Lin, and P. E. Savage. Hydrothermal liquefaction of *Nannochloropsis* sp.: Systematic study of process variables and analysis of the product fractions. *Biomass and Bioenergy*, 46:317–331, 2012. doi: 10.1016/j.biombioe.2012.08.009.
- [25] J. L. Faeth, P. J. Valdez, and P. E. Savage. Fast Hydrothermal Liquefaction of *Nannochloropsis* sp. To Produce Biocrude. *Energy & Fuels*, 27(3):1391–1398, 2013. doi: 10.1021/ef301925d.
- [26] J. L. Garcia-MoscOSO, W. Obeid, S. Kumar, and P. G. Hatcher. Flash hydrolysis of microalgae (*Scenedesmus* sp.) for protein extraction and production of biofuels intermediates. *The Journal of Supercritical Fluids*, 82(x):183–190, 2013. doi: 10.1016/j.supflu.2013.07.012.
- [27] P. S. Christensen, G. Peng, F. Vogel, and B. B. Iversen. Hydrothermal Liquefaction of the Microalgae *Phaeodactylum tricorutum* : Impact of Reaction Conditions on Product and Elemental Distribution. *Energy & Fuels*, 28(9):5792–5803, 2014. doi: 10.1021/ef5012808.
- [28] D. López Barreiro, C. Samorì, G. Terranella, U. Hornung, A. Kruse, and W. Prins. Assessing microalgae biorefinery routes for the production of biofuels via hydrothermal liquefaction. *Bioresource Technology*, 174:256–265, 2014. doi: 10.1016/j.biortech.2014.10.031.
- [29] P. J. Valdez, V. J. Tocco, and P. E. Savage. A general kinetic model for the hydrothermal liquefaction of microalgae. *Bioresource Technology*, 163:123–127, 2014. doi: 10.1016/j.biortech.2014.04.013.
- [30] C. Jazrawi, P. Biller, Y. He, A. Montoya, A. B. Ross, T. Maschmeyer, and B. S. Haynes. Two-stage hydrothermal liquefaction of a high-protein microalga. *Algal Research*, 8: 15–22, 2015. doi: 10.1016/j.algal.2014.12.010.
- [31] W. Costanzo, U. Jena, R. Hilten, K. Das, and J. R. Kastner. Low temperature hydrothermal pretreatment of algae to reduce nitrogen heteroatoms and generate nutrient recycle streams. *Algal Research*, 12:377–387, 2015. doi: 10.1016/j.algal.2015.09.019.
- [32] C. Gai, Y. Zhang, W.-T. Chen, Y. Zhou, L. Schideman, P. Zhang, G. Tommaso, C.-T. Kuo, and Y. Dong. Characterization of aqueous phase from the hydrothermal liquefaction of *Chlorella pyrenoidosa*. *Bioresource Technology*, 184:328–335, 2015. doi: 10.1016/j.biortech.2014.10.118.
- [33] T. Selvaratnam, H. Reddy, T. Muppaneni, F. Holguin, N. Nirmalakhandan, P. J. Lamers, and S. Deng. Optimizing energy yields from nutrient recycling using sequential

- hydrothermal liquefaction with *Galdieria sulphuraria*. *Algal Research*, 12:74–79, 2015. doi: 10.1016/j.algal.2015.07.007.
- [34] D. C. Hietala, J. L. Faeth, and P. E. Savage. A quantitative kinetic model for the fast and isothermal hydrothermal liquefaction of *Nannochloropsis* sp. *Bioresource Technology*, 214:102–111, 2016. doi: 10.1016/j.biortech.2016.04.067.
- [35] U. Ekpo, A. B. Ross, M. A. Camargo-Valero, and P. T. Williams. A comparison of product yields and inorganic content in process streams following thermal hydrolysis and hydrothermal processing of microalgae, manure and digestate. *Bioresource Technology*, 200:951–960, 2016. doi: 10.1016/j.biortech.2015.11.018.
- [36] H. K. Reddy, T. Muppaneni, S. Ponnusamy, N. Sudasinghe, A. Pegallapati, T. Selvaratnam, M. Seger, B. Dungan, N. Nirmalakhandan, T. Schaub, F. O. Holguin, P. Lambers, W. Voorhies, and S. Deng. Temperature effect on hydrothermal liquefaction of *Nannochloropsis gaditana* and *Chlorella* sp. *Applied Energy*, 165:943–951, 2016. doi: 10.1016/j.apenergy.2015.11.067.
- [37] J. Jiang and P. E. Savage. Metals and Other Elements in Biocrude from Fast and Isothermal Hydrothermal Liquefaction of Microalgae. *Energy & Fuels*, page acs.energyfuels.7b03144, 2017. doi: 10.1021/acs.energyfuels.7b03144.
- [38] C. Jazrawi, P. Biller, A. B. Ross, A. Montoya, T. Maschmeyer, and B. S. Haynes. Pilot plant testing of continuous hydrothermal liquefaction of microalgae. *Algal Research*, 2(3):268–277, 2013. doi: 10.1016/j.algal.2013.04.006.
- [39] D. López Barreiro, C. Zamalloa, N. Boon, W. Vyverman, F. Ronsse, W. Brilman, and W. Prins. Influence of strain-specific parameters on hydrothermal liquefaction of microalgae. *Bioresource Technology*, 146:463–471, 2013. doi: 10.1016/j.biortech.2013.07.123.
- [40] S. Leow, J. R. Witter, D. R. Vardon, B. K. Sharma, J. S. Guest, and T. J. Strathmann. Prediction of microalgae hydrothermal liquefaction products from feedstock biochemical composition. *Green Chem.*, 17(6):3584–3599, 2015. doi: 10.1039/C5GC00574D.
- [41] R. B. Madsen, P. Biller, M. M. Jensen, J. Becker, B. B. Iversen, and M. Glasius. Predicting the chemical composition of aqueous phase from hydrothermal liquefaction of model compounds and biomasses. *Energy & Fuels*, 2016. doi: 10.1021/acs.energyfuels.6b02007.
- [42] D. C. Hietala, C. K. Koss, A. Narwani, A. R. Lashaway, C. M. Godwin, B. J. Cardinale, and P. E. Savage. Influence of biodiversity, biochemical composition, and species identity on the quality of biomass and biocrude oil produced via hydrothermal liquefaction. *Algal Research*, 26(May):203–214, 2017. doi: 10.1016/j.algal.2017.07.020.
- [43] R. B. Madsen, R. Z. K. Bernberg, P. Biller, J. Becker, B. B. Iversen, and M. Glasius. Hydrothermal co-liquefaction of biomasses - quantitative analysis of bio-crude and aqueous phase composition. *Sustainable Energy Fuels*, 1(4):789–805, 2017. doi: 10.1039/C7SE00104E.

- [44] R. Shakya, S. Adhikari, R. Mahadevan, S. R. Shanmugam, H. Nam, E. B. Hassan, and T. A. Dempster. Influence of biochemical composition during hydrothermal liquefaction of algae on product yields and fuel properties. *Bioresource Technology*, 243:1112–1120, 2017. doi: 10.1016/j.biortech.2017.07.046.
- [45] R. B. Madsen, H. Zhang, P. Biller, A. H. Goldstein, and M. Glasius. Characterizing Semi-volatile Organic Compounds of Bio-crude from Hydrothermal Liquefaction of Biomass. *Energy & Fuels*, page acs.energyfuels.7b00160, 2017. doi: 10.1021/acs.energyfuels.7b00160.
- [46] A. A. Peterson, R. P. Lachance, and J. W. Tester. Kinetic evidence of the maillard reaction in hydrothermal biomass processing: Glucose-glycine interactions in high-temperature, high-pressure water. *Industrial and Engineering Chemistry Research*, 49(5):2107–2117, 2010. doi: 10.1021/ie9014809.
- [47] J. L. Faeth, P. E. Savage, J. M. Jarvis, A. M. McKenna, and P. E. Savage. Characterization of products from fast and isothermal hydrothermal liquefaction of microalgae. *AIChE Journal*, 62(3):815–828, 2016. doi: 10.1002/aic.15147.
- [48] G. Teri, L. Luo, and P. E. Savage. Hydrothermal Treatment of Protein, Polysaccharide, and Lipids Alone and in Mixtures. *Energy & Fuels*, 28(12):7501–7509, 2014. doi: 10.1021/ef501760d.
- [49] M. Déniel, G. Haarlemmer, A. Roubaud, E. Weiss-Hortala, and J. Fages. Modelling and Predictive Study of Hydrothermal Liquefaction: Application to Food Processing Residues. *Waste and Biomass Valorization*, 2016. doi: 10.1007/s12649-016-9726-7.
- [50] S. Sunphorka, K. Prapaiwatcharapan, N. Hinchiranan, K. Kangvansaichol, and P. Kuchonthara. Biocrude oil production and nutrient recovery from algae by two-step hydrothermal liquefaction using a semi-continuous reactor. *Korean Journal of Chemical Engineering*, 32(1):79–87, 2015. doi: 10.1007/s11814-014-0165-5.
- [51] D. C. Hietala and P. E. Savage. Reaction pathways and kinetics of cholesterol in high-temperature water. *Chemical Engineering Journal*, 265(1):129–137, 2015. doi: 10.1016/j.cej.2014.12.020.
- [52] A. Kruse, A. Krupka, V. Schwarzkopf, C. Gamard, and T. Henningsen. Influence of Proteins on the Hydrothermal Gasification and Liquefaction of Biomass. 1. Comparison of Different Feedstocks. *Industrial & Engineering Chemistry Research*, 44(9):3013–3020, 2005. doi: 10.1021/ie049129y.
- [53] P. J. Valdez and P. E. Savage. A reaction network for the hydrothermal liquefaction of *Nannochloropsis* sp. *Algal Research*, 2(4):416–425, 2013. doi: 10.1016/j.algal.2013.08.002.
- [54] J. D. Sheehan and P. E. Savage. Modeling the effects of microalga biochemical content on the kinetics and biocrude yields from hydrothermal liquefaction. *Bioresource Technology*, 239:144–150, 2017. doi: 10.1016/j.biortech.2017.05.013.

- [55] B. Zhang, M. von Keitz, and K. Valentas. Thermal Effects on Hydrothermal Biomass Liquefaction. *Applied Biochemistry and Biotechnology*, 147(1-3):143–150, 2008. doi: 10.1007/s12010-008-8131-5.
- [56] P. J. Valdez, M. C. Nelson, J. L. Faeth, H. Y. Wang, X. N. Lin, and P. E. Savage. Hydrothermal Liquefaction of Bacteria and Yeast Monocultures. *Energy & Fuels*, 28(1):67–75, 2014. doi: 10.1021/ef401506u.
- [57] Q.-V. Bach, M. V. Sillero, K.-Q. Tran, and J. Skjermo. Fast hydrothermal liquefaction of a Norwegian macro-alga: Screening tests. *Algal Research*, 6:271–276, 2014. doi: 10.1016/j.algal.2014.05.009.
- [58] P. Biller, B. K. Sharma, B. Kunwar, and A. B. Ross. Hydroprocessing of bio-crude from continuous hydrothermal liquefaction of microalgae. *Fuel*, 159:197–205, 2015. doi: 10.1016/j.fuel.2015.06.077.
- [59] X. Cheng, M. D. Ooms, and D. Sinton. Biomass-to-biocrude on a chip via hydrothermal liquefaction of algae. *Lab Chip*, 16:256–260, 2016. doi: 10.1039/C5LC01369K.
- [60] M. Sasaki, Z. Fang, Y. Fukushima, T. Adschiri, and K. Arai. Dissolution and Hydrolysis of Cellulose in Subcritical and Supercritical Water. *Industrial & Engineering Chemistry Research*, 39(8):2883–2890, 2000. doi: 10.1021/ie990690j.
- [61] T. Rogalinski, K. Liu, T. Albrecht, and G. Brunner. Hydrolysis kinetics of biopolymers in subcritical water. *The Journal of Supercritical Fluids*, 46(3):335–341, 2008. doi: 10.1016/j.supflu.2007.09.037.
- [62] P. Biller and A. B. Ross. Hydrothermal processing of algal biomass for the production of biofuels and chemicals. *Biofuels*, 3(5):603–623, 2012. doi: 10.4155/bfs.12.42.
- [63] B. Eboibi, D. Lewis, P. Ashman, and S. Chinnasamy. Effect of operating conditions on yield and quality of biocrude during hydrothermal liquefaction of halophytic microalga *Tetraselmis* sp. *Bioresource Technology*, 170:20–29, 2014. doi: 10.1016/j.biortech.2014.07.083.
- [64] N. Sudasinghe, H. Reddy, N. Csakan, S. Deng, P. Lammers, and T. Schaub. Temperature-Dependent Lipid Conversion and Nonlipid Composition of Microalgal Hydrothermal Liquefaction Oils Monitored by Fourier Transform Ion Cyclotron Resonance Mass Spectrometry. *Bioenergy Research*, 8(4):1962–1972, 2015. doi: 10.1007/s12155-015-9635-9.
- [65] S. Stumm and J. J. Morgan. *Aquatic Chemistry: Chemical Equilibria and Rates in Natural Waters*. Wiley, 1996.
- [66] S. P. Cadogan, G. C. Maitland, and J. P. M. Trusler. Diffusion Coefficients of CO<sub>2</sub> and N<sub>2</sub> in Water at Temperatures between 298.15 K and 423.15 K at Pressures up to 45 MPa. *Journal of Chemical & Engineering Data*, 59(2):519–525, 2014. doi: 10.1021/je401008s.

- [67] J. L. Garcia-MoscOSO, A. Teymouri, and S. Kumar. Kinetics of Peptides and Arginine Production from Microalgae (*Scenedesmus* sp.) by Flash Hydrolysis. *Industrial & Engineering Chemistry Research*, 54(7):2048–2058, 2015. doi: 10.1021/ie5047279.
- [68] R. B. Levine, A. Bollas, and P. E. Savage. Process improvements for the supercritical in situ transesterification of carbonized algal biomass. *Bioresource Technology*, 136: 556–564, 2013. doi: 10.1016/j.biortech.2013.03.022.
- [69] Y. Lu, R. B. Levine, and P. E. Savage. Fatty Acids for Nutraceuticals and Biofuels from Hydrothermal Carbonization of Microalgae. *Industrial & Engineering Chemistry Research*, 54(16):4066–4071, 2015. doi: 10.1021/ie503448u.
- [70] Q. Guan, C. Wei, and P. E. Savage. Kinetic model for supercritical water gasification of algae. *Physical Chemistry Chemical Physics*, 14(9):3140, 2012. doi: 10.1039/c2cp23792j.
- [71] C. Tian, B. Li, Z. Liu, Y. Zhang, and H. Lu. Hydrothermal liquefaction for algal biorefinery: A critical review. *Renewable and Sustainable Energy Reviews*, 38:933–950, 2014. doi: 10.1016/j.rser.2014.07.030.
- [72] Y. Chisti and J. Yan. Energy from algae: Current status and future trends. Algal biofuels - A status report. *Applied Energy*, 88(10):3277–3279, 2011. doi: 10.1016/j.apenergy.2011.04.038.
- [73] D. R. Georgianna and S. P. Mayfield. Exploiting diversity and synthetic biology for the production of algal biofuels. *Nature*, 488(7411):329–335, 2012. doi: 10.1038/nature11479.
- [74] B. J. Cardinale, J. E. Duffy, A. Gonzalez, D. U. Hooper, C. Perrings, P. Venail, A. Narwani, G. M. Mace, D. Tilman, D. A. Wardle, A. P. Kinzig, G. C. Daily, M. Loreau, J. B. Grace, A. Larigauderie, D. S. Srivastava, and S. Naeem. Biodiversity loss and its impact on humanity. *Nature*, 489(7415):326–326, 2012. doi: 10.1038/nature11373.
- [75] D. U. Hooper, E. C. Adair, B. J. Cardinale, J. E. K. Byrnes, B. A. Hungate, K. L. Matulich, A. Gonzalez, J. E. Duffy, L. Gamfeldt, and M. I. O’Connor. A global synthesis reveals biodiversity loss as a major driver of ecosystem change. *Nature*, 486(7401):105–108, 2012. doi: 10.1038/nature11118.
- [76] D. T. Newby, T. J. Mathews, R. C. Pate, M. H. Huesemann, T. W. Lane, B. D. Wahlen, S. Mandal, R. K. Engler, K. P. Feris, and J. B. Shurin. Assessing the potential of polyculture to accelerate algal biofuel production. *Algal Research*, 19:264–277, 2016. doi: 10.1016/j.algal.2016.09.004.
- [77] M. Loreau and C. de Mazancourt. Biodiversity and ecosystem stability: a synthesis of underlying mechanisms. *Ecology Letters*, 16(SUPPL.1):106–115, 2013. doi: 10.1111/ele.12073.

- [78] J. B. Shurin, R. L. Abbott, M. S. Deal, G. T. Kwan, E. Litchman, R. C. McBride, S. Mandal, and V. H. Smith. Industrial-strength ecology: trade-offs and opportunities in algal biofuel production. *Ecology Letters*, 16(11):1393–1404, 2013. doi: 10.1111/ele.12176.
- [79] A. Narwani and A. Mazumder. Bottom-up effects of species diversity on the functioning and stability of food webs. *Journal of Animal Ecology*, 81(3):701–713, 2012. doi: 10.1111/j.1365-2656.2011.01949.x.
- [80] M. Stockenreiter, A.-K. Graber, F. Haupt, and H. Stibor. The effect of species diversity on lipid production by micro-algal communities. *Journal of Applied Phycology*, 24(1): 45–54, 2012. doi: 10.1007/s10811-010-9644-1.
- [81] M. Stockenreiter, F. Haupt, A.-K. Graber, J. Seppälä, K. Spilling, T. Tamminen, and H. Stibor. Functional group richness: implications of biodiversity for light use and lipid yield in microalgae. *Journal of Phycology*, 49(5):838–847, 2013. doi: 10.1111/jpy.12092.
- [82] M. Bhattacharjee and E. Siemann. Low algal diversity systems are a promising method for biodiesel production in wastewater fed open reactors. *ALGAE*, 30(1):67–79, 2015. doi: 10.4490/algae.2015.30.1.067.
- [83] K. Gross, B. J. Cardinale, J. W. Fox, A. Gonzalez, M. Loreau, H. Wayne Polley, P. B. Reich, and J. van Ruijven. Species Richness and the Temporal Stability of Biomass Production: A New Analysis of Recent Biodiversity Experiments. *The American Naturalist*, 183(1):1–12, 2014. doi: 10.1086/673915.
- [84] C. M. Godwin, D. C. Hietala, A. R. Lashaway, A. Narwani, P. E. Savage, and B. J. Cardinale. Algal polycultures enhance coproduct recycling from hydrothermal liquefaction. *Bioresource Technology*, 224:630–638, 2017. doi: 10.1016/j.biortech.2016.11.105.
- [85] C. A. Klausmeier, E. Litchman, and S. A. Levin. Phytoplankton growth and stoichiometry under multiple nutrient limitation. *Limnology and Oceanography*, 49(4part2): 1463–1470, 2004. doi: 10.4319/lo.2004.49.4\_part\_2.1463.
- [86] R. W. Sterner and J. J. Elser. *Ecological stoichiometry: The biology of elements from molecules to the biosphere*. 2002. ISBN 9780691074917.
- [87] G. Markou and E. Nerantzis. Microalgae for high-value compounds and biofuels production: A review with focus on cultivation under stress conditions. *Biotechnology Advances*, 31(8):1532–1542, 2013. doi: 10.1016/j.biotechadv.2013.07.011.
- [88] E. C. Goncalves, A. C. Wilkie, M. Kirst, and B. Rathinasabapathi. Metabolic regulation of triacylglycerol accumulation in the green algae: identification of potential targets for engineering to improve oil yield, 2016.
- [89] D. Tilman, S. Ecology, and N. Jul. The Ecological Consequences of Changes in Biodiversity : A Search for General Principles. *Ecology*, 80(5):1455–1474, 1999. doi: 10.1890/0012-9658(1999)080[1455:TECOCI]2.0.CO;2.

- [90] M. J. Griffiths and S. T. L. Harrison. Lipid productivity as a key characteristic for choosing algal species for biodiesel production. *Journal of Applied Phycology*, 21(5): 493–507, 2009. doi: 10.1007/s10811-008-9392-7.
- [91] L. Rodolfi, G. Chini Zittelli, N. Bassi, G. Padovani, N. Biondi, G. Bonini, and M. R. Tredici. Microalgae for oil: Strain selection, induction of lipid synthesis and outdoor mass cultivation in a low-cost photobioreactor. *Biotechnology and Bioengineering*, 102(1):100–112, 2009. doi: 10.1002/bit.22033.
- [92] T. M. Mata, A. A. Martins, and N. S. Caetano. Microalgae for biodiesel production and other applications: A review. *Renewable and Sustainable Energy Reviews*, 14(1): 217–232, 2010. doi: 10.1016/j.rser.2009.07.020.
- [93] H. Hillebrand, C.-D. Dürselen, D. Kirschtel, U. Pollinger, and T. Zohary. Biovolume calculation for pelagic and benthic microalgae. *Journal of Phycology*, 35(2):403–424, 1999. doi: 10.1046/j.1529-8817.1999.3520403.x.
- [94] R. B. Levine, A. A. Bollas, M. D. Durham, and P. E. Savage. Triflate-catalyzed (trans)esterification of lipids within carbonized algal biomass. *Bioresource Technology*, 111:222–229, 2012. doi: 10.1016/j.biortech.2012.02.055.
- [95] C. J. Patton and J. R. Kryskalla. Methods of Analysis by the U.S. Geological Survey National Water Quality Laboratory-Evaluation of Alkaline Persulfate Digestion as an Alternative to Kjeldahl Digestion for Determination of Total and Dissolved Nitrogen and Phosphorus in Water. Technical report, U.S.G. Survey, 2003.
- [96] APHA. *Standard Methods for the Examination of Water and Wastewater: Including Bottom Sediments and Sludges*. American Public Health Association, New York, 1995.
- [97] S. Ringuet, L. Sassano, and Z. I. Johnson. A suite of microplate reader-based colorimetric methods to quantify ammonium, nitrate, orthophosphate and silicate concentrations for aquatic nutrient monitoring. *J. Environ. Monit.*, 13(2):370–376, 2011. doi: 10.1039/C0EM00290A.
- [98] M. Piorreck, K.-H. Baasch, and P. Pohl. Biomass production, total protein, chlorophylls, lipids and fatty acids of freshwater green and blue-green algae under different nitrogen regimes. *Phytochemistry*, 23(2):207–216, 1984. doi: 10.1016/S0031-9422(00)80304-0.
- [99] S. A. Channiwala and P. P. Parikh. A unified correlation for estimating HHV of solid, liquid and gaseous fuels. *Fuel*, 81(8):1051–1063, 2002. doi: 10.1016/S0016-2361(01)00131-4.
- [100] H.-Y. Shin, J.-H. Ryu, S.-Y. Park, and S.-Y. Bae. Thermal stability of fatty acids in subcritical water. *Journal of Analytical and Applied Pyrolysis*, 98:250–253, 2012. doi: 10.1016/j.jaap.2012.08.003.
- [101] G. Knothe. Improving biodiesel fuel properties by modifying fatty ester composition. *Energy & Environmental Science*, 2(7):759, 2009. doi: 10.1039/b903941d.

- [102] F. Jin, H. Zhong, J. Cao, J. Cao, K. Kawasaki, A. Kishita, T. Matsumoto, K. Tohji, and H. Enomoto. Oxidation of unsaturated carboxylic acids under hydrothermal conditions. *Bioresource Technology*, 101(19):7624–7634, 2010. doi: 10.1016/j.biortech.2010.04.056.
- [103] T. J. Benson, R. Hernandez, W. T. French, E. G. Alley, and W. E. Holmes. Elucidation of the catalytic cracking pathway for unsaturated mono-, di-, and triacylglycerides on solid acid catalysts. *Journal of Molecular Catalysis A: Chemical*, 303(1-2):117–123, 2009. doi: 10.1016/j.molcata.2009.01.008.
- [104] T. Bell, A. K. Lilley, A. Hector, B. Schmid, L. King, and J. A. Newman. A Linear Model Method for Biodiversity–Ecosystem Functioning Experiments. *The American Naturalist*, 174(6):836–849, 2009. doi: 10.1086/647931.
- [105] B. Gawel, M. Eftekhardadkhah, and G. Øye. Elemental Composition and Fourier Transform Infrared Spectroscopy Analysis of Crude Oils and Their Fractions. *Energy & Fuels*, 28(2):997–1003, 2014. doi: 10.1021/ef402286y.
- [106] D. R. B. Anderson and K. P. Burnham. *Model selection and multimodel inference*. Springer, 2nd edition, 2002. ISBN 0387953647.
- [107] D. C. Hietala, C. M. Godwin, B. J. Cardinale, and P. E. Savage. The effects of biochemical composition, microalgal species, concentration, temperature, and time on biocrude production by hydrothermal liquefaction. *Submitted*, 2018.
- [108] P. J. L. B. Williams and L. M. L. Laurens. Microalgae as biodiesel & biomass feedstocks: Review & analysis of the biochemistry, energetics & economics. *Energy & Environmental Science*, 3(5):554, 2010. doi: 10.1039/b924978h.
- [109] B. J. Bellinger, B. A. S. Van Mooy, J. B. Cotner, H. F. Fredricks, C. R. Benitez-Nelson, J. Thompson, A. Cotter, M. L. Knuth, and C. M. Godwin. Physiological modifications of seston in response to physicochemical gradients within Lake Superior. *Limnology and Oceanography*, 59(3):1011–1026, 2014. doi: 10.4319/lo.2014.59.3.1011.
- [110] S. O. Lourenço, E. Barbarino, P. L. Lavín, U. M. Lanfer Marquez, and E. Aidar. Distribution of intracellular nitrogen in marine microalgae: Calculation of new nitrogen-to-protein conversion factors. *European Journal of Phycology*, 39(1):17–32, 2004. doi: 10.1080/0967026032000157156.
- [111] S. Guo, X. Dong, C. Zhu, Y. Han, and Z. Wang. A simple modeling approach for characteristics analysis of hydrothermal liquefaction products from low-lipid aquatic plants. *Applied Thermal Engineering*, 125:394–400, 2017. doi: 10.1016/j.applthermaleng.2017.07.042.
- [112] J. M. Jarvis, J. M. Billing, Y. E. Corilo, A. J. Schmidt, R. T. Hallen, and T. M. Schaub. FT-ICR MS analysis of blended pine-microalgae feedstock HTL biocrudes. *Fuel*, 216(December 2017):341–348, 2018. doi: 10.1016/j.fuel.2017.12.016.

- [113] A. Croce, E. Battistel, S. Chiaberge, S. Spera, F. De Angelis, and S. Reale. A Model Study to Unravel the Complexity of Bio-Oil from Organic Wastes. *ChemSusChem*, 10(1):171–181, 2017. doi: 10.1002/cssc.201601258.
- [114] W.-T. Chen, Y. Zhang, J. Zhang, G. Yu, L. C. Schideman, P. Zhang, and M. Minarick. Hydrothermal liquefaction of mixed-culture algal biomass from wastewater treatment system into bio-crude oil. *Bioresource Technology*, 152:130–139, 2014. doi: 10.1016/j.biortech.2013.10.111.
- [115] W.-T. Chen, Y. Zhang, J. Zhang, L. Schideman, G. Yu, P. Zhang, and M. Minarick. Co-liquefaction of swine manure and mixed-culture algal biomass from a wastewater treatment system to produce bio-crude oil. *Applied Energy*, 128:209–216, 2014. doi: 10.1016/j.apenergy.2014.04.068.
- [116] O. Palardy, C. Behnke, and L. M. L. Laurens. Fatty Amide Determination in Neutral Molecular Fractions of Green Crude Hydrothermal Liquefaction Oils From Algal Biomass. *Energy & Fuels*, 31(8):8275–8282, 2017. doi: 10.1021/acs.energyfuels.7b01175.
- [117] P. Biller, R. Riley, and A. B. Ross. Catalytic hydrothermal processing of microalgae: decomposition and upgrading of lipids. *Bioresource Technology*, 102(7):4841–4848, 2011. doi: 10.1016/j.biortech.2010.12.113.
- [118] A. Ottolenghi, F. Bernheim, and K. M. Wilbur. The inhibition of certain mitochondrial enzymes by fatty acids oxidized by ultraviolet light or ascorbic acid. *Archives of Biochemistry and Biophysics*, 56(1):157–164, 1955. doi: 10.1016/0003-9861(55)90345-3.
- [119] J. S. Martinez-Fernandez and S. Chen. Sequential Hydrothermal Liquefaction characterization and nutrient recovery assessment. *Algal Research*, 25(May):274–284, 2017. doi: 10.1016/j.algal.2017.05.022.
- [120] C. Miao, M. Chakraborty, T. Dong, X. Yu, Z. Chi, and S. Chen. Sequential hydrothermal fractionation of yeast *Cryptococcus curvatus* biomass. *Bioresource technology*, 164:106–12, 2014. doi: 10.1016/j.biortech.2014.04.059.
- [121] F. Cheng, Z. Cui, L. Chen, J. Jarvis, N. Paz, T. Schaub, N. Nirmalakhandan, and C. E. Brewer. Hydrothermal liquefaction of high- and low-lipid algae: Bio-crude oil chemistry. *Applied Energy*, 206(August):278–292, 2017. doi: 10.1016/j.apenergy.2017.08.105.
- [122] DOE (U.S. Department of Energy). National Algal Biofuels Technology Review. Technical report, U.S. Department of Energy, Office of Energy Efficiency and Renewable Energy, Bioenergy Technologies Office, 2016.
- [123] M. C. Johnson and J. W. Tester. Lipid Transformation in Hydrothermal Processing of Whole Algal Cells. *Industrial & Engineering Chemistry Research*, 52(32):10988–10995, 2013. doi: 10.1021/ie400876w.

- [124] D. C. Hietala, C. M. Godwin, B. J. Cardinale, and P. E. Savage. The impacts of temperature, time, concentration, biochemical composition, and microalgal species on the aqueous co-product from hydrothermal liquefaction. *In preparation*, 2018.
- [125] D. López Barreiro, M. Bauer, U. Hornung, C. Posten, A. Kruse, and W. Prins. Cultivation of microalgae with recovered nutrients after hydrothermal liquefaction. *Algal Research*, 9:99–106, 2015. doi: 10.1016/j.algal.2015.03.007.
- [126] D. Klingler, J. Berg, and H. Vogel. Hydrothermal reactions of alanine and glycine in sub- and supercritical water. *Journal of Supercritical Fluids*, 43(1):112–119, 2007. doi: 10.1016/j.supflu.2007.04.008.
- [127] G. W. Roberts, B. S. M. Sturm, U. Hamdeh, G. E. Stanton, A. Rocha, T. L. Kinsella, M.-O. P. Fortier, S. Sazdar, M. S. Detamore, and S. M. Stagg-Williams. Promoting catalysis and high-value product streams by in situ hydroxyapatite crystallization during hydrothermal liquefaction of microalgae cultivated with reclaimed nutrients. *Green Chem.*, 17(4):2560–2569, 2015. doi: 10.1039/C5GC00187K.
- [128] L. Leng, J. Li, Z. Wen, and W. Zhou. Use of microalgae to recycle nutrients in aqueous phase derived from hydrothermal liquefaction process. *Bioresource Technology*, 256 (January):529–542, 2018. doi: 10.1016/j.biortech.2018.01.121.
- [129] M. R. Brown and S. W. Jeffrey. Biochemical composition of microalgae from the green algal classes Chlorophyceae and Prasinophyceae. 1. Amino acids, sugars and pigments. *Journal of Experimental Marine Biology and Ecology*, 161(1):91–113, 1992. doi: 10.1016/0022-0981(92)90192-D.
- [130] L. Zhang, H. Lu, Y. Zhang, B. Li, Z. Liu, N. Duan, and M. Liu. Nutrient recovery and biomass production by cultivating *Chlorella vulgaris* 1067 from four types of post-hydrothermal liquefaction wastewater. *Journal of Applied Phycology*, 28(2):1031–1039, 2016. doi: 10.1007/s10811-015-0640-3.
- [131] M. Déniel, G. Haarlemmer, A. Roubaud, E. Weiss-Hortala, and J. Fages. Bio-oil Production from Food Processing Residues: Improving the Bio-oil Yield and Quality by Aqueous Phase Recycle in Hydrothermal Liquefaction of Blackcurrant (*Ribes nigrum* L.) Pomace. *Energy and Fuels*, 30(6):4895–4904, 2016. doi: 10.1021/acs.energyfuels.6b00441.
- [132] J. B. Cotner and R. G. Wetzel. Uptake of dissolved inorganic and organic phosphorus compounds by phytoplankton and bacterioplankton. *Limnology & Oceanography*, 37 (2):232–243, 1992. doi: 10.4319/lo.1992.37.2.0232.
- [133] L. Garcia Alba, M. P. Vos, C. Torri, D. Fabbri, S. R. A. Kersten, and D. W. F. Brilman. Recycling Nutrients in Algae Biorefinery. *ChemSusChem*, 6(8):1330–1333, 2013. doi: 10.1002/cssc.201200988.
- [134] W. Costanzo, R. Hilten, U. Jena, K. C. Das, and J. R. Kastner. Effect of low temperature hydrothermal liquefaction on catalytic hydrodenitrogenation of algae biocrude

- and model macromolecules. *Algal Research*, 13:53–68, 2016. doi: 10.1016/j.algal.2015.11.009.
- [135] J. K. Volkman, M. R. Brown, G. A. Dunstan, and S. W. Jeffrey. The biochemical composition of marine microalgae from the class eustigmatophyceae. *Journal of Phycology*, 29:69–78, 1993.
- [136] A. B. Meggy. 175. Glycine peptides. Part I. The polymerization of piperazine-2 : 5-dione at 180°. *J. Chem. Soc.*, 1(1):851–855, 1953. doi: 10.1039/JR9530000851.
- [137] M. Faisal, N. Sato, A. T. Quitain, H. Daimon, and K. Fujie. Hydrolysis and cyclodehydration of dipeptide under hydrothermal conditions. *Industrial and Engineering Chemistry Research*, 44(15):5472–5477, 2005. doi: 10.1021/ie0500568.
- [138] J. S. Cox and T. M. Seward. The reaction kinetics of alanine and glycine under hydrothermal conditions. *Geochimica et Cosmochimica Acta*, 71(9):2264–2284, 2007. doi: 10.1016/j.gca.2007.01.020.
- [139] L. Sheng, X. Wang, and X. Yang. Prediction model of biocrude yield and nitrogen heterocyclic compounds analysis by hydrothermal liquefaction of microalgae with model compounds. *Bioresource Technology*, 247(June 2017):14–20, 2018. doi: 10.1016/j.biortech.2017.08.011.
- [140] J. G. Speight. *Petroleum Chemistry and Refining*. Taylor & Francis, Washington, DC, xiv edition, 1998. ISBN 1-56032-587-9.
- [141] J. J. Carroll, J. D. Slupsky, and A. E. Mather. The Solubility of Carbon Dioxide in Water at Low Pressure. *Journal of Physical and Chemical Reference Data*, 20(6): 1201–1209, 1991. doi: 10.1063/1.555900.
- [142] R. Wiebe and V. Gaddy. The solubility of carbon dioxide in water at various temperatures from 12 to 40 and at pressures to 500 atmospheres. critical phenomena\*. *Journal of the American Chemical Society*, 315(1):61–63, 1940. doi: 10.1021/ja01861a033.